

AN INVESTIGATION OF THE RELATIONSHIP BETWEEN LATERAL SPREADING AND
MASS DEPLETION OF AN LNAPL BODY IN CONTACT WITH GROUNDWATER AT
THE BEMIDJI, MN CRUDE OIL RELEASE SITE

by

DON A. LUNDY

(Under the Direction of John F. Dowd)

ABSTRACT

We tested a mass-balance mechanism that controls lateral spreading of a pool of crude oil, a light non-aqueous phase liquid (LNAPL), to a stable configuration on the water table in glacial outwash. This designated "North Pool" oil body is located at U.S. Geological Survey (USGS) research site near Bemidji, MN. The hypothesis states that any LNAPL body stops expanding when the rate of oil mass inflow into a downgradient area of the body balances with rates of mass depletion from that area. A periodic slug-test device was developed to provide aquifer parameters near the North Pool. During a 20-min trial test it obtained a transmissivity within 10% of that determined by the USGS with a 45-hr pumping test in the same aquifer. Recent and archived oil samples were analyzed for mobility-controlling fluid properties and chemical compositions. Mass losses based on changes in moles normalized to Pristane in all samples were used to develop relative mass losses and mass remaining over time. The results were used to estimate the 1979 oil release volume and mass based on an oil volume developed by the USGS using 1990-1992 core analyses. The derivative of the first-order decay function for

declining total mass provided mass loss rates in the range of reported historical CO₂ mass effluxes. Dated oil-body footprint areas were mapped and integrated with the mass depletion rates to obtain mean historical rates per unit area. Historical fluid and matrix properties were combined with oil thicknesses to model historical LNAPL transmissivities and oil potential gradients for a Darcy expression used to estimate mass inflow rates. During early spreading when the leading edge was advancing, daily mass inflow exceeded mass depletion rates. During slower late-time spreading, stability occurs within a period defined by intersecting mass-gain and mass-loss curves. Testing with individual oil flow-tubes showed that points along the leading edge can stabilize many years apart. When the LNAPL is unconfined in an effectively homogeneous media, time-dependent changes with LNAPL thickness, transmissivity, mass spreading, and mass depletion are approximated by first-order decay functions. LNAPL body stability testing is recommended at other sites with different LNAPLs and hydrogeologic conditions. Defensible predictions of when and where stability occurs can support LNAPL site management decisions and evolving regulatory policies.

INDEX WORDS: LNAPL, crude oil, mass-balance, oil body stabilization, oil composition, oil fluid properties, oil weathering, LNAPL transmissivity, sinusoidal testing, aquifer properties

AN INVESTIGATION OF THE RELATIONSHIP BETWEEN LATERAL SPREADING AND
MASS DEPLETION OF AN LNAPL BODY IN CONTACT WITH GROUNDWATER AT
THE BEMIDJI, MN CRUDE OIL RELEASE SITE

by

DON ANTHONY LUNDY

B.S. Geology, University of Texas at Austin, 1970

M.S. Geology, University of Wyoming, 1978

A Dissertation Submitted to the Graduate Faculty of The University of Georgia in Partial
Fulfillment of the Requirements for the Degree

DOCTOR OF PHILOSOPHY

ATHENS, GEORGIA

2014

© 2014

DON ANTHONY LUNDY

All Rights Reserved

AN INVESTIGATION OF THE RELATIONSHIP BETWEEN LATERAL SPREADING AND
MASS DEPLETION OF AN LNAPL BODY IN CONTACT WITH GROUNDWATER AT
THE BEMIDJI, MN CRUDE OIL RELEASE SITE

by

DON ANTHONY LUNDY

Major Professor:	John F. Dowd
Committee:	Todd C. Rasmussen
	Bruce L. Railsback
	Valentine Nzengun
	Adam Milewski

Electronic Version Approved:

Julie Coffield
Interim Dean of the Graduate School
The University of Georgia
December 2014

DEDICATION

This dissertation is dedicated to Mark Hult and others in the USGS who, with support from individuals in the Minnesota Pollution Control Agency, Albany County, and Enbridge Energy (formerly Lakeland Pipeline), established the National Crude Oil Spill Fate and Natural Attenuation Research Site in 1983 near Pineville, Minnesota. Over the past 30 years, research conducted by the USGS and university students and faculty has expanded our understanding of fundamental processes that influence the migration of all phases of light non-aqueous liquids (LNAPLs), thereby benefiting environmental professionals working on sites impacted by LNAPLs. Their contributions to the scientific community have also had a positive influence on the evolution of regulatory policies for LNAPL sites. It is an honor to be able to work on the site, to offer this contribution, and show appreciation of those who came before and made this possible.

ACKNOWLEDGEMENTS

I gratefully acknowledge the funding support received from the following entities and the individuals who helped me “make it happen:”

- American Petroleum Institute (API), Bruce Bauman;
- BP America, Mark Adamski;
- Enbridge Energy, Scott Lounsbury;
- Minnesota Pollution Control Association, Jim McCann;
- Groundwater & Environmental Services, Inc. (GES), Anthony Kull; and
- Watts-Wheeler Fund for geological research at the University of Georgia.

The USGS Minnesota office, led by Melinda Erickson, provided essential field support with field technicians coordinated by Jared Trost. Several USGS researchers offered helpful advice and support including Barbara Bekins, Mary Jo Baedecker, Isabelle Cozzarelli, Geoff Delin, William Herkelrath, and Ean Warren. Natasha Sihota, as a graduate student at the University of British Columbia, shared CO₂ efflux data that were useful for testing my hypothesis. Bruce Torkelson of Torkelson Geochemistry, Tulsa, OK provided laboratory analyses of oil and water samples and helped design two crude oil weathering experiments. Michael Brady and Rachel Spitz of PTS Laboratories, Santa Fe Springs, CA provided advice and support with the core collection and analyses. Brad Varhol of EON Products, Snellville, GA provided monitoring equipment and introduced me to Kurt DePeu, who provided critical assistance with the final design, construction, and local testing of the oscillating slug test device. Randall St. Germaine of Dakota Technologies, Fargo, ND provided guidance with the field

application and later with my interpretation of LIF data. To Roger Bannister and John Wiggert with GES who provided professional support with ArcGIS applications, my heartfelt thanks. And to the five members of my graduate committee who asked the right questions, gave sound advice, and taught me about performing scientific research, I will always be grateful. The UGA Geology Department with its cooperative arrangement with the Warnell School of Forestry and Natural Resources was a good fit for me and my research interests.

TABLE OF CONTENTS

	Page
ACKNOWLEDGEMENTS	v
LIST OF TABLES	x
LIST OF FIGURES	xi
CHAPTER	
1 INTRODUCTION	1
Purpose of Study	1
Expected Results	2
Literature Review	4
2 TESTING A CONCEPTUAL MODEL FOR LNAPL SPREADING TO A STABLE CONFIGURATION, PART 1 – HISTORICAL MASS DEPLETION AND FLUID PROPERTY CHANGES	13
Abstract	14
Introduction	15
Literature Review	19
Approach to Testing the Conceptual Model	22
Study Area Selection and Description	24
Hydrogeologic Setting	26
Sampling and Analysis Methods	29

Physical Fluid Property Changes	32
Estimation of Oil Mass Loss Rates	33
Historical Trend in Oil Mass Depletion	39
Summary and Conclusions	44
3 TESTING A CONCEPTUAL MODEL FOR LNAPL SPREADING TO A STABLE CONFIGURATION, PART 2 – ASSESSMENT OF MASS BALANCE	63
Abstract	64
Introduction	65
Method of Testing the Hypothesis	68
Oil Release and Initial Response	73
LNAPL Body Delineation and Migration	74
Aquifer Hydraulic Properties	77
Core Analyses	79
Baildown Test Analyses	82
Historical Oil Transmissivities	85
Testing for Stability at the LNAPL-Body Scale	89
Testing for Stability at the LNAPL-Flowtube Scale	92
Resistance at the Leading Edge	94
Summary and Conclusions	95
4 A PERIODIC SLUG TEST SYSTEM FOR DETERMINING AQUIFER PARAMETERS	125

Abstract.....	126
Introduction.....	128
Field Site Description	129
Oscillating Slug Test Equipment Description.....	131
Conversion of Slug Movement to Pumping/Injection Rates	132
Field Trial Testing.....	134
Results of Trial Testing.....	135
Summary and Conclusions	138
5 FINDINGS AND CONCLUSIONS	150
Testing the LNAPL Conceptual Model – Part 1.....	150
Testing the LNAPL Conceptual Model – Part 2.....	152
Periodic Oscillating Slug Test Method.....	154
Applications of Findings to Other LNAPL Sites	155
REFERENCES	161
APPENDICES	
A LIST OF GAS CHROMATOGRAPH (GC) PEAK COMPOUNDS.....	168
B LIST OF COMPOUNDS QUANTIFIED BY GC/MS ANALYSES.....	170
C GC PEAK MOLES RELATIVE TO 1 MOLE OF PRISTANE.....	173
D GC, PAH, BIOMARKERS, UCM MASS IN GRAMS, PERCENT, AND	
FRACTIONS LOST – PART 1	176
D GC, PAH, BIOMARKERS, UCM MASS IN GRAMS, PERCENT, AND	

FRACTIONS LOST – PART 2	182
E GRAIN-SIZE AND WATER RETENTION PLOTS, AND VAN-GENUCHTEN PARAMETER PLOTS OF API 2006 DATABASE AND BEMIDJI CORE DATA	188
F BAILDOWN TEST ANALYSIS FOR WELL 315.....	193
G EXAMPLE OF PARAMETRIC ANALYSIS OF MEAN OIL TRANSMISSIVITY FOR THREE BAILDOWN TESTS.....	198
H AQTESOLV PRINTOUTS FOR PERIODIC SLUG TESTS.....	202

LIST OF TABLES

	Page
Table 2.1: Historical Events, Processes, and Parameters Relevant to North Pool Stabilization. ..	47
Table 2.2: Results of Laboratory Physical Property Tests.....	48
Table 3.1: Hydraulic Properties for Upper and Lower Strata at the North Pool and Vicinity.....	99
Table 3.2: Summary of Soil Core Analytical Data for the North Pool Oil Body.	99
Table 3.3: LNAPL Transmissivity and Storativity Estimates from Baildown test Analyses.....	101
Table 3.4: Expressions for Estimating van Genuchten Water Retention Parameters – Functions of Hydraulic Conductivity based on two National Matrix Property Databases.....	101
Table 3.5: Results of Inverse Parametric Analyses of Oil Transmissivities for Baildown Test Wells.....	102
Table 3.6: Summary of Areas and Mass Losses Associated with Historical North Pool Footprints.....	102
Table 3.7: Summary of Areas and Mass Losses Associated with Flowtubes.....	103

Table 4.1: U.S. Geologic Survey aquifer test results for the Glacial Aquifer at the National Crude Oil Spill Fate and Natural Attenuation Research Site, Bemidji, MN.....	141
Table 4.2: Construction Details and Water Levels (7/21/2010) for Test Wells in the Glacial Aquifer at the Research Site, Bemidji, MN, USA.....	131
Table 4.3: Comparison of Aquifer Hydraulic Properties between the Periodic Slug Test and a Conventional Aquifer Test at the Research Site, Bemidji, MN, USA.....	132

LIST OF FIGURES

	Page
Figure 2.1: Conceptual model of LNAPL body spreading (Schwille, 1967)	49
Figure 2.2: Conceptual sketch of a stable LNAPL body in which lateral spreading is balanced by mass depletion that is most dominant in the distal flanks, and cannot build sufficient head to overcome capillary resistance at the leading edge.....	50
Figure 2.3: Cyclic relationships between fundamental processes affecting LNAPL mobility.....	51
Figure 2.4: Location of the USGS crude oil research site and North Pool for testing the hypothesis.	52
Figure 2.5: Average water-table contour map showing gradient direction through the North Pool footprint in 2012 and dissolved BTEX groundwater plume footprint in 1996.....	53
Figure 2.6: Geochemical zones within the saturated and unsaturated zones at a crude oil pipeline release site near Bemidji, MN (Delin et al., 1997)	54
Figure 2.7: Map of sampling locations within and near the North Pool oil body.....	55
Figure 2.8: Plots of laboratory determined physical fluid properties at 8.5 °C for both recent (2010-2012) and archived (1984-2008) oil/water samples.	56

Figure 2.9: Historical changes in oil density and viscosity at four wells in the North Pool.....	57
Figure 2.10: Normalized moles of GC analytes in the reference oil and two well 411 oil samples.....	58
Figure 2.11: Plots of calculated trends for (a) fraction of North Pool mass remaining relative to the reference oil based on changes in oil composition, and (b) base-case estimate of mass of remaining North Pool oil following the 1979 release event.	59
Figure 2.12: Calculated historical remaining North Pool oil mass decline curves developed from 1990-1992 total volume estimate based on core analyses (Delin and Herkelrath, 2014). .	60
Figure 2.13: Plot of calculated historical North Pool base rate of mass depletion and mass losses inferred from direct measurements and modeling of CO ₂ efflux to the land surface.	60
Figure 2.14: Histograms of oil saturations in core samples collected during (a) 1990-1992 at ten locations by the USGS, and (b) 2010-2011 at eight locations within the North Pool area	61
Figure 2.15: Plot of benzene concentrations in groundwater (USGS website) and equilibrium benzene concentrations calculated with mole fractions of benzene in oil samples collected 2010-2012.	62
Figure 3.1: Oblique aerial photograph looking east of the August 1979 crude oil release site, including an open recovery trench in the North Pool area (upper left), and surface staining along the sinuous flowpath of oil to a wetland located approximately 200 m south of the release point (lower right; Delin, 2012, personal communication).....	104
Figure 3.2: Map of research site with pipeline release location, excavation area, and USGS monitoring wells relative to inferred locations of inferred historical North Pool leading edges.....	105

Figure 3.3: Topographic base map showing the pipeline and 1979 release point with inferred approximate limit of the North Pool oil body in 2012.....106

Figure 3.4: Map of the North Pool 2012 footprint area with locations of wells, soil borings, LIF soundings, and coreholes107

Figure 3.5: Map and section views of the North Pool oil body defined by May 2011 LIF signatures. Weaker responses above the historical high water table represent residual oil in the vadose zone; strong responses between the high and low water-table positions represent potentially mobile oil.108

Figure 3.6: Plots of depths to oil and water at: a) 532A, and b) 604A that illustrate the inverse relationship between water table position and presence or absence of oil. Well 532A is the most downgradient well and 604A is the most upgradient well within the North Pool footprint area.....109

Figure 3.7: Map of mean water-table contours and ENE gradient beneath the North Pool. The 34-year average magnitude of 0.002644 is used to estimate historical oil-table gradients using time-dependent changes in oil density110

Figure 3.8: Mobile oil potentiometric surfaces (oil tables) for a) fall 1989 (data from Landon, 1993), and b) summer 2010 including inferred limits of the North Pool in 2012111

Figure 3.9: Groundwater potentiometric surfaces (water tables) for a) fall 1989 (data from Landon, 1993), and b) summer 2010 including inferred limits of the North Pool in 2012.112

Figure 3.10: Core lab photologs, lithologies, and fluorescence levels plotted with nearby LIF signature plots, and the highest, lowest, and July 2010 water-table elevations along a

traverse oriented WSW to ENE following the hydraulic gradient of the North Pool.....	113
Figure 3.11: Best-fit trends of historical oil thicknesses observed in wells 315, 411, and 421B.....	114
Figure 3.12: Oil densities at selected wells plotted with elapsed time since the 1979 pipeline release. Best-fit functions for wells 315, 411, and 421B were used in estimating historical oil transmissivities.	115
Figure 3.13: Oil dynamic viscosities at selected wells plotted with elapsed time since the 1979 pipeline release. Best-fit functions for wells 315, 411, and 421B used in estimating historical oil transmissivities.....	116
Figure 3.14: Sequences of possible historical oil saturations at location 421B based on matrix properties inferred from baildown test results and core lab analyses, combined with oil thickness records, and changes in fluid properties caused by weathering.....	117
Figure 3.15: Calculated historical oil transmissivities at the three baildown test wells	118
Figure 3.16: Plot of North Pool leading edge vs. time based on first occurrences of oil at selected wells. Distances are measured downgradient from LIF location TG1117 located near well 421B.....	118
Figure 3.17: Map of the approximate historical North Pool footprint areas inferred from USGS well gauging data, observations in soil borings, a geophysical (LIF) survey, and a CO ₂ efflux investigation.	119
Figure 3.18: Inferred historical oil flow directions in relation to historical footprint areas and boundaries between the northwest, central, and downgradient areas. Flowtubes from	

three wells are composed of flow-arrow segments connecting sequential positions of the leading edge	120
Figure 3.19: Historical oil flow directions from three baildown test wells inferred from elevation contours on the surface of highest occurrences of LIF-detected oil within the 2012 North Pool footprint area.....	121
Figure 3.20: Plots of a) calculated and b) projected mass gain and loss rates in downgradient area of the North Pool and showing a stabilization window of opportunity with an oil body-scale analysis.....	122
Figure 3.21: Plots of a) calculated and b) projected rates of mass gains and losses in three oil flowtubes starting at baildown test wells in the North Pool, showing when stabilization can occur at the intersection of paired mass-gain and mass-loss curves for each well. ...	123
Figure 3.22: Critical in-well LNAPL thicknesses calculated with measured displacement heads and best-fit estimates of air-water, air-oil, and oil-water tensions when oil density is 0.9 gm/mL observed near the 2012 downgradient leading edge of the North Pool	124
Figure 4.1: Location of the National Crude Oil Spill Fate and Natural Attenuation Research Site near Bemidji, MN, and locations of the 1979 crude oil pipeline release, migration pathways on the land surface, and three oil bodies in contact with shallow groundwater.	144
Figure 4.2: Photograph of the oscillating slug test device set up to begin a test at a site control well.	145
Figure 4.3: Conceptual sketch of selected components of the sinusoidal slug test equipment. Positions of rotating arm are lettered A, B, C, and D.	146

Figure 4.4: Plot of transducer-logger data for a trial oscillating slug test, July 10, 2010. Slug dimensions were length = 5 ft and diameter = 2.5 inches; and test well diameter = 4 inches... 147

Figure 4.5: Locations of periodic trial test well cluster and well locations for the USGS pumping test shown with other wells within and near the North Pool oil body148

Figure 4.6: Water level response to multiple slug oscillations at control well 534A, including shutdown/recovery periods at approximately 6.9 and 16.8 min of elapsed time.....149

Figure 4.7: Plots of modeled slug movement, recorded water level response, and calculated pumping rates for the first three slug oscillations in control well 531A.....150

CHAPTER 1

INTRODUCTION

Purpose of Study

In the past decade the stability of a light non-aqueous phase liquid (LNAPL) source zone for subsurface vapor and aqueous phase plumes has become an essential element of a growing number of risk-based regulatory policies at the state level. If the LNAPL body is still spreading laterally downgradient, further movement of the source zone can allow growth of vapor and groundwater plumes, thereby increasing risks of exposure. This study investigates the relationship between the lateral spreading and simultaneous mass depletion of an LNAPL body that is approaching a stable configuration in contact with groundwater.

There are two fundamental undisputed premises in addressing these phenomena. The first is that a sudden release of LNAPL with a finite volume large enough to reach the water table will spread laterally and vertically away from the initial water-table contact zone. Following physical laws governing multiphase fluid flow, the LNAPL initially spreads radially and assuming the media is not strongly anisotropic, moves generally downgradient along the water table. The second premise is that along its migration route, the LNAPL is continuously losing mass by partitioning of hydrocarbon compounds to subsurface air, water, and the solid matrix, where it can be transformed by indigenous microbial populations. Compounds that are not readily biodegraded can still be transported away from the LNAPL body, and some of the mobile LNAPL can be transferred to a residual state as it spreads laterally and vertically with water-table fluctuations (API, 2004).

The natural rate of spreading declines over time and eventually comes to rest occupying a stable configuration. It seems intuitively obvious that the loss of mass along the migration route must influence spreading, eventually reaching a point where these two “opposing forces” balance. But many questions come to mind about the mechanisms that control the time and place that stability occurs. When and where does the mass balance occur? What is the best way to measure the mass fluxes? Would the time to reach a stable configuration be predictable? Which among the following factors have the greatest effect: composition or type of LNAPL released, when the release occurred, the release volume, hydraulic properties of the porous media, depth to and gradient on the water table, or the geochemical environment at the time of the release or at a later time as the microbial communities evolve? Is the mass balance demonstration all that is needed to prove an LNAPL body is stable? Do we also need to evaluate the resistance of penetration of pristine earth materials at the leading edge with field samples and laboratory tests? Because the questions are so numerous and concern by regulators and the regulated community so keen, our understanding of how the physical and bio-geochemical processes control the timing and spatial distribution of a spreading to a stable configuration works is attracting attention among an increasing number of environmental professionals.

Expected Results

The basic hypothesis being tested in this investigation is that a finite and sudden LNAPL release volume that reaches the water table will spread laterally to a stable configuration with continual internal LNAPL migration that becomes offset and balanced by mass depletion over a downgradient area and is supported by non-wetting fluid capillary resistance at a stable leading edge. Chapter 2 provides several figures and a written description of the basic conceptual model of LNAPL spreading, mass depletion, and stabilization, with the added condition that the

LNAPL will continue moving slowly from the area it first encountered the water table towards the leading downgradient edge and lateral outer fringes of the body that has a stable footprint area. That is, the LNAPL is still flowing towards the edges but is going away before it can build sufficient head at the leading edges to overcome the resistance to further invasion of pristine soils. This implies that one may be able to show a measureable recoverability of the LNAPL after it has reached a stable configuration.

The study plan was to select a well characterized LNAPL site where the history of the release -- timing and volume -- were known and movement of the LNAPL had been detected in monitoring wells, and where the hydrogeologic conditions were also well characterized by previous research. The site and LNAPL body chosen to test the basic hypothesis was a crude oil released from a pipeline break in 1979. Due to the location of the site in a remote and uninhabited area in northern Minnesota, the risks of exposure were considered minimal and the site was dedicated to research overseen by the U. S. Geological Survey in 1983. The value of site-specific historical data gathered on the site to the methods applied here is demonstrated in Chapters 2 and 3. The results and conclusions were expected to be easy to achieve without major surprises.

While a series of coupled mass balance equations can be specified, it is challenging to measure all the parameters that must be quantified in order to apply it. The subsurface processes influencing stabilization are inter-dependent and heterogeneously distributed, so that an above-average resolution of site conditions is needed to quantify the uncertainty of when and where the leading edge will stop advancing. Given a large enough sample, findings can be expressed within confidence intervals at a specified probability. A higher level of certainty can only be found in continued monitoring near the leading edge. This investigation provides a way to

investigate the stabilization issue by a method that can be used for making plume management decisions based on the likelihood of the LNAPL body being stable, rather than being absolutely stable.

Literature Review

Stabilization of an LNAPL body is controlled by physical, chemical, and biological processes that interact with the bulk LNAPL fluid and with hydrocarbon compounds of which it is composed. The investigation of these processes is multi-disciplinary and for that reason the literature review was organized around different but related topics. These topics become the focus of each succeeding chapter. Accordingly, the literature reviews are organized around the weathering of crude oil (Chapter 2), LNAPL flow through in porous media (Chapter 3), and well hydraulics/aquifer mechanics (Chapter 4). Because a significant amount of research on these topics has occurred at the research site, relevant documents covering site-specific conditions are included with citations from other sources in the scientific literature.

Crude Oil Weathering

The effects of weathering on physical properties of crude oil at the North Pool site are similar to the effects observed and studied for decades by the petroleum industry. Crude oils start out being composed of a greater percentage of lighter hydrocarbons and with smaller densities and viscosities. As the oil migrates away from the source rock area, it loses mass by the processes of dissolution to flowing groundwater and by microbial degradation of the dissolved fraction. The oil can be temporarily held in structural or stratigraphic traps, which gain and lose oil, as it migrates toward submarine or terrestrial seeps. The latter create the world's largest reservoirs of crude oil, which are the tar sand deposits having the most severely weathered oil (Head et al. 2003).

Weathering changes the chemical composition and increases oil density, viscosity, and interfacial tensions between the oil and other fluids (gas and water). Long-term abiotic (“water washing”) and biological (microbial degradation) processes combine to reduce oil mobility and recoverability, which increases production costs for crude oil producers (Head et al. 2003).

In 34 years following a pipeline release at the study site, the oil changed from unweathered to a Peters and Moldowan (1993) classification of moderately weathered oil. This classification is based on the oil density changing from approximately 0.85 gm/mL in the fresh oil in 1979 to a maximum value of 0.90 gm/mL (API gravity change from 36 to 26) in the most weathered oil sample collected in 2012. It is also based on many C4-C35 hydrocarbons having been completely or partially removed based on gas chromatography (GC) tests performed in 2010-2012 on USGS archived oil samples collected from various dates between 1984 and 2008 and those collected during 2010-2012 field seasons.

A number of research projects at the North Pool have focused directly or indirectly upon weathering of the crude oil. In the late 1980s, Landon (1993) collected 13 oil samples, including ten from North Pool wells and three from south pool wells. He performed GC/MS analyses that identified 57 compounds in the C4-C12 range and performed physical property tests including, refractive index, density and specific gravity, dynamic viscosity, and refractive index. He used the least weathered sample from well 604A as a reference for determining the degree of alteration and the relative amount of mass losses for each of the other samples. He performed a 70-hour laboratory weathering experiment involving evaporation of the 604A sample collected in June 1989 and used the lab results to quantify mass losses from field samples. Landon estimated that the mass losses varied spatially in the North Pool and ranging from 0 to 11% and averaging 3.8% among 13 oil samples. He found a correlation between changes in physical

properties (density, viscosity, and refractive index) with changes in composition (loss of C4 to C12 compounds relative to Decane, a C10 compound). He noted that these losses were minimal estimates because they only represented changes in C4-C12 compounds. The spatially averaged rate of mass depletion over the North Pool footprint area from 1979-1989 was estimated to be approximately 0.112 kg/m²/yr. Using North Pool footprint shown by Landon (1993), this would have been equivalent to approximately 0.43 kg/day over the affected area. Given a larger area extending upgradient to the pipeline release point and further north as justified by more recent observations in cores and laser-induced fluorescence (LIF; covered in Part 2), the average total mass depletion rate may have been at least 40 to 50% larger (0.60 to 0.64 kg/day) for the North Pool during the first decade following the release.

Chaplin et al. (2002) estimated rates of mass loss from the oil body based on modeling production and movement of gases through the vadose zone above the oil body. They applied a gas transport model R-UNSAT (Lahvis and Baehr, 1997) and calibrated to the soil gas concentrations of O₂, CO₂, and CH₄ in samples from vadose zone wells along a transect oriented down the water table gradient along the central axis of the North Pool. Rates of O₂ loss and CO₂ production represented the rate of aerobic degradation, and rates of CH₄ production represented the rate of methanogenesis within and below the oil body. They estimated mass loss rates of 10.5 kg/day in 1985 and 1.99 kg/day in 1997. The predominant oil weathering and mass loss mechanisms in 1985 were volatilization and aerobic degradation. By 1997 the dominant weathering processes had changed to biodegradation under methanogenic conditions.

Molins et al. (2009) used the geochemical and gas flow model of Molins and Mayer (2007) which allows for both diffusion and advection of the gas phase, aerobic through methanogenic reactions, the transport of N₂ and Ar, but assumes the oil phase is not spreading.

They calibrated their model to O₂, CO₂, and CH₄ using N₂ and Ar to constrain the results. They simulated reactions and gas distributions for the summer of 2007, representing 28 years following the 1979 release. The average rate of mass release from the oil body (“smear zone”) was 0.13 mol CH₄/m²/day, which was approximately double the rate reported by Chaplin et al. (2002) of 0.07 mol CH₄/m²/day. Uncertainties identified with model results included soil gas saturations (percentages of the void space occupied by gas), tortuosities, and a lack of CO₂, and CH₄ efflux measurements at the land surface to better define that boundary condition.

While the oil is known to be composed of 150 to 200 hydrocarbon compounds, previous site work reveals that there may be between 500 and 1000 individual organic compounds dissolved in the groundwater (Thorn and Aiken, 1998) resulting from a complex sequence of biodegradation steps by microbes within micro-environments (Bekins et al. 1999). Some of these compounds may partition back into the oil in low concentration. Listing and capturing all compounds and biogeochemical reactions is currently intractable. Small oil samples (few mL) drained from soil cores exhibit a greater degree of weathering at the upper and lower boundaries of the oil body, where the oil is more exposed to air or groundwater (Bekins et al. 2005), consistent with weathering rinds observed in crude oil reservoirs (Head et al., 2003). Microenvironments in the subsurface altered the originally homogenous oil by different degrees and created spatially heterogeneous oil within the heterogeneous porous media near the water table fluctuation zone.

Between 2010 and 2013, a team of researchers from the University of British Columbia (UBC) have measured the efflux of CO₂ at the land surface overlying and near the North Pool footprint area. They took repeated direct readings of CO₂ efflux with the dynamic closed chamber method developed for the agricultural engineering industry at numerous stations

forming a grid pattern over the oil body. Monitoring at locations near and outside the North Pool was performed to estimate and subtract production of CO₂ by soil respiration. Sihota et al. (2011) estimated the total rate of mass depletion by biodegradation in the saturated and unsaturated zones to be approximately 4.29 kg/day over the North Pool area.

LNAPL Conceptual Model Developments

The earliest description of processes associated with the migration of petroleum product into the subsurface and spreading along the water table was described by Schuille (1967). He recognized that spreading of the light non-aqueous phase liquid (LNAPL) body (here synonymous with “oil pool” and “oil body”) would eventually stabilize but did not attribute that to the loss of mass as it was migrating. For several decades, many workers assumed that oil body stability was reached only by spreading to immobile residual oil saturations as evidenced by popular texts and technical guidance (e.g., de Pastrovich et al., 1979; Freeze and Cherry, 1979; API, 1989).

By the early 1990s, conceptual and mathematical models for the growth, stabilization, and shrinkage of aqueous phase contaminant plumes controlled by rates of mass depletion from source and plume areas was established in the groundwater literature (National Research Council, 1993). Statewide investigations of BTEX plumes associated with historical petroleum fuel releases in California (Rice et al. 1995) and in Texas (Mace et al. 1997) documented that over 90% of the groundwater plumes had reached a stable configuration or were shrinking. These studies served to validate the idea that groundwater plumes that do not reach natural discharge areas or active wells will eventually equilibrate when the rates of mass discharges from source areas balance with mass depletion rates in downgradient areas. Huntley and Beckett (2002) cited both reports as evidence of light non-aqueous phase liquid (LNAPL) area stability,

which occurred when the rates of dissolution, vaporization, and degradation exceed lateral LNAPL migration.

In the mid-2000s a growing number of environmental professionals approached the LNAPL stability question by evaluating multiple lines of evidence driven by available site data, using both qualitative observations and quantitative methods (Science Advisory Board, 2006; ASTM, 2007; ITRC, 2009). Qualitative evidence generally includes a stable dissolved-phase (e.g. BTEX) plume, an LNAPL source zone known to be decades old, and the lack of LNAPL detections in monitoring wells located near and downgradient of the LNAPL leading edge. The quantitative elements may include an estimate of the non-wetting fluid entry pressure at the leading edge (Charbeneau, 2007), small LNAPL mobility and transmissivity values based on field baildown tests and fluid properties (ITRC, 2009), and finally on depletion of contaminant mass in the source zone that could balance with lateral spreading.

Relatively few sites have been adequately investigated to characterize the history of LNAPL spreading, weathering, and hydraulic and fluid property parameters that have controlled historical spreading rates. Mahler et al. (2012a) conducted field tests assuming a stability status of LNAPL bodies at seven sites with in-well dilution tracer tests to estimate LNAPL transmissivity and mass flux rates against mass depletion rates estimated with CO₂ mass efflux measurements. However, plume stability was assumed and not proved (Mahler et al. 2012a)

In a laboratory sand-box experiment with pure MTBE as the LNAPL, Mahler et al. (2012b) observed that LNAPL body spreading ceased when a mass balance existed between the rate of mass input at the source balanced with the rate of mass depletion over the downgradient LNAPL body. They developed a conceptual and mathematical model based on the lab experiment with simplifying assumptions. Scenario calculations showed the sensitivity of a

stable LNAPL footprint size to the constant rates of mass input and output. While the lab experiment confirmed the validity of a mass-balance control on the process of plume stabilization and showed that residual saturations are not required to ensure a stable LNAPL body, “the applicability of the predictive model to real-world field situations” remained in question in their concluding remarks.

The approach taken in the current investigation is to define an historical trend for the oil mass losses attributed to weathering, and develop a similar trend for oil mass migration with the intention of converting these to rates per unit time over the same areas. While the mass losses are based on the history of compositional changes, the mass gains are obtained by modeling the oil movement from the infiltration source zone into a downgradient zone. That effort requires a conceptual and mathematical model for calculating the flow of oil in the presence of water and air in response to natural gradients influenced by the water table and fluid properties consistent with the basic principles of multiphase fluid flow through porous media.

The application of Darcy’s law to non-aqueous fluids (oil and gas) and the non-wetting fluid threshold pressure needed for the analysis of resistance at the leading edge of an oil pool were established in the 1930s and 1940s in the petroleum engineering literature (Bear, 1972). These were applied to LNAPL in contact with shallow groundwater in the 1960s and 1970s by European investigators, including Schwille (1967) and van Dam (1967). Zilliox and Muntzer (1975) and Schiegg (1980, 1983) extended their work to explain the occurrence of LNAPL in wells screened across the water table. These papers provided the first conceptual model that accounted for effects of capillarity and LNAPL fluid properties on in-well LNAPL thicknesses at static equilibrium. The development of mathematical expressions for saturations of immiscible fluids sharing space in porous media developed for applications in petroleum and soil physics

were used by Lenhard and Parker (1990) and Farr et al. (1990) for a new model with the LNAPL saturation profile balanced around a static water table in porous media in equilibrium with an in-well thickness of LNAPL. Huntley and Beckett (2002) extended the saturation profile model with a homogeneous-isotropic matrix to a heterogeneous model composed of two or three layers with contrasting matrix properties. The multi-layered model still assumes a homogenous LNAPL fluid unevenly distributed in vertical hydraulic equilibrium across all three layers. No simplified mathematical model for spatially heterogeneous fluids in heterogeneous porous media is available for testing the stability hypothesis.

The saturation profile model provides a way to relate in-well thickness to the distribution of LNAPL in porous media near the water table at static equilibrium. In order to estimate transmissivity of the mobile LNAPL-bearing zone in the single homogenous matrix, one must quantify the following ten parameters: a) in-well LNAPL thickness at static equilibrium; b) five fluid properties affecting mobility at approximate field temperatures – density and viscosity of LNAPL and water (or specific gravity and relative viscosity), air-water and air-oil surface tensions, and oil-water interfacial tension; and c) four matrix properties of the porous media – hydraulic conductivity (or intrinsic permeability), capillary properties (van Genuchten *alpha* and van Genuchten *n*; or Brooks-Corey non-wetting fluid entry pressure and pore-size distribution index), and residual water saturation.

The matrix porosity can be used for estimating specific LNAPL or water volumes and residual LNAPL saturations can be used to account for LNAPL mass temporarily stored above and below the mobile LNAPL zone, or to account for transfer of mass associated with water table changes (Parker et al., 1987; Lenhard and Parker, 1990).

Hydraulic Testing for Aquifer Parameters

The estimation of aquifer parameters from periodic hydraulic-head fluctuations is not new to aquifer testing. Ferris (1951) presented a method for estimating hydraulic diffusivity (ratio of transmissivity to storativity) from the lag time and amplitude of pressure-head sine waves on the water table propagating landward from the shoreline in coastal areas. Following the 1964 Alaskan earthquake, which caused sinusoidal water-level fluctuations in wells thousands of miles away, Cooper et al. (1964) presented a solution for estimating aquifer transmissivity and storativity based on the sine wave dissipation.

Rasmussen et al. (2003) analyzed periodic water level responses to sinusoidal pumping and re-injecting groundwater at a control well. Successful field trials involving observation wells in unconfined, semi-confined, and confined aquifers were carried out at the Savannah River site in South Carolina, USA. Transmissivity and storativity values obtained with their analytical solution agreed within a few percent of solutions obtained using the commercial software AQTESOLV (Duffield, 2010 personal communication).

Slug tests are commonly used to estimate hydraulic conductivity of aquifers using the methods of Hvorslev (1951), Bouwer and Rice (1976), Cooper et al. (1967) to name a few. However, slug tests are considered to only represent conditions in the immediate vicinity of the test well and for that reason are not as representative of aquifer properties as longer-term pumping tests with use observation wells such as the Theis (1935) solution and others.

For these reasons, a sinusoidal test method was developed and field tested in order to combine the benefits of the slug test with those of the pumping test to provide aquifer parameter estimates without the expense of pumping and handling large quantities of groundwater.

CHAPTER 2

TESTING A CONCEPTUAL MODEL FOR LNAPL SPREADING TO A STABLE CONFIGURATION, PART 1 – MASS DEPLETION RATES AND FLUID PROPERTY CHANGES¹

¹ Lundy, D.A., Dowd, J. F., Railsback, L. B. To be submitted without the appendices to *Ground Water, Journal of the Association of Ground Water Scientists and Engineers*.

Abstract

Part 1 of this two-part paper presents an algorithm used to estimate historical rates of mass depletion within an LNAPL footprint area associated with the “North Pool” crude oil body at the USGS crude oil research site near Bemidji, MN. Samples of oil were collected from monitoring wells and cores during the summers of 2010-2012 and were analyzed along with ten archived oil samples collected from the same set of wells plus a 1984 pipeline oil sample to represent the oil released in August 1979. Fluid properties that influence LNAPL mobility were measured in 27 samples at an average field temperature of 8.5 °C. All samples were analyzed by gas chromatography (GC), and three samples representing the most to least weathered oils were selected for GC/MS analysis to identify PAHs and biomarkers. The moles of each GC-detected compound were normalized to moles of Pristane, a biomarker detected in all samples. Normalized moles of each GC compound in each sample were converted to equivalent incremental masses and summed, then divided by the corresponding sum of incremental volumes to obtain sample densities. Additional mass was added by accounting for recalcitrant biomarkers, PAHs, and by adding 4 to 6% of an unresolved complex mixture in order to achieve a mass balance with lab-determined densities. Mass losses by weathering were defined as the differences between total summed masses for each sample relative to the summed masses of the same compounds in a reference oil. A best-fit first-order decay trend with a decay constant of 0.0308 yr^{-1} expresses the fraction of mass lost as a function of elapsed time in years since 1979. Subtracting that function from unity provided the fraction of total mass remaining, treated as the base-case estimate for the North Pool. The original release volume and mass, 128,000 L and 109,000 kg, were estimated by dividing the North Pool mass in mid-1991 (estimated by the

USGS with core analyses) by the base-case fraction calculated for 1991. The base-case depletion trend and the starting mass were used to estimate average loss rates from 1979 (2.7 kg/day) until mid-2013 (7.2 kg/day). These compare favorably with loss rates reported by others based on rates of biogenic CO₂ efflux from the North Pool footprint area. The mass loss rates are considered suitable for modeling historical mass depletion rates over downgradient footprint or flowtube areas of the North Pool in the Part 2 companion paper.

Introduction

The earliest description of processes associated with the migration of petroleum product into the subsurface and spreading along the water table was described by Schwille (1967). Figure 2.1 shows his conceptual model for staged migration of oil released near the land surface as it migrated through the vadose zone and reached the water table. Under the influence of gravity and capillary forces, the oil spreads within the capillary fringe and uppermost saturated zone at declining rates until the last stage that involved creeping of the leading edge in the capillary fringe. Schwille (1967) recognized that the floating oil plumes eventually reached a stable configuration and that the oil body transferred hydrocarbon compounds in the gas phase to the vadose zone and in the aqueous phase to the groundwater zone. But he did not suggest a relationship between the loss of mass to air and water that affected the rate of spreading or the eventual stabilization. For several decades, many workers assumed that oil body stability was reached only by spreading to immobile residual oil saturations as evidenced by popular texts and technical guidance (e.g., de Pastrovich et al., 1979; Freeze and Cherry, 1979; and API, 1989).

By the early 1990s, conceptual and mathematical models for the growth, stabilization, and shrinkage of aqueous phase contaminant plumes controlled by rates of mass depletion from source and plume areas was established in the groundwater literature (National Research

Council, 1993). Statewide investigations of BTEX plumes associated with historical petroleum fuel releases in California (Rice et al. 1995) and in Texas (Mace et al. 1997) documented that over 90% of the groundwater plumes had reached a stable configuration or were shrinking. These studies served to validate the idea that groundwater plumes that do not reach natural discharge areas or active wells will eventually equilibrate when the rates of mass discharges from source areas balance with mass depletion rates in downgradient areas. Huntley and Beckett (2002) cited both reports as evidence of light non-aqueous phase liquid (LNAPL) area stability, which occurred when the rates of dissolution, vaporization, and degradation exceed lateral LNAPL migration.

Expanding on earlier API guidance, Charbeneau (2007) developed expressions for evaluating the LNAPL mobility and recoverability, and thickness of mobile LNAPL needed to overcome capillary resistance at the leading edge of a stable LNAPL body. Models and methods for demonstrating LNAPL body stability are currently being developed and tested with field and laboratory data. A conceptual model and semi-analytical solution was recently presented by Mahler et al., 2012a and colleagues at Colorado State University (CSU), who found evidence to support the conceptual model at seven sites (Mahler et al., 2012 b).

These developments reflect a national trend of environmental professionals, including trade organizations and regulators, taking more interest in the relationships between the LNAPL source areas and the vapor and groundwater plumes that drive exposure risks to humans and ecosystems. The American Petroleum Institute (API) has funded research focused on improved methods for characterizing LNAPL release sites for the purposes of evaluating limits to recoverability of mobile LNAPL, the nature of residual LNAPL, and limits of engineered solutions to reducing the longevity of LNAPL contaminant sources (Sale, 2001; Huntley and

Beckett (2002); Bondy et al. (2006); Charbeneau (2007, and 2011). API funded the development of a free browser-based compendium of LNAPL educational content and software (API, 2004), and is currently developing a website portal with technical information for the environmental community that can more easily be updated. ASTM subcommittees were formed with missions to create new standards for developing an LNAPL Conceptual Site Model (LCSM) for release sites (ASTM, 2007), and for estimating LNAPL transmissivity (ASTM, 2012), which is now recognized as a more workable metric for evaluating LNAPL recoverability. The outpouring of information and guidance has caused a growing number of regulatory agencies to revisit their policies regarding practical endpoints to LNAPL removal and to re-focus attention more on long-term risk reduction (ITRC, 2009 and 2011).

Our understanding of the mechanisms that control the spreading and stabilization of an LNAPL body fits with our understanding of the natural attenuation of contaminant sources and vapor and groundwater plumes that may cause exposure risks. The environmental community could benefit from a conceptual model to underpin predictive mathematical models for evaluating when a release could reach a sensitive receptor (e.g., well, spring, or surface water), or whether further spreading will occur by shutting down an LNAPL mass recovery system that has become marginally feasible due to reductions in LNAPL transmissivity.

This two-part paper presents results of testing and refining this conceptual model of light non-aqueous phase liquid (LNAPL) body spreading to a stable configuration at the National Crude Oil Spill Fate and Natural Attenuation Research Site near Bemidji, MN (Lundy et al. 2011; Lundy and Dowd, 2013). The terms *LNAPL* and *oil* are considered to be synonymous and will be used interchangeably.

Part 1 characterizes the changes in oil composition and fluid properties since the release occurred in 1979, and presents rates of mass depletion used in the Part 2 stability analysis.

Specific objectives of Part 1 include:

- a) Estimate time- and location-dependent oil mass and volume depletion rates from changes in oil composition,
- b) Compare these mass depletion rates with rates based on the generation of biogenic methane or carbon dioxide reported by others, and
- c) Provide historical oil density, viscosity, and interfacial tensions inputs for modeling historical oil transmissivities and mass fluxes leaving the oil infiltration area in three oil flowtubes that indirectly represent rates of historical spreading.

Part 2 focuses on hydraulic parameters of LNAPL-bearing media, declining rates of movement of the leading edge of the North Pool based on historical well gauging by the U.S. Geological Survey, and historical oil flux estimates from the source area into three flowtubes with approximate historical lengths based on historical gauging data and potentiometric surface gradients. The history of oil flux leaving the infiltration area in each flowtube is modeled and compared to estimated rates of mass depletion along each flowtube. For the early and middle years, the influx must exceed efflux in order to sustain leading edge movement by building sufficient oil mass and head to overcome non-wetting fluid resistance at the interfaces between oil-bearing and pristine soil materials. As a first approximation, the stability of the LNAPL body is evaluated within an assumed homogeneous average media within a range of controlling matrix parameters and consistent with the history of observed leading edge migration. Calculations supporting the conclusion that the North Pool leading edge reached a stable configuration by year 2012 depend on model inputs that vary with methods of measurement and confidence in the

results. These uncertainties are managed by calculating a range of elapsed times within which a mass balance between rates of mass inputs mass losses have a 95% probability of being reached.

Literature Review

Juvenile crude oils are composed of a greater percentage of lighter hydrocarbons and with densities and viscosities comparable to lighter commercial petroleum products. As the oil migrates away from the source rock, it loses mass by the processes of dissolution to flowing groundwater (“water washing”) and by microbial degradation of the dissolved fraction. The oil can be temporarily held in structural or stratigraphic traps, which gain and lose oil as it migrates toward submarine or terrestrial seeps. Weathering changes the chemical composition and increases oil density, viscosity, and interfacial tensions between the oil and other fluids (gas and water). Long-term abiotic and micro-biotic processes combine to reduce oil mobility and recoverability, which increases production costs for crude oil producers (Head et al. 2003).

The oil released at the Bemidji site was light Alberta crude. In 30+ years following the release, the oil was altered to a Peters and Moldowan (1993) classification of moderately weathered oil. That classification is based on the oil density changing from approximately 0.85 gm/mL in the fresh oil to a maximum value of 0.90 gm/mL, equivalent to an API gravity change from 36 to 26. Partial to complete removal of C4-C35 hydrocarbons also typify the moderately weathered Peters and Moldowan classification.

A number of research projects at the research site have focused directly or indirectly upon weathering of the crude oil. In the late 1980s, Landon (1993) collected 13 oil samples, including ten from North Pool wells and three from south pool wells. He performed GC/MS analyses that identified 57 compounds in the C4-C12 range and performed physical property tests including, refractive index, density and specific gravity, dynamic viscosity, and refractive index. He used

the least weathered sample from well 604A as a reference for determining the degree of alteration and the relative amount of mass losses for each of the other samples. He performed a 70-hour laboratory weathering experiment involving evaporation of the 604A sample collected in June 1989 and used the lab results to quantify mass losses for his field samples. Among 13 oil samples, Landon estimated that the mass losses varied spatially in the North Pool and ranging from 0 to 11% and averaging 3.8%. He found good agreement between changes in physical properties (density, viscosity, and refractive index) and changes in composition, expressed as the loss of C4 to C12 compounds relative to Decane, a C10 compound. He noted that these losses were minimal estimates because they only represented changes in lighter hydrocarbons. The spatially-averaged rate of mass depletion over the North Pool footprint area from 1979 to 1989 was estimated to be approximately 0.112 kg/m²/yr. Using North Pool footprint shown by Landon (1993), this would have been equivalent to approximately 0.43 kg/day over the total area.

Chaplin et al. (2002) estimated rates of mass loss from the oil body based on modeling production and movement of gases through the vadose zone above the oil body. They applied a gas transport model R-UNSAT (Lahvis and Baehr, 1997) and calibrated to the soil gas concentrations of O₂, CO₂, and CH₄ in samples from vadose zone wells along a transect oriented down the water table gradient along a central axis of the North Pool. Rates of O₂ loss and CO₂ production represented the rate of aerobic degradation, and rates of CH₄ production represented the rate of methanogenesis within and below the oil body. They estimated plume-wide mass loss rates of 10.5 kg/day in 1985 and 1.99 kg/day in 1997. The predominant oil weathering and mass loss mechanisms in 1985 were volatilization and aerobic degradation. By 1997 the dominant weathering processes had changed to biodegradation under methanogenic conditions.

Molins et al. (2009) used the geochemical and gas flow model of Molins and Mayer (2007) to simulate reactions and gas distributions observed in the summer of 2007, 28 years following the 1979 release. That model accounts for diffusion and advection of the gas phase, aerobic through methanogenic reactions, and the transport of N₂ and Ar, but assumes the oil phase is not spreading. They calibrated the model to O₂, CO₂, and CH₄ using N₂ and Ar to constrain the results. The average rate of mass release from the oil body (“smear zone”) was 0.13 mol CH₄/m²/day, which was approximately double the rate reported by Chaplin et al. (2002) of 0.07 mol CH₄/m²/day. Uncertainties identified with model results included soil gas saturations of void space, tortuosities, and a lack of CO₂, and CH₄ efflux measurements at the land surface to better define that boundary condition.

While the oil is known to be composed of 150 to 200 hydrocarbons, previous site work reveals that there may be between 500 and 1000 individual organic compounds dissolved in the groundwater (Thorn and Aiken, 1998) resulting from a complex sequence of biodegradation steps by the consortium of microbes within micro-environments (Bekins et al. 1999). Some of these compounds may partition back into the oil in low concentrations. Listing and capturing all compounds and biogeochemical reactions is considered intractable. Small oil samples drained from soil cores exhibit a greater degree of weathering at the upper and lower boundaries of the oil body, where the oil is more exposed to air or groundwater (Bekins et al. 2005), consistent with weathering rinds observed in crude oil reservoirs (Head et al., 2003). Microenvironments in the subsurface altered the originally homogenous oil by different degrees and created spatially heterogeneous oil within the heterogeneous porous media near the water table fluctuation zone.

Between 2010 and 2013, researchers from the University of British Columbia (UBC) measured the efflux of CO₂ at the land surface overlying and near the North Pool footprint area.

They took repeated direct readings of CO₂ efflux with the dynamic closed chamber method at numerous stations in a grid pattern over the oil body. Monitoring at several locations near outside the North Pool was performed to estimate and subtract production of CO₂ by soil respiration. Sihota et al. (2011) estimated the total rate of mass depletion by biodegradation of in the saturated and unsaturated zones to be approximately 4.29 kg/day over the North Pool area.

Approach to Testing the Conceptual Model

The basic hypothesis to be tested is that any finite and sudden LNAPL release volume that reaches the water table will spread laterally to a stable configuration with continual internal LNAPL migration offset by mass depletion and resistance at a stable downgradient leading edge. The rate and duration of lateral spreading of the LNAPL body will continue at declining rates within a stabilized LNAPL footprint area, being controlled by a complex and time-varying set of inter-related physical, biogeochemical, and thermal processes.

Figure 2.2 provides an idealized section and plan view depiction of a generic LNAPL body that is spreading from a mounded area beneath a release location assumed to be near the land surface. The groundwater shares the void space with the LNAPL and the water table gradient influences the direction and slope of the LNAPL or “oil table” along which the LNAPL pressure is equal to atmospheric pressure, consistent with the conceptual model of Lenhard and Parker (1990). The groundwater and LNAPL will have similar but different flow directions depicted with colored arrows. These flow directions and rates are controlled by different potentiometric head distributions and gradients related to spatial variations in stratigraphy, grain size, void space, intrinsic hydraulic properties, and the relative permeability for each fluid (Parker et al. 1987; Huntley and Beckett, 2002; and Charbeneau, 2007).

The most rigorous approach to testing the conceptual model for oil-body stabilization is to apply fundamental concepts of fluid mechanics of multiphase (oil, water, and gas) flow with chemical thermodynamics controlling mass transfer from the oil to porous media, and with rates of microbial degradation of hydrocarbon compounds in the media. These principles would be applied in the analysis and interpretation of the historical and recent field and laboratory data for a case study site.

However; there are severe limitations to taking a rigorous high-resolution approach even at a well-characterized site. The physical, chemical, biological, and thermal processes work in concert, influencing each other at different rates in a heterogeneous subsurface environment. Figure 2.3 shows generalized cyclic influences and interdependencies of these the process groupings. For example, oil mobility and rates of migration are reduced over time by the chemical weathering of the oil, which increases viscosity thereby *reducing* mobility. The abiotic transfer of hydrocarbons from the oil to adjacent media is enhanced by biological degradation that maintains diffusion gradients and a constant disequilibrium. Metabolic microbial activity liberates heat that raises ambient water temperatures, which reduce oil viscosity thereby *enhancing* mobility. From the thermodynamic view point, a state of equilibrium with maximum stability requires reversible processes within a closed system (Stumm and Morgan, 1970). Neither condition is met in a real-world natural system open to the exchange of mass and energy. The land surface boundary condition includes time-dependent fluxes of gases and recharge from infiltrating snow melt and precipitation. While bringing nutrients for microbial activity this raises the water table and can reduce oil saturations and mobility to the point of temporarily halting advancement of the leading edge.

Any sampling plan must consider the fact that the saturation and movement of LNAPL in geologic media is sensitive to small-scale variations in grain size that control spatial distribution of hydraulic properties. Capturing all the time and space dependent processes and heterogeneities is widely recognized as a major challenge in developing a workable LNAPL Conceptual Site Model (LCSM; ASTM, 2007). An LCSM is only based on inferences of historical and recent data subjected to an analysis that fits with physical, chemical, biological, and thermal principles. A similar practical approach is adopted here that remains faithful to basic principles but is limited by field and laboratory measurements of parameters at enough locations to be a representative sample. A focus on quantifying the controlling processes is further supported by multiple lines of evidence based on historical records developed by previous research at the North Pool. Table 2.1 provides a summary listing of the relevant historical events, processes, and parameters to be addressed with different levels of effort in this investigation.

Study Area Selection and Description

The National Crude Oil Spill Fate and Natural Attenuation Research Site was selected as the best available site for testing the hypothesis. It is located in Beltrami County in northern Minnesota, approximately 16 km (10 mi) northwest of Bemidji and approximately 140 km (87 mi) south of the Canadian border (Figure 2.4). The primary land use in this uninhabited forested study area is hunting, fishing, and snowmobiling. Lakeland Pipeline owned a pipeline crossing the study area and assumed responsibility for remediation following a significant release on August 20, 1979. The Minnesota Pollution Control Agency (MPCA) has had regulatory oversight for the environmental work at the site. In 1983, with cooperation from MPCA, Beltrami County, and Lakeland Pipeline, the Minnesota office of the U. S. Geological Survey (USGS) convinced headquarters in Reston, VA to include the crude oil spill site in its national

Toxic Substances Hydrology Program Research Program. The MPCA suspended its policies of requiring groundwater remediation at the site, allowing the USGS to study the natural processes associated with further spreading of the LNAPL, vapor, and aqueous phase plumes. That decision made the site an ideal candidate for investigating the processes that control the rates of spreading and the eventual stabilization of the LNAPL source area for the vapor and groundwater plumes. Most of the research conducted at the site has focused on groundwater and geochemical processes controlling contaminant migration and biodegradation, which is relevant to testing the stabilization hypothesis.

Figure 2.4 shows the locations of the pipeline release point and three crude oil bodies that formed on the water table, designated as the *North, Middle, and South Pools*. The North Pool was selected for the stability investigation for the following reasons:

- a) The date, type, and approximate volume of the sudden release of crude oil are known;
- b) Gauging of fluid levels in monitoring wells are available for tracking historical movement of the leading edge of the spreading oil body;
- c) Hydrogeological features relevant to the study of LNAPL migration are characterized;
- d) Biogeochemical conditions of the subsurface near and downgradient of the oil body and its progressive evolution over 3 decades are characterized;
- e) Archived samples of oil from monitoring wells are available for analysis; and
- f) USGS and other university researchers will share knowledge, guidance, and field support to the stability investigation.

Numerous research projects have been carried out by the USGS and university faculty and graduate students. A recent review article by Essaid et al. (2011) summarizes over 25 years of monitoring and modeling that increased our understanding of the hydrogeology and

biogeochemistry of the site. Among three LNAPL bodies in contact with groundwater, the North Pool is the most studied oil body on the site and offered the most opportunity for leveraging relevant data collected by others over a 3-decade period.

Hydrogeologic Setting

The local unconfined aquifer impacted by the crude oil is the saturated lower two-thirds of the outwash deposit. Local surface drainage at the site is northeastward towards an unnamed lake approximately 300 m (900 ft) from the pipeline break, and to swamp-filled depressions about 900 m (2,700 ft) south of the release point (Hult, 1984). The heterogeneous outwash deposit is comprised of fine to coarse sand beds with minor percentages of silt, clay, and pebble gravel. North Pool oil is predominantly found in well-sorted medium to fine sand facies (Strobel et al. 1998). The mineralogy of the sand is predominantly quartz with a coating of iron hydroxide but also includes feldspars (Siegel and Franzi, 1984). The average mineral composition of six sand samples collected in 1985 near the water table was 57% quartz, 11% K-feldspar, 17% plagioclase feldspar, 4.4% calcite, 2.4% dolomite, 2.2% hornblende, and 6.3% other minerals (Bennett et al., 1993).

Figure 2.5 shows the location of USGS research site on a contour map of the water table based on gauging data from 1983-2013. The average water table slopes ENE towards an unnamed lake at a magnitude of approximately 0.00264 beneath the North Pool. Based on a tracer test in 1997, the average pore velocity beneath the North Pool was estimated to be 0.7 m/day (Essaid et al. 2003). The depth to the water table in the vicinity of the North Pool ranges from approximately 6 to 10 m (9.3 to 23 ft). The lower boundary of the aquifer is the undulating contact with a less permeable glacial till. The saturated thickness of the aquifer ranges from approximately 11 to 18 m (36 to 59 ft), controlled by undulations in the outwash-till contact.

Surface topography controls natural runoff and recharge (Delin and Herkelrath, 1999), which controls the availability of nutrients to indigenous microbes within the LNAPL-bearing zone (Bekins et al. 2005). Hydrographs of water levels in wells developed with gauging data for selected wells in the North Pool (<http://mn.water.usgs.gov/projects/bemidji/data.html>) show that water table fluctuations since 1983 have ranged from approximately 0.3 to 0.6 m (1 to 2 ft) at observation wells on the Bemidji site. These are attributed to natural aquifer recharge and discharge and exhibit no long-term trends and estimates range between 0.1 and 0.3 m/yr (Delin and Herkelrath 1999, and 2005).

Groundwater in contact with the North Pool has progressed from being aerobic to anaerobic, with methanogenic zones developing in close proximity to the oil body. Figure 2.6 shows five geochemical zones in the groundwater zone and three in the vadose zone identified on the basis of composition of dissolved crude oil constituents, degradation products, and geochemical indicator parameters in the vicinity of the North Pool. Salient characteristics of each zone are summarized as follows (Bennett et al., 1993 and Eganhouse et al., 1993):

- a) **Zone 1** represents background aerobic conditions with average groundwater temperature of 6.5 °C, with a major ion composition predominated by Ca^{+2} and HCO_3^- , low background ferric Fe^{+3} and Mn^{+4} concentrations, low total dissolved solids (TDS) and low total dissolved organic carbon (TDOC) levels, low specific conductance, near neutral pH, DO levels > 1 mg/l, and strong positive redox potentials (ORP).
- b) **Zone 2** represents groundwater altered by oil-impacted soils in the vadose zone beneath the spray zone, with near neutral pH, but higher levels of Ca^{+2} , Mg^{+2} and HCO_3^- , similar low levels of Fe^{+3} and Mn^{+4} , and somewhat greater TDS and TDOC levels, neutral pH, low DO levels, and positive ORP.

- c) **Zone 3** represents anoxic methanogenic groundwater altered by direct contact with the crude oil with an average temperature of 8.5 °C, above-background Ca^{+2} and HCO_3^- , high reduced ferrous Fe^{+2} and Mn^{+2} concentrations and higher TDS and TDOC levels, slightly acidic pH, non-detectable DO levels, and strongly negative ORP.
- d) **Zone 4** represents an anaerobic groundwater transition zone from the anoxic zone with above-background levels of Ca^{+2} and HCO_3^- , lower reduced ferrous Fe^{+2} and Mn^{+2} , moderate to high TDS and TDOC levels, near neutral pH, low DO levels, and weak negative ORP.
- e) **Zone 5** represents a groundwater transition zone to the ambient groundwater zone with above-background but declining levels of Ca^{+2} and HCO_3^- , low Fe^{+3} and Mn^{+4} levels, moderate TDS and TDOC levels, neutral pH, low DO levels, and near neutral to positive ORP.

During 1999-2003, two recovery wells were installed and operated inside the north and south pool footprints, and contributed to stabilization of the North Pool. Delin and Herkelrath (2014) studied the effects of pumping groundwater and oil from five recovery wells in the three oil pools on site. Two wells were located along the centerline of the North Pool (designated RW-1 and RW-2 on Figure 2.7), two were similarly located in the middle pool, and another one was located in the south pool. The flow of groundwater and oil from the wells was piped to an oil/water separator in a treatment building. The groundwater was returned, without any pre-treatment, to the aquifer upgradient of the North Pool via an infiltration gallery, and the oil was drummed and recycled off site. Delin and Herkelrath reported that approximately 115,000 liters of oil were recovered, which they estimated to be 36 to 41% of the total oil volume the subsurface (280,000 to 316,000L). Based on the analysis of core samples collected from ten

locations within the North Pool during the summers of 1990 and 1992, they estimated that the North Pool initially had 88,000 L of oil in contact with groundwater, and another 88,000 L in the vadose zone prior to the onset of remedial pumping. However, they assumed no loss of volume and mass due to weathering between 1979 and 1990-1992.

Sampling and Analysis Methods

Figure 2.7 shows the locations of monitoring wells and coreholes where samples of oil, groundwater, and oil-bearing sediments were collected. Oil and groundwater samples were collected from wells using a new HDPE bailer (EON Products, Snellville, GA). Both fluids were discharged together in a controlled manner from the base of the bailer into two 32-oz. amber glass bottles that were labeled, packed with bubble wrap and kitty litter, and shipped unrefrigerated to Torkelson Geochemistry in Tulsa, OK for analysis of physical properties and chemical compositions.

During the USGS summer field seasons of 2010, 2011, and 2012, 2-liter sample pairs of crude oil and contacting groundwater were collected from monitoring wells for analysis. Small aliquots of 25 ml each from archived oil samples collected in the 1980s from the release pipeline and North Pool wells were made available by the USGS. These well samples were supplemented with smaller 1 to 3-mL oil samples drained from soil cores collected from the North Pool sediments in 2010 and 2011 by the core laboratory.

In July 2010, a dozen 2-L oil-water sample pairs were collected from wells 306, 315, 317, 319, 411, 420D, 421B, 422, 423, 521, 533D, and 534A (Figure 2.7). During June 2011, wells 315 and 521 were resampled to assess temporal variability, and Well 309 located in the south pool was sampled and analyzed to confirm that the oil composition and fluid properties

continued to exhibit a greater degree of weathering due to the larger distance from the pipeline release point demonstrated previously (Landon, 1993).

Above-average precipitation during 2010-2011 in northern MN caused the water table to be relatively high at the research site thereby reducing oil thicknesses in shallow North Pool wells. Precipitation was below average in 2012, resulting a lowering of the water table. This caused oil thicknesses to increase and allowing oil to accumulate in two key wells near boundaries of the oil body. This change allowed oil sampling at 604A, the most upgradient well in the North Pool that had insufficient oil for collection in 2010-2011, and well 532A at the downgradient leading edge that exhibited orange bacterial filaments and groundwater on sampling equipment in 2010-2011. Evidence of trapping and releasing mobile oil near a fluctuating water table affecting the first observed occurrence of oil at 532A is discussed further in the Part 2 paper.

Soil cores were collected from the LNAPL-bearing zone at eight locations inside the North Pool oil body using the cryogenic (“freezing shoe”) method (Durnford et al. 1991). Each length of core was collected in a transparent acrylic liner inside a continuous steel core barrel driven with a pneumatic hammer. Approximately 2 m (6 ft) of continuous core material was collected from three locations (C-1008, C-1009, and C-1056) in July 2010 and four locations (C-1103, C-1108, C-1109, and C-1122) in June 2011 (Figure 2.7). One additional coring location downgradient of the leading edge of the oil body (C-1102) was selected to confirm the location of the leading edge and for additional lab tests. At each location, continuous core was collected through the oil-bearing zone beginning approximately 0.3 m (1 ft) above the expected water table depth based on fluid levels in nearby monitoring wells. Lengths of core remained inside the acetate sleeves and were stabilized by freezing on dry ice before being shipped to PTS

Laboratories (PTS) in Santa Fe Springs, CA for analysis. For the Part 1 analysis, small oil volume samples were drained from soil core samples from selected locations in the North Pool. Drainage of oil from core was done in a centrifuge following an ASTM method. Fluid saturations and other matrix property lab test are documented in Part 2.

Torkelson Geochemistry of Tulsa, OK performed laboratory analyses of oil sample physical properties in accordance with API and ASTM standards. The physical property analyses included oil density, oil dynamic viscosity, air-water and air-oil surface tensions, and oil-water interfacial tensions at an average North Pool groundwater field temperature of 8.5 °C (Ean Warren, personal communication, 2010). Table 2 provides a summary of physical property test results.

GC analyses on the well and core oil samples, and on archived USGS oil samples (total of 45) were carried out with a Hewlett Packard 5890 system with a J&W 30-m DB-1 column, having a 0.25-mm inside diameter and 0.25-um film thickness, with a Flame Ionization Detector (FID). The GC system was calibrated to identify 60 hydrocarbons, but included a few compounds found primarily in refined petroleum products (e.g., MTBE and Olefins), leaving a total of 56 detectable crude oil compounds in the crude oil. Appendix A provides a list of the compounds identified and quantified as peak areas on chromatograms, along with the molar mass and fluid density reported at either 0 (STP) or at 20 °C from online sources.

The results of the GC analyses were compiled and examined to identify three wells to represent North Pool oil weathered to the least, most, and intermediate degrees. Using contrasting oil density, viscosity, and GC data, wells 423, 411, and 521 were identified as meeting these criteria in that order. Aliquots obtained from oil samples collected in July 2010 were analyzed by TDI Brooks Laboratories in College Station, TX by gas chromatography/mass

spectrometry (GC/MS). The GC/MS analyses focused on polycyclic aromatic (PAH) compounds and alkyl-isomers and hopanes (biomarkers). Appendix B lists the PAH and biomarker compounds identified and quantified, with associated molar mass and density data from online sources.

Two laboratory experiments were performed to test related hypotheses about the relationship between oil mass depletion and physical properties. This was followed by a series of mass loss calculations using GC and GC/MS laboratory analyses. The following is a summary list of 37 oil samples from different dates, locations, and media that were tested with methods noted above:

- a) one 1984 Bemidji pipeline sample serving as a reference for physical property and compositional changes of the oil spilled in 1979, for which no samples are available;
- b) 16 oil samples collected from the North Pool wells, and one sample from the south pool for comparison, during the summers of 2010, 2011, and 2012;
- c) nine archived oil samples collected by the USGS from the selected North Pool wells on dates between 1983 and 2008; and
- d) ten weathered oil samples drained from core samples collected at five locations within the North Pool oil body.

Physical Fluid Property Changes

The five laboratory-determined physical fluid properties that influence oil mobility are density, dynamic viscosity, air-water surface tension, air-oil surface tension, and oil-water interfacial tensions. Table 2.2 lists these parameter values for 27 samples, all determined at the average field temperature of 8.5 °C. Graphical plots of oil viscosity and the surface and interfacial tensions were plotted as functions of density in Figure 2.8(a) through 2.8(d). Oil

density is used as the independent variable on the horizontal scale to indicate of the degree of weathering consistent with the Peters and Moldowan crude oil classification scheme.

Figure 2.8(a) shows how sensitive viscosity is to small changes density with a best-fit exponential function. At the lower end of the density scale it shows an almost linear and slower rate of viscosity change because the weathering mechanism involved loss of more volatile and soluble lighter compounds, as observed in our lab experiment and previously by Landon (1993). At the higher end of the density scale the rate of viscosity change increases reflecting the influence of loss of larger and heavier compounds, including n-alkanes above C17 removed under methanogenic conditions. Figures 2.8(b-d) show plots of surface tensions and interfacial tension between non-wetting and wetting fluid pairs. Each of these exhibits relatively small changes associated with increases in oil density caused by weathering. The curving trends of change are characteristically unique and are adequately described with second-order polynomial functions that represent trends with changes in density.

Three or more oil samples were available for four wells that together represent the full range of changes in oil density and viscosity since 1979. Figure 2.9(a) is a plot of changes in oil density, and Figure 2.9(b) shows changes in viscosity at these wells. Well 423 represents the least weathered oil and well 411 represents one of the most weathered oils in the North Pool. Both wells exhibited oil when drilled in 1984, but 411 is within the oil infiltration area and well 423 is approximately 10-12 m downgradient of that area (Figure 2.7).

Estimation of Oil Mass Loss Rates

The estimation of crude oil hydrocarbon compound mass depletion relative to a recalcitrant compound is driven by the available historical and recently collected site data, taking

advantage of previous investigations at this site, and following an algorithm that is similar to the method of Landon (1993), but with the following differences:

- a) The range of hydrocarbons identified by Landon's GC analysis was limited to C4-C12 compounds, while the current study considers C4-C40 compounds;
- b) Landon selected *Decane* (C₁₀H₂₂) as the recalcitrant compound for normalizing the GC compound peak areas, while we selected *Pristane* (2,6,10,14-tetramethylpentadecane, C₁₉H₄₀), a biomarker detected in all oil samples;
- c) Landon quantified mass losses observed in a laboratory experiment involving evaporation of compounds in a reference oil from well 604A, the freshest North Pool sample in 1989, but in 2012 well 604A yielded one of the most weathered oil samples observed to date; and
- d) The current study estimates mass losses relative to the 1984 Bemidji pipeline oil sample and performed similar abiotic laboratory weathering experiments on the pipeline oil sample that removed lighter compounds without biological processes, which more recent studies show were the dominant weathering mechanism (Bekins et al. 2005).

Landon noted mass gains or losses in an unresolved complex mixture (UCM) of unidentified compounds that increased as detected GC compounds were depleted by weathering. The current investigation tested the assumption that many other compounds not identified by GC analysis is a small percentage of total mass and can be approximated by mass balance calculations. This was initially tested during a laboratory weathering experiment and the following results:

- a) By accounting for additional moles and mass identified by the GC/MS analysis, and additional UCM needed to achieve a mass balance between measured and calculated oil density in the Bemidji pipeline samples, and later applied to other oil samples, and
- b) By a favorable comparison of USGS reported benzene concentrations in groundwater samples from the shallow North Pool wells to benzene concentrations estimated with mole fractions based only on GC-defined molar ratios in oil samples from North Pool wells.

The following is a list of assumptions needed for the mass loss estimates:

- a) Pristane is assumed to be conservative and unaltered by weathering processes after the pipeline release;
- b) Pristane concentrations will increase in weathered oil samples as more volatile, water-soluble, or biodegradable compounds are removed;
- c) GC compound peak areas are proportional to the number of moles present in the volume (a few microliters) of oil injected into the GC column;
- d) By using the reference oil sample Pristane areas to normalize the areas of other GC compounds, the resulting ratios become molar ratios relative to the amount Pristane, i.e., the number of moles relative to a single mole of Pristane.

Normalized peak areas for each GC compound in each sample are expressed as:

$$NA_i = (Area_i / Area_{pristane})_{sample} \quad , \quad (1)$$

where NA_i is the normalized GC peak area of compound i , $Area_i$ is the GC peak area for compound i , and $Area_{pristane}$ is the GC peak area for Pristane in the sample. Equation 1 was applied to all GC-detected compounds in all oil samples from the study site and the reference pipeline sample. Figure 2.10 shows plots of normalized moles for detected GC compounds for

three oil samples, including the pipeline reference oil, and oil from centrally located well 411 in 1989 and 2011. Compounds are identified by numbers on the horizontal scale listed in the order they were eluted (as listed in Appendix A).

The following expression was used to obtain a fractional loss of moles for each compound relative to the normalized peak area in a reference oil sample:

$$\textit{Fraction of Moles Lost} = \left[\frac{(\textit{Area}_i / \textit{Area}_{\textit{pris}})_{\textit{reference}} - (\textit{Area}_i / \textit{Area}_{\textit{pris}})_{\textit{sample}}}{(\textit{Area}_i / \textit{Area}_{\textit{pris}})_{\textit{reference}}} \right] \quad (2)$$

Equation 1 and 2, are based on the approach of Landon (1993) and provide changes in the moles for each GC-identified compound relative to the moles for the same compound in the reference oil sample. Relative numbers of moles must be converted to an equivalent mass for each GC-identified compound and summed for all compounds in each sample to estimate the total mass fraction relative to the total mass of corresponding compounds in the reference oil. It must also account for other conservative compounds not identified by GC analyses including recalcitrant polynuclear aromatic hydrocarbons (PAHs) and biomarkers (listed in Appendix B), and UMC mass to provide a comprehensive mass change relative to the pipeline reference oil.

The procedure used here proceeds through the following steps applied to 56 GC-identified compounds in 39 oil samples (Appendix A):

- a) Normalize the GC peak areas of the compounds to the peak area of Pristane in the each oil sample (Appendix C);
- b) Multiply the normalized moles by the molar mass (gm/mole) of each associated compound to obtain an incremental mass for each compound, and sum these values to obtain a total mass, in grams in the sample (Appendix D-Part 1);

- c) Divide the calculated mass by the molar volume (mL/mole) of each associated compound to obtain an incremental volume for each compound, and sum these values to obtain a total volume in mL for each sample (Appendix D-Part 2);
- d) Divide the sums of incremental masses by the sum of incremental volumes for each sample to obtain a density (gm/mL) of the blend of GC-detectable compounds (Appendix D-Part 2); and
- e) Add the additional mass of PAH and Biomarkers then estimate the additional mass of UCM needed to equate calculated and measured density values (Appendix D-Part 2).

Normalized moles obtained with Equation 1, $NA_{i,sample}$, were converted to an equivalent amount of mass by multiplying by the molar mass for each compound, generating an incremental mass for each compound in the sample aliquot injected into the GC column:

$$GCM_i = NA_{i,sample} MW_i \quad , \quad (3)$$

where GCM_i is the incremental mass of GC compound i , in grams, and MW_i is the molar mass of compound i , in gm/mole. Incremental mass is then divided by the pure compound density, ρ_i , to obtain an incremental volume in the sample aliquot with the following expression:

$$GCV_i = GCM_i / \rho_i \quad , \quad (4)$$

where GCV_i is the incremental volume of GC compound i , in mL. Compound densities under standard conditions are used for each individual GC compound (Appendix C). These may represent a boiling point at standard pressure for the lightest compounds (e.g., butane boils at 15 °C), otherwise they are reported at a standard 20 °C temperature. Because densities of the oil samples were all performed at 8.5 °C, the pure compound densities are expected to be understated at higher temperatures (reducing density), causing mass loss to be overstated with Equation 4, but by an amount that is here assumed to be negligible.

For each sample for which a laboratory density was determined, the sum of incremental GC compound masses is divided by the sum of incremental volumes to obtain a density of the blend of GC compounds, $\rho_{GCblend,i}$, for each sample aliquot, written with previously defined terms as follows:

$$\rho_{GCblend,i} = \frac{\sum_{n=1}^i GCM_i}{\sum_{n=1}^i GCV_i} , \quad (5)$$

The sum of compound masses for a given sample accounts for contributions of PAHs, biomarkers, and UCM compounds in each oil sample with the following expression:

$$M_{sample} = \sum_{i=1}^n GCM_{i,sample} + \sum_{i=1}^n PAHM_{i,sample} + \sum_{i=1}^n BioM_{i,sample} + UCM_{sample} , \quad (6)$$

where M_{sample} is the sum of incremental masses of all compounds in the sample aliquot, $PAHM_i$ is the incremental mass of PAH compound i in the sample, $BioM_i$ is incremental mass of biomarker compound i in the sample, and UCM_{sample} is the additional mass in grams needed to obtain a mass balance with laboratory density for the sample.

The incremental volumes of GC/MS-detected PAH and biomarker compounds are computed using molar masses and volumes like the GC compounds. These are summed to obtain an aliquot volume with the following expression:

$$V_{sample} = \sum_{i=1}^n GCV_{i,sample} + \sum_{i=1}^n PAHV_{i,sample} + \sum_{i=1}^n BioV_{i,sample} , \quad (7)$$

where $GCV_{i,sample}$ was defined above, and $PAHV_{i,sample}$ and $BioV_{i,sample}$ are the incremental volumes of PAH and biomarker compounds in an oil sample.

The ratio of incremental mass and volume sums (Equation 6 divided by Equation 7) obtains a larger density than the GC compound blend obtained with Equation 5 that is smaller than the laboratory oil density values determined on the corresponding field samples. Additional

UCM mass with no change in volume in the blend of GC and GC/MS compounds is added to achieve the lab density for that particular sample.

Fractions of mass loss for each field sample are then estimated with:

$$MassLoss_{sample} = \frac{M_{reference} - M_{sample}}{M_{reference}}, \quad (8)$$

for which the reference and sample mass terms are defined with Equation 6. The results of mass loss calculations for each oil sample are summarized with the sample collection dates in Appendix D, and are used in the next step of determining mass loss rates over time.

Historical Trend in Oil Mass Depletion

Seventeen oil samples collected during 2010-2012, plus ten USGS archived samples collected during 1983-2008 provided sufficient volume for laboratory density determinations (Table 2.2). The mass-density calculations included the reference pipeline oil, 27 samples from North Pool wells, and 10 samples drained from cores. Only the well-oil samples with lab density values were used to obtain mass loss results that qualified for determining the trend of historical total mass depletion from 1979-2012. Among qualifying oil samples, total GC compound mass accounts for 91.4 to 92.8% of the total mass. The sum of PAH, biomarker, and UCM masses ranges from 7.2 to 8.6% of the total mass, with the additional UCM mass ranges from 4.9 to 6.5% of the total mass. Bulk mass removal of oil by pumping during 1999-2003 was a physical process, and therefore not included in mass losses by partitioning.

The historical trend of mass losses for the North Pool oil body were estimated at the LNAPL-body scale using the fractional mass losses for the 27 well oil samples relative to the reference oil sample. Historical fractional mass losses were calculated for each sample with Equation 8, and represent mass losses at different elapsed times since 1979. These values were each subtracted from unity to provide the remaining fraction of oil mass since the 1979 release.

Figure 2.11(a) is a plot of the remaining fraction of the starting oil mass vs. elapsed time and includes a best-fit exponential regression curve representing the trend from 1979 to 2012, express as:

$$\textit{Fraction of Mass Remaining} = e^{-0.0308x} \quad , \quad (9)$$

where x is the elapsed time in years since the August 1979 release. Vertical clusters of points represent sampling events in 1989, 2008, and 2010. The vertical point spread widens over time, consistent with spatial heterogeneity in oil composition (e.g., Figure 2.10) and degrees of weathering observed here and in previous studies. The most weathered oil occurs in the fringes of the oil body and less weathered oil appears between this weathering rind and the oil beneath the infiltration zone, where increased recharge of both oxygenated water and nutrients has facilitated weathering (Bekins et al. 2005) and is only slightly less weathered than the oil in the fringes (e.g. at 604A and 532A). The proposed conceptual model depiction of oil weathering in Figure 2.2(b) does not fit this pattern because it assumes a uniform recharge boundary condition across the land surface above the LNAPL body.

Equation 9 was used to calculate mass depletion rates from 1979-2013 by calibrating to an oil volume estimate by the USGS based on extensive core analyses representing the summer field seasons of 1990 and 1992 (Herkelrath, 1999; Herkelrath, 2014). Cores were collected from the oil-bearing zone at 10 locations and 142 individual core samples were analyzed for oil saturations, expressed in percent of total porosity (Herkelrath, 2014). The volume of North Pool oil in contact with groundwater (excluding mass in the vadose zone) was estimated to be 88,000 L (Delin and Herkelrath, 2014). Assuming the oil saturations in the North Pool follow a normal distribution and the samples were randomly selected, the mean saturation of 15.8% has a $\pm 3.22\%$ confidence interval ($\pm 20.4\%$ of the mean) at the 95% confidence level. Using this confidence

interval as a measure of uncertainty in the estimate, the 88,000-L volume can be treated as the 1990-1992 estimate with a 95% confidence interval of $\pm 17,900$ L. Hence, there is a 0.95 probability that the North Pool oil volume was in the range of 70,100 to 106,000 L when cores were collected in 1990-1992.

Using laboratory historical oil density data for selected monitoring wells (Table 2.2; Figure 2.9), the average oil density in the summer of 1991, a midpoint between the summers of 1990 and 1992, is estimated to be approximately 0.867 kg/L. Multiplying the 1990-1992 volume and confidence interval values by that density provides a mass estimate of 75,700 kg \pm 15,500 kg. When Equation 9 is evaluated at 11.92 yr of elapsed time (July 1991), the mass estimate represents 0.693 times the 1979 starting mass (Figure 2-10). Dividing the mid-1991 oil mass range by 0.693 provides a mass range of approximately 109,200 kg \pm 22,300 kg for 1979. Dividing that mass range by the reference pipeline oil density of 0.855 kg/L, we obtain an equivalent volume of 128,000 L \pm 26,500 L of crude oil that reached the water table in late August to early September 1979 (allowing time for drainage through the vadose zone). By allowing for the 95% confidence interval around the mean oil saturation, this approach provides a starting volume contacting groundwater in the range of 102,000 to 154,000 L.

The next step is to calculate the remaining North Pool mass by multiplying the 1979 starting mass by Equation 9 evaluated at a series of elapsed times after the release. We selected a 2-year time step to obtain mass estimates for dates July 15, 1981 through July 15, 2013. Those are plotted in Figure 2.11(b) and define a new quantitative trend of mass remaining, a function of elapsed time represented by the expression:

$$\text{Oil Mass Remaining} = 109,210e^{-0.0308x} \quad , \quad (10)$$

Taking the first derivative of Equation 10 with respect to x , we obtain the rate of fractional mass change with elapsed time, which is negative and equivalent to a mass loss with the following expression:

$$\text{Mass Depletion Coefficient} = e^{-0.0308} (109,210e^{-0.0308x}) \quad , \quad (11)$$

The total North Pool oil mass remaining from 1979 to 2013 plotted in Figure 11(b) is considered the base case and is re-plotted in Figure 2.12 with two other bounding mass-remaining curves. These curves begin at time zero with the base case mass $\pm 22,300$ kg to account for the 95% confidence interval around the 1979 base-case mass.

The base-case starting oil mass (109,210 kg) was multiplied by the mass loss coefficient (Equation 11) at each elapsed time step following the release date to obtain a base-case estimate of historical North Pool oil mass losses plotted in Figure 2.13. The mass loss rate starts at 9.21 kg/day in 1979 and decreases to 3.24 kg/day in 2013. Mass loss rates for the upper and lower confidence intervals of starting mass based on the 1990-1992 oil saturation data were used to create bounding mass loss curves for the base case using the same methodology. That is, each mass loss curve in Figure 2.12 has a best-fit polynomial and derivative which represents the coefficient to be multiplied by the starting mass to obtain daily mass loss rates over elapsed time.

Literature-reported rates of mass depletion based on CO₂ mass production from biodegradation within and beneath the North Pool oil body are added to Figure 2.13 for comparison. The mass depletion rates based on oil saturations and compositional changes are within the range of historical estimates based on CO₂ efflux rates, which reflect variations in rates of bio-decay at different times and with the different methods used to make the estimates.

An decreasing rate of mass loss is consistent with significant losses of volatile compounds during the first decade following the release reported by Landon (1993) and by

relative mole fraction changes shown in Figures 2.10(a) and 2.10(b). The rate of mass loss decreased with depletion of both lighter and heavier compounds in the second and third decades following the release. Compositional changes illustrated in Figure 2.10 are consistent with oil density and viscosity changes in Figure 2.9. Relatively small increases in density and viscosity were observed by the end of the first decade, and rates of change increased for both but mostly with viscosity in later decades. Greater changes in viscosity are attributed to the loss of lighter volatiles and long-chain n-alkanes in the C12-C40 range, which increased concentrations of larger and more complexly-shaped molecules of hydrocarbon groups in the blend.

As a check on these results, we compared the average mass lost between the reduction in the oil saturations in cores collected in 1990-1992 by the USGS and in 2010-2012 in this study. Figure 2.14 shows two histograms of oil saturations for these two sampling events. The average oil saturation of 15.8% of void space for 142 core samples in 1990-1992 was approximately twice the average saturation of 7.97% for 48 samples in 2010-2012. The reduction in average saturation was 49.6%. This is consistent with an approximate 41% loss of mass based on composition changes when one allows for reduction in saturations due to mass removal by remedial pumping (1999-2003) and further spreading of the oil body.

The small UCM percentages in the oil composition analyses is inconsistent with what Landon (1993) reported in his analyses. Our estimates of the relative mass of UCM did not change significantly with biological degradation of oil constituents in groundwater, and had no significant effect on mole fractions of the GC compounds. Figure 2.15 shows that benzene groundwater concentrations in samples collected by the USGS from North Pool wells are in the same range as benzene concentrations estimated with Raolt's law using benzene mole fractions based only on GC analytical data for both archived and more recent (2010-2012) oil samples.

These findings support the idea that using GC and limited GC/MS analyses of historical and recent oil samples can suffice for estimating mass losses relative to the reference pipeline oil on this and similar LNAPL sites.

Summary and Conclusions

Seventeen oil samples collected from monitoring wells and ten drained from oil cores in 2010-2012 were analyzed with ten archived well oil samples collected by the USGS during 1983-2008, including a 1984 pipeline sample assumed to be similar to oil released in 1979. Compositional analyses were performed using GC and GC/MS methods and physical fluid property analyses were determined with API and ASTM methods. Moles of detected GC compounds were normalized to one mole of Pristane, a conservative biomarker assumed to be unremoved by partitioning or biodegradation. Molar mass losses, expressed as the change in moles of 56 GC compounds relative to the 1984 reference oil range from an average of 20% in 1987-89 samples to 65% in 2010-2012 samples. Average oil density and viscosity values at an average field temperature of 8.5 °C increased by approximately 3% and 150%, respectively. Molar mass-loss calculations performed on the reference pipeline oil during a 24-hr laboratory weathering experiment removed volatile GC compounds and increased the oil density and viscosity, generally agreeing with our field oil sample analyses. Oil sample mole-fractions based estimates of benzene concentrations are in the same range as benzene concentrations in water samples from wells located in the oil body area. Our study results are not significantly affected by additional mass associated with an unresolved complex mixture of organics.

Changes in oil composition, physical properties, and associated mass losses vary spatially within the mapped oil body. Interstitial oil is more weathered at the upper and lower boundaries of the oil body where oil saturations are lower. Mobile oil from wells is most altered within

upgradient and downgradient fringes of the oil body footprint area. Oil samples from the historical oil infiltration area to a distance of 10-15 m downgradient are almost as weathered as oil in the fringe areas. Core and well samples taken between the infiltration and downgradient fringe areas are moderately weathered. The degree of weathering and mass loss is controlled by time- and space-dependent exposure to subsurface air and groundwater, and where aquifer recharge is focused on topographically low areas like the historical oil infiltration area.

Mass loss calculations of archived oil samples from the 1980s and more recent samples exhibit a quantifiable trend of decreasing rates of mass loss with time. By estimating the percentage of mass lost for a USGS total oil volume estimate representing 1990-1992 (mean of 11.9 years after the release), we estimated the starting volume and mass for the North Pool in 1979 and developed a full history of mass depletion from 1979-2013 (34yr). Those rates were in the same order of magnitude range and have a similar overall trend as historical mass losses for the North Pool based on CO₂ mass effluxes reported by other researchers (Chaplin et al. 2002, Molins et al. 2009, Sihota et al. 2011, Sihota et al. 2012).

The corroboration between using compositional changes and CO₂ efflux is significant. While the compositional approach is more direct and comprehensive, it requires knowledge of the composition of the reference LNAPL that was collected near or during the time of the release and was analyzed, or archived for later analysis. The CO₂ efflux modeling and monitoring approach has become increasingly popular, can help delineate areas of the LNAPL body that were missed during conventional subsurface investigations, but must only be differentiated from background noise of natural soil respiration rates and atmospheric cross-contamination. However, this limitation can be overcome by including a few C¹⁴ analyses in the efflux monitoring program. In summary, the agreement between these two methods lends credence to

both, which gives site investigators the option of using either or both. Only a small percentage of the total mass portioned to the groundwater and vadose zones is biodegraded downgradient of the LNAPL source zone.

Oil composition-based mass loss rates estimated by the algorithm proposed here agree with observed increases in oil density and viscosity and the types of hydrocarbon compounds lost over time, the percentages of reductions in mean oil saturations between 1990-1992 and 2010-2011, and produced mole fractions of benzene that, after applying Raolt's Law, yielded concentrations in the same range as independently observed groundwater concentrations in samples collected beneath the floating oil. We therefore conclude that the mass depletion rates are reasonable and can be used in Part 2 for modeling the time-dependent LNAPL spreading and stabilization process.

Table 2.1

Historical Events, Processes, and Parameters Relevant to North Pool Stabilization.

<p>History of Migration and Spreading of Each Phase</p>	<p>History of LNAPL Removal by Pumping and Smearing</p>	<p>History of Biochemical Weathering and Mass Losses</p>	<p>Changes in Physical Parameters Influencing LNAPL Mobility and Migration</p>
<ul style="list-style-type: none"> • Release and migration to water table • Mounding then lateral LNAPL spreading • Aqueous phase plume • Vapor phase plume 	<ul style="list-style-type: none"> • Mass removal and smearing by remedial pumping of LNAPL and groundwater • Mass transfer/smearing by water table fluctuations 	<ul style="list-style-type: none"> • Biodegradation mass depletion represented by CH₄ and CO₂ flux • Aqueous phase mass flux leaving source area • Vapor phase mass flux leaving source area 	<ul style="list-style-type: none"> • Declining oil gradient • Declining in-well oil thickness • Declining oil saturations • Increasing temperature • Increasing oil density • Increasing oil viscosity • Matrix heterogeneity

Table 2.2

Results of Laboratory Physical Property Tests.*

No.	Sample	Density of NAPL (gm/ml)	Viscosity of NAPL (centipoise)	Surface Tension Air/Water (dynes/cm)	Interfacial Tension NAPL/Water (dynes/cm)	Surface Tension Air/NAPL (dynes/cm)	Temperature of Measurements
1	Well 306 7-29-10	0.8890	31.4	67.7	18.0	27.9	8.5C
2	Well 312 6-22-11	0.8769	19.9				8.5C
3	Well 315 7-24-10	0.8885	30.9	66.9	20.2	28.5	8.5C
4	Well 315 6-23-11	0.8908	31.8	66.3	19.2	28.5	8.5C
5	Well 317 7-29-10	0.8687	15.0	70.1	20.8	27.1	8.5C
6	Well 319 6/23/83	0.8532	9.7				8.5C
7	Well 319 6/28/89	0.8566	11.3				8.5C
8	Well 319 3/26/08	0.9091	99.9				8.5C
9	Well 319 7-28-10	0.8773	18.1	68.0	19.4	26.4	8.5C
10	Well 411 6/28/89	0.8629	13.9				8.5C
11	Well 411 7-26-10	0.8976	44.7	65.1	18.7	27.3	8.5C
12	Well 420D 6/28/89	0.8697	18.5				8.5C
13	Well 420D 7-29-10	0.8717	18.0	68.4	20.0	26.6	8.5C
14	Well 421B 7-26-10	0.8857	25.0	66.7	19.2	26.5	8.5C
15	Well 422 7-27-10	0.8914	38.0	63.8	19.4	27.1	8.5C
16	Well 423 10/30/85	0.8546	10.2				8.5C
17	Well 423 6/28/89	0.8583	12.1				8.5C
18	Well 423 3/26/08	0.8635	12.9				8.5C
19	Well 423 7-28-10	0.8644	13.2	68.9	20.7	25.6	8.5C
20	Well 521 7-27-10	0.8783	23.9	65.1	20.7	27.4	8.5C
21	Well 521 6-23-11	0.8732	22.5	66.4	18.9	26.5	8.5C
22	Well 532A 6/21/12	0.9001	78.5				8.5C
23	Well 533D 7-28-10	0.8803	22.7	69.9	19.7	27.6	8.5C
24	Well 534A 7-29-10	0.8709	16.5	69.8	20.2	26.6	8.5C
25	Well 604A 6/28/89	0.8555	13.0				8.5C
26	Well 604A 6/21/12	0.8940	36.1	67.8	11.9	28.3	8.5C
27	Pipeline #3 4/10/84	0.8555	13.0				8.5C

* ASTM and API standard methods were used. Samples from monitoring wells were collected in 2010-2012 with a bailer made of inert materials. One-liter samples of oil and groundwater were transferred from the bailer to amber glass bottles, stored at ambient temperatures, packed securely in coolers, and shipped with a signed chain-of-custody by courier to the offsite laboratory in Tulsa, OK.

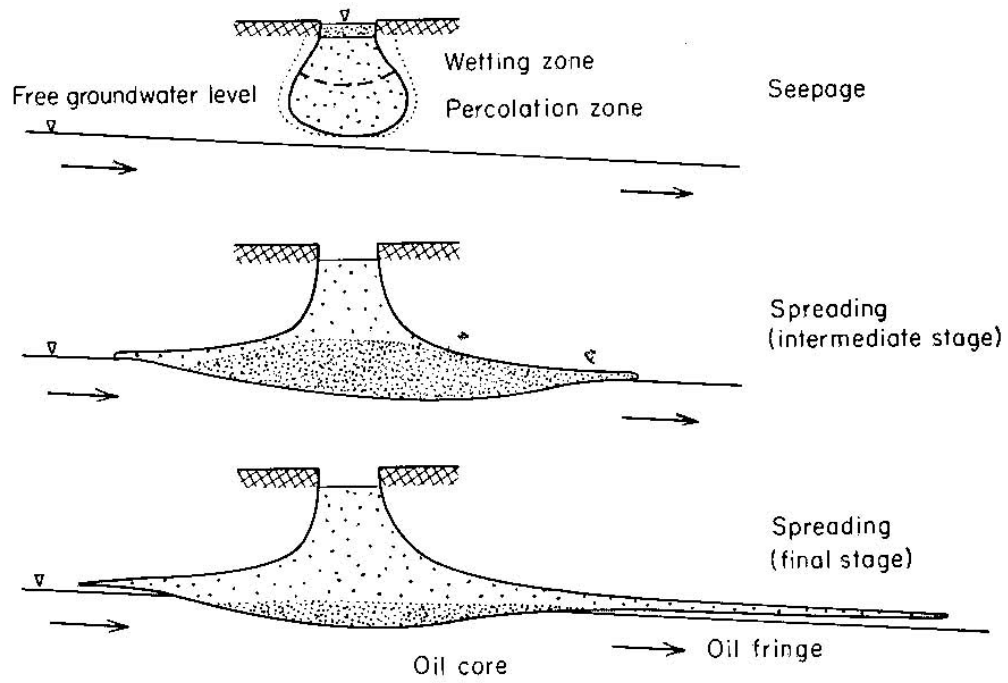
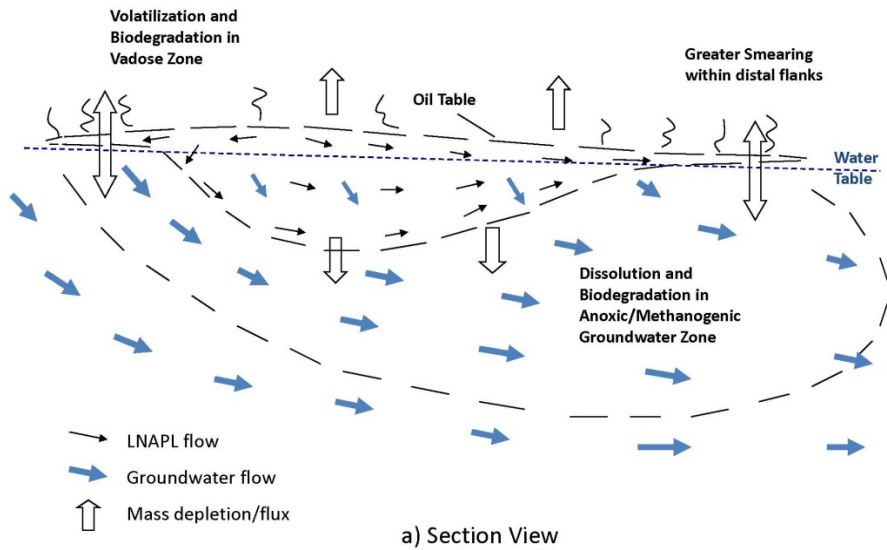
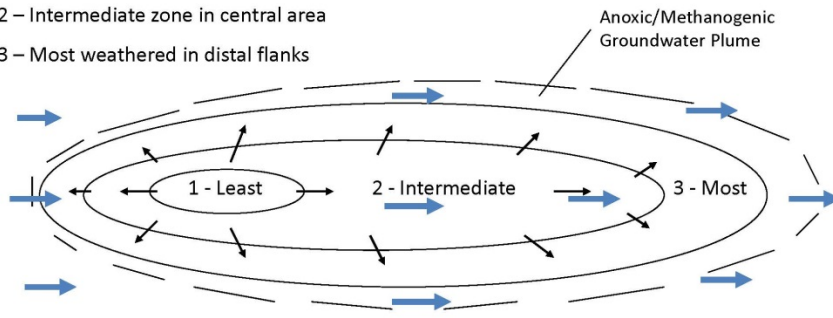


Figure 2.1 Conceptual model of LNAPL body spreading (Schwille, 1967).



Three zones of Weathered LNAPL:

- 1 - Least weathered near release point
- 2 - Intermediate zone in central area
- 3 - Most weathered in distal flanks



b) Plan View

Figure 2.2 Conceptual sketch of a stable LNAPL body in which lateral spreading is balanced by mass depletion that is most dominant in the distal flanks, and cannot build sufficient head to overcome capillary resistance at the leading edge.

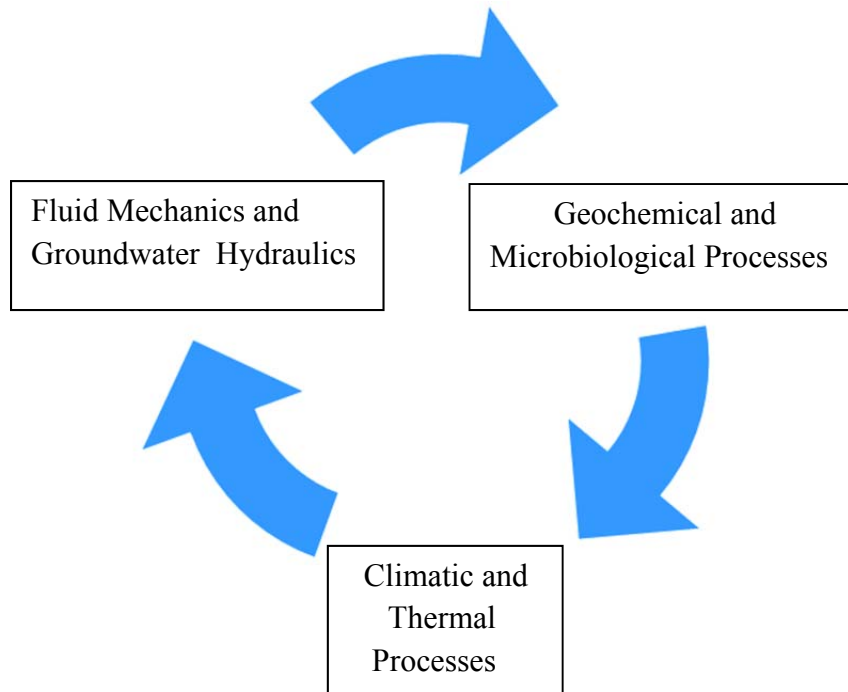


Figure 2.3. Cyclic relationships between fundamental processes affecting LNAPL mobility.

North Pool Oil Body and Site Features

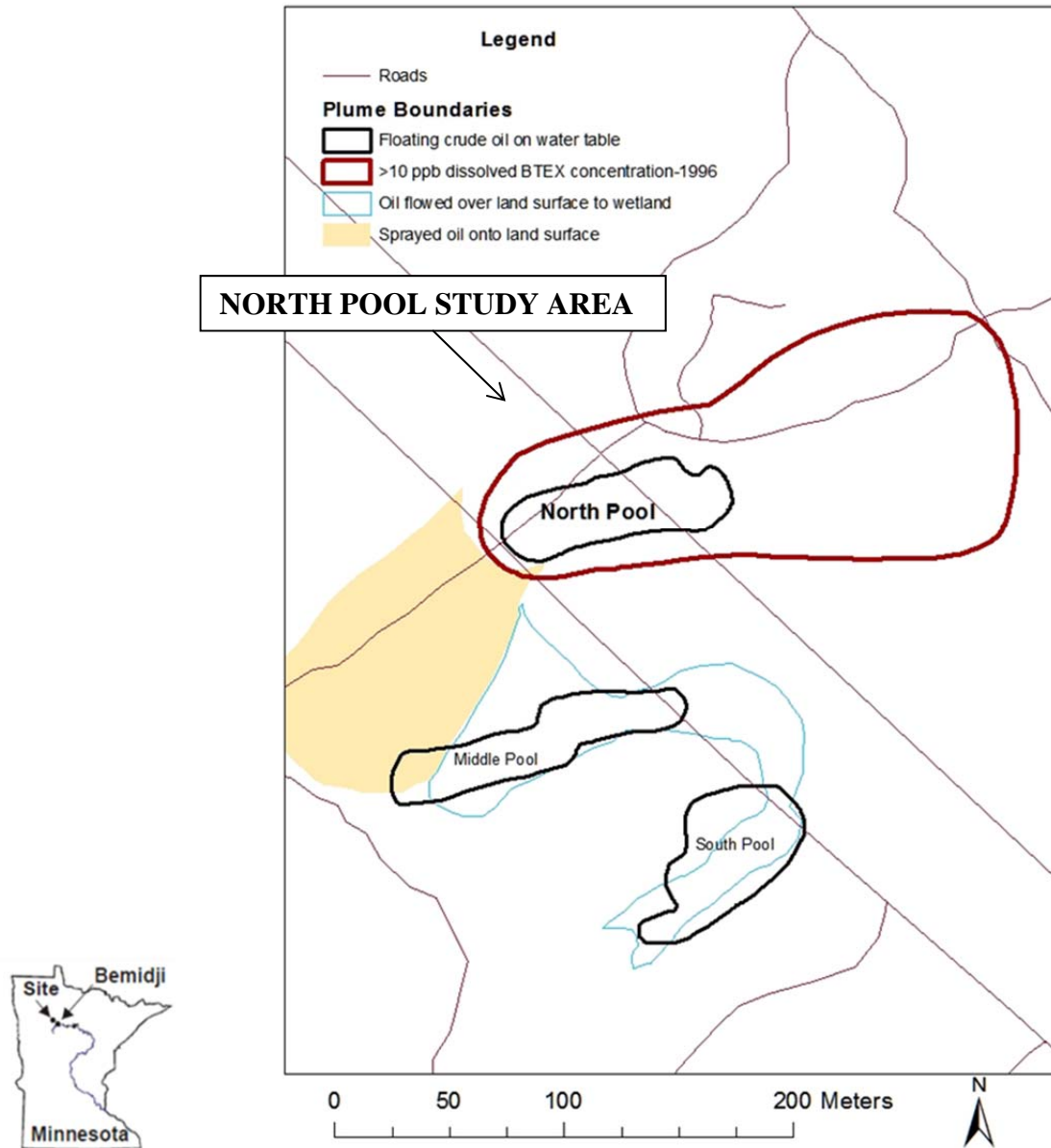
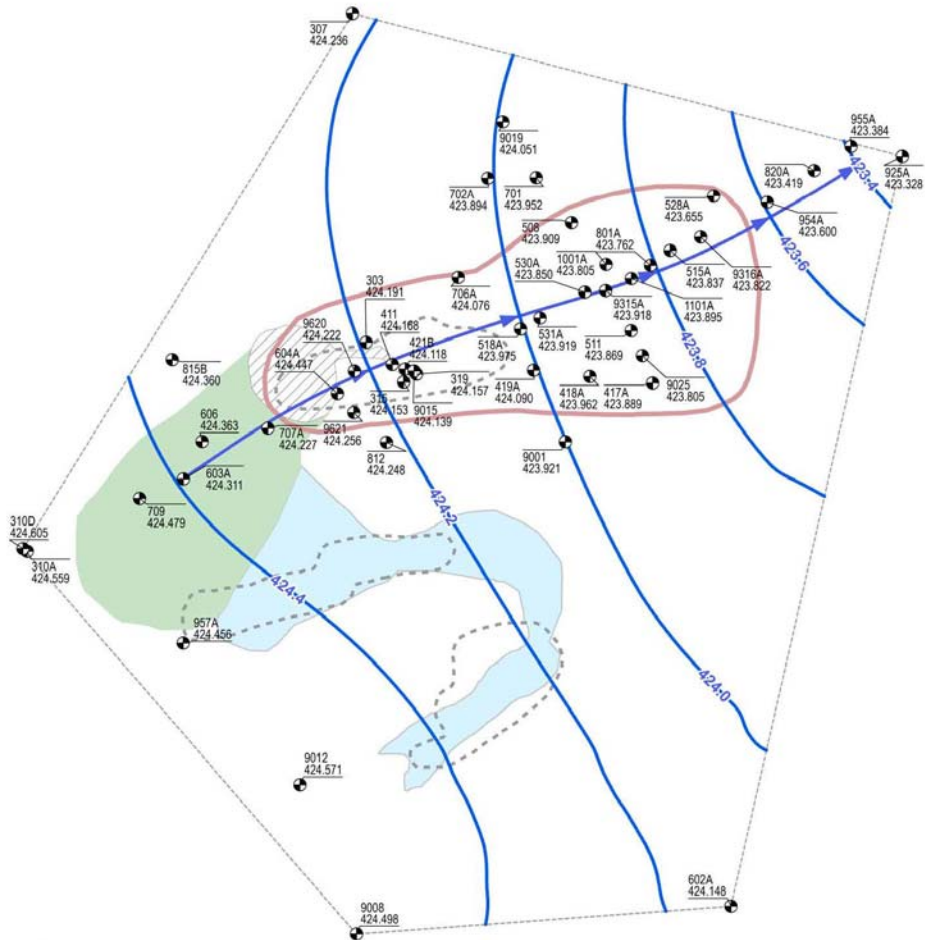
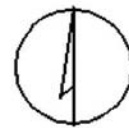


Figure 2.4 Location of the USGS crude oil research site and North Pool for testing the hypothesis.



Legend

- Wells Used For Average Corrected Water Level
- Water Level Contour (0.2 mASL Interval)
- Average Gradient Direction
- Convex Hull Around Measurement Points
- Plumes**
- Description**
- Oily substrate excavation
- Floating crude oil on WT
- >10 ppb dissolved BTEX Concentration-1996
- Spray Zone
- Oil flowed over land surface to wetland



SCALE IN METERS
0 50

Figure 2.5 Average water-table contour map showing gradient direction through the North Pool footprint in 2012 and dissolved BTEX groundwater plume footprint in 1996.

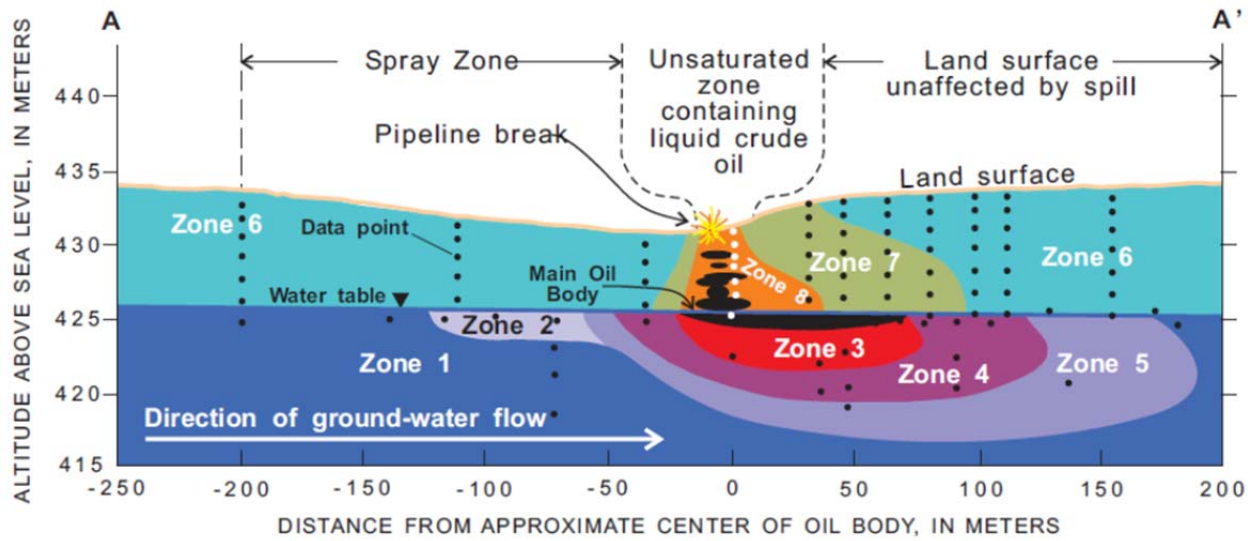


Figure 2.6. Geochemical zones within the saturated and unsaturated zones at the crude oil pipeline release site near Bemidji, MN (Delin et al., 1997).

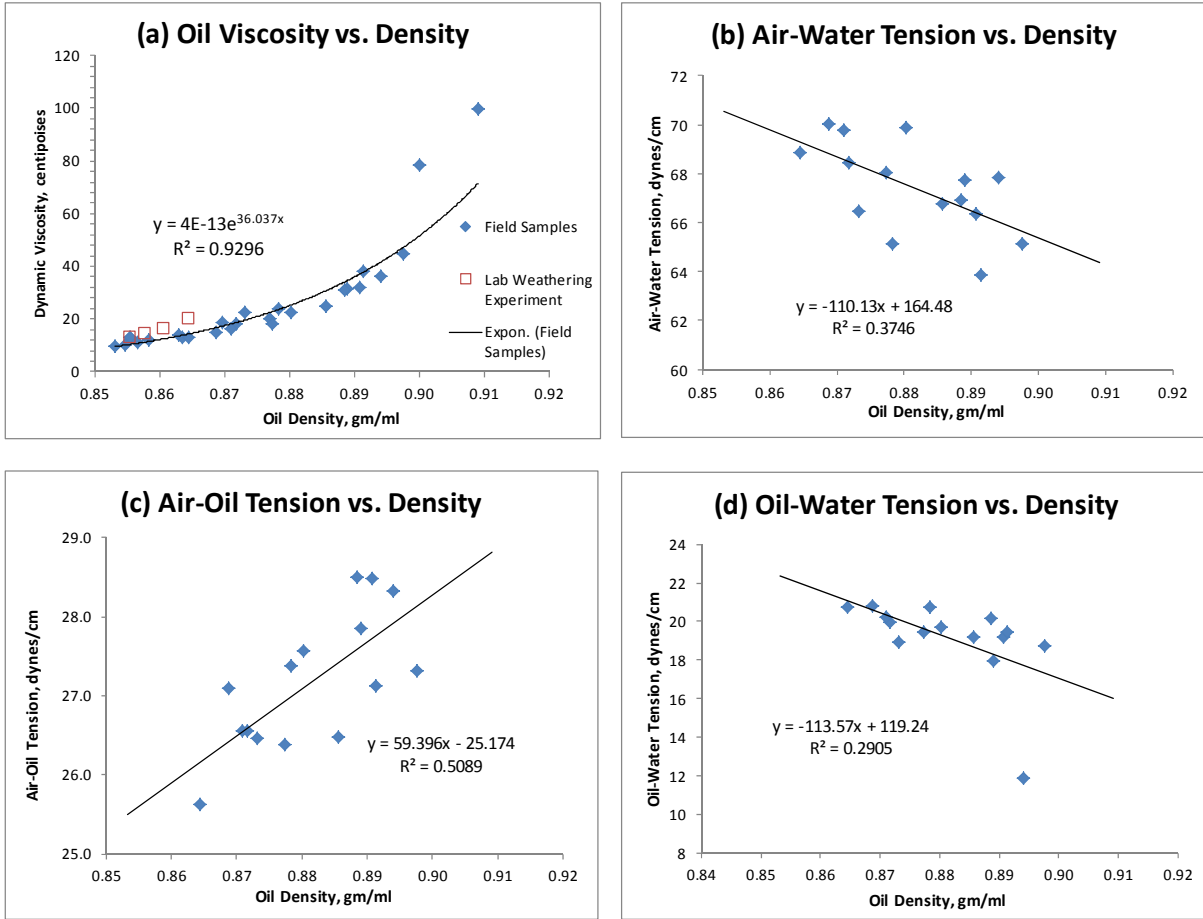


Figure 2.8 Plots of laboratory determined physical fluid properties at 8.5 °C for both recent (2010-2012) and archived (1984-2008) oil/water samples.

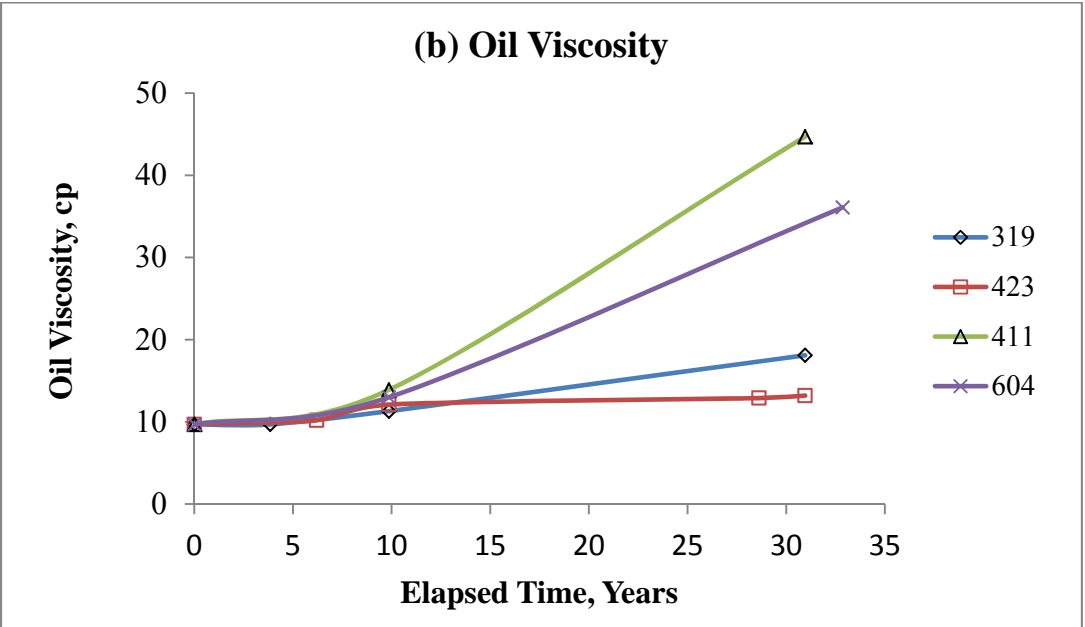
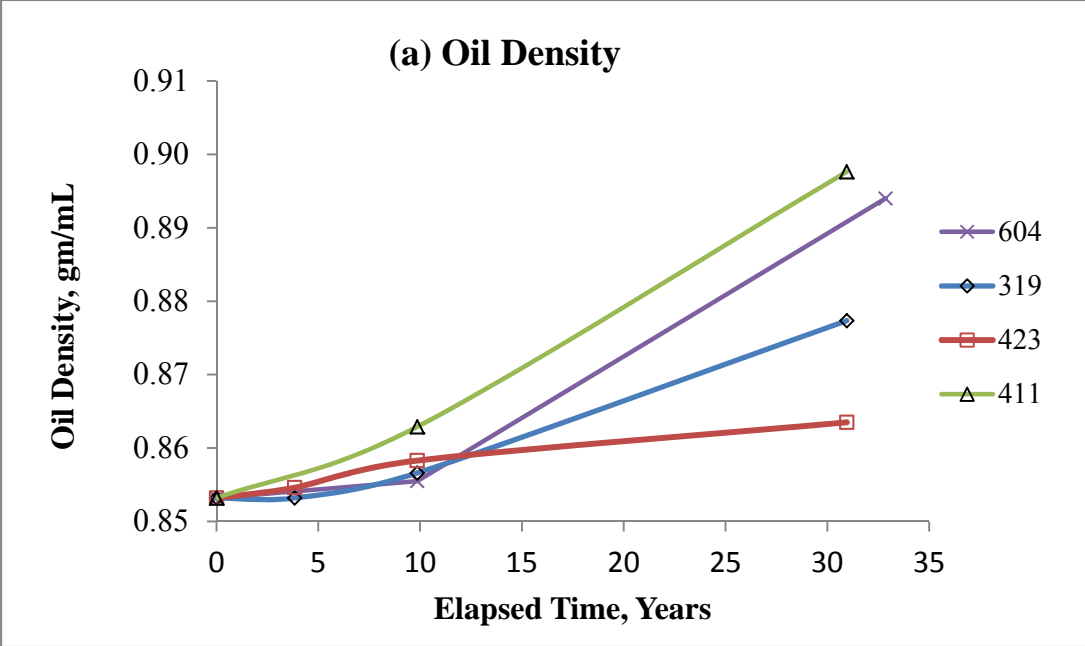


Figure 2.9 Historical changes in oil density and viscosity at four wells in the North Pool.

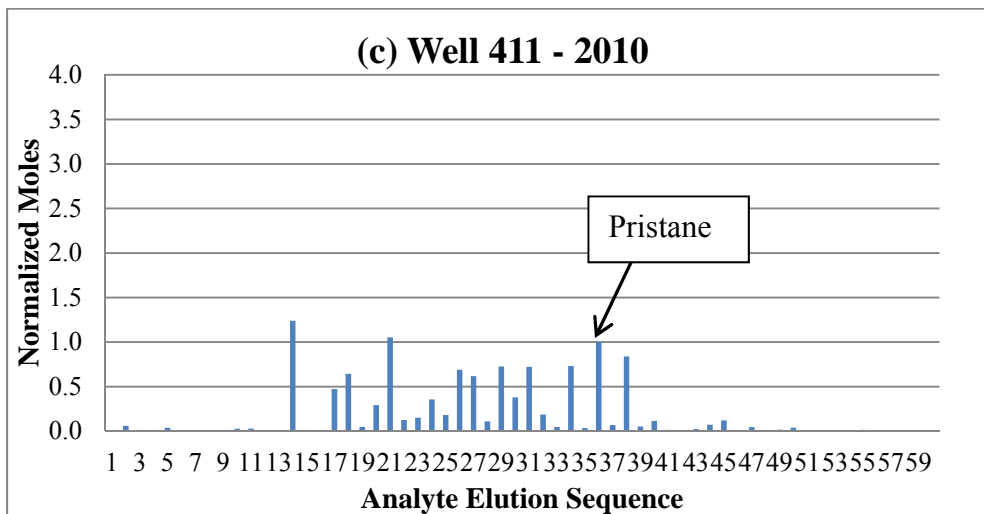
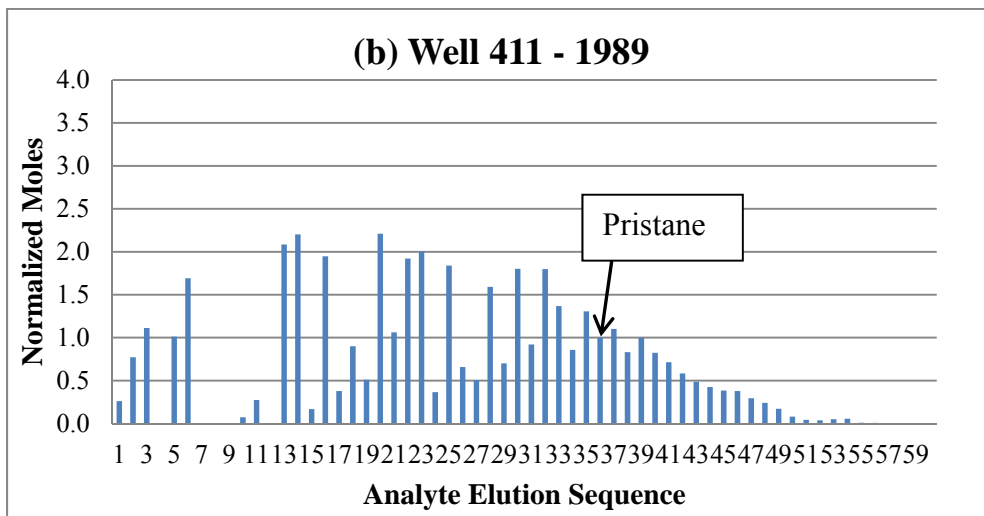
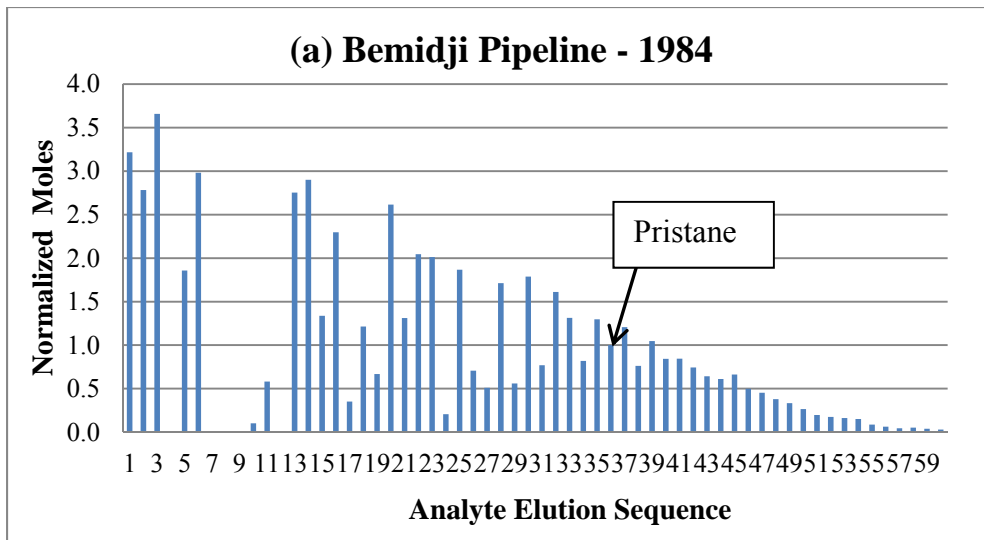


Figure 2.10 Normalized moles of GC analytes in the reference oil and two well 411 oil samples.

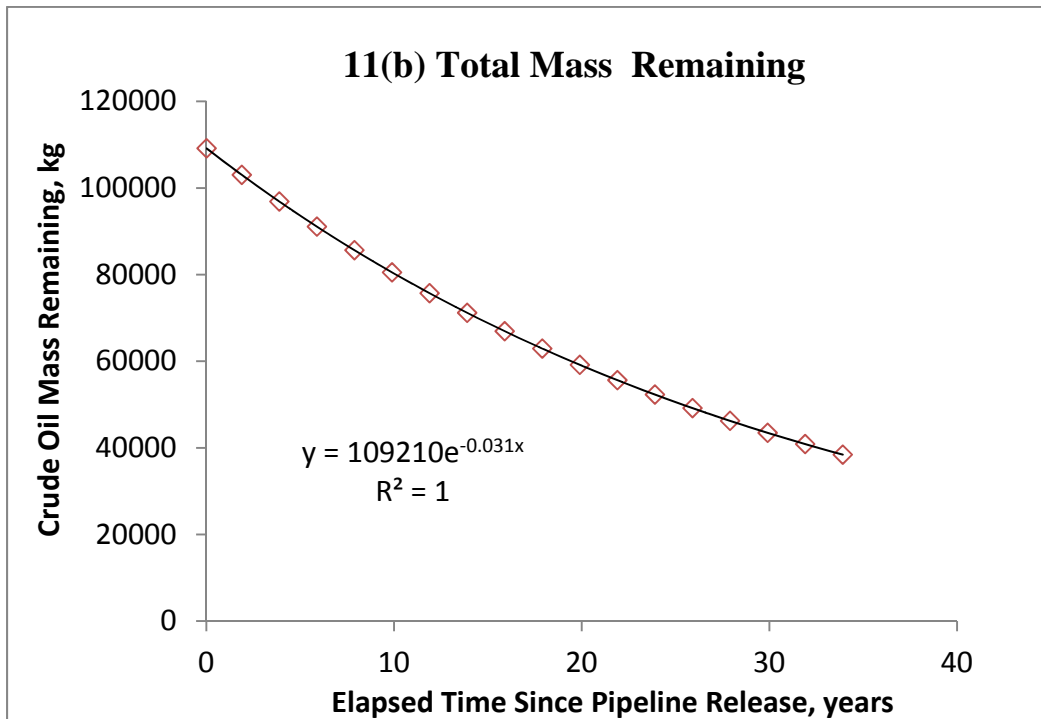
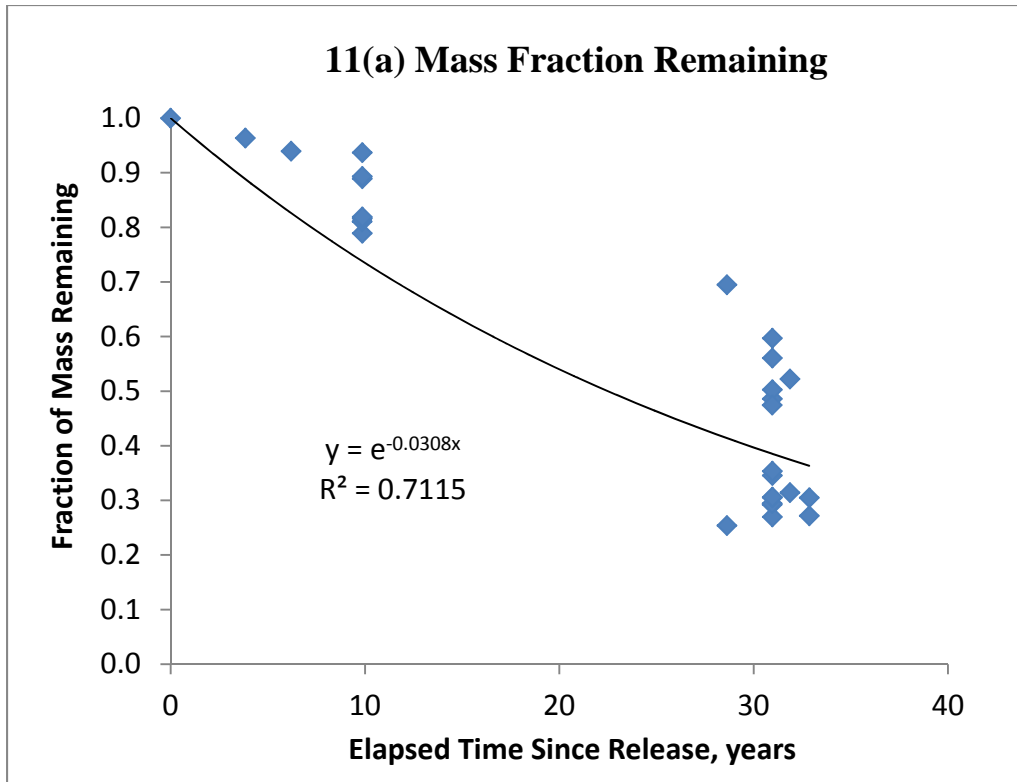


Figure 2.11 Plots of calculated trends for (a) fraction of North Pool mass remaining relative to the reference oil based on changes in oil composition, and (b) base-case estimate of mass of remaining North Pool oil following the 1979 release event.

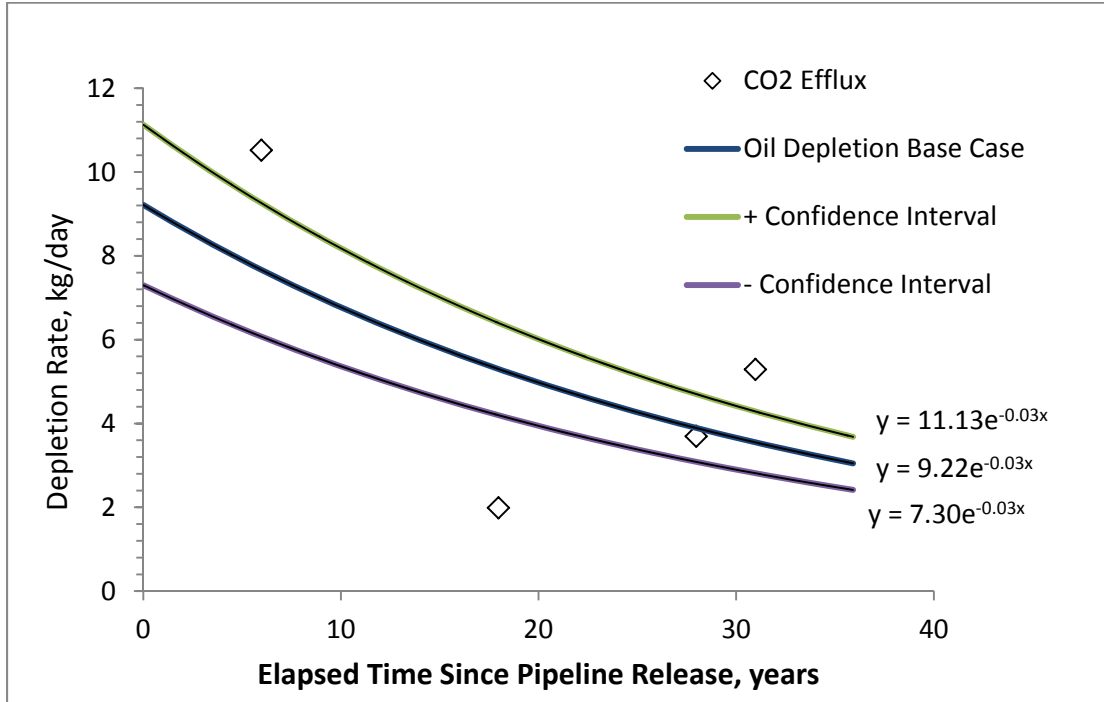


Figure 2.12 Calculated historical remaining North Pool oil mass decline curves developed from 1990-1992 total volume estimate based on core analyses (Delin and Herkelrath, 2014).

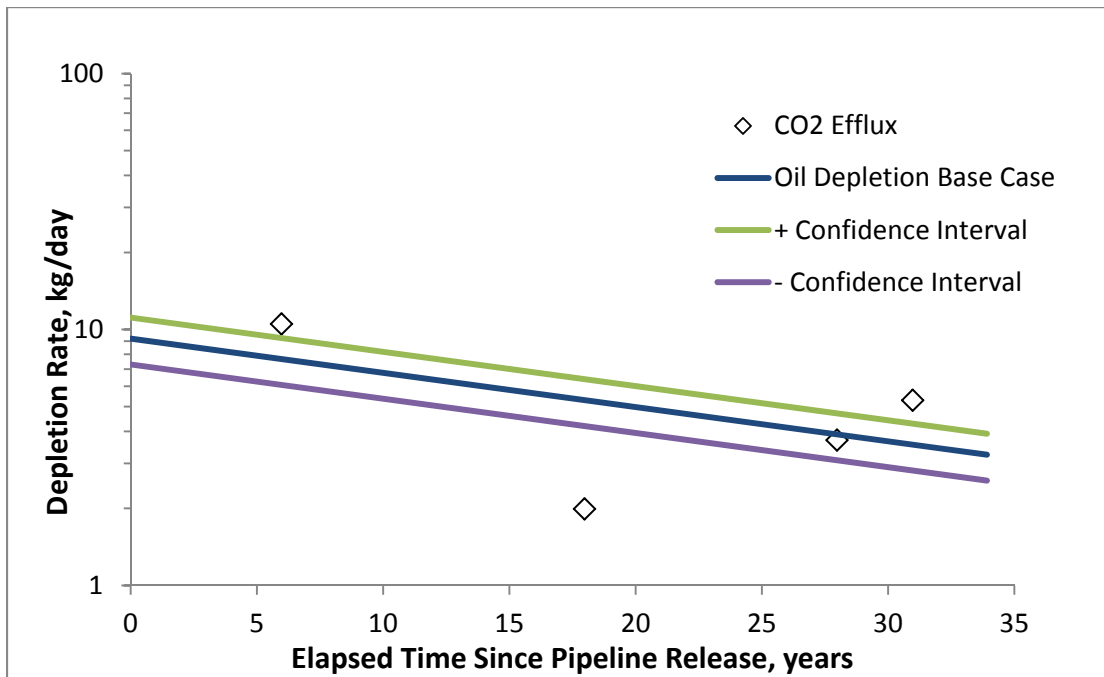


Figure 2.13 Plot of calculated historical North Pool base rate of mass depletion and mass losses inferred from direct measurements and modeling of CO2 efflux to the land surface.

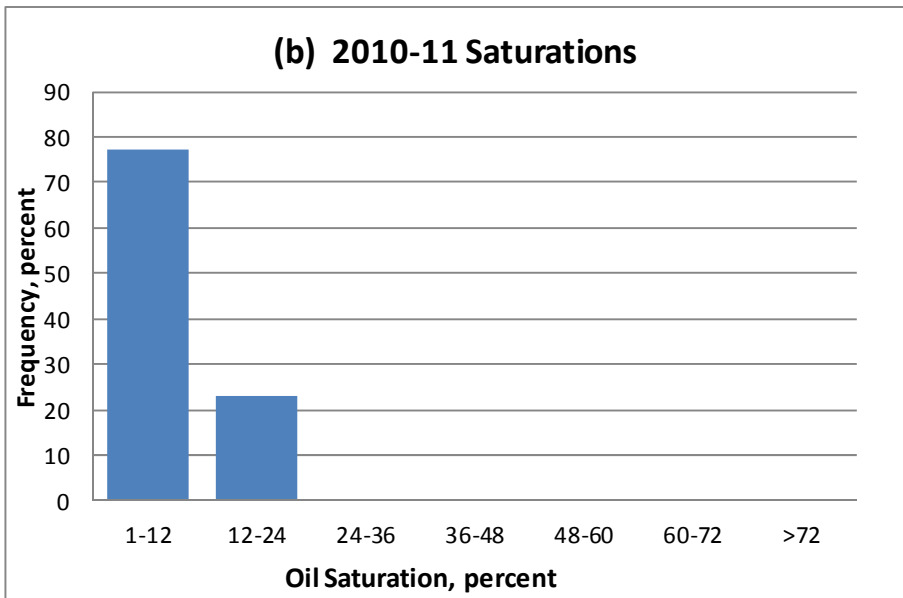
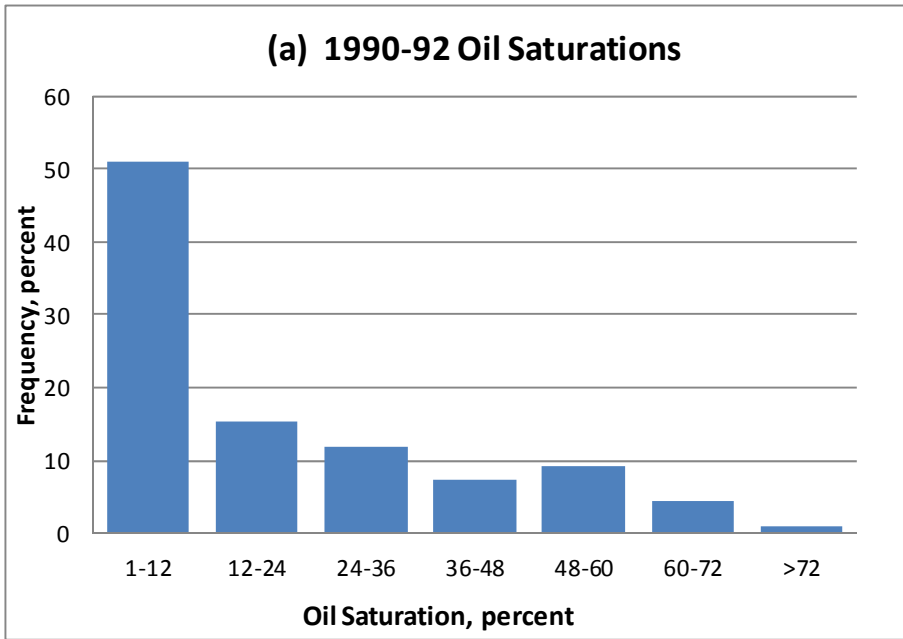


Figure 2.14 Histograms of oil saturations in core samples collected during (a) 1990-1992 at ten locations by the USGS, and (b) 2010-2011 at eight locations within the North Pool area.

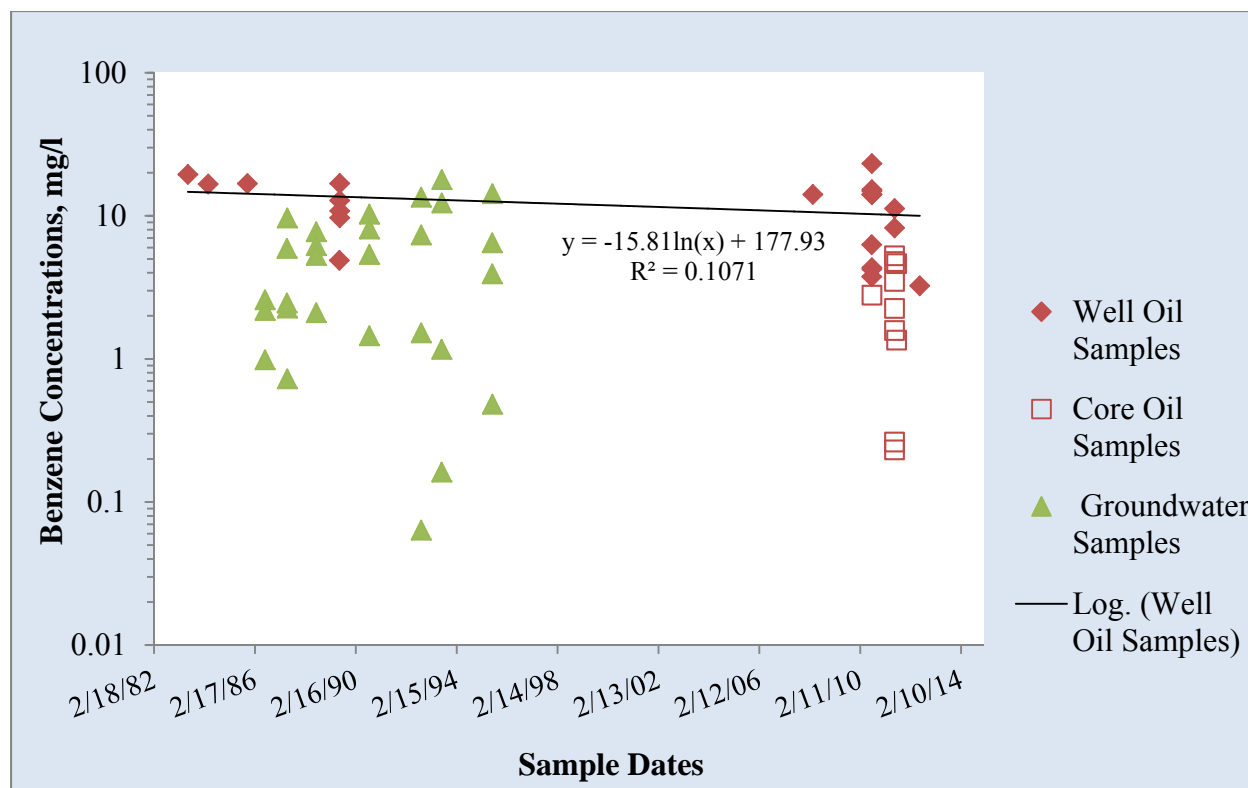


Figure 2.15 Plot of benzene concentrations in groundwater (USGS website) and equilibrium benzene concentrations calculated with mole fractions of benzene in oil samples collected 2010-2012.

CHAPTER 3

A CONCEPTUAL MODEL FOR LNAPL SPREADING TO A STABLE CONFIGURATION, PART 2 – ASSESSMENT OF MASS BALANCE¹

¹Lundy, D.A., Dowd, J. F., and Rasmussen, T. C. To be submitted without the appendices to *Ground Water, Journal of the Association of Ground Water Scientists and Engineers*.

Abstract

A Part 1 companion paper focused on the history and rates of oil weathering inferred from changes in chemical composition and fluid properties that reduce oil mobility attributed to the anaerobic and methanogenic biogeochemical environments in the contacting groundwater. Part 2 integrates fluid property history and mass depletion rates from Part 1 with oil mass inflow rates from the infiltration source zone into the downgradient region of the North Pool oil body where progressive deceleration of the leading edge is known from historical data. A 2010-2012 field investigation re-delineated the extent of the North Pool and generated matrix properties controlling oil migration with core analysis and baildown tests. Our conceptual model uses the 34-year average water-table gradient for estimating oil potentiometric gradients for calculating oil mass fluxes. Mass balance tests are performed at the LNAPL-body scale with modeled horizontal oil mass inflow rates into a downgradient area, and mass depletion outflow rates from the same area as it expanded. A mass balance between the rates of mass gains and losses in the downgradient area of the North Pool oil body is demonstrated for a 15-year “window of opportunity for stabilization” beginning in 2020. Rates of oil discharge into the downgradient area from the upgradient infiltration area were greater than mass depletion rates during 1984-1998 when monitoring well gauging data indicated ongoing advancement of the leading edge. Between 1998 and 2012, including a 4-yr period of recovery-well pumping, the leading edge advancement slowed but did not with certainty reach an asymptotic level. Because stability assessments are inherently uncertain and subject to different degrees of resolution, forecasting leading edge stability is best expressed in probabilistic terms, but is only confirmed by long-term monitoring with wells, soil cores, and direct sensing tools.

Introduction

Within the last decade, the stability of an LNAPL source zone has become an essential element of a growing number of risk-based regulatory policies at the state level. Further movement of the source zone can allow continued growth of vapor and groundwater plumes if the LNAPL body is still spreading laterally. Previously, Rice et al. (1995) and Mace et al. (1997) reported that hundreds of groundwater plumes originating from LNAPL sources were stable or shrinking. Their findings provided field evidence that the influx of contaminant mass into the plume eventually balances with mass losses downgradient over a footprint area. Once the mechanism of plume stabilization was understood, it became acceptable to regulators and was included with a demonstration of natural attenuation as an element of risk-based plume management. By the early 2000s, the stability of the dissolved phase plumes associated with petroleum product release sites was cited as evidence that the LNAPL source areas had reached stable configuration by a similar mass balance mechanism (Huntley and Beckett, 2002; API, 2004).

In the mid-2000s a growing number of environmental professionals approached the LNAPL stability question by evaluating multiple lines of evidence driven by available site data, using both qualitative observations and quantitative methods (Science Advisory Board, 2006; ASTM, 2007; ITRC, 2009). Qualitative evidence generally includes a stable dissolved-phase (e.g. BTEX) plume, an LNAPL source zone known to be decades old, and the lack of LNAPL detections in monitoring wells located near and downgradient of the LNAPL leading edge. The quantitative elements may include an estimate of the non-wetting fluid entry pressure at the leading edge (Charbeneau, 2007), small LNAPL mobility and transmissivity values based on

field baildown tests and fluid properties (ITRC, 2009), and finally on depletion of contaminant mass in the source zone that could balance with lateral spreading.

Mass depletion estimations are often based on biological degradation rates in the vadose and/or groundwater zones immediately above and/or beneath the LNAPL body. Proposed methods involve either: a) changes in contaminant and electron acceptor concentrations inferred from a stoichiometric analysis of biogeochemical reactions (Johnson et al. 2006; Lundegard and Johnson, 2006), or b) measurement of CO₂ effluxes at the land surface above the LNAPL footprint area (Sihota et al. 2011, 2012; Zibron et al. 2013; and Palaia et al. 2013). These approaches have both been referred to as the Source Zone Natural Depletion (SZND) and the Natural Source Zone Depletion (NSZD). In addition to accounting for compounds that drive risks (e.g., BTEX, etc.), these assessments should include mass losses associated with volatilization of non-degradable species in the source area and biodegradable mass (e.g., DOC) in groundwater leaving the source area. When archived and current LNAPL samples are available for analysis, interpreting historical and spatial changes in LNAPL composition appears to be a more direct and comprehensive method for estimating rates of LNAPL mass depletion.

Relatively few sites have been adequately investigated to characterize the history of LNAPL spreading, weathering, and hydraulic and fluid property parameters that have controlled historical spreading rates. Mahler et al. (2012a) conducted field tests assuming a stability status of LNAPL bodies at seven sites with in-well dilution tracer tests to estimate LNAPL transmissivity and mass flux rates against mass depletion rates estimated with CO₂ mass efflux measurements. However, plume stability was assumed and not proved.

In a laboratory sand-box experiment with pure MTBE as the LNAPL, Mahler et al. (2012b) observed that LNAPL body spreading ceased when a mass balance existed between the

rate of mass input at the source balanced with the rate of mass depletion over the downgradient LNAPL body. They developed a conceptual and mathematical model based on the lab experiment with simplifying assumptions. Scenario calculations showed the sensitivity of a stable LNAPL footprint size to the constant rates of mass input and output. While the lab experiment confirmed the validity of a mass-balance control on the process of plume stabilization and showed that residual saturations are not required to ensure a stable LNAPL body, the applicability of the predictive model to real-world field situations remained in question in their concluding remarks.

Based on our observations and analysis of stabilizing parameters for the North Pool oil body at the Bemidji, MN research site, a mass balance is the key factor to prove stability, but measuring and demonstrating that a balance has been reached is challenging. An objective in Part 2 is to demonstrate evidence that the historical trends in the rates of mass flux into and out of the downgradient half of the North Pool will plot as intersecting lines that are equal at their intersection. After that condition occurs, there may still be evidence that internal lateral migration of oil from the source area continues towards the leading edge. However, knowing precisely when and where this condition occurs at points along a sinuous leading edge is inherently uncertain and can only be approximated by additional field observations near a mapped leading edge.

Method of Testing the Hypothesis

Our basic hypothesis is that a finite and sudden LNAPL release volume that reaches the water table will spread laterally to a stable configuration when the rate of oil mass depletion along a flowpath area balances with the rate that LNAPL mass is being added to the flowpath area. We consider the non-wetting fluid capillary resistance at the leading edge to facilitate

stability only after the mass balance comes into play, but can contribute to an irregular shape of the leading edge. Estimates of the historical lateral flux of mobile LNAPL mass can be estimated with a history of declining LNAPL transmissivity and gradients and a form of the Darcy equation written for the LNAPL phase. Estimates of the non-wetting fluid entry pressure for the LNAPL at the leading edge can be made with core laboratory analyses of fluid and matrix properties expected at the leading edge, but these will vary spatially in heterogeneous media causing fingering at a small scale.

While we could evaluate the hypothesis by simulating physical, chemical, and biological processes from 1979-2012, that approach may not necessarily provide a more reliable conclusion than a simple mass-balance box-model using a large comprehensive set of historical field and laboratory data for a well-studied LNAPL site. For that reason, we selected the National Crude Oil Spill Fate and Natural Attenuation Research Site near Bemidji, MN to test the hypothesis and refine a conceptual model for LNAPL stabilization. Over the past three decades, the U.S. Geological Survey (USGS) and university research teams have characterized the basic hydrogeological and biogeochemical conditions at the North Pool oil body. They archived oil samples and analyzed cores collected from the oil-bearing zone. These could be supplemented by core and oil sampling/analyses during our investigation of 2010-2012. In Part 1, those data were used to estimate historical oil plume-wide rates of mass depletion. Part 2 focuses on the declining rates of historical movement of the oil body leading edge and historical mass discharges of mobile LNAPL from the historical oil infiltration zone into the downgradient LNAPL zone, at both the plume and flowtube scales.

Applications of the mass-balance mechanism to stabilization cited above have generally occurred late in the spreading history of the studied LNAPL body, when the assumption of

stability is supported by qualitative evidence. Also, the spatial- and temporal-dependent mechanisms leading to stabilization over time are typically characterized at a LNAPL-body scale. The approach here is to integrate the history of LNAPL mass discharges from the infiltration area with the history of mass depletion in the downgradient area to: a) test for a mass-flux imbalance in early years when spreading was known to be ongoing, and b) to re-test in later years to estimate when the fluxes would balance at both the LNAPL body and flowtube scales.

The application of Darcy's law to non-aqueous fluids (crude oil and natural gas) and the non-wetting fluid threshold pressure needed for the analysis were established in the 1930s and 40s in the petroleum engineering literature (Bear, 1972). These were applied to LNAPL in contact with shallow groundwater in the 1960s and 70s by European investigators, including Schwille (1967) and van Dam (1967). Zilliox and Muntzer (1975) and Schiegg (1980, 1983) extended their work to explain the occurrence of LNAPL in wells screened across the water table. These papers provided the first conceptual model that accounted for effects of capillarity and LNAPL fluid properties on in-well LNAPL thicknesses at static equilibrium. The development of mathematical expressions for saturations of immiscible fluids sharing space in porous media developed for applications in petroleum and soil physics were used by Lenhard and Parker (1990) and Farr et al. (1990) for a new model with the LNAPL saturation profile balanced around a static water table in porous media in equilibrium with an in-well thickness of LNAPL. Huntley and Beckett (2002) extended the saturation profile model with a homogeneous-isotropic matrix to a heterogeneous model composed of two or three layers with contrasting matrix properties. The multi-layered model still assumes a homogenous LNAPL fluid unevenly distributed in vertical hydraulic equilibrium across all three layers. No simplified mathematical

model for spatially heterogeneous fluids in heterogeneous porous media is available for testing the stability hypothesis.

The saturation profile model provides a way to relate in-well thickness to the distribution of LNAPL in porous media near the water table at static equilibrium. In order to estimate transmissivity of the mobile LNAPL-bearing zone in the single homogenous matrix, one must quantify the following ten parameters:

- a) In-well LNAPL thickness at static equilibrium;
- b) Five fluid properties affecting mobility at approximate field temperatures – density and viscosity of LNAPL and water (or specific gravity and relative viscosity); air-water and air-oil surface tensions, and oil-water interfacial tension; and
- c) Four matrix properties of the porous media – hydraulic conductivity (or intrinsic permeability), capillary properties (van Genuchten α and n , or Brooks-Corey non-wetting fluid entry pressure and pore-size distribution index), and residual water saturation.

The matrix porosity can be used for estimating specific LNAPL or water volumes and residual LNAPL saturations can be used to account for LNAPL mass temporarily stored above and below the mobile LNAPL zone, or to account for transfer of mass associated with water table changes (Parker et al., 1987; Lenhard and Parker, 1990).

The challenge of estimating LNAPL transmissivity controlled by ten or more parameters is managed by: 1) performing field slug-withdrawal (baildown) tests to estimate transmissivity at multiple well locations, 2) assuming that heterogeneous LNAPL-bearing media can be represented by an effective homogeneous matrix, and 3) using an inverse parametric solution that finds a set of best-fit average capillary and hydraulic properties from one or more national

databases (Carsel and Parrish, 1988; Becket and Joy, 2003) at each baildown test well location (Lundy, 2006). Given the history of LNAPL thickness (USGS well gauging database) and fluid properties (Part 1) at each test well location, historical LNAPL transmissivity values are calculated with the best-fit matrix properties at each location. These are to be multiplied by the long-term average water-table gradient adjusted for oil density values for each test well location.

Estimates of LNAPL transmissivity in 2010-2011 were made at three wells near the downgradient limit of the infiltration area. These estimates were based on field baildown tests analyzed with methods described in Lundy (2006) and recent API (2012) guidance. The history of LNAPL transmissivity values from 1979 through 2012 at these locations is calculated with the history of LNAPL thickness, fluid properties, and unchanging matrix properties at each well. LNAPL transmissivity values will appear to be contrived if back-calculated to fit with estimates of mass loss and an assumed stable LNAPL configuration. To be credible, they must be calculated from fluid saturations that are consistent with core sample saturations for at least the 1990-1992 and 2010-2011 core collection and lab analyses. The history of LNAPL fluxes are based on an average water-table gradient, adjusted for the oil potentiometric gradient, controlled by the history of LNAPL thickness and specific gravity fluid property changes and invariant matrix properties (the ten parameters listed earlier).

The Darcy mass fluxes of LNAPL from the infiltration area are compared to mass depletion rates at two scales: a) the LNAPL-body scale; and b) the LNAPL-flowtube scale. At the LNAPL-body scale, we estimate a sequence of mass discharge rates exiting the LNAPL infiltration zone and entering the downgradient LNAPL discharge area. A sequence of historical mass depletion rates are applied to the growing downgradient area based on compositional changes and the history of mapped leading edge positions provided in Part 1. At the flowtube

scale, we calculate the influx of LNAPL at each of the three baildown test wells into each of three 1-m wide flowtubes. These follow curving pathways inferred from historical positions of LNAPL body boundaries and terminate at the leading edge of the LNAPL body, which was updated in 2012. We estimate a sequence of mass depletion rates along each lengthening flowtube surface area using unit-area loss rates and leading edge positions (Figure 8 in Part 1).

The mass balance test at the LNAPL-body scale is performed at multiple dates: a) from 1984-1998 when the leading edge was known to be advancing and the rate of total mass input must have been greater than mass losses, and b) in 2010-2012 when the leading edge was suspected of being stable and total mass input would have been less than the mass depletion rate. The mass balance test at the flowtube scale is performed for each flowtube to test the idea that each flowtube may have a unique history of stabilizing, meaning the leading edge does not stabilize at all points at the same time, providing a more irregular shape to the leading edge for any date.

Our approach reduces to a set of box-model mass-balance calculations similar to what others have used to test for stability at LNAPL sites. Previous mass-balance assessments have been performed only at the LNAPL-body scale with late-time data in the spreading history of a decades-old LNAPL body. By developing quantitative trends for LNAPL mass spreading and depletion at the plume and flowtube scales, our approach tests the hypothesis during early time when spreading was on-going and again at a later time when advancement had significantly decelerated. Testing at the flowtube scale provides a way to investigate whether stabilization at points along the leading edge are time and space-dependent. Our observations suggest one should expect some parts of the leading edge to stabilize earlier than others that continue

advancing until equilibrium between when chemical, physical, and biological processes exists at all points along the leading edge.

Oil Release and Initial Response

Hult (1984) provided the first account of the August 20, 1979 release and migration of approximately 10,500 barrels (1,700 m³) of crude oil into the local environment. Figure 3.1 shows a low-altitude oblique photograph of the spill site, an active recovery trench cut into the North Pool and the flow path taken by the oil to a wetland south of the release point. The North Pool oil body was created by oil sprayed eastward that collected in a topographic low area between the elevated pipeline corridor and the former Soo Line railroad line. The middle and south pools were created by oil sprayed westward that infiltrated to the water table at two locations along a sinuous surface drainage path to a small wetland (Figure 3.1; Figure 2.4 in Part 1). Figure 3.2 shows the locations of the pipeline release point, spray and excavation areas, the approximate 2012 footprint area, and dated positions of the leading edge from 1984-2012. Figure 3.3 is a topographic base map for the study area that shows two topographic low areas inferred to be the primary oil infiltration areas for the North Pool.

From near the pipeline break location an oil recovery trench was excavated to the water table and extended eastward into the topographic low considered to be the primary infiltration area above the North Pool (Figures 3.1 and 3.2). An unknown volume of oil and groundwater was siphoned off of the water table in the trench. During the site-wide emergency response, approximately 7,880 barrels (1,250 m³) were recovered leaving a balance of 2,630 barrels (418 m³) that infiltrated or was lost to the atmosphere. No further remedial pumping was undertaken until 1999-2004 during which two recovery wells were installed and operated at locations RW-1

and RW-2 in the North Pool (Figure 3.4) in response to directives from the Minnesota Pollution Control Agency (MPCA).

Within a few weeks of the release, temporary monitoring wells were installed in the general vicinity of release point and eastward of the pipeline and railroad line, but available records do not show detections of free-phase oil any these wells (Steve Lee, 2012 correspondence from the MPCA). Temporary wells were located too far north, east, and south of the North Pool infiltration area. Oil and grease detections were the only analytical parameter reported by Phannkuch (1979) for these wells. Based on limited data, the groundwater impacts were considered to be localized and diminishing. Weekly sampling of wells in 1979 became monthly events in 1980; after a few years groundwater monitoring was discontinued and the wells were abandoned.

LNAPL Body Delineation and Migration

The first recorded occurrences of oil in contact with groundwater began in 1983 with the installation of USGS monitoring wells along and downgradient of the overland oil flow pathways. The initial map of the North Pool footprint area was restricted to the vicinity the temporary excavation trench (Figures 3.1 and 3.2) based on four wells (301A, 306, 315, and 319; Figure 3.4) in the infiltration area (Hult, 1984). Wells installed during 1983-1986 provided stations for tracking the location and further movement of the leading edge inferred from first occurrences of oil in wells that previously only had groundwater.

The North Pool leading edge boundaries in Figure 3.2 are inferred from: a) first recorded occurrences of oil at monitoring wells during 1983-2012, b) delineation with direct-push soil borings in 1998 and again with LIF soundings in 2011, c) vertical delineations of oil within the vadose zone into the upper saturated zone with core sampling/analysis in 1990-1992 and 2010-

2011, and d) CO₂ and equivalent mass efflux rates collected in 2010-2012 by another university research team (Sihota et al., 2011 and 2012). Collectively, these diverse datasets are the basis for the footprint shapes and areas over time. North Pool footprint maps prepared in previous investigations have evolved, adjusting earlier footprints as the oil body spread laterally at declining rates. The nested footprint areas are our primary geographic frame of reference for mass spreading and depletion rate estimates.

Landon (1993) provided an updated delineation of the North Pool based on occurrences of oil in 14 wells in 1987-1989. His North Pool footprint map shows a maximum length of 80.0 m and maximum width of 26.6 m. It extended about 13.3 m upgradient (WSW) from well 604A approaching Pipeline #3 from which the release occurred. That is the most upgradient well completed in the North Pool, having been limited by safety concerns that prevent drilling near active pipelines. Maps prepared during our investigation show the upgradient edge of the North Pool extending beneath the pipeline on the basis of proximity of the trenching shown in Figure 3.2 based on earlier maps by the USGS and high CO₂ efflux measurements at the land surface above the pipelines (Sihota, 2013, personal communication; Lundy and Dowd, 2013b).

In May 2011, we re-delineated the positions of the leading edge and lateral and vertical extent of the oil-bearing sediments using a direct-push rig and a laser-induced fluorescence (LIF) detection-recording system (Dakota Technologies, Inc.). Preliminary field testing of two LIF technologies (UVOST and TarGOST) was performed near well 423 with the least weathered oil and just inside the downgradient leading edge where the oil is most weathered. Both tools showed equal ability to detect LNAPL near 423, but only TarGOST detected LNAPL near the leading edge, and was selected for 24 additional sounding locations.

Figure 3.5 shows the lateral extent of the North Pool inferred from the LIF survey, while accounting for fluid levels and oil occurrences in wells and consistent with above-average CO₂ efflux data (Sihota, personal communication, 2013). The lower half of the figure shows LIF graphic logs along a transect line near the centerline of the North Pool, oriented along the hydraulic gradient of the water table. The largest thicknesses of oil-bearing sediments underlie topographic lows represented by closed contours on Figure 3.5. A significant volume of oil drained to lower residual saturations in the vadose zone above the regional water table in the former oil infiltration area encompassed by the 3-m contour. Between the fifth and sixth LIF stations (TG1117 and TG1122), the thickness of the oil body declines sharply as one moves downgradient away from the infiltration area west of the elevated former railroad line, now a gravel road. Beneath and east of the gravel road, no significant stranded oil is observed in the vadose zone. In that downgradient LNAPL discharge area, mobile oil shares the void space with groundwater below a fluctuating water table and its capillary fringe. At the most downgradient LIF location (TG1102, Figure 3.5), the oil body tapers down to a 0.23-m thickness, the smallest observed above weak background signals at TG1104 on the transect and at seven other LIF locations just outside the mapped leading edge. The bounding contour was fixed at 0.2 m, a conservative lower-bound thickness capable of overcoming non-wetting fluid entry pressure in the coarsest-grained sediment within the capillary fringe.

In June 2012, measurable oil was observed for the first time at well 532A and the previously mapped leading edge was moved ~ 1 m east of that well. Observations of floating orange biomass in wells 532A and 520 in the summers of 2010 and 2011 and the steady increase in oil thickness as the water table declined in 2012-2013 would be consistent with oil having reached 532A before 2010, prior to the high water table period (Figure 3.6a) associated with the

unusually wet years of 2009-2011. Most but not all monitoring wells are gauged every summer field season. As of the fall of 2013, no oil has been observed in well 520. A falling water table during 2012-2013 caused the re-appearance of oil in well 604A (Figure 3.6b). GC analyses of oil samples collected in 2012 from these two wells, representing the most upgradient and downgradient locations, provided evidence that the fringes of the North Pool oil have the most weathered oil as hypothesized in Figure 2.2 of Part 1.

While the thickness of oil in a monitoring well does not directly correlate with the thickness of the mobile zone in the formation under heterogeneous conditions and a long history of water table fluctuations, the trend in the change is expected to correlate with declining oil saturations, which lead to smaller relative oil permeabilities and declining mobility. In addition to the physical hydraulic changes that naturally reduce the rate of migration, changes in oil composition will change physical fluid properties – primarily viscosity – which causes further reductions in rates of movement, essential for estimating historical LNAPL spreading rates.

Aquifer Hydraulic Properties

The movement of LNAPL in contact with groundwater is influenced by the local hydraulic gradient of the water table. Given the specific gravity of the floating LNAPL, the LNAPL potentiometric gradient can be estimated from the water-table gradient (Charbeneau, 2007). Because the average historical water table gradient is needed for modeling LNAPL discharge within the North Pool oil body, available historical well gauging data for shallow wells with floating LNAPL within oil body footprint and within the larger research site were used to develop a comprehensive estimate. Figure 3.7 is a contour map of the water table prepared by averaging all historical USGS gauging data at subset of shallow wells with short screens positioned near or across the water table, while accounting for the thickness and specific gravity

of the oil in selected wells in the north and south pools. The average hydraulic gradient through the center of the North Pool and trending ENE towards an un-named lake off the map has a magnitude of approximately 0.002644.

Figures 3.8 and 3.9 are maps of the oil and water tables on two dates during which the oil density (and/or specific gravity) had been measured in samples from wells used for calculating a “corrected water table,” where the thickness of floating oil is multiplied by specific gravity to convert it to an equivalent thickness of water above the oil/water interface in the well. These both show steeper gradients on both the oil and water tables in the infiltration area compared to the downgradient area east of the gravel road. This may be related to timing of the measurements during wet summers, preferential recharge collocated with the oil infiltration area with smaller water conductivities within the saturated zone near the water table, and very shallow wells that penetrate less than 1.5 m of the saturated zone.

Table 3.1 provides a summary of hydraulic conductivity (K) values of the outwash sediments developed by previous USGS laboratory and field testing efforts at the research site. Results are organized by the sampling depth relative to the water table, predominant lithology, and test method. The full range and spatial distribution of K values are consistent with prevailing stratigraphic models of fluvial deposits that tend to fine upwards from sands and gravels in the lower half to medium-to-fine sands in the upper half with occasional lenses of sandy silt that become more frequently encountered in the vadose zone. The 7 order-of-magnitude K range based on grain-size analyses (using the Krumbein and Monk, 1940 method), represents over 600 individual core samples collected in the early 1990s from the North Pool area. This wide range reflects a high degree of heterogeneity in the upper few meters, especially in the vadose zone but to some degree in the saturated zone where the LNAPL body is found.

The slug test K range and median values represent three replicated tests at each of 57 monitoring wells outside of the North Pool footprint area. Slug tested wells had short screens less than or equal to 2.5 m positioned in the upper to lower zones in the outwash aquifer. The upper zone is defined as being within 3 m of the average water table depth and lower part is at greater depths where coarser strata are found. The dissolved-phase groundwater plume emanating from the North Pool source area is associated within the lower zone, where K values are generally 5 to 10 times larger than the upper zone K values.

The pumping test result is based on a 45-hr constant-rate test on a well installed through the mobile oil zone near the center of the North Pool area with a screen set 3.5 to 9.5 m below the water table. The USGS estimated an average transmissivity of approximately 1,300 m²/day, based on the analysis of drawdown-time responses at 14 observation wells, which with aquifer thickness provides the range of average K values. These test results were approximately duplicated using a sinusoidal pumping rate created by an oscillating solid slug device at a trial test location approximately 30 m downgradient of the North Pool footprint area (see Chapter 4 in this dissertation for details).

Core Analyses

During the field seasons of 1990-1992, core collection from the oil-bearing zone was carried out by the USGS to characterize the spatial distribution and volume of the oil (Herkelrath, 1999; Delin and Herkelrath, 2014). Cores were collected with a cryogenic method (Durnford et al., 1991) adapted to conventional auger rig equipment. This “freezing-shoe” method was used to achieve 100% recovery of cohesionless sediments at ten locations along two lines near the centerline of the North Pool. The laboratory method of fluid saturation measurements documented by Hess et al. (1992), oil saturations ranged from 0.1 to 73.6%. Oil

saturations in the vadose and upper saturated zones were mapped along a vertical transect of the North Pool were used for calibration of a multiphase flow model (Dillard et al. 1997).

During the field seasons for 2010 and 2011, we collected core from the oil-bearing zone starting near or above the water table to the base of the North Pool oil body. Four coring locations were completed each year for a total of eight (C-1008, C-1009, C-1051, and C-1056 in July 2010; and C-1103, C-1108, C-1109, and C-1112 in June 2011; Fig. 3.4). An additional ninth location (C-1101) was located outside and approximately 5 m downgradient of the leading edge near an LIF station to verify that the background signatures indicated no detectable oil, and to provide additional samples for matrix property testing.

The cores were collected using the same freezing shoe method used by the USGS. Approximately 2-m of core was collected in 2-1/8th inch (5.5 cm) diameter transparent acetate sleeves, offering a view of oil-stained materials and methane bubble formation. Cores were cut in the field, labeled, capped, and frozen on dry ice before being shipped by overnight courier to the petroleum core lab (PTS Laboratories, Santa Fe Springs, CA). In the core lab, cores were sawed vertically, allowed time for the surface to thaw, placed on a table next to a scale, and photographed with a digital camera in white and then UV light. Core imagery was used to select the depth intervals for core sampling (cylindrical “plugs”) cut from the center of the cores, usually in a horizontal orientation.

Core samples were analyzed for the matrix parameters that control oil saturations and mobility listed above. Table 3.2 provides a summary of analytical results of testing performed on 76 individual core samples, including fluid saturations, total porosity, grain-size classifications, hydraulic conductivities, and two van Genuchten (1980) water retention capillary parameters (*vG-alpha* and *vG-N*) and the irreducible water content needed to obtain oil saturations.

Appendix E includes graphs of water retention curves, grain-sized distributions, and hydraulic properties for the North Pool cores plotted with those in the API (2006) database.

Figure 3.10 shows an upgradient-to-downgradient columnar section of core data with “column pairs” for each coring location and nearby field LIF signatures. The pair of left-hand columns are color-coded to represent lithology by predominant grain-size and the relative level of laboratory UV fluorescence. The right-hand column-pair is the laboratory photologs showing the white-light image and UV fluorescence image.

Figure 3.10 includes vertical positions of the highest, lowest, and July 2010 water table near each core location. Together, these features show that in 2010 approximately 80% the oil resided within the medium-grained sand and 20% was approximately divided equally between predominantly fine and coarse sand lithologies. The finding that most oil occurs in medium-grained sand is consistent with earlier North Pool investigations by Dillard et al. (1997), based on the 1990-1992 core data. The good agreements between the stronger lab and field fluorescence levels with greater oil saturations, and with the vertical position of these zones relative to the historical range of water table positions shown in Figure 3.5 are significant. These findings allow the oil-bearing zone to be treated as an equivalent homogeneous matrix for baildown test data analysis, and for later estimates of historical oil transmissivities needed to test the stability hypothesis.

Baildown Test Analyses

LNAPL baildown (slug-withdrawal) tests were performed at wells 315, 411, and 421B, located near each other in the historical oil infiltration area defined by the 3-m closed contour (Figure 3.5). The field methods for performing and analyzing these tests for estimating LNAPL

transmissivity conform to guidance from API (2012) and ASTM (2012). The field method involved the following steps:

- a) Measure depths to fluid levels (air-oil and oil-water) with an electronic interface probe several times prior to the start of the test to determine pre-test static levels. Record the pre-test thickness of oil and estimate an equivalent oil volume.
- b) When using transducers, install one in the water phase near the bottom of well and another in the oil phase so that the lowermost point is within the oil phase some distance above the oil-water contact. Start the system recording before bailing.
- c) Remove most of the oil volume with repeated bails and track volumes removed in a calibrated container; consider the end of bailing to be time zero for the test.
- d) Collect and record manual fluid levels over 24 to 36 hours. Depths to the air-oil level were made in all three test wells (with and without transducers). Depths to both fluid levels were made in well 315 only; with two transducers and cables the diameters of 411 and 421B could not accommodate the interface probe.

Changes in oil potentiometric head were equivalent to changes in the depth to the air-oil interface in each test well. The initial oil head change following a single withdrawal at 315 was calculated from the volume of the slug; subsequent changes were measured manually with an interface probe. Oil head changes in wells 411 and 421B were tracked with a transducer set in the oil phase, where water pressure heads were converted to oil column changes by dividing by the oil specific gravity. In well 315, the thickness changes in the oil column were converted to equivalent thickness of water and added to the depth of the rising oil-water interface to represent recovery of the water table. Oil head recovery rates in 411 and 421B were much slower than in 315, and rates of water table recovery in 411 and 421B were assumed to be equal to or smaller than the rate in 315. North Pool water table recovery rates are two or more orders of magnitude

slower than rates observed in nearby wells lacking oil (Strobel et al. 1998). This is attributed to shallow well penetration in the smear zone, where the relative permeability of the water phase is reduced by the presence of residual or low mobility oil.

The API (2012) Excel workbook for determining LNAPL transmissivity from baildown tests provides three methods of analyzing the recovery of the air-oil and oil-water interfaces after withdrawal of LNAPL. These methods are modified forms of analogous analytical solutions from the groundwater literature, including the Bouwer and Rice (1976) slug test, Cooper and Jacob (1946) and Jacob and Lohman (1951) constant-drawdown declining-yield test, and the Cooper, Bredehoeft, and Papadopoulos (1968) slug test solutions. The latter two methods require the user to also find a best-fit value for both LNAPL transmissivity and storativity. Appendix F provides a printout copy of the analysis of the baildown test data for well 315.

The API software is designed to account for well construction details and filter-pack drainage based on the test well screen and borehole diameters. However, monitoring wells at the research site were constructed without filter packs. Except for the finer-grained sand zones, the wells were installed directly into sandy zones having similar grain-size ranges that would encompass the range of most commercial filter sands. This simplifies the baildown analysis by eliminating the need to judge when filter-pack drainage of oil ends and significant drainage from the formation begins. The analysis can therefore use the early-time response, as with the Bouwer and Rice solution for a well with a screen set entirely below the water table (Bouwer, 1989).

Table 3.3 provides a summary of baildown test results using the API workbook. Mean oil transmissivity values for the three test wells range from 0.0043 to 0.055 m²/day and average 0.035 m²/day. These values are 5 orders of magnitude smaller than aquifer transmissivities determined with a 45-hr pumping test using wells having somewhat deeper screen settings

(Table 1; Delin and Herkelrath, 2014), and a short-term periodic slug test outside the North Pool using wells having comparable shallow screen settings as the baildown wells (Chapter 4 in this dissertation). Table 3.4 provides a summary of the functional expressions to find matrix parameter values that, together with pre-test in-well oil thicknesses and known fluid properties, can provide the same oil transmissivity determined with the API workbook at each test well location. These matrix parameters values are estimated by finding the inverse solution to the oil transmissivity, T_o , which can be expressed as follows (Zhu et al. 1993):

$$T_o = \int_{z_w}^{z_o} k_{ro} k_i \frac{\rho_o g}{\mu_o} dz , \quad (1)$$

where z_o is the elevation of the air-oil interface above z_w , the oil-water interface in the well at static equilibrium and taken as a datum, k_{ro} is the relative permeability of the oil phase, k_i is the intrinsic permeability of matrix i , ρ_o is the relative density to water, μ_o is the viscosity relative to water, and g is the acceleration due to gravity. Evaluation of Equation 1 requires values for the vG-*alpha* and vG-*N* water retention parameters and the irreducible water saturation. The relative permeability, a number between zero and unity, is found by adjusting the Mualem (1976) expression for an air-water fluid pair in the vadose zone to air-oil and oil-water fluid pairs in the oil-bearing zone, based on ratios of surface and interfacial tensions following the methods of Parker et al. (1987) and Lenhard and Parker (1990).

Best-fit parameter values for the capillary properties and hydraulic conductivity using from grain-size correlations for baildown test oil transmissivity estimates was demonstrated by Zhu et al. (1993) with a numerical solution to the flow of oil, and then by Lundy and Zimmerman (1996) with a modified Bouwer & Rice solution. A parametric baildown test analysis proposed by Lundy (2006) uses the Carsel and Parrish (1988) database representing USDA agricultural soil classes, and the API database from cores collected from petroleum

release sites (Bondy et al., 2006). Table 4 provides the expressions for each water retention parameter as a function of hydraulic conductivity developed from each of these two matrix property databases. The Carsel and Parrish expressions were obtained by plotting mean parameter values of the water-retention parameters against mean hydraulic conductivity values for each USDA soil class to identify the best-fit function with the largest correlation coefficient. The API expressions were found by plotting all values of each water retention parameter against corresponding conductivity values for each sample followed by identifying trendline function with the largest correlation coefficient.

Table 3.5 provides the best-fit hydraulic conductivity and water retention parameters obtained for the three baildown test wells in the current study. These values were calculated using the mean LNAPL transmissivity values reported for the three baildown test methods at each test well (far right-hand column in Table 3.4). Being field-based rather than lab-based, the baildown test parametric analysis results have the advantage of representing field-scale values at specific well locations with historical fluid level and fluid property data. Co-located matrix and fluid property data can then readily be integrated into the mathematical model for estimating historical oil transmissivity and spreading rates.

Historical Oil Transmissivities

Equation 1 was used to estimate historical oil transmissivity values based on input values from the following: a) oil thicknesses for each well from the 30-yr USGS database, b) historical oil fluid properties (density, viscosity, and three interfacial tensions) that account for oil weathering characterized in Part 1, and c) four matrix properties from parametric analyses listed in Table 3.4 and treated as constants. Figure 3.11 provides plots and best-fit functions for calculating time-dependent values of oil thicknesses in wells 315, 411, and 421B. Figures 3.12

and 3.13 provide plots and best-fit functions for calculating time-dependent values of oil density and viscosity at 8.5 °C. Time-dependent values of air-water and air-oil surface tensions, and oil-water interfacial tensions are calculated using best-fit functions for the relationships between each of these and oil density at 8.5 °C (Figures 2.9a – 2.9d in Part 1). The trendline functions for oil thickness and fluid properties are continuous functions of elapsed time, providing a way to select an arbitrary sequence of time steps to calculate model inputs and obtain an oil saturation profile and oil transmissivity for each baildown test well location, followed by an oil flow and mass influx calculation. Time steps are allowed to lengthen in a non-linear fashion to accommodate non-linear decreasing rates of oil spreading. For each time step, a corresponding oil thickness is calculated from the functions that exhibit declining trends with time.

The most representative set of matrix properties for calculating oil saturation profiles at each time step was determined by testing three data sets. These included baildown test parametric values using the Carsel and Parrish (1988) and API (2006) databases as shown in Table 3.4 (see Appendix G), and average matrix properties measured with recent core samples (Table 3.2 and Appendix E). Each set was combined with same sets of historical oil thicknesses and fluid property functions to generate oil saturation profiles for the three baildown test wells. Figure 3.14 shows an example set of saturation profiles for well 421B. The nested oil saturation profiles are positioned vertically about an average water table, calculated as a distance above the baseline and original oil-water interface at static equilibrium equal to the starting oil thickness multiplied by the starting oil specific gravity (0.855, measured on the 1984 pipeline sample).

The peak values of the oil saturations in Figure 3.14 coincide with the oil table, where oil and atmospheric pressures are equal and analogous to the water table (Lenhard and Parker, 1990). The peak oil saturation values shift progressively downward with each time and thickness

step change, approaching the constant long-term average water table. Under field conditions, water-table fluctuations can reduce oil saturations by permanently transferring some mobile oil to residual oil at low saturations. Laboratory estimates of residual saturations, based on centrifuge drainage tests, averaged approximately 5.7% of porosity (Table 3.2). However, these can overstate or understate field residual saturations, which are unknown. By ignoring the loss of mobile oil to smearing, we may over-estimate the oil mass discharge but assume that to be a small and negligible error. Relative permeabilities calculated for small saturations with matrix and fluid properties would be tiny.

Oil saturation curves are converted to transmissivity values by numerical integration of Equation 1 where the integral is replaced by a summation sign. The expression to the right of the integral representing oil conductivity is evaluated at many incremental oil thicknesses (horizontal slices on the vertical scale, from the base to the top of the saturation profile) and summed to obtain the oil transmissivity. Saturations and relative permeability values required by the expression for oil conductivity are calculated with expressions in Parker et al. (1987), who adapted the on earlier work on air-water systems of Mualem (1976) and van Genuchten (1980) to oil-air and oil-water systems. Intrinsic permeability is the best-fit baildown test parametric or the laboratory hydraulic conductivity value. Oil density and viscosity values are estimated with functions in Figures 3.12 and 3.13, and the dz differential term becomes the incremental vertical spacing between points at which oil saturations were calculated. This approach follows methods described in Lenhard and Parker (1990) and included in API LNAPL guidance and software (Huntley and Beckett, 2002; Charbeneau, 2008).

Among the three options for matrix properties, those aligned with the Carsel and Parrish (1988) database were selected to best represent oil mobility calculations under field conditions for the following reasons:

- a) The highest oil saturations (~ 80% of porosity) obtained with Carsel and Parrish values are close to those observed in 1990-1992 cores (73.6%) while the other two sets generated much smaller maximum saturations (40% for API and 12% for core analyses).
- b) The hydraulic conductivity values obtained with Carsel and Parrish were within the range of slug tests obtained previously (Strobel et al. 1998, Table 1); while API database values were two orders of magnitude greater and core lab values agreed well but the water retention parameters (especially vG - α) were an order of magnitude too small.
- c) Estimates of oil transmissivities using the API database lead to excessive oil flow rates that with average gradients generate cumulative discharge volumes that greatly exceed the 1990-1992 North Pool oil volume.
- d) Estimates of oil transmissivities using core lab data lead to miniscule oil flow rates because the oil saturations are about twice the laboratory residual saturations making relative permeabilities for the oil be near zero.

Figure 3.15 shows calculated historical oil transmissivity values at well locations 315, 411, and 421B using the Carsel & Parrish parametric analysis value for matrix properties (Appendix G).

Testing for Stability at the LNAPL-Body Scale

From the mapped leading edge position dated 1984 to the position observed in the summer of 2012, the leading edge moved approximately 23 m (Figure 3.2) . The decreasing spacing between leading edge positions indicates that the rate of advancement was decelerating, with declining oil potential gradients and a trend in thinning of the mobile oil in all monitoring

wells. Figure 3.16 shows a best-fit curve of first observations of oil at wells located increasing distances ENE of well 421B, which is near the center of the oil body and the eastern edge of the infiltration area. The plot includes the first occurrence of oil at well 532A just inside the downgradient leading edge.

Figure 3.17 is a map of eight nested North Pool footprints that illustrate the inferred sequence of lateral spreading following the crude oil release in August 1979. The processes associated with overland flow, ponding, infiltration, and drainage to the water table were short-lived, probably ending in the fall of 1979. The snapshot sequence of North Pool footprint areas involved lateral spreading events taking place on the order of years. The date labels represent the summer field seasons when most well fluid levels, oil samples, and soil cores were collected.

Three parts of the North Pool in Figure 3.17 are referred to as the: 1) northwest, 2) central, and 3) downgradient areas. These are listed in order of increasing confidence in the plotted locations of the lateral boundaries with the central and downgradient areas used in testing the stability hypothesis. Historical rates of oil mass discharge from the central area moving into the downgradient area are compared to historical rates of oil mass depletion in the downgradient area.

Figure 3.18 adds a generalized historical oil flow pattern with arrows to Figure 3.17 starting from the ponding and infiltration area to adjoining footprint areas. The boundary between the northwest and central areas is assumed to be a flow divide beneath the overland flowpath taken by the oil sprayed eastward from the pipeline release location. The boundary between the central and downgradient areas represents an oil potentiometric contour serving as a variable-flux boundary placed west of the former railroad and east of the ponding and infiltration area. Dated leading edges in the downgradient area are assumed accurate within $\pm \sim 1$ to 2 m.

Figure 3.19 is a contour map of the uppermost surface of above-background LIF data with inferred oil flowlines from each baildown test well to the 2012 leading edge. The elevation of that surface and inferred flowlines are generally consistent with historical oil and water table contour maps presented earlier (Figures 3.8 and 3.9). The oil infiltration event would have caused mounding on both the water and oil tables, resulting in radial spreading from the ponding area and influenced by the regional water table gradient to the ENE. Focused recharge in the topographic low areas overlying the infiltration area would have caused episodic mounding, consistent with the flowlines and widening of the North Pool in the downgradient area.

Oil mass flow rates, Q_o , leaving the central-infiltration area and entering the downgradient area were calculated in a series of time steps with the following Darcy expression:

$$Q_o = -T_o \left(\frac{dh_o}{dx} \right) W \rho_o , \quad (2)$$

where T_o is the oil transmissivity, dh_o/dx is the oil-table gradient (negative), W is width of the flux boundary across the widening between the central and downgradient areas, and ρ_o is the oil density. Historical oil transmissivity values along the flux boundary between the central and downgradient areas are based on Carsel and Parrish parametric matrix values at the three baildown tests wells (Table 3.5). The transmissivity-controlled mass influx from the central area set is expressed with base-case values bounded by confidence intervals to be consistent with the Part 1 mass depletion estimates. Because the baildown data constitute a smaller sample than the oil composition and oil saturation samples, the nine oil transmissivity values reported in Table 3 are used with the Student t-test criteria for obtaining the confidence intervals around a mean value transmissivity of 0.035 m²/day. The best-fit matrix properties are then estimated using the Carsel & Parrish matrix properties determined with the mean pretest oil thicknesses and fluid properties. Other inputs included averaged historical oil thicknesses and fluid properties at the

bailedown wells, and 12 time steps to generate the mean base-case oil saturation profiles, and oil transmissivities. The base-case and two confidence intervals are primarily distinguished by parametric solution hydraulic conductivity values (9.2, 12, and 6.0 m/day), which control input values of the vG-alpha, vG-n, and residual water saturation matrix properties.

The historical oil table gradient was estimated using the long-term average water-table gradient of 0.002644 divided by the oil specific gravity for each time step (Charbeneau, 2007) and between 1979 and 2012 declined from - 0.00310 to - 0.00295. Historical changes in width of the North Pool along the inflow boundary were scaled off the map in Figure 3.17 and fit to a third order polynomial function to calculate widths a specified dates. Historical average oil density values were used to convert the volumetric discharges in liters/day to mass discharges in kg/day leaving the central area. Mass depletion rates from Part 1 were divided by areas of the North Pool footprints to provide rates per unit area and time for each. Mean base-case historical mass inflow rates, in kg/day/m², are listed with the mid-year dates in Table 3.6 with inflow rates for each bounding confidence interval.

Figure 3.20(a) is a plot of the LNAPL-body scale mass-gain and mass-loss curves with elapsed time since the pipeline release occurred and reached the water table (assumed to be September 1979). This plot is developed to determine a time range in which the mass gains equal mass losses, occurring at the intersections of the curves. It shows that the mass-gain and mass-loss curves are converging but do not intersect within 33 years, by the summer of 2012. This is viewed as consistent with the late-time trend of leading edge migration shown in Figure 3.16, in which the leading edge movement is slowing down, but is still approaching an asymptotic level after 33 years.

Figure 3.20(b) extrapolates the late-time trends of the mass gain and loss curves to define a time range for the bounding curves to intersect, and completes the window of opportunity for stabilization. These show a calculated elapsed time range of 40.7 to 55 yr (2020 to 2035), equivalent to a 15-yr window within which there is a 95% chance for the North Pool to reach a stable configuration.

Our modeling approach does not account for mass removed during 1999-2004 by remedial pumping, which increased the mass depletion rates by a physical process that probably affected the timing of the North Pool stabilization. The influence of pumping from wells RW-1N and RW-2N (Figure 3.4) during that period was not included due to a lack of LNAPL recovery rate and volume records for each recovery well. If the oil body stabilizes before the window of opportunity estimated with the mass-balance analysis, it can be taken as evidence that the remedial pumping reduced the time to reach a stable configuration.

Testing for Stability at the LNAPL Flowtube Scale

Testing oil body stability at the flowtube scale offers a higher resolution viewpoint that can demonstrate the influence of small-scale variations in hydraulic properties of the matrix and mass losses which are spatially heterogeneous. It can show that it is unlikely that all points along the leading edge will reach stability at the same moment in time. Variations were expected and are illustrated with its application at the North Pool.

The mass discharge estimates into each flowtube are calculated with Equation 2. The T_o values averaged for the LNAPL-body scale calculations represent individual baildown well locations where fluid and matrix properties are known. Flowtube width, W , is initially set at 1 m for each well but widens with distance along the flowtube. The rate of widening is based on the changing width of two large flowtubes defined by the flowlines from the three baildown wells in

Figure 19, which both increased by a factor of 2.6 over their full lengths. The unit area mass loss base rates associated with growing oil body areas listed in Table 6 were applied to the flowtube areas and the results are presented in Table 3.7.

The three baildown test-controlled starting points have unique sets of matrix and fluid properties that influence the mass fluxes entering the flowtubes. Given average rates of mass loss that are equally applied to the flowtube areas, the disparity in rates of mass input cause the disparity in the rates of growth and the cumulative lengths for any given time. For these reasons, the flowtube associated with location 315, which had the largest oil transmissivities (Figure 3.15) also has the longest flowtube (Figures 3.18 and 3.19), location 411 had the smallest transmissivities and the shortest flowtube, and location 421B was intermediate between these extremes. The most sensitive parameters influencing calculations of mass-gains and inferred lengths of the flowtubes are hydraulic conductivity and oil viscosity.

Figure 3.21(a) is a plot of the flowtube scale mass-gain and mass-loss curves with elapsed time since the pipeline release. These plots have a similar appearance as those for the LNAPL-body scale but lack the confidence intervals due to insufficient data to characterize those intervals. The late-time gain and loss curves form straight lines on the semi-log plot, and can be represented with best-fit first-order decay functions of elapsed time. Figure 3.21(b) shows plots of these trends projected beyond the time limits of available observations in order to determine future dates when the paired gain and loss lines for each starting location may intersect.

The elapsed times and dates needed for the curve intersections are 9.2 yr (1989) for well 411, 38.6 yr (2018) for 421B, and 40.6 yr (2020) for 315. Clearly, the stability time for the flowtube starting at 411 is inconsistent with mapped and plotted positions of the North Pool leading edge (Figure 3.18). But the flowtubes starting at wells 315 and 421B have stability times

close to the lower-bound window of opportunity time obtained with the LNAPL-body scale assessment. The flowtube results provide insight by showing variability in spreading and equilibration rates, they were not well suited for statistical analysis. Also it appears less reliable when the results do not agree with critical field observations, such as the lack of agreement in the 1989 stabilization date for flowtube 411 and the position of the leading edge in 1989 in Figure 3-18. However, the different distances of advancement and elapsed time to reach stability indicates that we cannot expect all points along that edge to stop advancing at the same time.

Resistance at the Leading Edge

Capillary forces of pristine sands just outside the leading edge of the North Pool provide resistance against penetration by the oil that was evaluated with laboratory and field observations. North Pool oil should be non-wetting where the porous media is composed of silica-based minerals (quartz, hornblende, and inorganic clays). However, it may behave as a wetting fluid when in contact with calcareous minerals (calcite and dolomite rock fragments) or with organic matter (plant fragments). Both groups are present in sediments at the site but silica-based minerals predominate (Bennett, et al. 1993). We assumed the oil was a wetting fluid for calculating a range of in-well oil thicknesses necessary to overcome the resistance, using the following expression (Charbeneau et al., 1999):

$$b_{n[crit]} = \left\{ \frac{\sigma_{nw}}{(1-\rho_r)\sigma_{aw}} - \frac{\sigma_{an}}{(\rho_r \sigma_{aw})} \right\} h_d, \quad (3)$$

where $b_{n[crit]}$ is the critical thickness of NAPL (oil), σ_{nw} is the NAPL-water interfacial tension, σ_{an} is the air-NAPL surface tension, σ_{aw} is the air-water surface tension, ρ_r is the relative density (specific gravity), and h_d is the air- water displacement pressure (aka, bubbling pressure or critical capillary head).

Core laboratory drainage tests performed on 12 samples representing a range of grain-size distributions provided 12 air-water displacement pressures ranging from 17 to 62 cm. When combined with fluid properties representing the most weathered oil in the fringes of the North Pool in 2012 (observed at 532A and 604A in 2012), a dozen critical oil thickness values were calculated with Equation 3. A probability plot of these data is shown in Figure 3.22. Critical thicknesses at the 0.05, 0.5, and 0.95 probabilities are 33.5, 65.6, and 124 cm (0.33, 0.66, and 1.24 m).

The critical thickness range has been exceeded in the past at all oil-bearing wells and many LIF sounding locations within the currently mapped North Pool footprint area. The recent maximum oil thicknesses observed in well 532A in April 2013 (Figure 3.6) are within the calculated critical thickness range. Oil thicknesses observed in other North Pool wells upgradient of 532A were also in this range during 2010-2012. Historical thicknesses represented by fluid level gauging data and smear zone thickness inferred from the LIF signatures are generally within this range in the downgradient area and above the range in the central and inferred infiltration area where historical mobile oil thicknesses were between 1 and 2 m in the early 1980s. Only location TG1102, near the leading edge in 2011 had an LIF signature thickness of 0.23 m, below the critical thickness range. However, that is likely within the range of very coarse pebbly sands, which have been observed in cores but were not represented in the displacement pressure tests.

By itself, critical LNAPL thickness cannot serve as the criteria for halting further lateral migration. It requires assistance from the mass depletion process over LNAPL body upgradient of the leading edge area. However, changes in fluid properties related to oil weathering increase the critical thickness values such that resistance at the leading edge where oil is more weathered

increases with aging of the oil body. The role of resistance at the leading edge has grown along with the rates of mass depletion, as weathering of the oil has facilitated both mechanisms.

Summary and Conclusions

In Part 1, time-dependent oil composition changes were integrated with one USGS oil volume estimate based on core analyses to form a basis estimating historical mass losses for the North Pool area over a 33-year period. Time-varying loss rates are in the same range as independently estimated losses based on CO₂ production above background levels over the footprint areas for multiple dates by other investigators. In Part 2, these mass losses were divided by the enlarging North Pool areas for seven dates, providing rates per unit area and time (kg/m²/day) for estimating loss rates over expanding oil body areas downgradient of the known historical oil infiltration area. Analyses of LNAPL baildown tests at three wells in the infiltration area provided hydraulic properties. When combined with historical changes in oil physical properties, and in-well thicknesses these inputs allowed development of oil saturation profiles for each test well location. The saturation profiles were used to obtain oil transmissivities for a series of time steps representing the 33-year history of North Pool spreading. Transmissivities were included with estimates of historical gradients, oil densities, and flowpath widths in a Darcy equation to calculate a sequence of mass discharges from the infiltration area into the downgradient area at both the LNAPL-body and LNAPL-flowtube scales.

The rates of mass inflow decline over time as oil saturations and transmissivities diminish with spreading. At the test site, we found that these can conveniently be represented by a first-order decay function of time. The LNAPL-body wide rate of mass loss by oil weathering also fits a first-order decay trend with a slope that is less steep than the mass-loss trend. With these different rates of change, the mass-gain and mass-loss curves will eventually intersect at a point

where they are equal. Empirical best-fit expressions are then used to calculate elapsed time and dates of intersection that represent when mass balance occurs.

When sufficient data are available to characterize these two opposing processes, LNAPL-body scale analysis offers a way to incorporate the probability of obtaining a mass balance within a time period defined by a mean with confidence intervals, assuming that the controlling inputs have distributions that approximate normal distributions. When included in the plotted trends for mass gains and losses, the analyst can infer a “window of opportunity for stabilization” that honors the natural variability multiple parameters influencing stabilization.

Using this approach, we found that the window of opportunity for the North Pool begins in 2020 and extends to 2035, spanning 15 years. The rate of leading edge advancement has decelerated over the past 30 years and is approaching an asymptotic level, but as of our investigation in 2010-2012, had not conclusively reached a flat-line trend. Our mass depletion methodology did not account for mass removed by remedial pumping during 1999 and 2004, which contributed to temporarily slowing the rate of leading edge advancement by removing mass and capturing some of the LNAPL migrating into, and some LNAPL within, the downgradient area tested for stability here. If field observations near the leading edge over the next 5 years show evidence of no further advancement, they can serve as evidence that the remedial pumping reduced stabilization time that was based on mass losses attributed only to compositional changes.

The reliability of our approach to define the window of opportunity of stabilization is limited by the quantity and quality of the historical records and the data collected during this investigation. The most reliable test for oil body stability is periodic field observations of the

occurrence of absence of oil in wells, soil cores, and direct sensing tools (e.g., LIF) near the leading edge to track further movement, or to confirm stability at selected locations.

Resistance at the leading edge caused by the non-wetting fluid entry pressure is a condition continually overcome until the mass balance condition is met. The mass balance must occur first after which the entry pressure can control further migration. However, given heterogeneous earth materials and fluids, satisfying both the mass balance and the resistance criteria will not happen at all locations along the leading edge at the same time. For that reason, the broad-brush LNAPL-body scale and high-resolution flowtube-scale evaluations have their advantages and disadvantages and could be applied at other sites where the LNAPL type and geologic settings differ from those reported here.

Table 3.1

Hydraulic Properties for Upper and Lower Strata at the North Pool and Vicinity.

Results are based on earlier investigations carried out by the USGS.

Depth Zone Tested	Lithology	Type of Test	Minimum K (m/day)	Maximum K (m/day)	Mean or Median K (m/day)	Data Source
Upper*	"Fine" (silty strata)	Grainsize Analyses	1.02E-07	0.907	0.038	Dillard et al., 1997 (means)
Upper	"Coarse" (sandy strata)		1.01	108.9	8.25	
Upper Lower**	Fine to Medium Sand Coarse Sand & Gravel	Slug Tests	1.52 0.38	8.48 46.3	4.68 20.0	Strobel et al. 1998 (medians)
Lower	Coarse Sand & Gravel	Pumping Test	--	-	77.0	Delin and Herkelrath, in press (mean)

* Upper = within 3 m of the water table

** Lower = greater than 3 m below water table

Table 3.2

Summary of Soil Core Analytical Data for the North Pool Oil Body

Core Location	Center of Subcore Depth (feet)	Predom- inant Grain Size	Median Grain Size (mm)	Native State LNAPL Sat'n (%)	Native State Water Sat'n (%)	Lab Residual LNAPL Sat'n (%)	Total Porosity (%)	Effective Porosity (%)	Hydraulic Conductivity (cm/sec)	Hydraulic Conductivity (ft/day)	vG alpha ² (1/ft)	vG-n ²	Residual Water Sat'n ^{1,2} (%)
C-1008-A	27.90	Medium sand	0.334				32.3	25.9					
C-1008-A	28.20			4.6			38.5	10.4					
C-1008-A	28.40	Fine sand	0.223	11.2	60.9	8.2	41.1						4.84
C-1008-A	28.80	Medium sand	0.524	14.8	53.0	7.0	42.3						7.84
C-1008-A	28.95						36.5	10.5	7.86E-03	22.28	0.332	2.631	14.53
C-1008-A	29.20			4.6			36.9	11.0					
C-1008-B	29.70	Fine sand	0.123				39.1	8.0	1.35E-03	3.84	0.166	3.351	20.11
C-1008-B	30.10	Fine sand	0.143				36.8	33.1					
C-1008-C	32.40						35.6	9.5	4.04E-03	11.46	0.387	2.460	22.46
C-1008-C	32.60	Fine sand	0.220	4.0	74.5	4.0	37.3	32.8					8.97
C-1008-C	32.80	Fine sand	0.200	6.4	70.6	6.4	40.1						6.18
C-1009-A	19.25	Fine sand	0.421	5.4			33.1	14.4					
C-1009-A	19.40	Medium sand	0.460	8.8	48.1	7.6	45.4						8.10
C-1009-A	19.60						47.4	21.6	8.38E-03	23.77	0.437	2.573	21.81
C-1009-A	19.80	Medium sand	0.605	8.9	53.2	5.5	47.6	31.2					12.39
C-1009-A	20.30			21.2			43.4	16.6					
C-1009-A	21.00			22.3			43.0	18.0					
C-1009-B	22.20			1.1			35.4	31.7					
C-1009-B	22.40	Fine sand	0.179				42.0	13.2	3.70E-03	10.48	0.236	3.304	12.51
C-1009-B	22.80	Fine sand	0.318	10.6			45.1	13.5					
C-1009-B	23.40			4.3	67.5	4.3	40.9						6.10

Table 3.2 conti.

Core Location	Center of Subcore Depth (feet)	Predom- inant Grain Size	Median Grain Size (mm)	Native State LNAPL Sat'n (%)	Native State Water Sat'n (%)	Lab Residual LNAPL Sat'n (%)	Total Porosity (%)	Effective Porosity (%)	Hydraulic Conductivity (cm/sec)	Hydraulic Conductivity (ft/day)	vG alpha ² (1/ft)	vG-n ²	Residual Water Sat'n ^{1,2} (%)
C-1051-A	25.40	Fine sand	0.311	1.0	50.7	1.0	45.2						5.88
C-1051-A	26.00			2.9			41.7	11.7					
C-1051-A	26.30			3.0	66.8	3.0	42.5						4.83
C-1051-A	26.40	Fine sand	0.172				42.5	13.6	4.94E-03	14.00	0.241	3.345	10.84
C-1051-A	26.60	Medium sand	0.426	15.7	48.3	7.5	39.4						8.19
C-1051-A	26.85						32.8	28.1					
C-1051-A	26.90	Medium sand	0.599										
C-1051-A	27.00			17.6			37.3	12.2					
C-1051-A	27.40			1.6			34.9	31.2					
C-1051-A	27.70	Medium sand	0.653	0.7	65.7	0.7	33.4						9.74
C-1051-B	28.20			2.4			33.7	7.4					
C-1051-B	28.40	Medium sand	0.444	1.1	73.4	1.1	35.0						10.26
C-1051-B	28.80						22.0	19.6	3.18E-03	9.01	0.540	2.200	13.57
C-1051-B	29.50	Medium sand	0.895	6.6			31.4	9.7					
C-1056-A	20.20	Medium sand	0.368	4.6	69.8	4.6	39.2						11.56
C-1056-A	20.50			7.8			40.7	11.5	3.89E-03	11.03	0.425	3.430	11.97
C-1056-A	20.70						36.3	32.2					
C-1056-A	21.00			8.3	68.8	8.3	38.0						5.86
C-1056-A	21.40			6.8			38.2	11.6					
C-1056-A	22.10			4.2			38.4	8.2					
C-1056-A	22.60	Fine sand	0.079	8.1			38.5	8.6	2.36E-04	0.67	0.099	2.083	13.49
C-1056-B	23.10						32.5	27.0					
C-1056-B	23.40			4.5			31.1	9.4	6.41E-04	1.82	0.314	2.466	20.19
C-1056-B	23.80	Coarse sand	1.402				26.9	20.8					
C-1102-A	28.00	Fine sand	0.329				37.7	10.0	5.36E-03	15.19	0.414	2.703	10.21
C-1102-B	30.00	Fine sand	0.232				39.1	10.3	1.01E-02	28.51	0.355	2.818	10.06
C1103-A	27.00			7.4	55.2	6.4	42.5						6.61
C-1103-A	26.60			1.1			38.1	13.2					
C-1103-A	26.80			6.8			39.1	12.2					
C-1103-A	27.00	Fine sand	0.306										
C-1103-A	27.50	Fine sand	0.265										
C1103-B	27.50			18.5	52.1	8.3	40.7						7.13
C-1103-B	28.10			16.4			42.5	9.6					
C-1103-B	28.50			3.7			37.3	7.6					
C1108-A	18.40			13.1	36.1	6.6	41.1						6.71
C-1108-A	17.30			4.0			41.4	12.3					
C-1108-A	18.10			2.0			43.9	25.7					
C-1108-A	18.40	Fine sand	0.309										
C1108-B	20.40			14.4	53.1	9.2	43.6						5.45
C-1108-B	19.00			11.2			41.2	17.2					
C-1108-C	20.40	Fine sand	0.363										
C-1108-D	22.50			6.8			39.2	3.7					
C-1109-A	27.00			1.1			39.3	14.5					
C1109-B	28.00			4.3	61.2	4.2	43.6						5.76
C1109-B	28.40			2.8	71.6	2.8	37.9						7.92
C-1109-B	27.80			1.7			40.6	13.3					
C-1109-B	28.00	Fine sand	0.263										
C-1109-B	28.20			13.6			39.5	6.3					
C-1109-B	28.40	Fine sand	0.253										
C-1109-C	30.00			6.9			36.6	6.3					
C-1112-A	23.60			1.7			40.9	25.0					
C-1112-A	24.30	Fine sand	0.219										
C1112-B	24.30			15.2	37.2	10.9	40.4						8.02
C-1112-B	25.30			21.3			40.8	11.9					
C-1112-C	26.00	Medium sand	0.383	11.2	62.8	8.0	37.1						9.24
C-1112-C	26.90			6.0			38.7	9.0					
Averages	25.14	Medium sand	0.4	7.20	58.2	5.51	38.2	14.3	4.04E-03	11.5	0.341	2.72	9.2

Notes:

- 1- Includes results of native-state air-oil-water drainage tests for residual oil and residual water saturations.
- 2- Includes best-fit van Genuchten parameters determined on capillary pressure-water saturation curves from air-water drainage tests.

Table 3.3

LNAPL Transmissivity and Storativity Estimates from Baildown test Analyses.

Results are based on API (2012) methods and software.

Test Well ID	Bouwer & Rice		Cooper & Jacob		Cooper, Bredehoeft, & Papadopulos		Means by Well ID	
	Transmissivity (m ² /day)	Storativity (unitless)						
315	0.058	N.A.	0.047	0.035	0.061	0.020	0.055	0.028
411	0.0074	N.A.	0.0037	0.028	0.0043	0.008	0.0051	0.012
421B	0.050	N.A.	0.027	0.035	0.057	0.035	0.044	0.023
Means	0.038	N.A.	0.026	0.033	0.040	0.021	0.035	0.018
Geomeans	0.028	N.A.	0.017	0.032	0.024	0.018	0.023	0.017

Table 3.4

Expressions for Estimating van Genuchten Water Retention Parameters –

Functions of Hydraulic Conductivity* based on two National Matrix Property Databases.

Parameter	Carsel and Parrish (1988) Database	API (2006) Database
van Genuchten alpha (cm ⁻¹)	$\alpha = 0.067K^{0.3915}$	$\alpha = 0.0132K^{0.0861}$
van Genuchten <i>N</i>	$N = 0.6947K^{-0.2592}$ $K < 0.029$	$N = 2.0077K^{0.0295}$
	$N = -3.0302K^2 + 0.3014K + 1.74$ $0.029 < K < 0.311$	
	$N = 0.377 \ln(K) + 1.9511$ $K \geq 0.311$	
Residual water saturation	$S_{rw} = 0.2439K^{-0.252}$	$S_{rw} = 0.2265K^{-0.142}$

* K = Hydraulic Conductivity, in m/day.

Table 3.5

Results of Inverse Parametric Analyses of Oil Transmissivities for Baildown Test Wells

Test Well ID	Carsel & Parrish (1988) Database				API (2006) Database			
	Hydraulic Conductivity (m/day)	vG-Alpha (1/cm)	vG-N (unitless)	Residual Water (saturation)	Hydraulic Conductivity (m/day)	vG-Alpha (1/cm)	vG-N (unitless)	Residual Water (saturation)
315	11.7	0.0163	2.88	0.13	2664.5	0.0260	2.62	0.07
411	2.0	0.0140	2.22	0.20	138.3	0.0202	2.22	0.20
421B	6.3	0.0155	2.65	0.15	593.4	0.0229	2.51	0.09
Means	6.7	0.0155	2.58	0.16	1132.1	0.0242	2.45	0.12
Geomeans	5.3	0.0152	2.57	0.16	602.5	0.0229	2.44	0.11

Table 6.

Summary of Areas and Mass Losses Associated with Historical North Pool Footprints

Date Summer Field Season (yr)	Elapsed Time (yrs)	Entire Footprint Area ^{a,b} (m ²)	North Pool Upgradient Northwest Area ^c (m ²)	North Pool Central Area ^c (m ²)	North Pool Downgradient Discharge Area (m ²)	Discharge Area Fraction of the Central Area	Sum of Central and Downgradient Areas (m ²)	Central and Downgradient Areas Mass Loss Rate ^d (kg/day)	Unit Area Base-Case Mass Loss Rate ^e (kg/day/m ²)	Down-gradient Area Base-Case Mass Loss Rate (kg/day)	Down-gradient Base Rate + 1 C.I. ^f (kg/day)	Down-gradient Base Rate - 1 C.I. (kg/day)
1979	0.05	506	99	482	80	0.17	561.81	9.21	1.64E-02	1.31	1.58	1.04
1984	5	1379	148	1009	222	0.22	1230.50	7.93	6.44E-03	1.43	1.73	1.13
1987	8	1886	297	1218	370	0.30	1588.63	7.23	4.55E-03	1.68	2.03	1.33
1989	10	2463	484	1395	584	0.42	1979.32	6.79	3.43E-03	2.01	2.42	1.59
1991	12	2707	612	1443	652	0.45	2094.65	6.39	3.05E-03	1.99	2.40	1.57
1994	15	2975	712	1485	777	0.52	2262.11	5.83	2.58E-03	2.00	2.42	1.59
1998	19	3368	838	1535	995	0.65	2529.84	5.15	2.04E-03	2.03	2.45	1.61
2012	33	3958	1155	1580	1222	0.77	2802.67	3.35	1.19E-03	1.46	1.76	1.16

a - 1979 infiltration area assumed equal to the 3-m contour on thickness of the north pool oil body (vadose/saturated oil-water bearing zone) inferred with LIF data.

b - 1990-92 north pool area based on Herkelrath et al. (1999) estimate, here increased to account for the northwest area (late 1980s-early 90s); the USGS area was ~ 2,032 m².

c - Defined by the area between the NW Lobe Area and the Discharge Area.

d - Mean rate based on LNAPL composition changes in oil samples from 12 north pool wells for various sampling events during 1979-2012.

e - Based on the 1990-92 volume-mass estimate, which is based on cores from 10 locations (Herkelrath et al. 1992; Delin and Herkelrath, 2014).

f - C.I. = amount of mass associated with a 95% confidence interval around the mean base rate.

Table 3.7

Summary of Areas and Mass Losses Associated with Flowtubes

Location Where Flowtube Begins	Date of Estimate (yr)	Flowtube Segment Length (m)	Flowtube Cumulative Length (m)	Flowtube Area^a (m²)	Rate of Mass Loss (kg/day)
Well 315	1979	5.53	5.53	5.53	0.100
	1984	11.77	11.77	18.44	0.119
	1987	8.70	20.47	33.72	0.153
	1989	11.05	31.52	55.95	0.192
	1991	3.14	34.66	62.57	0.191
	1994	4.76	39.42	73.09	0.188
	1998	7.23	46.65	90.74	0.185
	2012	6.47	53.13	108.04	0.129
Well 411	1979	5.30	5.30	5.30	0.096
	1984	11.27	11.27	17.66	0.114
	1987	6.36	17.63	28.83	0.131
	1989	6.00	23.63	40.90	0.140
	1991	1.38	25.00	43.80	0.134
	1994	2.19	27.19	48.63	0.125
	1998	2.14	29.33	53.85	0.110
	2012	2.57	31.90	60.73	0.072
Well 421B	1979	10.09	10.09	10.09	0.182
	1984	21.45	21.45	33.63	0.217
	1987	4.43	25.88	41.41	0.188
	1989	4.76	30.64	50.98	0.175
	1991	1.54	32.18	54.22	0.165
	1994	1.92	34.10	58.47	0.151
	1998	3.32	37.43	66.59	0.136
	2012	3.88	41.31	76.96	0.092

a - As flowtubes lengthen, they grow wider at a rate of 0.25 m/m.



Figure 3.1 Oblique aerial photograph looking east of the August 1979 crude oil release site, including an open recovery trench in the North Pool area (upper left), and surface staining along the sinuous flowpath of oil to a wetland located approximately 200 m south of the release point (lower right; Delin, 2012, personal communication).

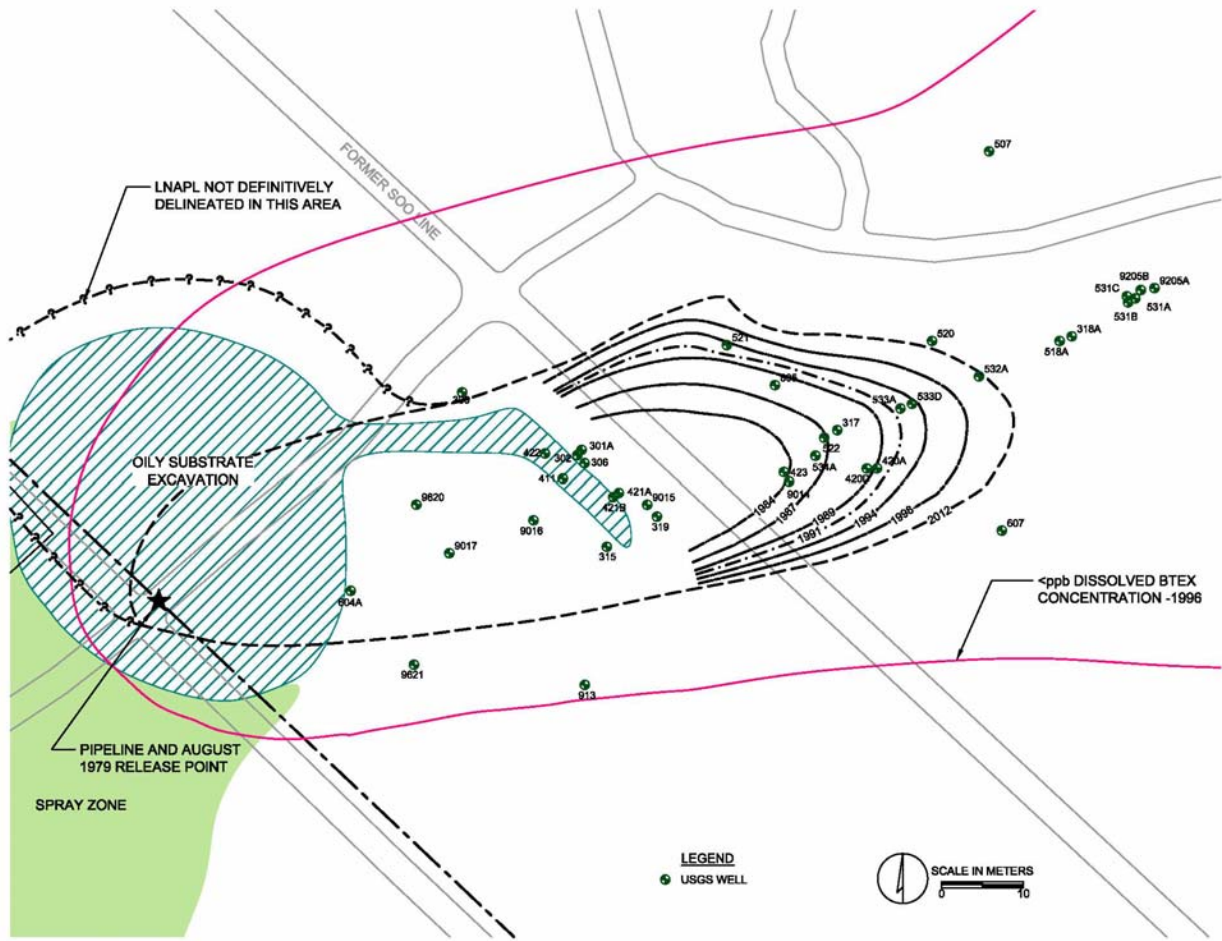


Figure 3.2 Map of research site with pipeline release location, excavation area, and USGS monitoring wells relative to inferred locations of historical North Pool leading edges.

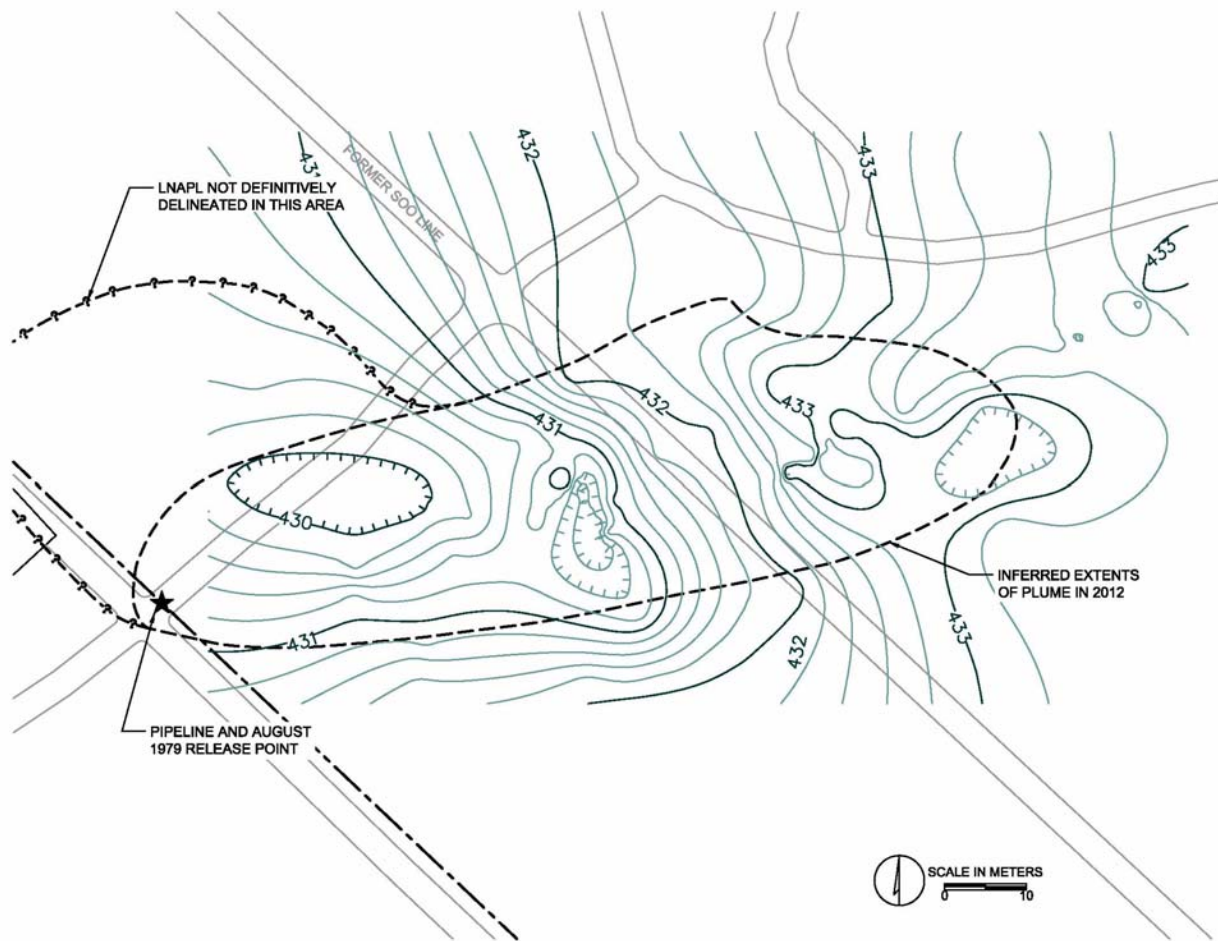


Figure 3.3 Topographic base map showing the pipeline and 1979 release point with inferred approximate limit of the North Pool oil body in 2012.

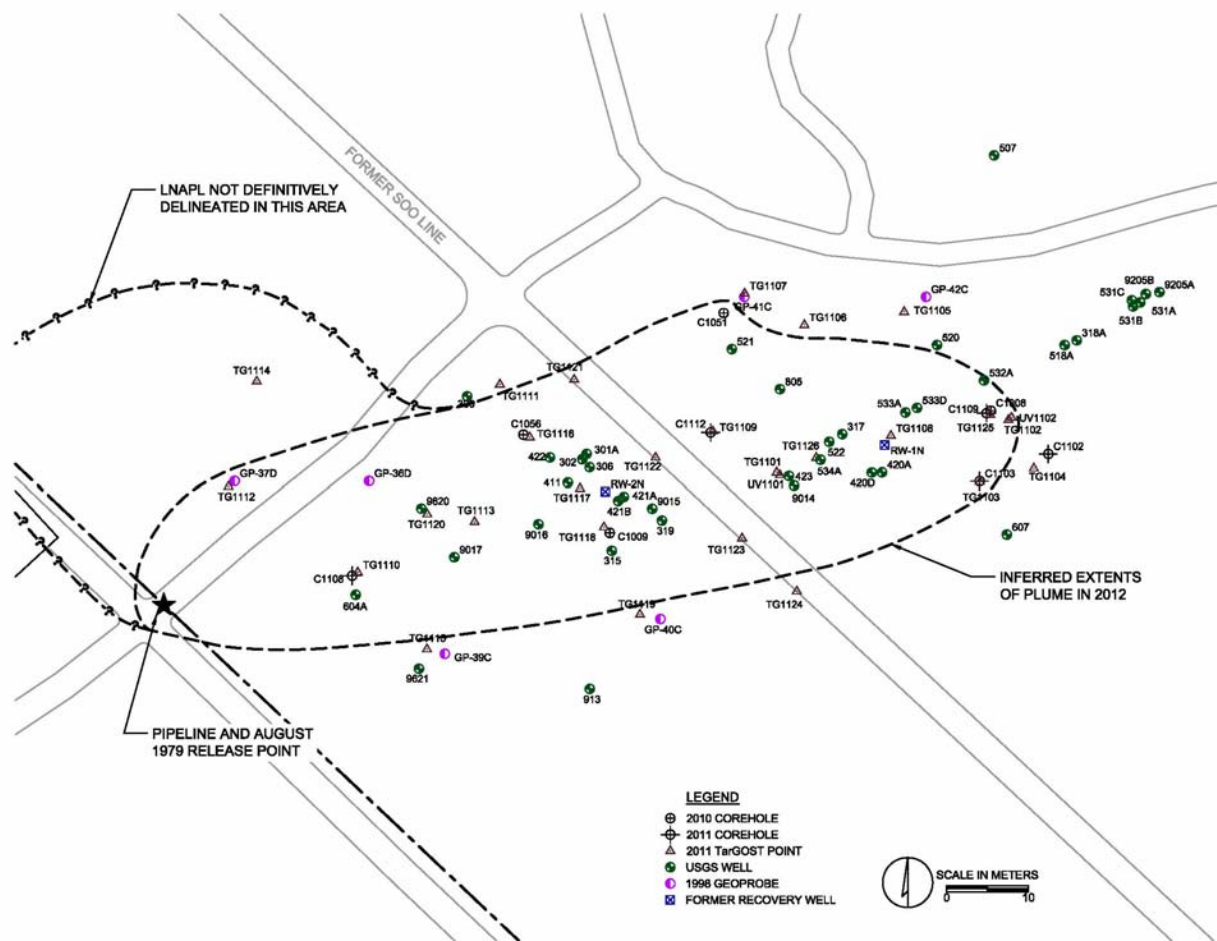


Figure 3.4 Map of the North Pool 2012 footprint area with locations of wells, soil borings, LIF soundings, and coreholes.

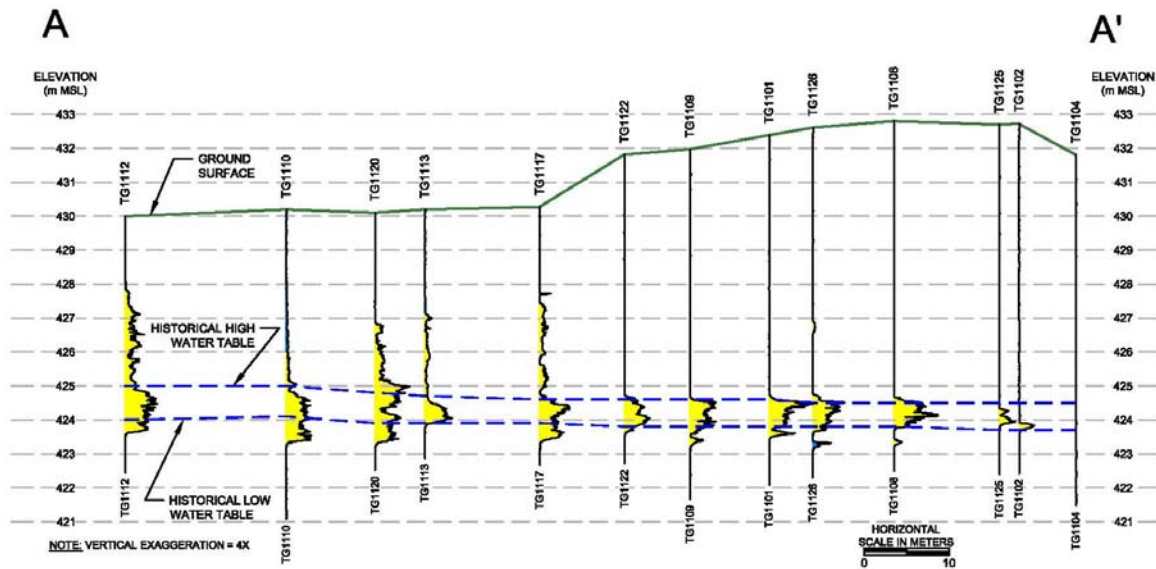
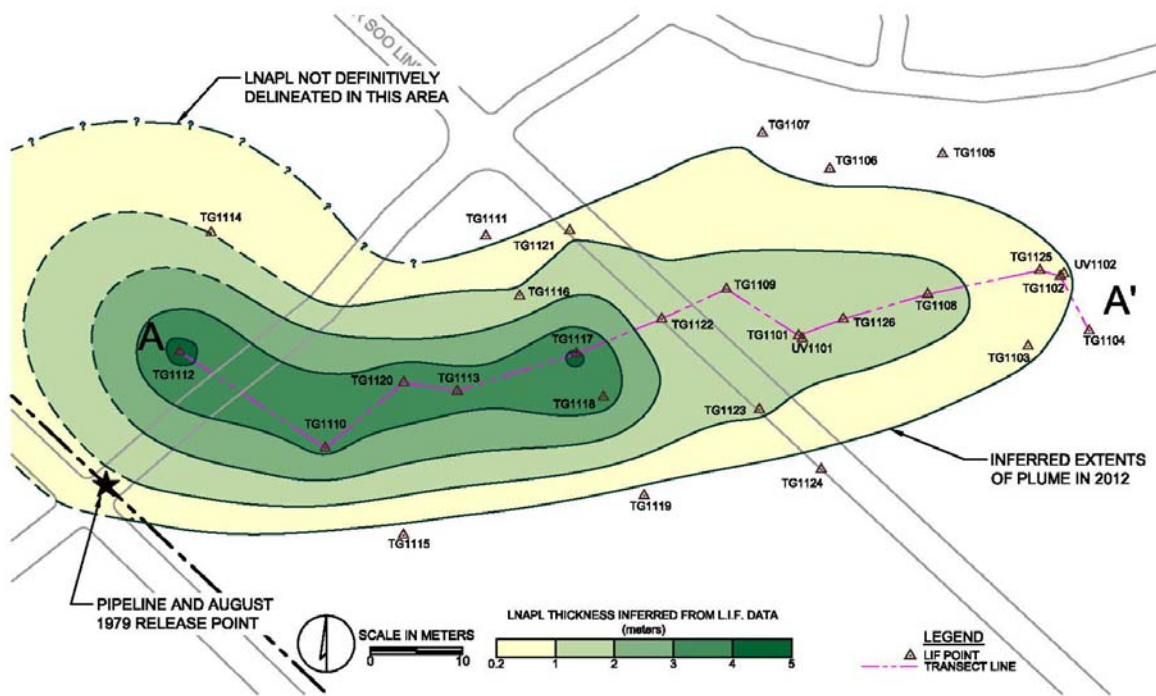


Figure 3.5 Map and section views of the North Pool oil body defined by May 2011 LIF signatures. Weaker responses above the historical high water table represent residual oil in the vadose zone; strong responses between the high and low water table positions represent potentially mobile oil.

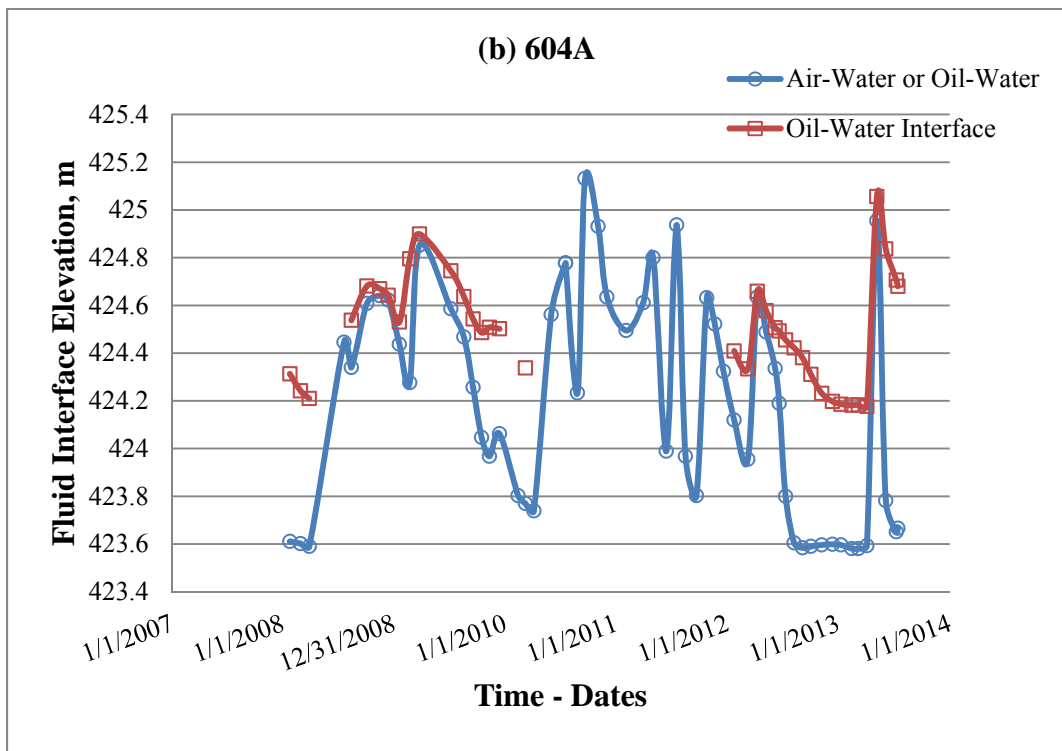
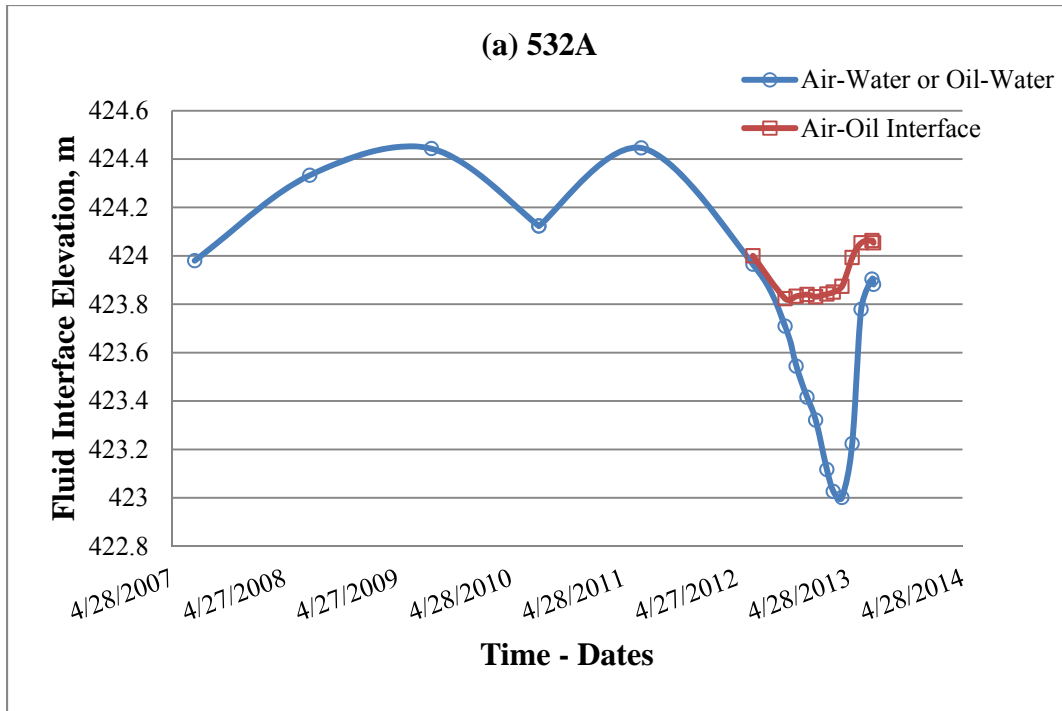


Figure 3.6 Plots of depths to oil and water at: a) 532A, and b) 604A that illustrate the inverse relationship between water table position and presence or absence of oil. Well 532A is the most downgradient well and 604A is the most upgradient well within the North Pool footprint area.

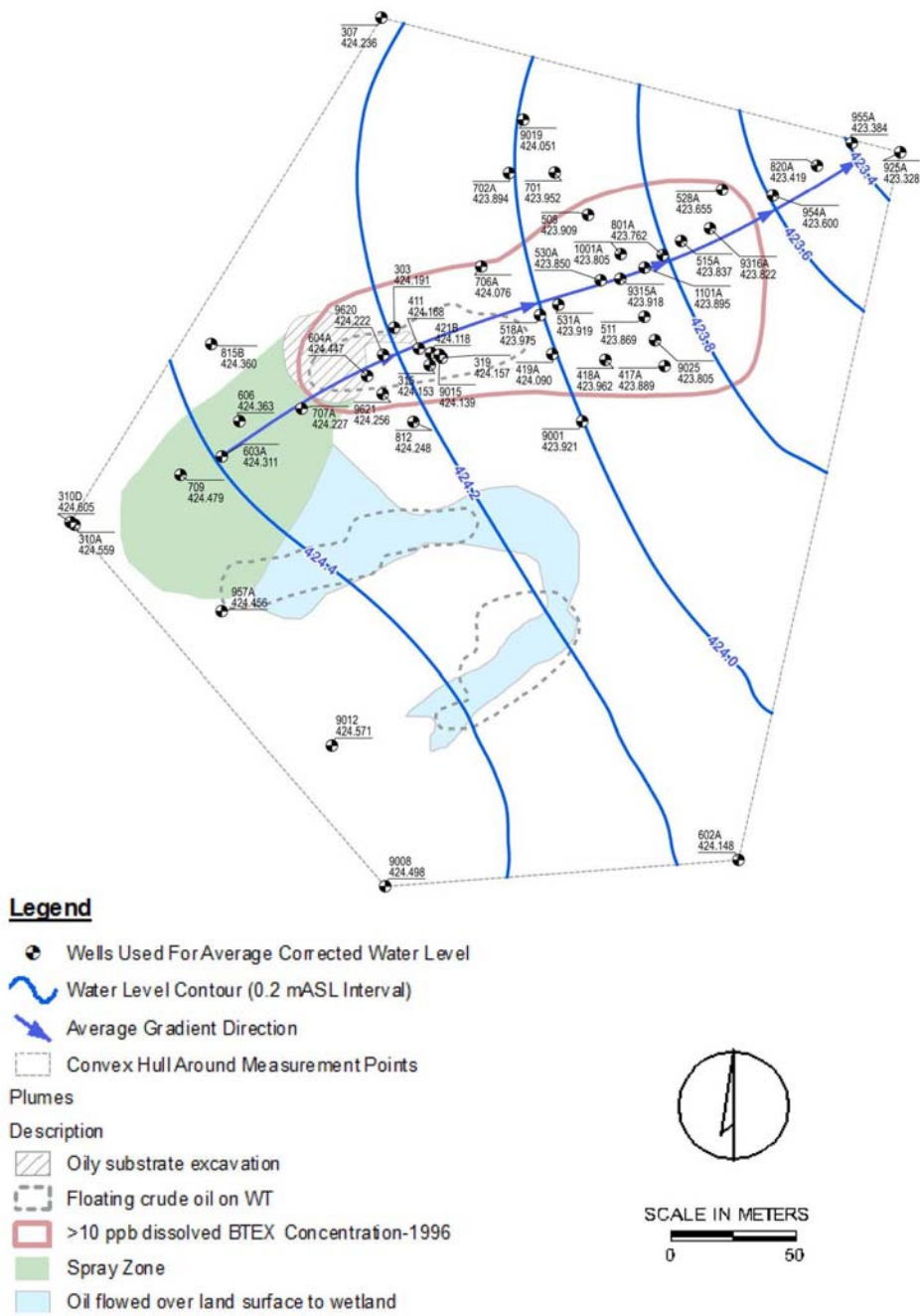


Figure 3.7 Mean water table and gradient direction to the ENW beneath the North Pool. The 34-year average magnitude of 0.002644 is used to estimate historical oil-table gradients using time-dependent changes in oil density.

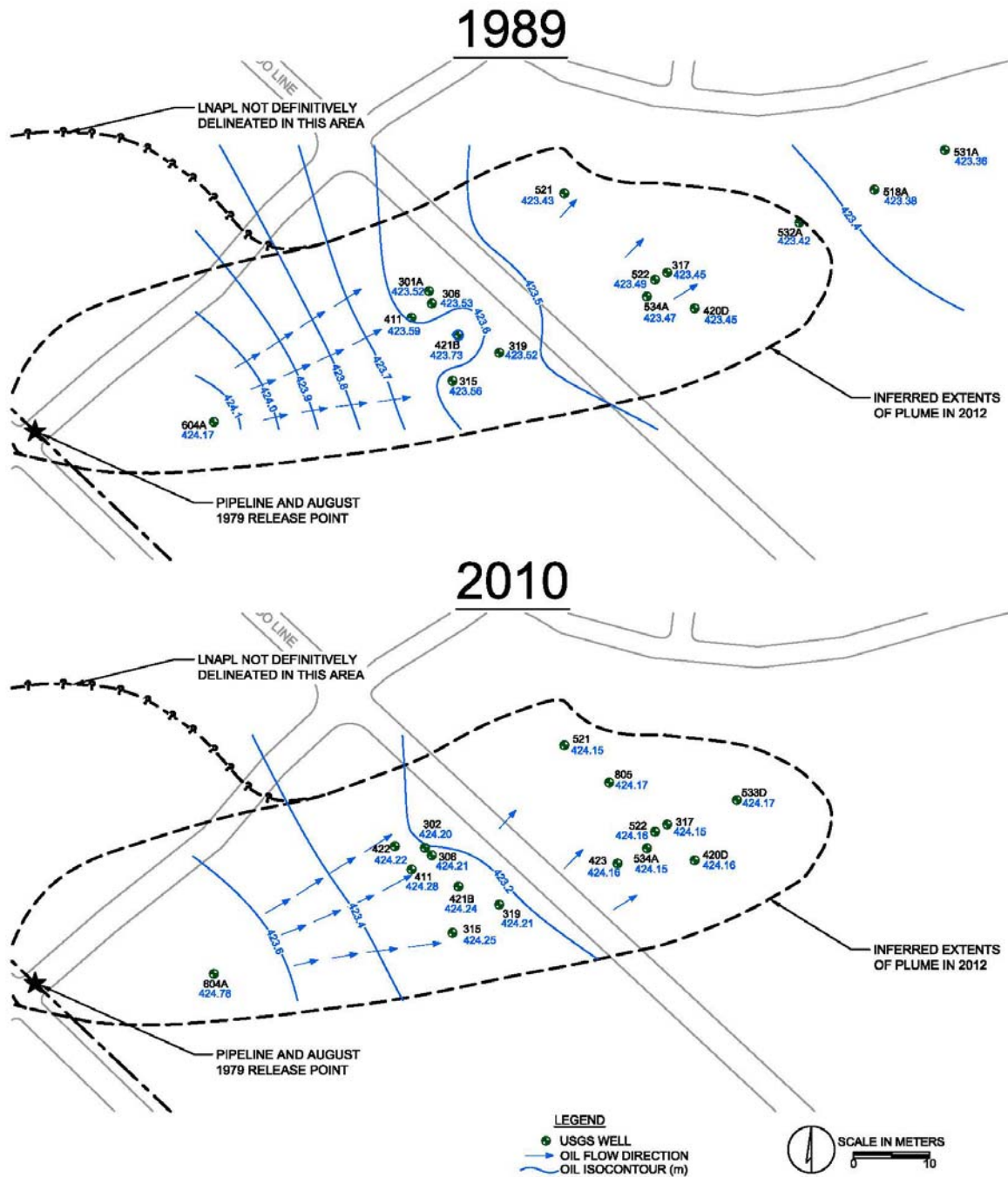


Figure 3.9 Groundwater potentiometric surfaces (water tables) for a) fall 1989 (data from Landon, 1993), and b) summer 2010 including inferred limits of the North Pool in 2012.

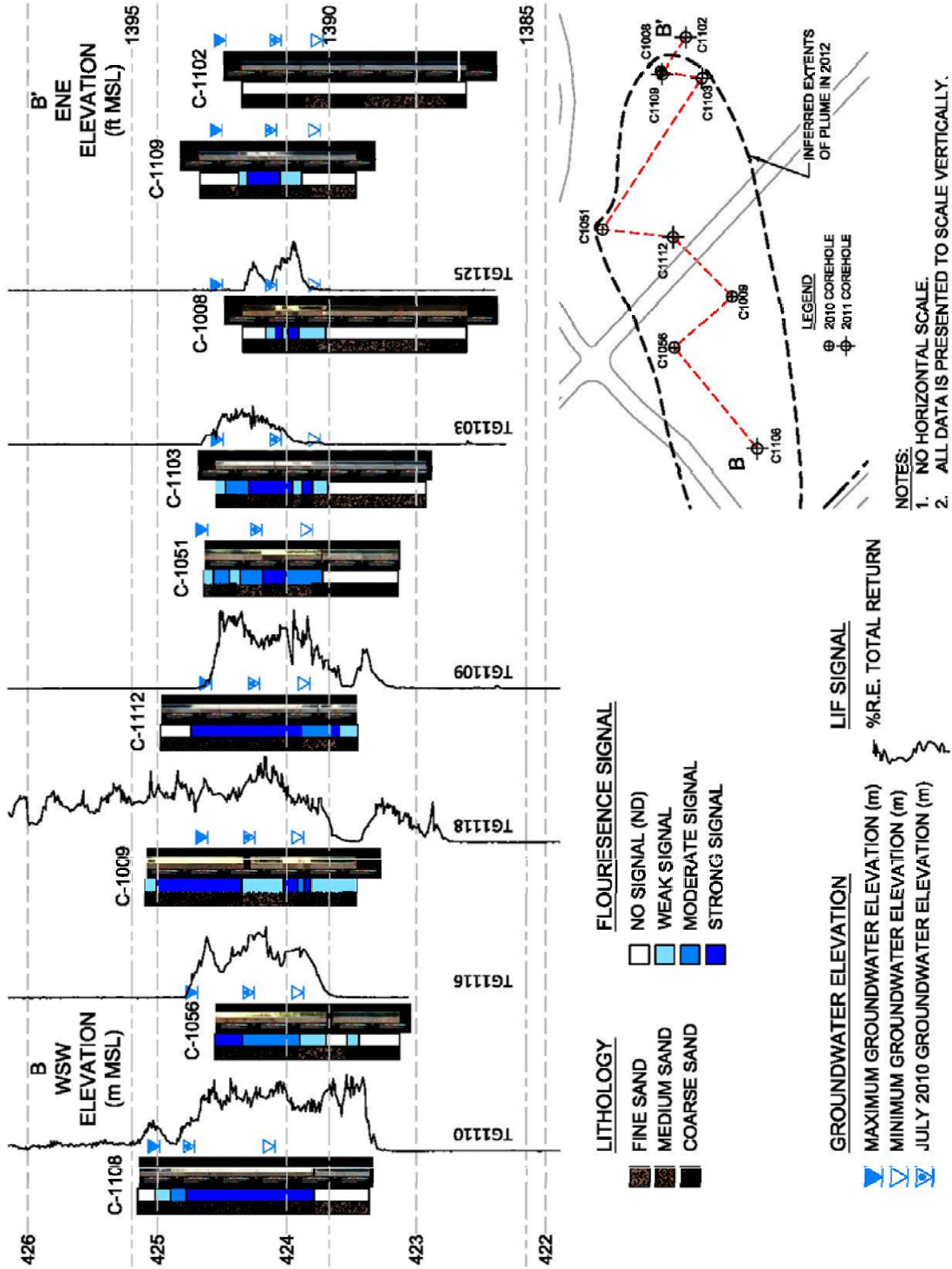


Figure 3.10. Core lab photologs, lithologies, and fluorescence levels plotted along a transect oriented WSW to ENE following the hydraulic gradient of the North Pool.

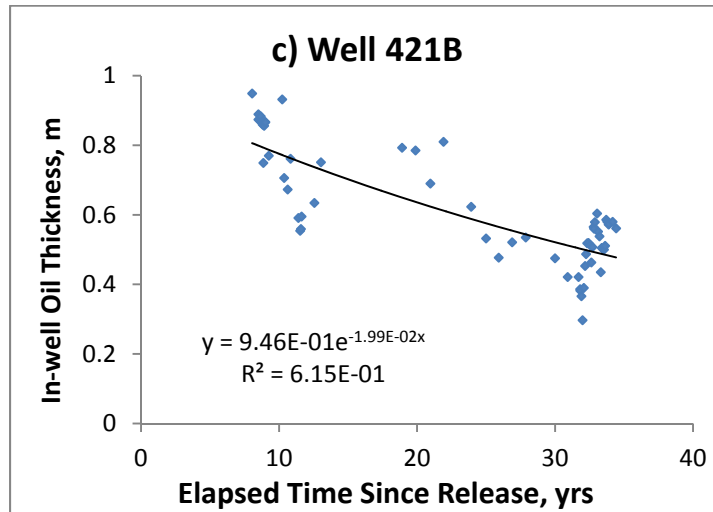
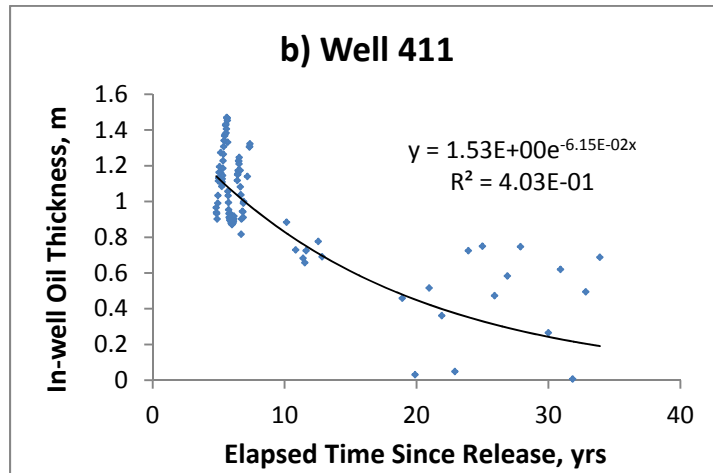
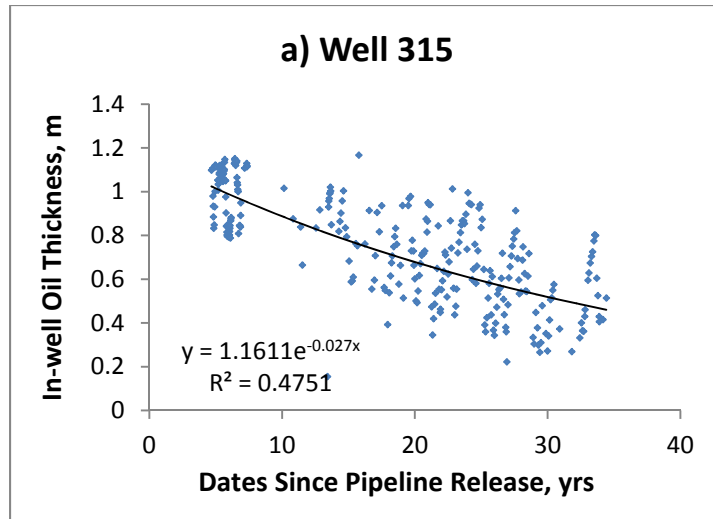


Figure 3.11 Best-fit trends of historical oil thicknesses observed in wells 315, 411, and 421B.

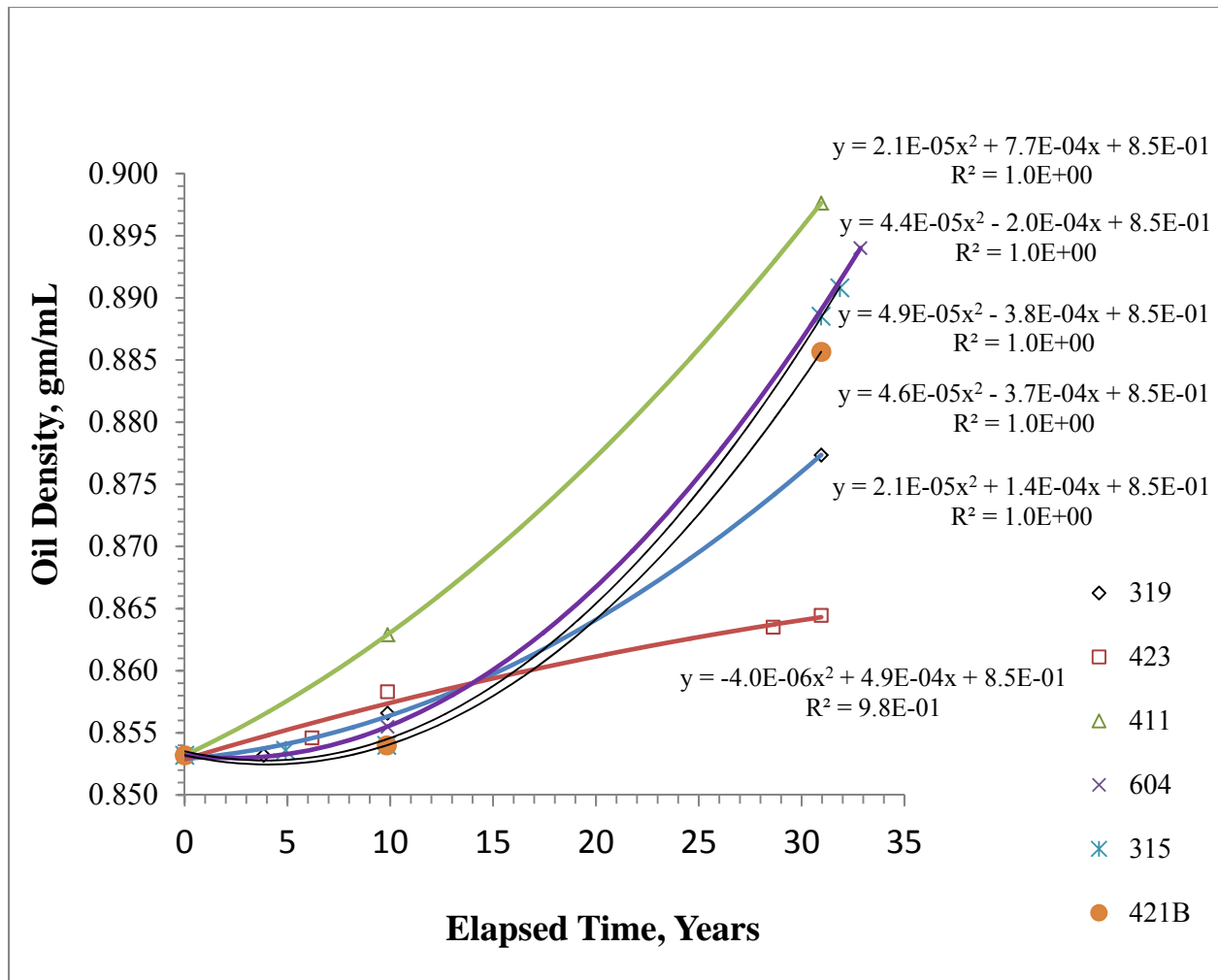


Figure 3.12 Oil densities at selected wells plotted with elapsed time since the 1979 pipeline release. Best-fit functions for wells 315, 411, and 421B were used in estimating historical oil transmissivities.

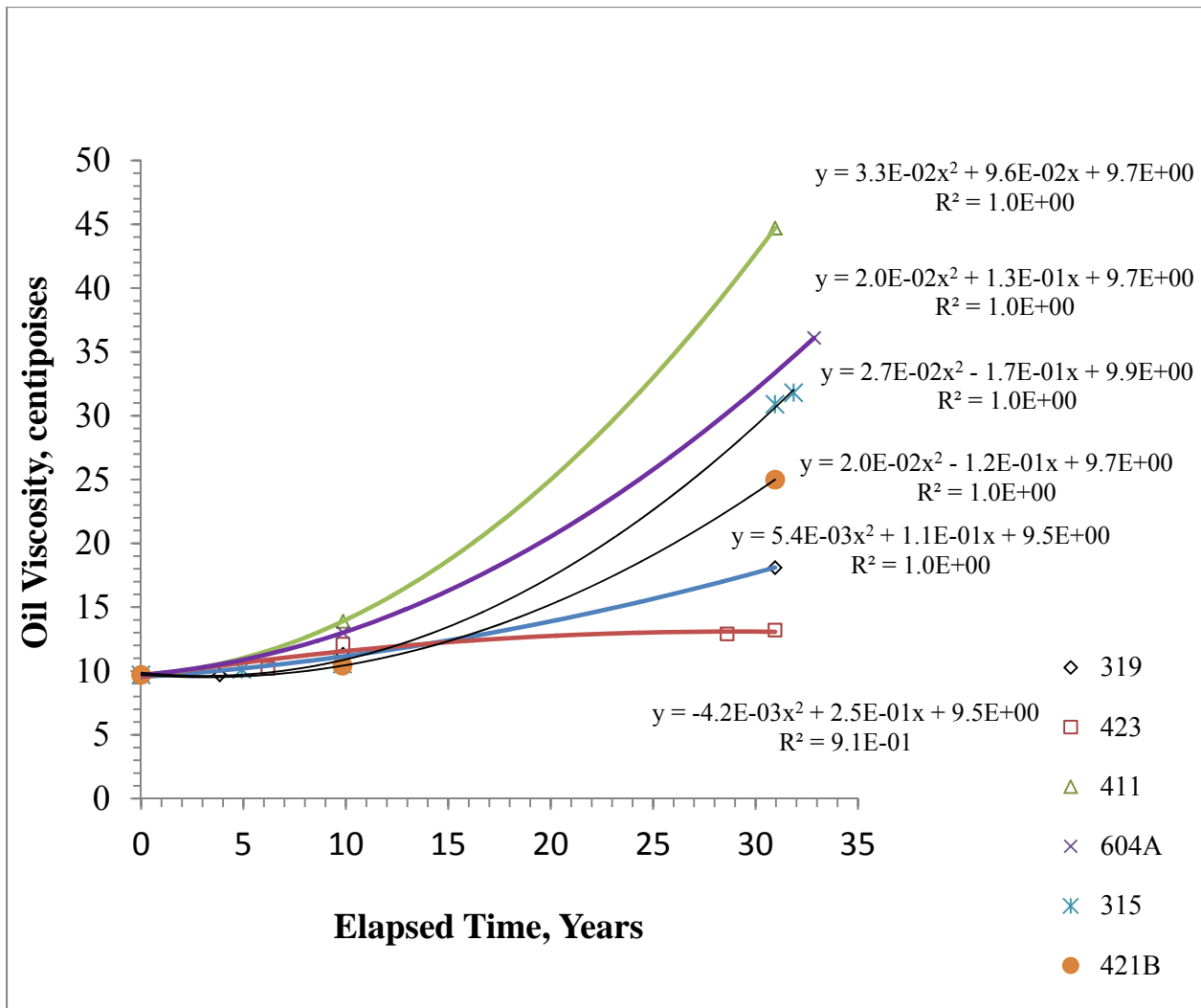


Figure 3.13 Oil dynamic viscosities at selected wells plotted with elapsed time since the 1979 pipeline release. Best-fit functions for wells 315, 411, and 421B used in estimating historical oil transmissivities.

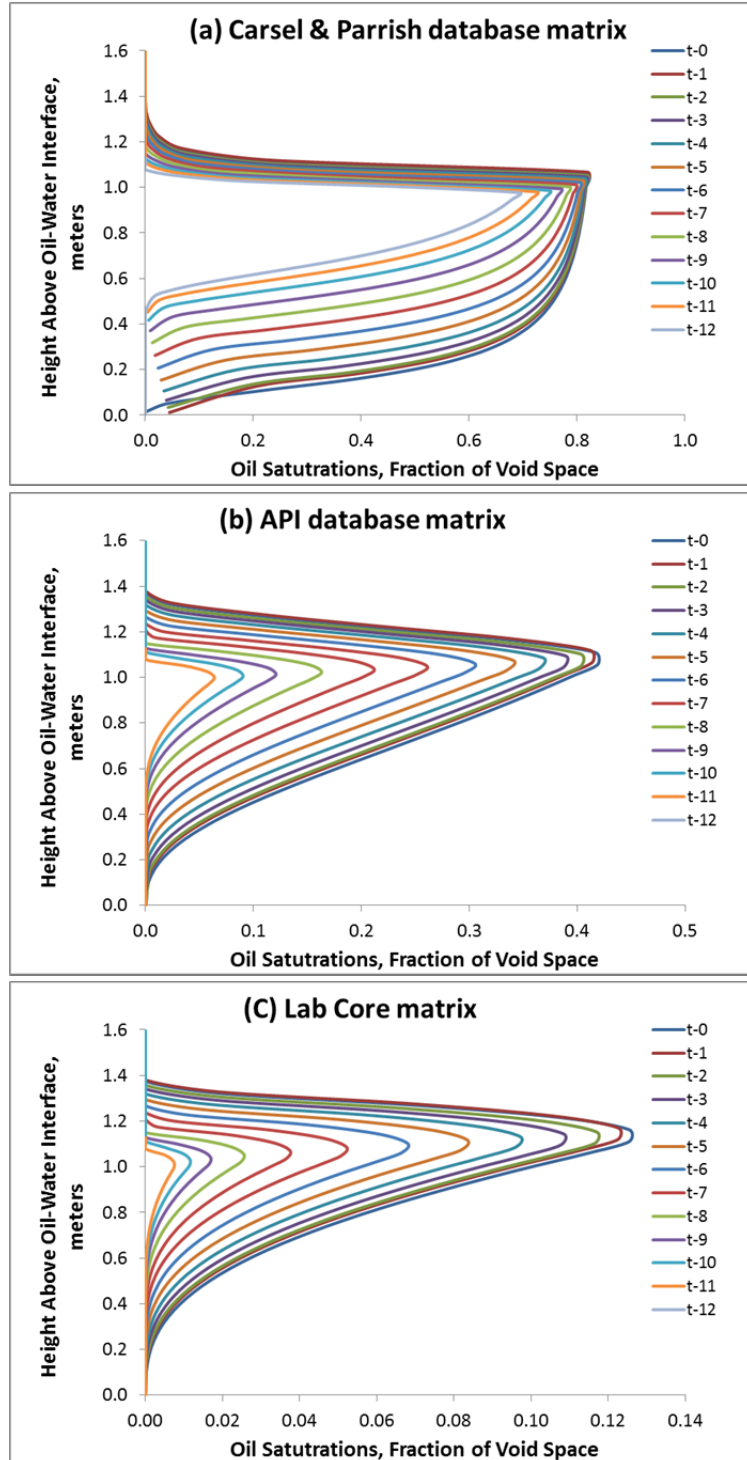


Figure 3.14 Sequences of possible historical oil saturations at location 421B based on matrix properties inferred from baildown test results and core lab analyses, combined with oil thickness records, and changes in fluid properties caused by weathering.

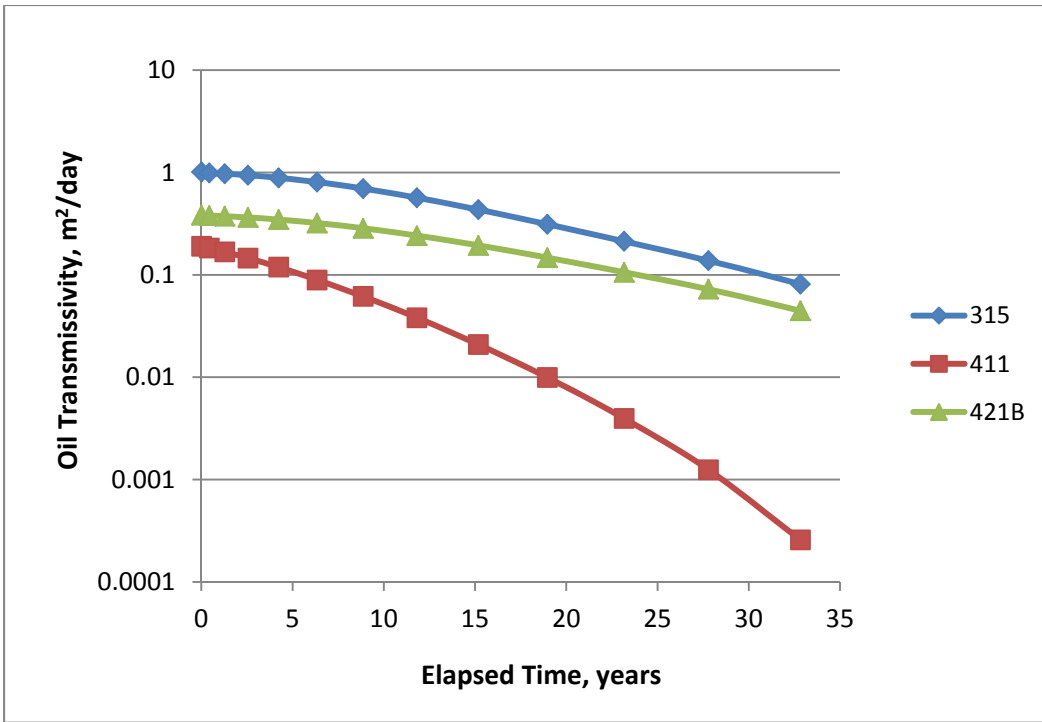


Figure 3.15 Calculated historical oil transmissivities at the three baildown test wells.

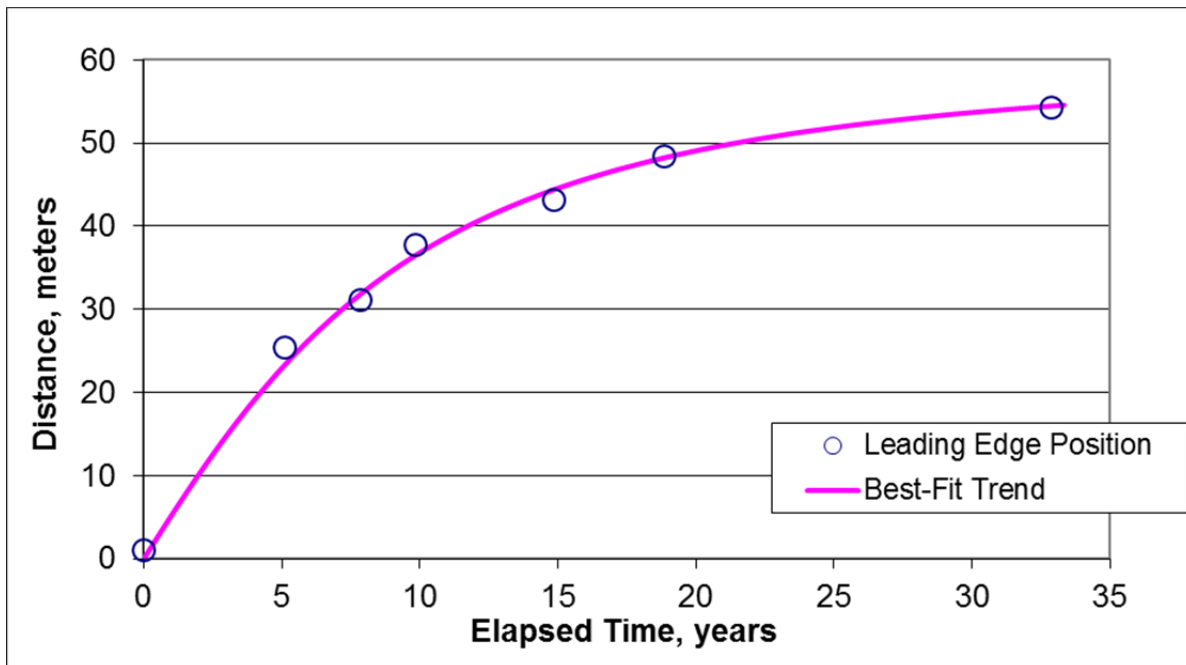


Figure 3.16 Plot of North Pool leading edge vs. time based on first occurrences of oil at selected wells. Distances are measured downgradient from LIF location TG1117 located near well 421B.

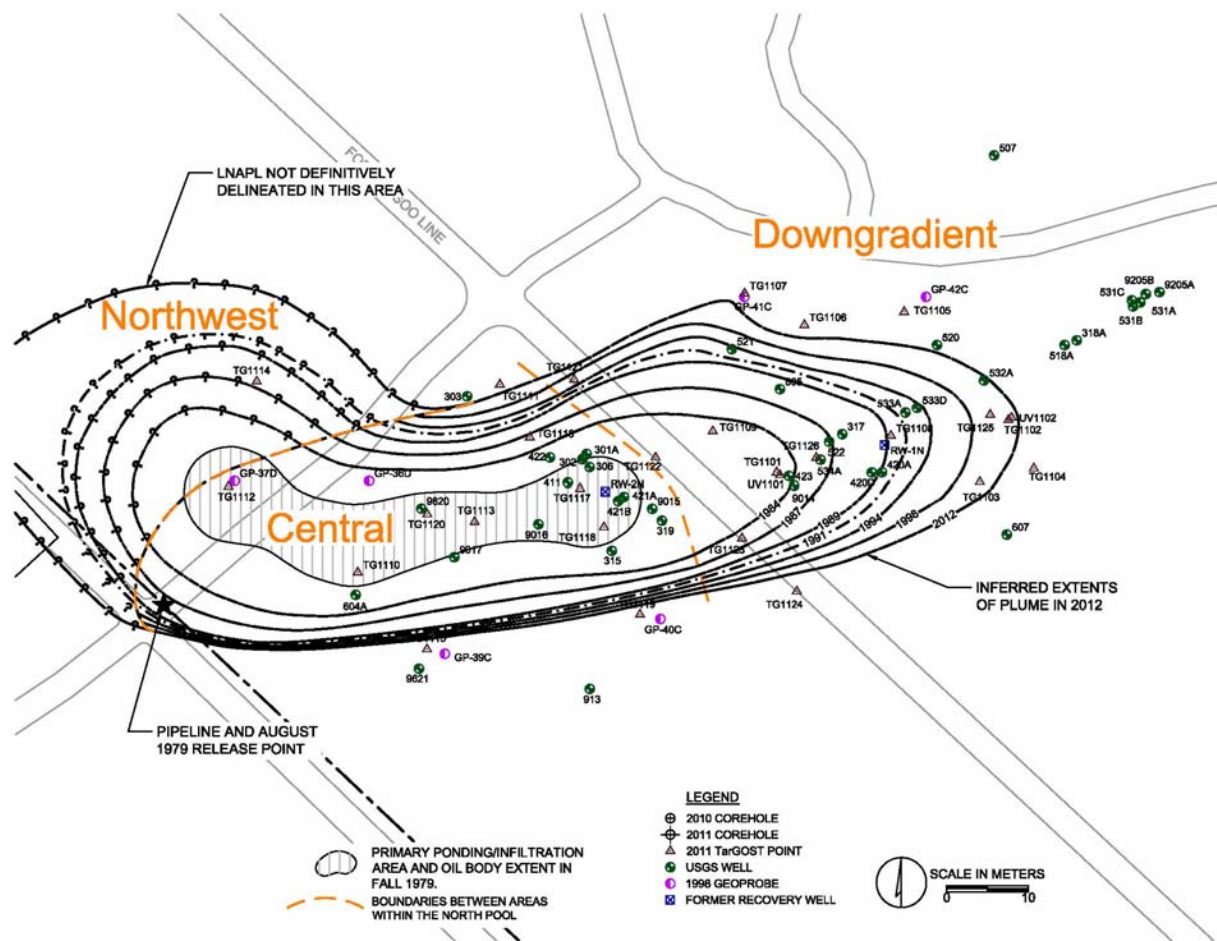


Figure 3.17 Map of the approximate historical North Pool footprint areas inferred from USGS well gauging data, observations in soil borings, a geophysical (LIF) survey, and a CO₂ efflux investigation.

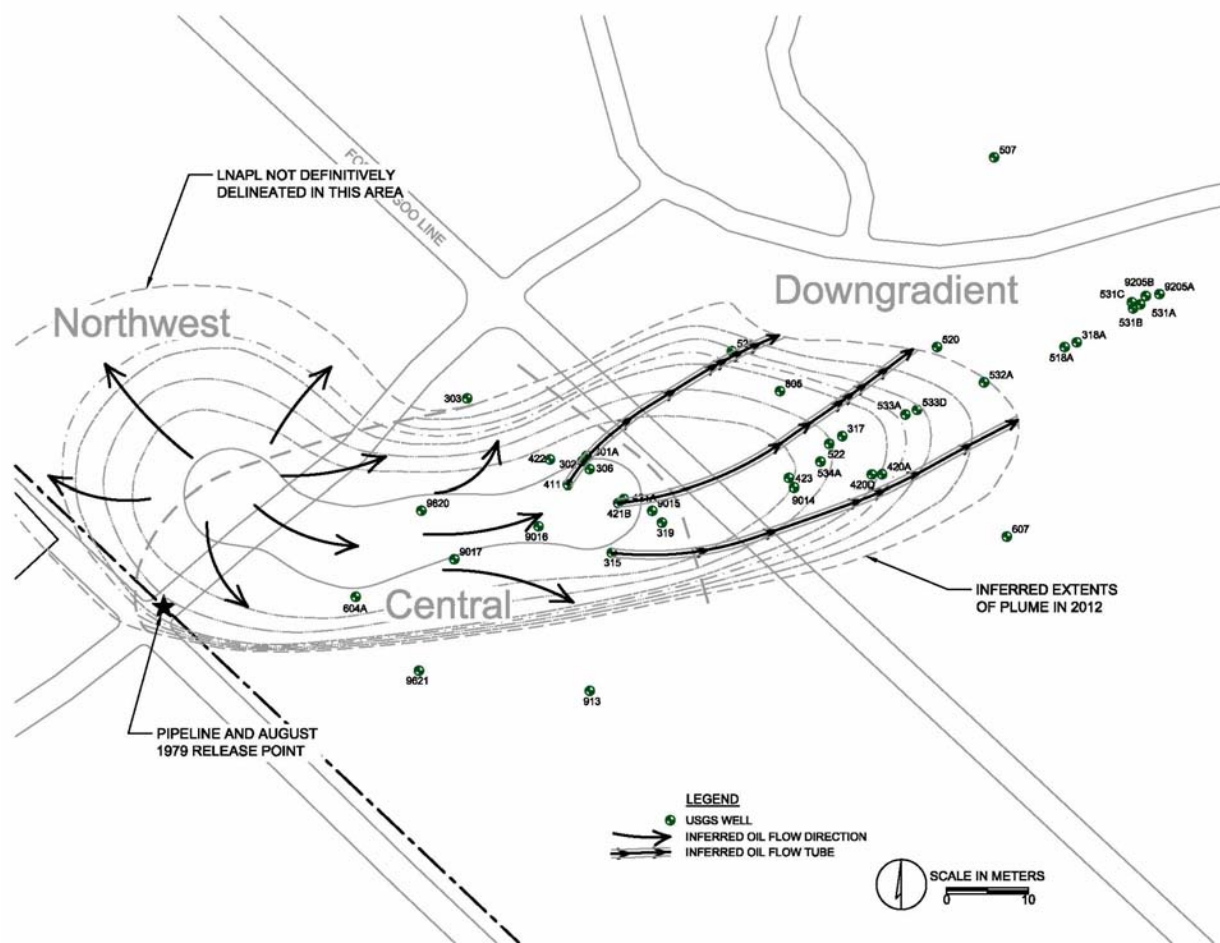


Figure 3.18 Inferred historical oil flow directions in relation to historical footprint areas and boundaries between the northwest, central, and downgradient areas. Flowtubes from three wells are composed of flow-arrow segments connecting sequential positions of the leading edge.

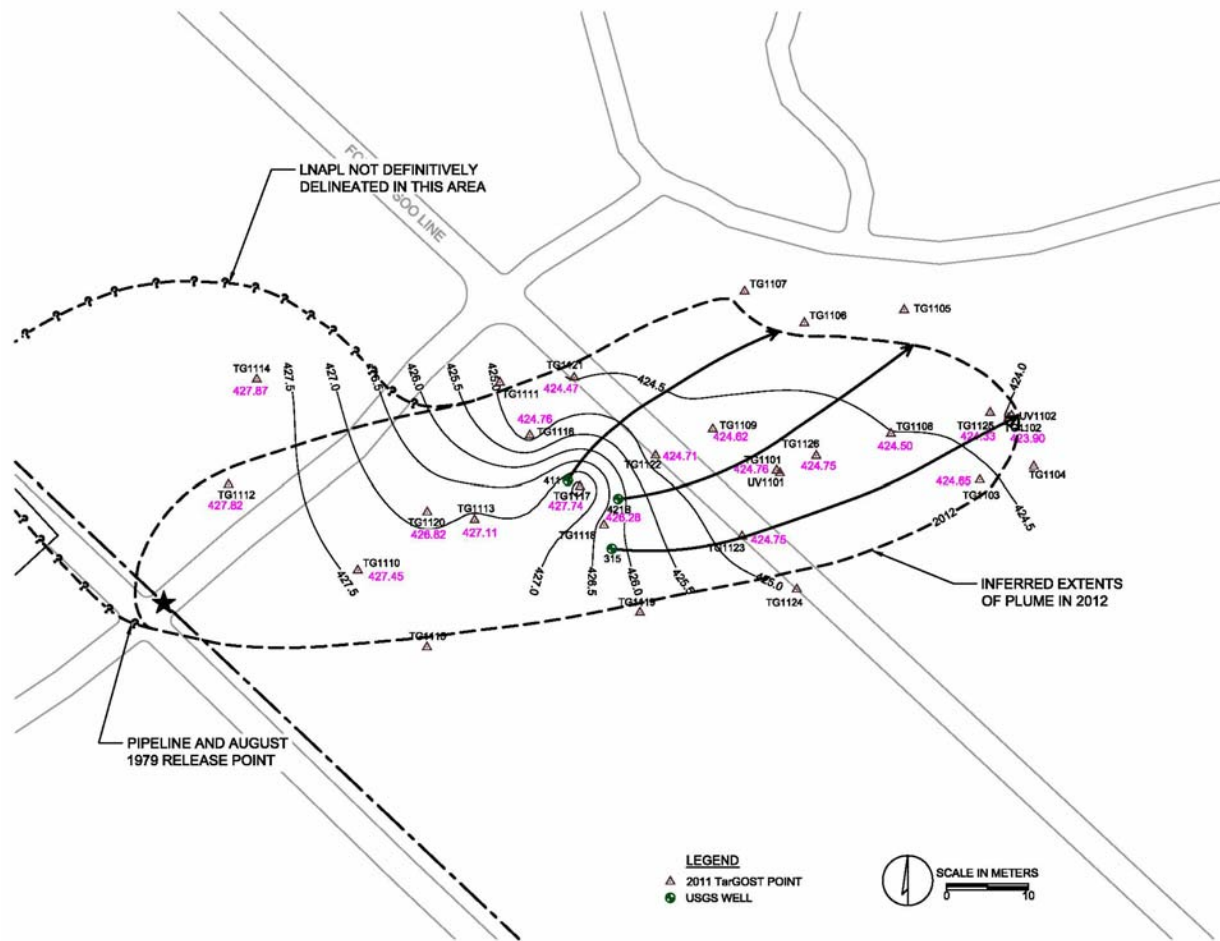


Figure 3.19 Historical oil flow directions from three baildown test wells inferred from elevation contours on the surface of highest occurrences of LIF-detected oil within the 2012 North Pool foot print area.

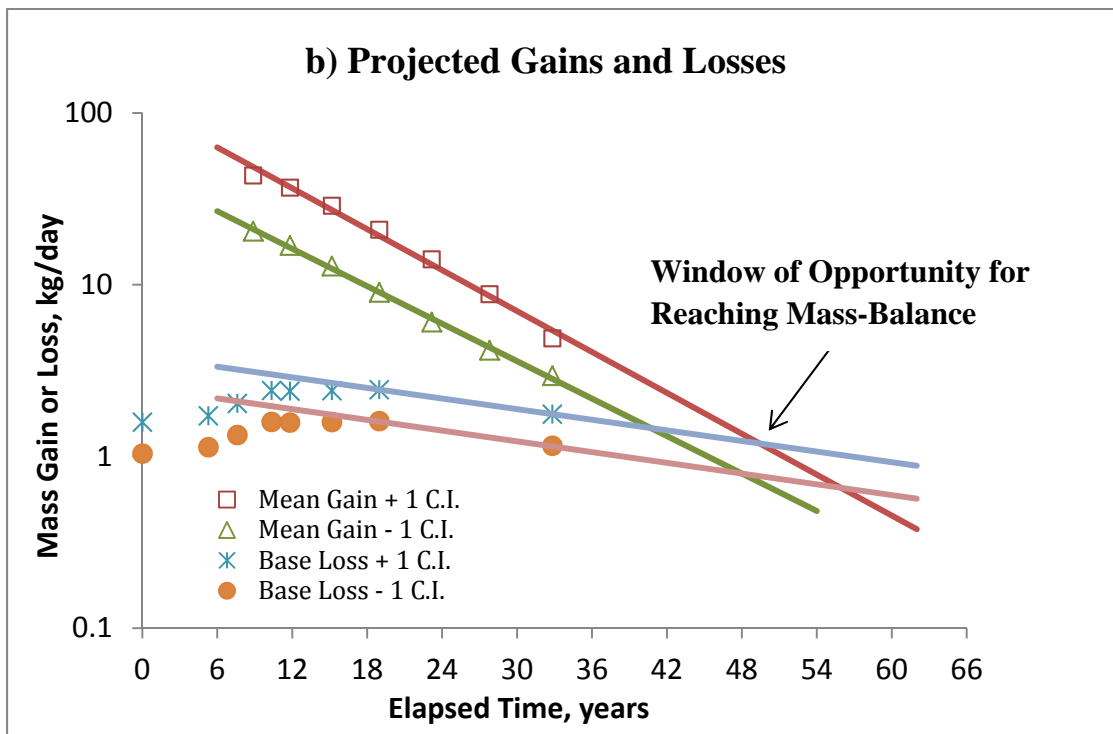
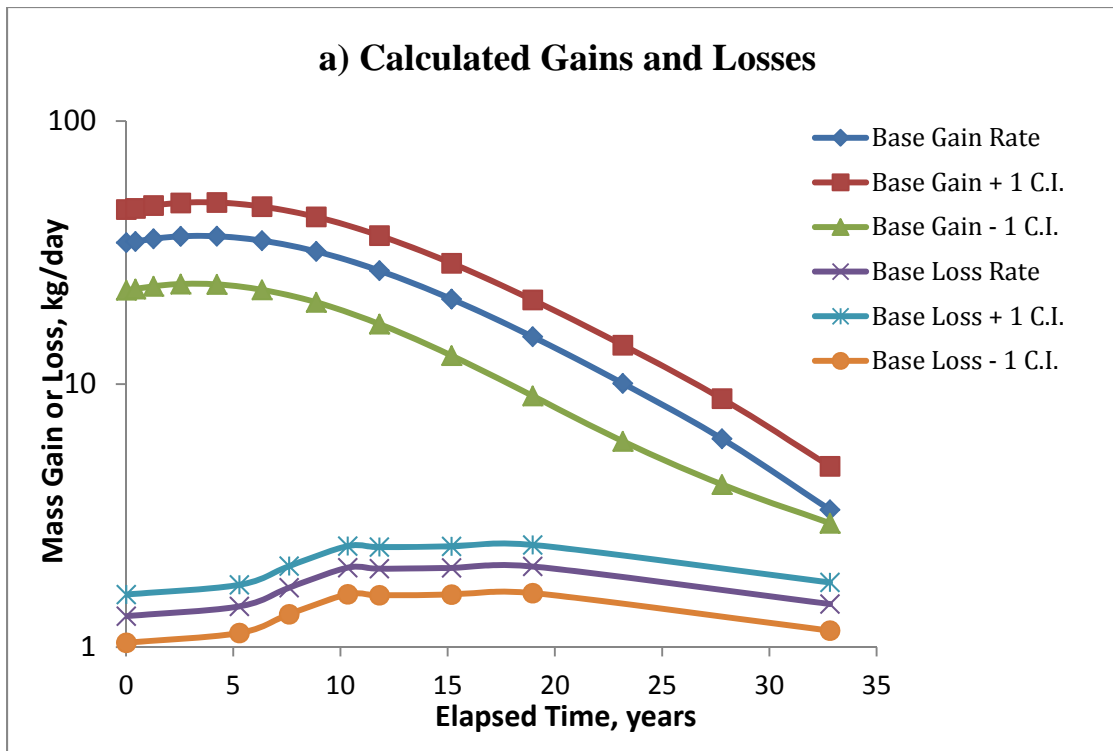


Figure 3.20 Plots of a) calculated and b) projected mass gain and loss rates in downgradient area of the North Pool and showing a stabilization window of opportunity with a LNAPL-body scale analysis.

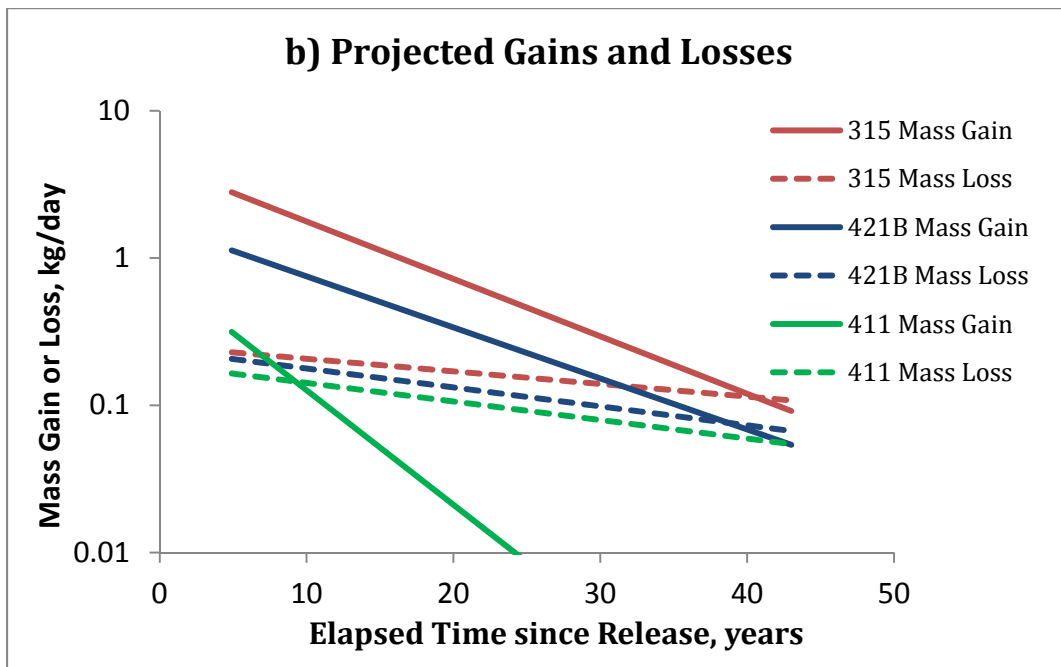
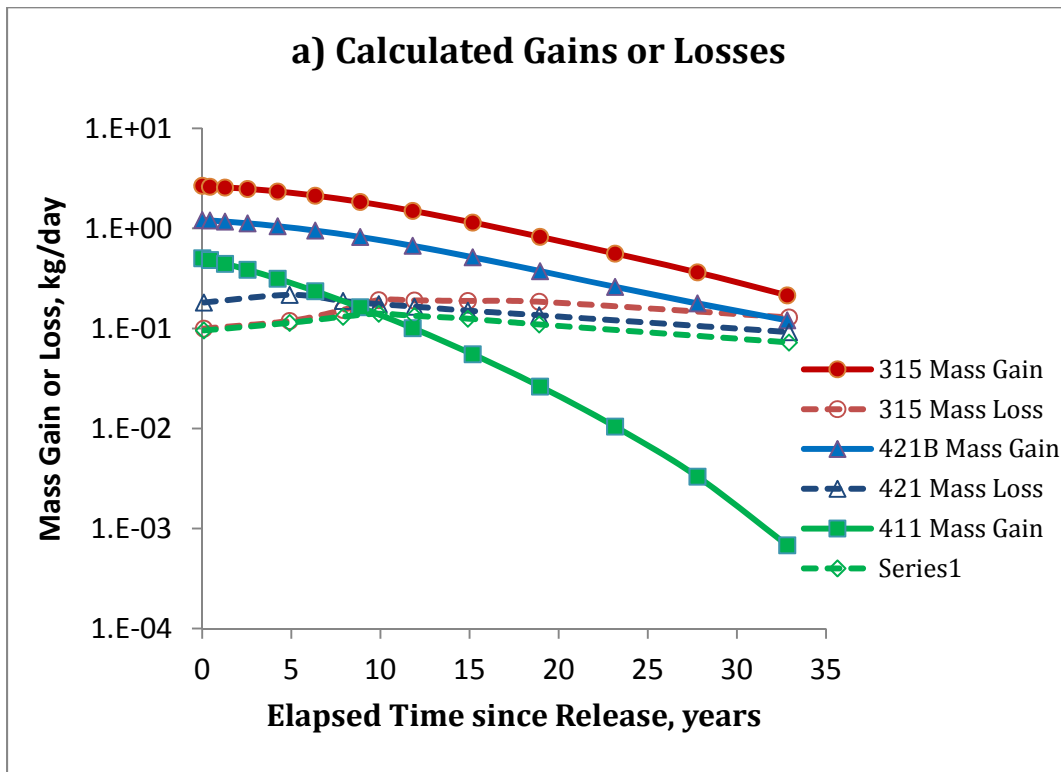


Figure 3.21 Plots of a) calculated and b) projected rates of mass gains and losses in three oil flowtubes starting at baildown test wells in the North Pool and showing when stabilization can occur at the intersection of paired mass-gain and mass-loss curves for each well.

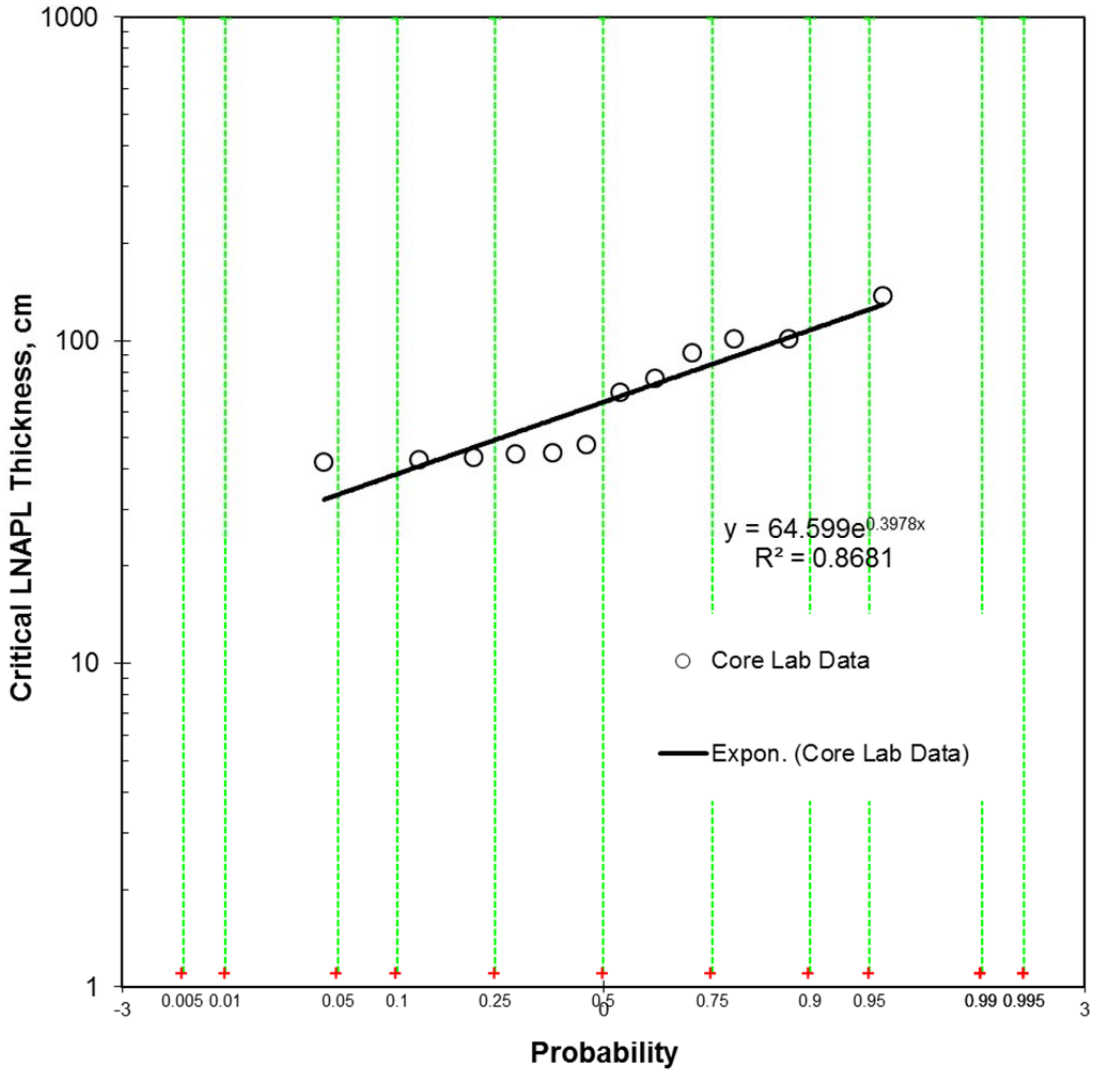


Figure 3.22 Critical in-well LNAPL thicknesses calculated with measured displacement heads and best-fit estimates of air-water, air-oil, and oil-water tensions when oil density is 0.9 gm/mL, observed near the 2012 downgradient leading edge of the North Pool.

CHAPTER 4

A PERIODIC SLUG TEST SYSTEM FOR DETERMINING AQUIFER PARAMETERS¹

¹Lundy, D.A., Dowd, J. F., and Rasmussen, T.C. To be submitted to *Groundwater Monitoring & Remediation*, A National Ground Water Association Publication.

Abstract

Periodic insertion and removal of a cylindrical slug in a borehole or test control well creates hydraulic disturbances that propagate radially to nearby observation wells, where the unique response can be used to estimate aquifer parameters with AQTESOLV, a commercial program used for interpreting aquifer tests. This hypothesis was field-tested using an oscillating slug testing device that produced periodic responses in observation wells from which aquifer transmissivity, storativity, and the vertical anisotropy were estimated. Tests were performed in a water-table aquifer at a well-characterized U.S. Geological Survey (USGS) research site near Bemidji, Minnesota. Effective pumping rates were found using the rate of insertion and withdrawal of the slug, along with borehole storage adjustments that included brief periods when the slug was either fully immersed or withdrawn. Well construction details, observation well distances, and the slug displacement during three slug oscillations served as inputs to AQTESOLV, which accommodates periodic pumping as well as intermittent non-pumping intervals. Observation well responses were analyzed using the Theis (1935) and Dougherty and Babu (1984) confined aquifer solutions. Results compare favorably with parameters estimated for an unconfined aquifer in the analysis of a U.S. Geological Survey 45-hr constant-rate pumping test near the trial test location using the Neuman (1974) delayed gravity drainage solution. The average transmissivity estimated with the Theis solution agreed within 10%, the Dougherty and Babu solution agreed within 40% of the constant-rate test transmissivity, and the storativity and the vertical-to-horizontal hydraulic conductivity ratio were within an order of magnitude of the U.S. Geological Survey estimates.

Keywords. Slug test, periodic pumping, aquifer hydraulic testing, Bemidji, AQTESOLV

Introduction

The estimation of aquifer parameters from periodic hydraulic-head fluctuations is not new to aquifer testing. Ferris (1951) presented a method for estimating hydraulic diffusivity (ratio of transmissivity to storativity) from the lag time and amplitude of pressure-head sine waves on the water table propagating landward from the shoreline in coastal areas. Cooper et al. (1964) presented a solution for estimating aquifer transmissivity and storativity based on the dissipation of sine wave water-level fluctuations in wells caused by the 1964 earthquake in Alaska.

Rasmussen et al. (2003) analyzed periodic water level responses to sinusoidal pumping and re-injecting groundwater at a control well. Successful field trials involving observation wells in unconfined, semi-confined, and confined aquifers were carried out at the Savannah River site in South Carolina, USA. Transmissivity and storativity values obtained with their analytical solution agreed within a few percent of solutions obtained using the commercial software AQTESOLV (Duffield, 2010 personal communication).

Slug tests are commonly used to obtain field estimates of aquifer hydraulic parameters during environmental investigations at sites where groundwater has been contaminated by releases of hazardous materials. Slug tests are favored over conventional aquifer pumping tests because they are less costly and take substantially less time to perform and analyze, largely because slug testing avoids the need to pump, store, treat, and dispose of potentially contaminated groundwater, which requires permitting by regulatory agencies.

Yet aquifer parameters obtained with slug tests are generally considered to be less representative than results obtained with conventional aquifer tests for the following reasons:

- a) They represent hydraulic properties within the heterogeneous media near the test well, and thereby under-estimate hydraulic parameters due to scale effects (Schulze-Makuch et al., 1999);
- b) They do not provide realistic estimates of aquifer storativity without one or more observation wells, which are commonly used with pumping tests; and
- c) They do not provide estimates of horizontal aquifer anisotropy without multiple observation wells positioned in different directions from the control well.

This paper demonstrates how the limitations of slug testing can be overcome by performing a sinusoidal slug test at the control well while observing the hydraulic response at observation wells. The method uses an oscillating slug to generate periodic pumping in the control well while recording the sinusoidal response in nearby observation wells with transducer-loggers. The unique perturbation introduced by the periodic slug makes it possible to measure small responses in observation wells, something that a conventional slug test would not provide. The method is suitable for the analysis of confined and unconfined aquifers, where well screens can be fully submerged or can straddle the water table.

Field trial testing was performed at a well-investigated U.S. Geological Survey research site near Bemidji, MN. Test data were analyzed using commercial software and hydraulic parameter estimates were evaluated against estimates of the same parameters quantified with a conventional constant-rate pumping test performed by the U.S. Geological Survey in the same aquifer (Delin and Herkelrath, 2014). The periodic slug test results were also evaluated against slug tests at 36 wells completed to different depths at the research site (Strobel et al., 1998).

Field Site Description

Field trials were performed at a 1979 crude-oil pipeline release site that became part of

the U.S. Geological Survey Toxic Substances Hydrology Program in 1983. The site is formally designated as the National Crude Oil Spill Fate and Natural Attenuation Research Site. Figure 4.1 shows the location of the site in north-central Minnesota, approximately 17 km NW of Bemidji.

The rupture of the buried 90-cm steel pipeline released approximately 1,700 m³ (10,500 bbl) of crude oil into the local environment. During an emergency response, approximately 1,250 m³ (7,880 bbl) were recovered leaving a balance of 418 m³ (2,630 bbl) the subsurface. The North Pool oil body was created by direct infiltration beneath the release point and infiltration to the water table beneath the overland flowpath into a nearby closed topographic depression. The Middle and South Pools (Figure 4.1) developed by the same mechanism of infiltration along the overland flowpath that ultimately reached a small wetland (Hult, 1984).

The shallow water-table aquifer affected by the pipeline release is a glacial outwash deposit with a saturated thickness that ranges from 7 to 20 m (23- 65 ft) at the research site, and was approximately 15 m (50 ft) thick at the field trial cluster in the summer of 2010. It is a heterogeneous package of fine-to-coarse sand and gravel beds with a few intermittent sandy and clayey silt beds, especially in the vadose zone and near the water table in selected areas. Field and laboratory studies were conducted during the 1980s and 1990s to characterize the stratigraphy and quantify hydraulic properties of the aquifer.

Table 4.1 summarizes mean or median hydraulic conductivity values obtained from U.S. Geological Survey investigations within and near the North Pool oil body. These show an increase in hydraulic conductivity with the scale of the volume of material being tested, which is consistent with other hydrogeologic literature (Shulze-Makuch et al., 1999).

Oscillating Slug Test Equipment Description

We designed and built a prototype device in the spring of 2010 that generates sinusoidal pumping from oscillatory movement of a solid slug in and out of the water in a test control well. A conceptual design was prepared and modified after working collaboratively with an outside subcontractor-engineer with experience in designing and building electrical-mechanical devices for EON Products of Snellville, GA (Kurt DePue, 2010, personal communication). The final design has the device mounted on a hand truck that facilitates transport and positioning of the device in proximity to a control well for slug testing. Figure 4.2 is a photograph of the oscillating slug tester positioned to begin a test on a monitoring well at the trial test site. The device is positioned in a way to show a control well with protective casing labeled 522 to the right side of the device, the red rotating arm is positioned horizontally extending to the left side of the device, and the small black electric motor and speed control knob are shown mounted in the center of the hand truck.

Figure 4.3 provides a sketch of key components of the sinusoidal slug test device when functioning. The rotating arm, with its axis attached near the center of the hand-truck frame, is used to create the oscillating movement of a cylindrical slug in and out of the water column in the control well. The slug is fabricated of plastic (PVC) pipe that is weighted so that its bulk density is greater than that of water to prevent floating. The rotating arm is designed to be half the length of the solid slug, but can be adjusted for shorter or longer slugs.

Rotation of the arm creates a sinusoidal rate of inserting and withdrawing of the slug in cycles with a constant radial velocity. The angular velocity is controlled by adjusting the speed of an electric motor-chain drive mechanism mounted on the back of the hand truck (not shown). The weight of the slug holds the wire cable taught during a full revolution of the arm, but loses

tension when the slug becomes fully submerged. The wire cable has a small loop that makes contact with but glides with movement of the radial arm wheel from location A to B in Figure 3. The cable glides over the top of a rotating wheel guide that is fixed in space over the center of the well by a stationary arm (Figures 1 and 3).

During the trial testing, the bottom of the slug was positioned in contact with the static water level in the well and the rotating radial arm was positioned horizontally. The length of cable from the guide wheel to the arm wheel is slightly longer than the length of the slug. When the arm rotates counter-clockwise (through points A, B, C and D), the slug is lowered into the water. As the angle of arm rotation approaches 180° (π radians) at point D, the length of cable between the two wheels reaches a minimum distance, and the slug is fully submerged below the static water level depth position. As the arm continues to rotate from 180° to 360° (π to 2π radians) returning to point A, it pulls the slug back out of the water, completing one revolution and one sine-wave of hydraulic head changes at the control well.

Conversion of Slug Movement to Pumping/Injection Rates

Arm rotation at a constant angular velocity produces oscillatory movement of the solid slug. In this study, observations under both laboratory and field experimental conditions produced oscillations that were sinusoidal. An example is given in Figure 4, a plot of water level changes recorded with transducer-logger during the first trial equipment test at a monitoring well at the EON facility in Snellville, GA.

Slug movements in and out of the water are used to approximate sequential injection and pumping rates, which are needed to perform the analysis of aquifer parameters. Movements of a solid slug with known length and radius are tracked relative to the pretest water level, which

serves as a datum. When the slug is initially positioned with its base contacting the pretest water level, the elevation of the top of the slug equals the slug length above the datum at the base of the slug. After selecting a constant angular velocity, the movement of the top and bottom of the slug relative to the datum is modeled as a function of elapsed time after the rotating arm begins moving.

A sine function used for modeling and plotting time-dependent elevation, $z(t)$, of the lowest point on the slug has the general form:

$$z = z_0 - R \sin \theta , \quad (1)$$

where z_0 is the initial elevation ($t = t_0$), t_0 is the start time, R is the periodic amplitude (equal to the length of the radial arm), $\theta = \omega (t-t_0)$ is the angular position, and $\omega = 2\pi / P$ is the periodic frequency (angular velocity) with period P . The position of the uppermost point on the slug is $2R$ higher than z_0 .

Sinusoidal changes in slug length and volume relate directly to the top and bottom slug movements. Incremental changes in the angular position translate into a series of incremental injection/withdrawal pumping steps. Insertion of the slug effectively adds water to the well and withdrawal of the slug effectively removes water.

Calculated slug movements and injection/pumping rates were compared to synoptic water level head changes in the control well recorded on a transducer log. Inside the control well oscillating water levels will move in opposing directions to solid slug movements. A smooth sinusoidal movement will be altered when: a) the top of the slug moves below the rising water level, or b) when the base of the slug moves above a falling water level. During short periods of time when the slug is either completely submerged or completely withdrawn from the rising and

falling water levels in the control well, the effective pumping rates equal zero. These non-pumping periods can alter otherwise smooth symmetrical sine waves in both control and observation wells.

Figure 4.4 shows recorded pressure-head readings of a transducer set in the bottom of the control well for the first trial test in Snellville, GA. The tops of the waves are much sharper than the bottoms and upper-half wave amplitude is approximately twice the amplitude lower half amplitude (both being separated by the initial pressure head reading of 3.84 m). Figure 4 also shows clear evidence that the water table is trending downward during the test period.

Field Trial Testing

Two field trials were conducted near and within the North Pool oil body during the 2010 summer field season. The first trial test was performed at a cluster of shallow monitoring wells within the groundwater plume associated with the North Pool. A second field trial was performed using monitoring wells located near the center of the North Pool where the transmissivity of the mobile oil zone and underlying groundwater zone was to be assessed. Only the first test involving groundwater is reported here for a proof of concept to identify practical limitations of the oscillating slug test device.

Monitoring well 531A was used as the control well for the oscillating slug and wells 9205A and 9205B were used as observation wells (Figure 4.5). The wells are constructed with 5.1-cm diameter plastic (PVC) well casing and screens without filter packs. Other construction details and distances to the observation wells are provided in Table 4.2.

Pressure transducers (Instrument Northwest PT2X Smart Sensors with 15 PSI maximum range and 0.1% accuracy) were set at the bottoms of the wells and recorded pressure heads at

0.1-s intervals. Pressure transducers and pretest static water levels shown were measured the day before the actual test, and rose slightly the following day before starting the oscillations. Background trends in the water table may need to be separated from the induced sine wave response before the response data are ready for analysis of aquifer parameters.

Because unconfined aquifers behave as confined aquifers during the initial drawdown response to pumping, confined aquifer analytical solutions can be used for the analysis of the short-term sinusoidal slug response. Commercial aquifer test software AQTESOLV Pro version 4.5 (Duffield, 2007) offers a number of confined aquifer solutions for analysis of aquifer parameters.

Results of Trial Testing

Field trials were performed on July 23, 2010, using a solid slug with a 3.45 cm diameter and 76.2 cm length. The rotating arm was set to make approximately 1-min (56.3 s) revolutions and made multiple slug oscillations inside control well 534A over an 18-min test period. The recorded hydraulic response verses time plot is shown in Figure 4.6. It clearly tracks with six slug oscillations, a brief shutdown-recovery period, nine more slug oscillations, and a final shutdown/recovery back to the pretest water level position. Inspection of the water-level fluctuations in Figure 4.6 reveals the following details:

- a) The time to make each arm rotation was approximately 56.3 s, equivalent to an angular velocity of 0.112 rad/s, and
- b) The lower half of each cycle is slightly distorted, and attributed to short-term periods of total slug immersion and withdrawal, discussed further below.

The analysis of aquifer parameters was performed using the water-level responses

recorded at the two observation wells 9205A and 9205B with the effective injection/extraction pumping rates at control well 534A. Figure 4.7 shows modeled positions of the top and bottom of the solid slug with water levels relative to the pretest water level (zero line), along with calculated pumping rates on the same synoptic time scale.

The slug position and pumping rates were calculated for a sequence of 2-s time steps in which the rotating arm moved 0.224 radians/step. There are 28 steps per rotation and three rotations yielding 84 pumping steps to represent three oscillations. The non-pumping, zero-rate steps occur whenever the top of the slug moves below the rising water level, and when the bottom of the slug rises above the falling water level. The duration of these, each lasting four steps (8 sec), were determined by visual inspection of the plotted data in Figure 4.7.

The sequence of pumping rates shown in Figure 4.7 and water level observations at wells 9205A and 9205B were analyzed using the Theis (1935) and Dougherty and Babu (1984) confined aquifer solutions. The transmissivity and storativity estimates were compared to each other and to earlier results obtained by the U.S. Geological Survey with an analysis of a conventional pumping test at other wells completed in the same aquifer and located inside the North Pool footprint area.

The pumping control well, 0501, was approximately 77 m (254 ft) upgradient and the three observation wells are roughly between 70 and 80 m (230 and 260 ft) upgradient of the trial test area (Figure 4.5). U.S. Geological Survey time-drawdown data were re-analyzed with AQTESOLV using the unconfined aquifer solution of Neuman (1972 and 1974), which accounts for partial penetration of the wells, storativity in early time, and specific yield by accounting for delayed gravity drainage in later time. The results obtained here agree with those reported earlier

by the U.S. Geological Survey (Table 4.1).

Table 4.3 provides a summary of the best-fit parameter values for the AQTESOLV analyses. Appendix H provides copies of AQTESOLV printouts for the analyses for each test and observation well in the order listed in Table 4.3. The Theis and Dougherty-Babu solutions both assume no leakage from bounding confining beds. They can include partial penetration and horizontal-vertical anisotropy (K_h/K_z) ratio, with AQTESOLV to fit with the test site conditions; and the Dougherty-Babu solution accounts for the wellbore skin effect. AQTESOLV uses the principle of superposition to account for multiple sequential pumping steps that can change sign and therefore accommodate the periodic changes from injection to pumping with both solutions. Best-fit parameter values are obtained with the automated matching algorithm. Because the Theis solution has fewer parameters, the algorithm will meet convergence criteria and provide values in less time than the Dougherty-Babu solution.

Transmissivity values for the sinusoidal slug and conventional pumping tests account for partial penetration of the aquifer, which is 14.6 m (48 ft) thick. Transmissivity values with the different test solutions are within the same order of magnitude, ranging from 551 to 1,763 m^2/day (5,930 to 18,970 ft^2/day). The mean Theis solution transmissivity is 45% larger than the mean Dougherty-Babu transmissivity. This difference is related to the borehole skin parameter with a value of -5 determined with the automated best-fit algorithm for the Dougherty-Babu solution. The best-fit transmissivity value was found to be highly sensitive to the borehole skin value, which is not included with either the Theis or Neuman solutions. The average Theis solution transmissivity for the sinusoidal test is within 10% of the average transmissivity obtained with the Neuman solution for U.S. Geological Survey test wells near the center of the North Pool (Figure 4.5).

The aquifer storativity and vertical anisotropy ratios for the sinusoidal slug tests are within one order of magnitude those values obtained for the pumping test. This is consistent with the general experience with aquifer tests that transmissivity values tend to be more reproducible than storativity and anisotropy values. The sinusoidal test analyses both exhibit a similar directional difference in the radial direction not seen with the conventional pumping test results because the observation wells were located one direction from the pumping well.

Summary and Conclusions

The objective of this investigation was to field test the idea of using an oscillating solid slug to generate sinusoidal pumping (periodic injection/extraction rates) in a control well, to record the propagating sine-wave response in observation wells, and use those data to estimate aquifer properties that would be compared to aquifer properties determined by a longer-term conventional pumping test. The following is list of tasks that were carried out to reach this objective:

- a) Design and build a device to perform the tests on shallow monitoring wells with screens that may straddle the water table;
- b) Perform a field trial test of the device using a cluster of wells at a well-characterized site and use the experience to identify and accommodate any operational limitations;
- c) Analyze the hydraulic response observed at two observation wells located different distances and directions from the control well where the oscillating slug tester is operated for a sufficient time to generate observable and analyzable responses; and
- d) Analyze the data to determining hydraulic properties and compare those to results obtained using a conventional pumping test method.

With outside funding and help from a contracted design engineer, the oscillating slug tester was

constructed in the spring of 2010. It was initially tested on a single monitoring well in Snellville, GA, instrumented with a transducer-logger to record the response. It was shipped to the trial test research site operated by the U.S. Geological Survey near Bemidji, MN, and was tested with a 1.52 m (5 ft) long 1-inch nominal ID solid slug in on shallow control well and two nearby observation wells. Based on field observations and analysis of field trial data, several limitations and lessons learned were recognized and are noted below.

The wells should have sufficient standing water to perform the tests, but it is not necessary that the well screens be completely submerged throughout the tests. The magnitudes of the water level changes will be a function of several variables, primarily the size of the slug and rate of insertion/withdrawal at the control well, and the distances to the observation wells. The observation wells should be located fairly close to the control well in order to obtain signals that are easily separable from any background noise in the system.

The effective pumping rate, based on rate of vertical movement of the slug per unit time, can be calculated using a sine-function and the dimensions of the slug. However, those rates must be compared to the actual synoptic water levels in the control well and adjusted because of the fact that the water level is rising when the slug is being inserted and is falling as the slug is being withdrawn. In any oscillating slug test, there will be non-pumping periods when the slug is completely submerged below a rising water level and when the slug is completely withdrawn from a falling water level. These will be observable as imperfections in the shape and symmetry of the sinusoidal trend of water levels recorded in the control well, and to a much lesser degree in the observation wells. As the periodic waves propagate radially from the control well to observation wells, these minor perturbations appear to be filtered out by the porous media. Available analytical solutions do not explicitly include or account for filtering of background

noise or perturbations. By using the principle of superposition, they can still accommodate variable pumping rates including periods of zero injection or extraction and thereby find reasonable best-fit parameter values for the sinusoidal test data.

Best-fit averaged values of aquifer transmissivity at the trial test well cluster using the Theis (1935) confined aquifer solution were within 10% of the average transmissivity obtained using the Neuman (1972; 1974) solution to a 45-hour constant rate pumping test and three observation wells located 70 to 80 m upgradient in the same aquifer. Best-fit averaged storativity values were within 15% and the vertical-to-horizontal (radial) hydraulic conductivity ratios differed by one order of magnitude. The Theis solution estimate of transmissivity was 45% larger than the average transmissivity using the Dougherty-Babu solution, but that may be attributed to a negative wellbore skin effect needed in that solution, which makes the comparison questionable. However, the Theis and Dougherty-Babu solutions both indicated similar evidence that the aquifer appears to be horizontally anisotropic in the trial test area. This consistent finding is encouraging, but should be confirmed by further testing at the trial test site and other sites.

Table 4.1

U.S. Geologic Survey Aquifer Test Results for the Glacial Aquifer at the National Crude Oil Spill Fate and Natural Attenuation Research Site, Bemidji, MN, USA.

Upper Zone is within three meters of the water table. Lower Zone is greater than three meters below the water table.

Lithology (strata) Test Type	Upper Zone			Lower Zone	
	Fine (silty) Grainsize	Coarse (sandy) Grainsize	Fine-Medium Sands Slug	Coarse Sands to Gravels Slug	Pumping
K (m/day)					
minimum	1.02E-07	1.01	1.52	0.38	
maximum	0.907	108.9	8.48	46.3	
average	0.038	8.25			77
median			4.68	20	
Source*	(1)	(1)	(2)	(2)	(3)

*Sources: (1) Dilliard et. al., 1997; (2) Strobel et al., 1998; and (3) Delin and Herkelrath, 2014

Table 4.2
 Construction Details and Water Levels (7/21/2010) for Test Wells
 in the Glacial Aquifer at the Research Site, Bemidji, MN, USA.

	Well ID		
	531A	9205A	9205B
Latitude (N)			
Longitude (W)			
Monitoring elevation (m)	433.74	433.50	433.58
Screen length (m)	1.52	0.15	0.15
Screen depth (m)	11.75	11.14	11.34
Pretest depth to water (m)	9.67	9.82	9.75
Pretest water column (m)	2.08	1.32	1.59
Distance from 531A (m)	0.00	2.67	1.24

Table 4.3

Comparison of Aquifer Hydraulic Properties Between the Periodic Slug Test
and a Conventional Aquifer Test at the Research Site, Bemidji, MN, USA

Location – Test Type (Analysis Method)	Well ID	Transmissivity (m^2/day)	Storativity (-)	Diffusivity (m^2/day)	Anisotropy Ratio (-)
531A - Periodic Slug Test (Theis, 1935)	9205A	1,763	2.04E-03	2.84E+06	980
	9205B	990	1.07E-03	3.03E+06	495
	Mean	1,376	1.56E-03	2.93E+06	738
	(Dougherty and Babu, 1984)	9205A	970	0.673E-03	4.73E+06
	9205B	551	0.112E-03	16.1E+06	10
	Mean	760	0.393E-03	10.4E+06	12
501 - USGS Aquifer Test (Neuman, 1972)	505	1,145	2.17E-03	1.73E+06	31
	506	1,206	2.72E-03	1.45E+06	33
	507	1,289	0.964E-03	4.39E+06	61
	Mean	1,213	1.95E-03	2.52E+06	42

North Pool Oil Body and Site Features

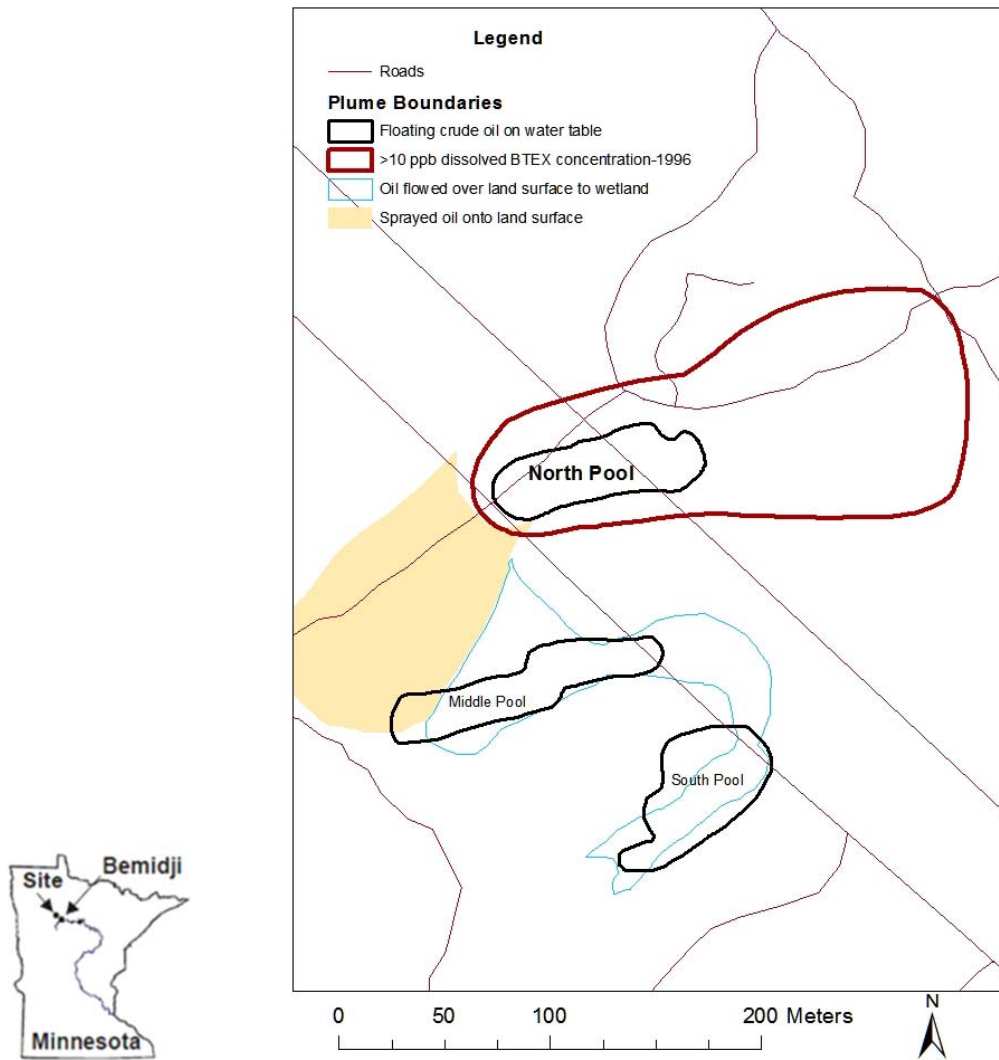


Figure 4.1 Location of the National Crude Oil Spill Fate and Natural Attenuation Research Site near Bemidji, MN, and locations of the 1979 crude oil pipeline release, migration pathways on the land surface, and three oil bodies in contact with shallow groundwater.



Figure 4.2. Photograph of the oscillating slug test device set up to begin a test at a site control well.

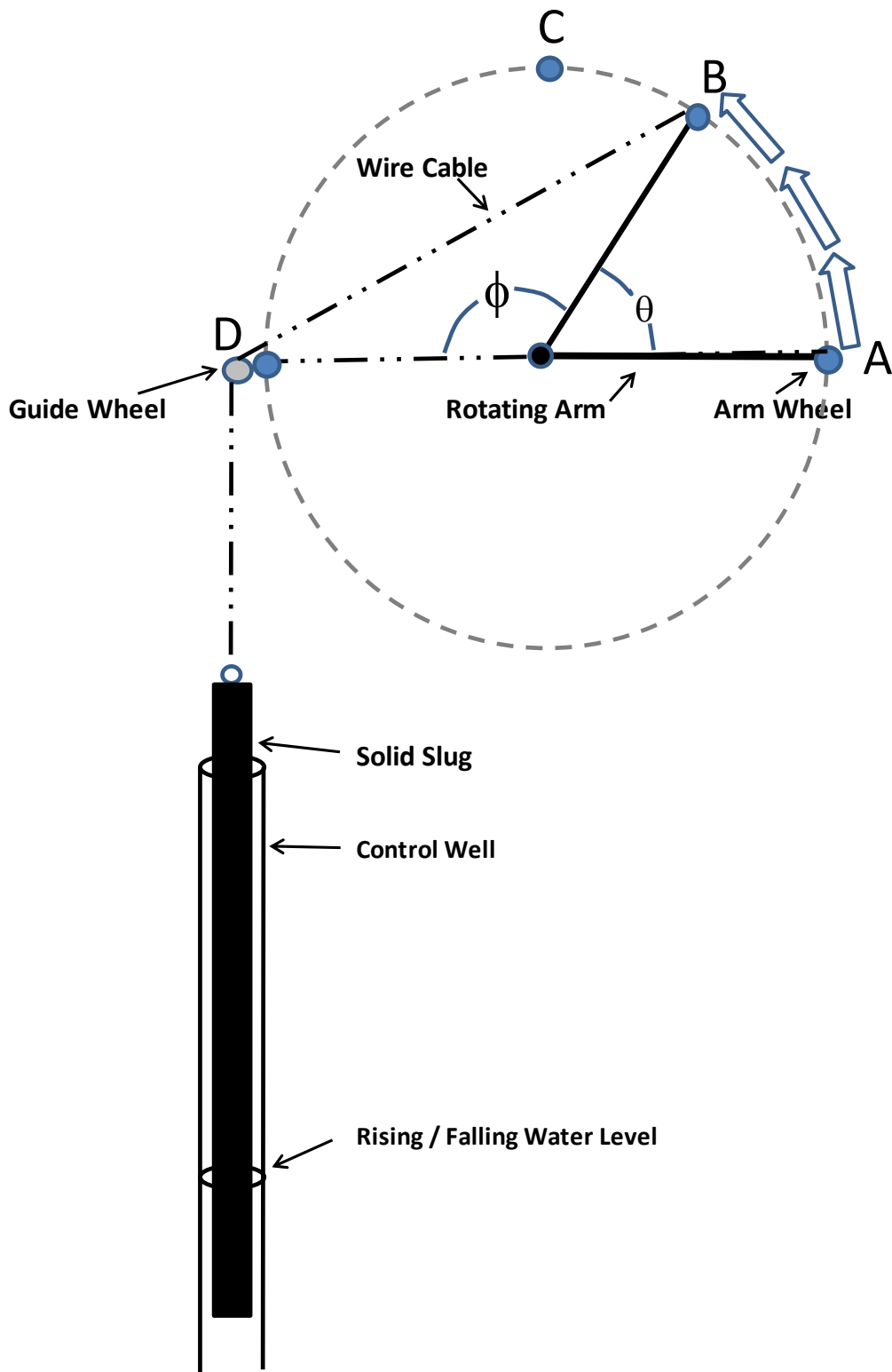


Figure 4.3 Conceptual sketch of selected components of the sinusoidal slug test equipment. Positions of rotating arm are lettered A, B, C, and D.

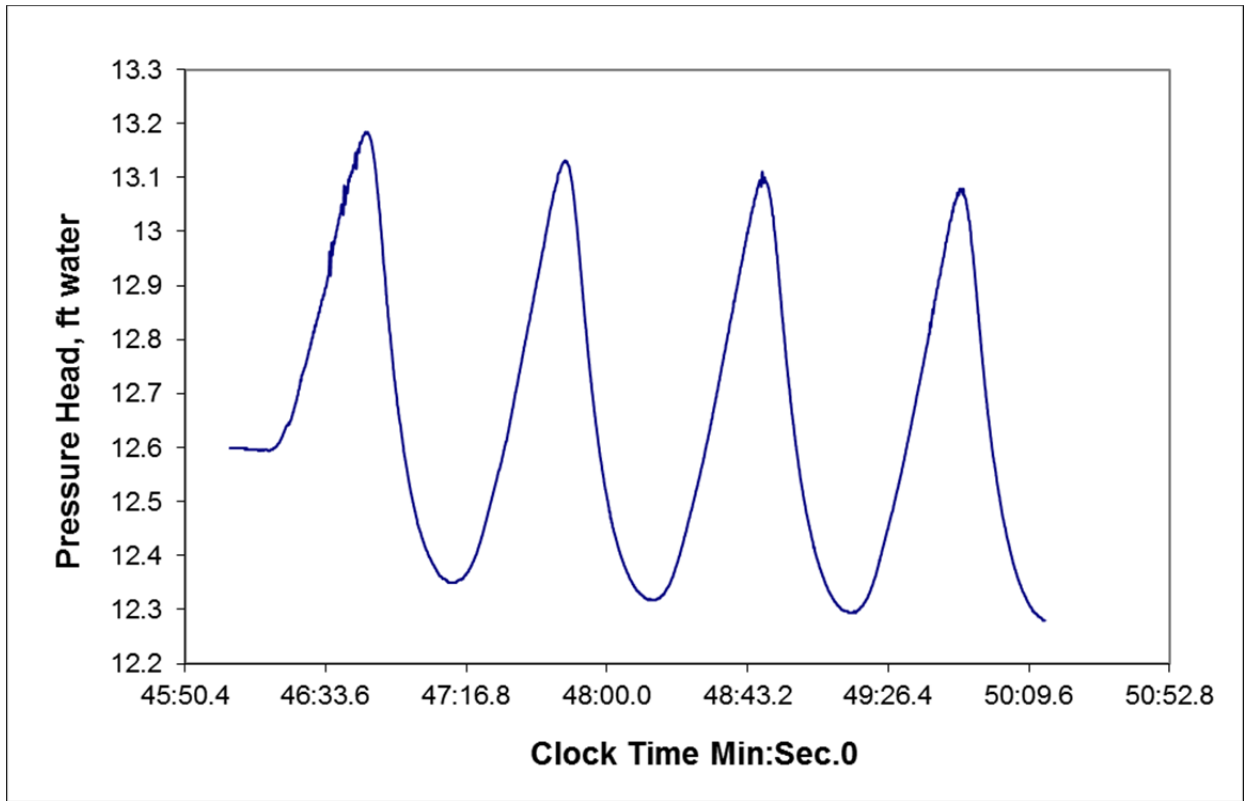


Figure 4.4 Plot of transducer-logger data for a trial oscillating slug test, July 10, 2010. Slug dimensions were length = 5 ft and diameter = 2.5 inches; and test well diameter = 4 inches.

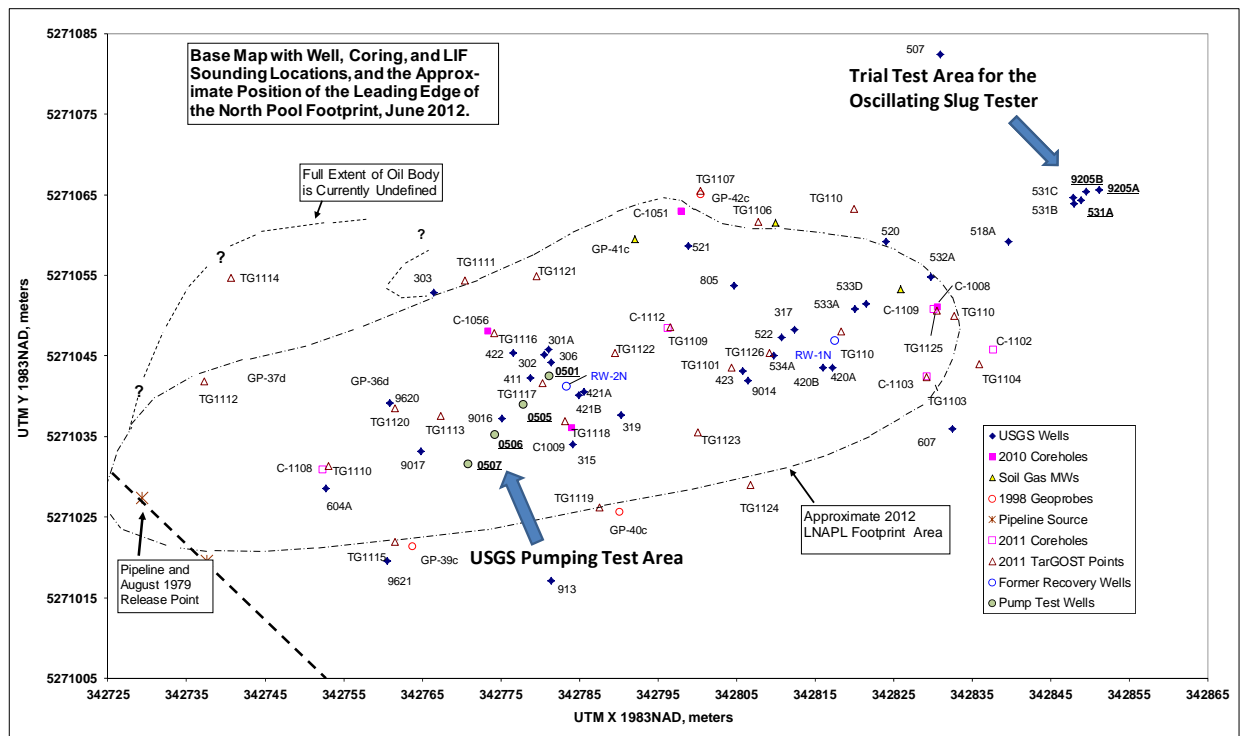


Figure 4.5 Locations of periodic trial test well cluster and well locations for the USGS pumping test shown with other wells within and near the North Pool oil body.

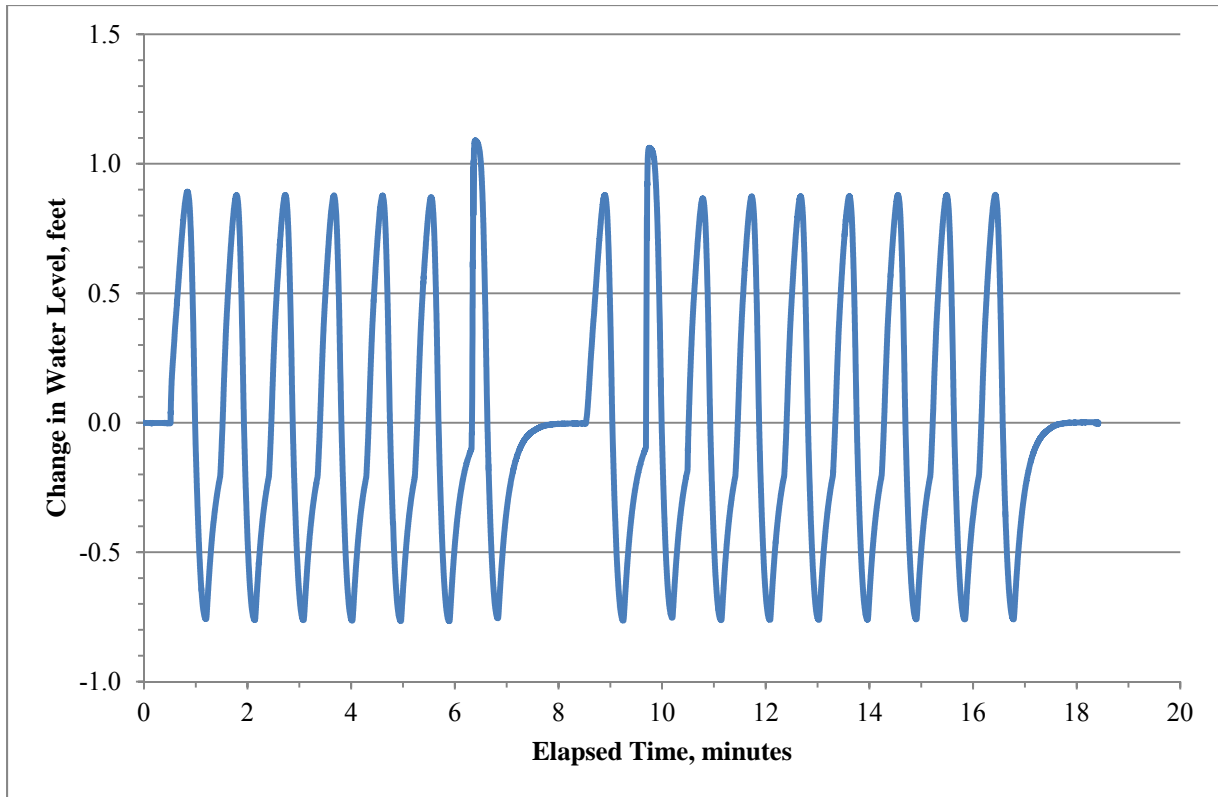


Figure 4.6 Water level response to multiple slug oscillations at control well 534A, including shutdown/recovery periods at approximately 6.9 and 16.8 min of elapsed time.

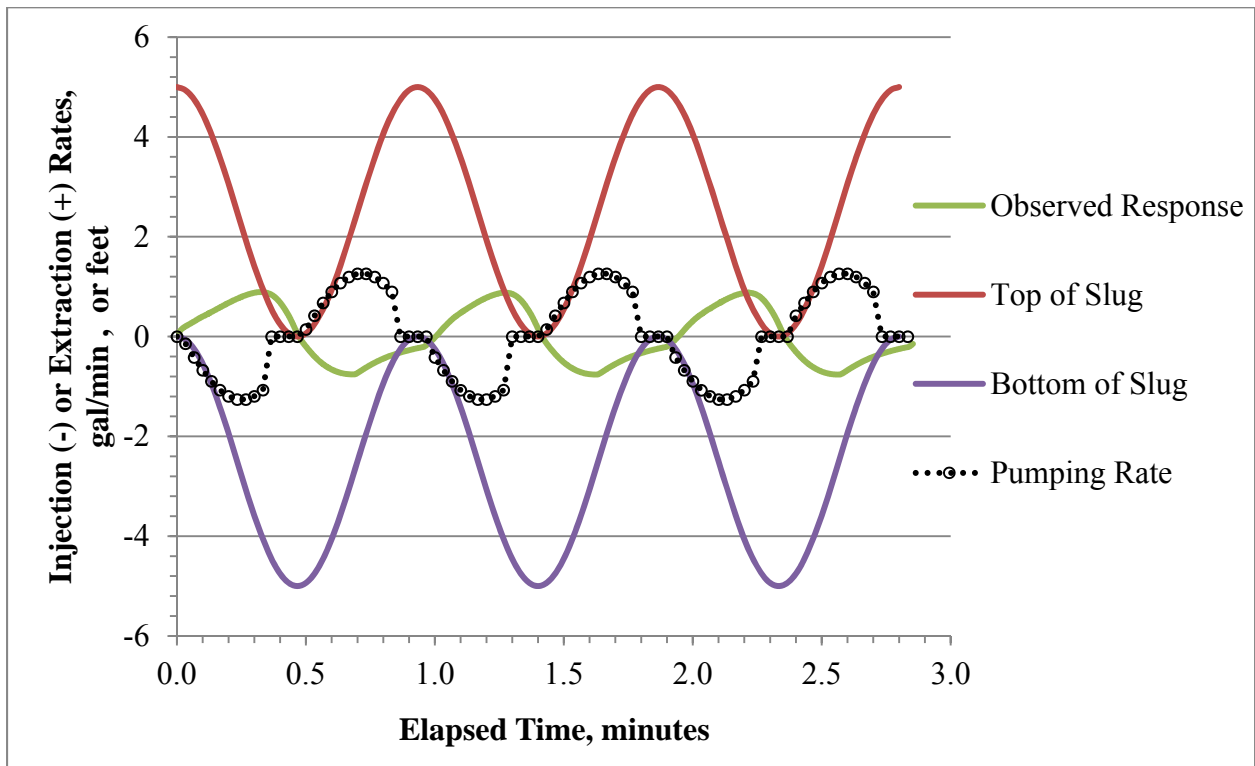


Figure 4.7 Plots of modeled slug movement, recorded water level response, and calculated pumping rates for the first three slug oscillations in control well 531A.

CHAPTER 5

FINDINGS AND CONCLUSIONS

Testing the LNAPL Conceptual Model – Part 1

Part 1 described the North Pool oil body and the basic conceptual model of LNAPL spreading to a stable configuration controlled by the hypothesized mass balance between the spreading of the oil and depletion of the oil. It used the GC and GC/MS analyses of historical oil samples with recently collected oil samples to identify changes in the relative moles of hydrocarbons relative to Pristane and converted those changes to equivalent fractions of mass loss over time, and changes in physical properties of the oil (density, viscosity, and tensions between air, oil, and water fluid pairs). The mass loss assessment accounted for 56 GC-detectable hydrocarbons, many PAH and biomarker compounds quantified by GC/MS, and a small percentage of an unidentified complex mixture (UCM) of compounds based on a mass balance between the physical property test for density and a calculated value for density based on oil composition for 27 samples.

The results were one of two findings that facilitated the assessment of the North Pool mass depletion history. The other finding that allowed estimation of mass depletion rates was how to use an earlier estimate of North Pool oil volume based on 147 core samples from ten locations in the North Pool collected and analyzed during 1990-1992 by the USGS. By subtracting the historical fraction of *mass loss* from unity, one obtains the historical fraction of *mass remaining*, expressed as function of elapsed time since the release occurred in August 1979.

This allows one to equate the mass remaining in 1990-1992 with the total mass of oil in 1990-1992, considered approximately equal to the USGS volume multiplied by the average oil density based the trend of archived oil sample densities. Using the elapsed-time trend of mass losses and mass remaining, along with one total mass estimate for a given date, the starting mass at time zero is readily obtained. Given the starting mass and the trend of mass remaining from time zero to time 33 years (1979-2012), one can calculate the mass remaining with a similar first-order decay regression curve developed from the relative mass-remaining trend to a trend for total mass. Taking the derivative of that expression yields the rate of oil mass change with time. When expressed in convenient units, e.g., kg/day, the rates compare favorably with rates based on CO₂ efflux from the oil body by previous investigations. The conclusion of Part 1 was that the historical rate of mass loss representing an oil-body-wide average mass depletion rate could be used in the mass balance analysis planned in Part 2 of the investigation.

Testing the LNAPL Conceptual Model – Part 2

Part 2 takes the mass loss rates from Part 1 and combines them with the re-delineated North Pool foot print areas to provide mass losses by unit area and time (kg/m²/day), which are used to estimate mass loss rates for two downgradient areas of the oil body for stability testing at the plume- and flowtube-scales. The larger scale encompasses plume areas downgradient of the central part of the North Pool as the leading edge advanced. The smaller scale test focuses on a unit-wide oil flowtubes that widen downgradient in proportion to the larger-scale oil body widening. Flow directions are inferred from historical gauging and mapping of the oil and water tables and mapping of LIF data showing the highest occurrences of oil revealing the pathway of historical migration. The flowtubes start at three baildown test wells in the infiltration area and extend stepwise to the advancing leading edges. Both scales use mapped positions of the leading

edge on seven dates between 1984 and 2012 defined by first occurrences of oil at selected monitoring wells.

Mass inflow to the larger scale downgradient areas and each flowtube was modeled assuming baildown test oil transmissivities at three flowtube-starting wells is found in homogenous medium-grained sand (Strobel et al. 1998) with matrix properties (hydraulic conductivity and three water-retention parameters that correlate with hydraulic conductivity). Model input values for these properties were determined by an inverse parametric analysis (Lundy, 2006) that utilizes the Carsel and Parrish (1988) database, measured fluid properties, and pretest oil thickness to match the oil transmissivity estimated at each baildown test well, which were determined using ASTM (2012) methods and API (2012) software. Historical oil transmissivities at the baildown wells were calculated for a set of elapsed times after the 1979 release, using the fixed matrix properties and changing fluid properties from Part 1 and trend in oil thicknesses from USGS gauging data.

Historical inflow rates were calculated for 12 time steps to represent the period of 1979-2012. These values were calculated using a Darcy equation with changing values for oil transmissivity, oil potentiometric gradient, widths of the downgradient plume or the 1-m wide flowtube scales, and the historical trend estimates of increasing average oil density. At both scales of analysis these mass influx curves exhibit negative slopes on a semilog plot with elapsed time. The plots of mass losses over growing areas for the same time steps and semilog plot exhibit curves less steep negative slope. The intersections of the mass-gain and mass-loss curves for the base case and confidence intervals represent elapsed times when rates of mass inflow and outflow are balanced.

The LNAPL-body scale method of testing produce a 15-yr range of elapsed time (here referred to as a “window of opportunity for stabilization”), equivalent to years 2020-2035, within which there is a 95% chance that the mass balance would be achieved. That range encompassed the site investigation and appears to generally agree with the early time best-fit trend on rate of the leading edge advancement, which began to flatten after 1998 but was still not at an asymptotic level as of 2012. The flowtube-scale method produced a range of elapsed times and dates for each individual flowtube. These ranged from 10 yr (1989) to 55 yr (2034). While the flowtube-scale approach has shortcomings, it suggests that some parts of the leading edge will stabilize at earlier times than other parts – and that the assumption that all points along an advancing leading edge would stop moving together is unsupportable. Neither analysis accounts for additional mass pumped from two wells in the North Pool during 199-2004, which may have facilitated an earlier stabilization, still not observed with confidence, but which may be proved by continued monitoring efforts over the next 5 years.

The capillary force resistance to entry of oil at the leading edge was evaluated with laboratory-determined matrix and fluid properties and showed that the resistance at the North Pool grew with the degree of oil weathering, observed to be greater at the leading edge than other area. A range critical in-well thickness based on these data and a homogenous medium sand was calculated and supports the notion that the leading edge should advance in a complex pattern of fingering at small scales, that would agree with the flowtube-scale testing. However, it was concluded that while resistance is theoretically important, it is not as useful in estimating when and where the leading edge stabilizes as the mass balance tests.

Periodic Oscillating Slug Test Method

The objective of this investigation was to field test the idea of using an oscillating solid slug to generate sinusoidal pumping (periodic injection/extraction rates) in a control well, to record the propagating sine-wave response in observation wells, and use those data to estimate aquifer properties that would be compared to aquifer properties determined by a longer-term conventional pumping test.

The device was designed, constructed and tested locally in Georgia, then shipped to the USGS research site where the North Pool investigation was carried out. Trial testing was performed at a cluster of shallow monitoring wells located approximately 50 m downgradient of the North Pool. Oscillatory movement of the solid slug in and out of the water in a control well was converted to an equivalent series of pumping steps approximately on a 2-s frequency. The sine wave created at the control well by the oscillating slug propagated to two nearby observation wells and recorded with transducer-loggers. The timing and amplitudes of the wave at the observation wells were inferred from the response after some filtering of background noise.

The aquifer transmissivity and storativity values were determined using commercial software for aquifer test analyses (Duffield, 2007). Assuming the water table aquifer at the site would behave as a confined aquifer in early time, the solutions of Theis (1935) and Dougherty and Babu (1996) were selected in addition to the delayed gravity drainage solution of Neuman (1972), which was used to analyze a 45-hr pumping test conducted by the USGS in the other wells completed in the North Pool area (with screens set below the floating oil).

Transmissivity and storativity values obtained with the oscillating slug device agreed reasonably well with the USGS pumping test results. It was concluded that the device could be

used for obtaining reliable estimates of aquifer parameters in much less time, without pumping and handling large volumes of groundwater, therefore with fewer resources. However, because observation wells must be located near the control well to observe a signal that can be separated from background noise, new observation wells may need to be installed before testing.

Applications of Findings to Other Sites

A growing number of state regulatory programs are updating policies related to LNAPL remediation endpoints, including the notion that an LNAPL body in contact with groundwater that is known to be spreading must be controlled with a remedial response. When exposure points are located near and downgradient of a spreading LNAPL body, environmental professionals increasingly need to determine whether the body is still expanding or has reached a stable configuration. This may include estimating spreading rates to resolve the question of how soon an LNAPL body could reach an identified exposure points such as a well, basement, or surface water boundary, or whether the body is sufficiently stable that further remediation is unnecessary. Based on findings of our study of the history and stability of the North Pool, the application of a mass-balance approach for other LNAPL sites having either new or old releases is addressed below.

A large new release can trigger an emergency response focused on containment and recovery of LNAPL. For that condition, characterizing site conditions to fully assess the risks of exposure by further spreading is not the highest priority, and may not be addressed. Nevertheless, records of the remedial response, including drilling and well logs, fluid recovery pumping rates, or groundwater and LNAPL volumes recovered from multiple wells per day, can be used later to estimate a range of parameter values for making a first-approximation of spreading potential. Older sites with ongoing LNAPL remediation in an area upgradient and near

exposure points or near property lines may need to know if or when remedial actions can be safely discontinued without a resumption of spreading .

Either situation can be addressed using the approach taken here with less data and more conservative assumptions regarding model inputs. Emergency responders can help by observing and recording critical information. At older sites background data on site conditions can be used, starting with the data typically required by regulatory agencies. These will include previous reports with well logs, contour maps of the water table and concentrations of regulated compounds (e.g. benzene), fluid-level records (especially, LNAPL thicknesses in wells), and possibly slug tests and LNAPL baildown tests on selected monitoring wells.

The most relevant and useful information would include a map showing the lateral extent of the LNAPL body, average water table gradients, hydraulic conductivity values for the impacted earth materials, LNAPL transmissivity values, and CO₂ efflux estimates at stations over the LNAPL footprint area. To strictly apply the methods used in the North Pool study, analyses of archived and recently collected LNAPL samples are needed, along with one reliable LNAPL volume estimate in order to calculate the relative mass remaining and from that the actual historical mass loss rates. But, very few sites will have archived samples or reliable volume estimates. Given knowledge of the type of LNAPL released, the analyst has the option of using an assumed composition based on other available records or published data for generic petroleum types, e.g. Huntley and Beckett (2002) and API (2004). In a smaller percentage of cases, records of the release volume will be available, as when a known quantity was lost to the subsurface during an accident. A reliable volume and mass estimate will require a sufficient number of soil cores and fluid saturations from the LNAPL-bearing zone. Knowledge of the spill volume and cumulative volume of LNAPL recovered permits one to make an estimate of

the volume remaining underground. That volume is then used to perform a mass-balance check on the volume estimated with cores and fluid saturation analyses (Lundy et al, 2008).

Based on the North Pool study, in-well LNAPL thickness, transmissivity, mass spreading, and mass depletion can be approximated by first-order decay functions. These trends depend on the LNAPL-bearing strata being “effectively homogeneous” and unconfined, that is, neither perched above the water table, nor confined by overlying low-K strata below the water table (Kirkman et al. 2013). The matrix properties inferred with the parametric analysis of three LNAPL baildown tests requires fluid properties of the LNAPL and the software to perform the analysis. One could use API software to achieve these results, for example Charbeneau (2007) guidance and free LNAPL Distribution and Recovery Model (LDRM) software both downloadable from the API LNAPL Resources website. The following lists provide suggested types of data and analyses one could apply for new and older LNAPL release sites:

Investigation Tasks at New Release Sites

- a) Determine the type of LNAPL released based on release documentation or inventory records, and petroleum products stored/transported on the site.
- b) Collect LNAPL samples from one or more well(s) for physical property analysis (esp. density) to determine the most likely LNAPL type.
- c) Estimate a range of physical properties of the original spill material based on API fluid properties of fresh generic products (gasoline, jet fuel, diesel, home heating oil, bunker C, lubrication oil, or crude oil types).

- d) If a water-table map is not available, infer depth and direction of water-table gradient from USGS topographic maps, assuming a perennial stream elevations approximate the water-table elevations.
- e) Infer type(s) of geologic media likely to be effected from soils maps, previous reports and geologic maps, and site inspection. Estimate a range of hydraulic conductivity values for the LNAPL-bearing zone.
- f) Estimate rate of LNAPL migration and advancement of leading edge using a 1-D solution such as that offered in Mahler et al. (2012b) with conservative worst-case value estimates for model inputs. Use API guidance and software (Charbeneau, 2007) to estimate model inputs, such the average oil saturation of the migrating LNAPL.

Investigation Tasks at Older Release Sites

- a) Use direct sensing tools such as LIF probing near monitoring wells with LNAPL to delineate the extent of LNAPL remaining in the vadose and saturated zones, and use the cumulative signal pattern to locate an area within which most of the LNAPL was released and infiltrated to the water table.
- b) Use historical well measurements to show changing trends with in-well thicknesses, and relate these to LIF signatures and known stratigraphic conditions – variations in grain size distributions – to estimate a starting maximum thickness.
- c) Plot the LNAPL thickness data against elapsed time and fit a first-order decay function to describe the trend, and check it against the maximum based on LIF data.
- d) Perform baildown tests at wells following ASTM (2012) and API (2012) guidance to obtain estimates of LNAPL transmissivity. Collect LNAPL samples at each baildown test wells and analyze fluid properties at these locations. Perform parametric analyses to

estimate ranges of matrix properties; laboratory core matrix properties may not be representative of field-scale parameter values.

- e) Use API guidance and software (Charbeneau, 2007) to estimate LNAPL transmissivities using measured or generic fluid and matrix properties.
- f) If the LNAPL is unconfined and the LNAPL-bearing zone can be represented by an effective homogenous medium obtained with the parametric analysis for each baildown test transmissivity, historical transmissivities can be estimated with historical thickness data and trends.
- g) Collect CO₂ efflux data at a sufficient number of stations over the footprint area to capture the range, and account for background soil respiration (with C¹⁴ or background sample collections).
- h) Use the LNAPL body-scale approach with the Darcy equation (described in Chapter 3) to estimate the mass inflow rate across an area on the downgradient edge of the LNAPL source area, moving into a downgradient LNAPL body area where depletion of mass is occurring.
- i) Estimate the mass balance between mass inflow and outflow. If the outflow exceeds the inflow, the oil body is stable. If the inflow exceeds outflow it is still expanding, and the analyst may estimate the rates and timing of equilibration with the equations in Mahler et al. (2012b) supplemented with parameter input values estimated with free API software (Charbeneau, 2007).

If LNAPL remediation is required to control further migration of the LNAPL, consider using the periodic oscillating slug test method to provide estimates of aquifer transmissivity, storativity, and vertical anisotropy (ratio of hydraulic conductivity in the vertical to horizontal

directions). These parameters can be used with software to design the number, spacing, and pumping rates of the underlying groundwater zone contacting the LNAPL body to capture and control both the LNAPL body and associated groundwater plume. Unlike conventional pumping tests there is no need for pumping, storing, and treating groundwater, and the additional time for permitting the discharge of treated groundwater with a regulatory agency is also avoided.

REFERENCES

API, 1989. *A Guide to the Assessment and Remediation of Underground Petroleum Releases*, API Publ. 1628, 2cd Addition, August 1989, American Petroleum Institute, 1220 L Street, Northwest, Washington, D. C. 20005, 81 pp.

API. 2004. *Interactive LNAPL Guide*, Version 2.0. American Petroleum Institute, Washington, D.C.

API, 2012. A User Guide for the API LNAPL Transmissivity Workbook: A Tool for Baildown Test Analysis, prepared by R. J. Charbeneau, Andrew Kirkman, and Rangaranujam Muthu for the Regulatory & Scientific Affairs Department, American Petroleum Institute, Washington, D.C., 40 pp.

ASTM, 2007. *Standard Guide for Development of Conceptual Site Models and Remediation Strategies for Light Non-Aqueous Phase Liquids Released to the Subsurface*, Publ. E 2531-06, American Society of Testing and Materials, 100 Bar Harbor Drive, New Conshohocken, PA, USA.

ASTM, 2012. *Standard Guide for the Estimation of LNAPL Transmissivity*, E2856-11e1, American Society for Testing and Materials, West Conshohocken, PA.

Bastin, E., 1926. Microorganisms in oilfields, *Science*, vol. 63, pp. 21-24.

Bekins, B. A., F. D. Hostettler, W. N. Herkelrath, G. N. Delin, Ean Warren, and H. I. Essaid, 2005. Progression of methanogenic degradation of crude oil in the subsurface, *Environmental Geosciences*, vol. 12, no. 2, pp. 139-152.

Bennett, P. C., D. E. Siegel, M. J. Baedecker, and M. F. Hult, 1993. Crude oil in a shallow sand and gravel aquifer – II. Inorganic geochemistry, *Applied Geochemistry*, Vol. 8, pp. 529-549.

Bondy, B., G. D. Beckett, and S. Joy. 2006. *Light Non-Aqueous Phase Liquid (LNAPL) Parameters Database User Guide for Data Retrieval*. American Petroleum Institute, Regulatory Analysis and Scientific Affairs Dept., Washington, D. C., Oct. 2006. 13 pp.

Beckett, G.D. and Steven Joy, 2003. Light non-aqueous phase liquid (LNAPL) database, version 2.0, users guide, Publ. 4731, American Petroleum Institute, Washington, D.C., 13pp.

Bouwer, H. (1989) "The Bouwer and Rice Slug Test – An Update," *Ground Water*, Vol. 27, No. 3, pp. 304-309.

Bouwer, H. and R. C. Rice (1976) "A Slug Test for Determining Hydraulic Conductivity of Unconfined Aquifers with Completely or Partially Penetrating Wells," *Water Resources Research*, Vol. 12, No. 3, pp. 423-428.

Chaplin, B.P., G. N. Delin, R. J. Baker, and M. A. Lahvis, 2002. Long-term evolution of biodegradation and volatilization rates in a crude-oil contaminated aquifer. *Bioremediation Jour.*, Vol. 6, pp. 237-255.

Charbeneau, Randall, 2007. *LNAPL Distribution and Recovery Model 1. Distribution and Recovery of Petroleum Hydrocarbon Liquids from Porous Media*, American Petroleum Institute, Publication 4760, January 2007, 53 pp.

Charbeneau, R. J., R. T. Johns, L. W. Lake, and M. J. McAdams III, 1999. *Free-product recovery of petroleum hydrocarbon liquids*, API Publ. 4682, American Petroleum Institute, Washington, D.C.

Cooper, H. H. and C. E. Jacob, 1946. A generalized graphical method for evaluating formation constants and summarizing well-field history, *Amer. Geophys. Union Trans.*, Vol. 27, No. 4, pp. 526-534.

Cooper, H. H., J. D. Bredehoeft, and I. S. Papadopoulos, 1967, Response of a finite-diameter well to an instantaneous charge of water, *Water Resources Research*, Vol. 3, No. 1, pp.263-269.

Cooper H.H., J.D. Bredehoeft, I.S. Papadopoulos, R.R. Bennett, 1965. "The response of well-aquifer systems to seismic waves", *J Geophys. Res.* 70:3915-3926.

de Pastrovich, T. G., V. Barndat, R. Barthel, A. Chiarelli, and D. Fussel, 1979. *Protection of Groundwater from Oil Pollution*, CONCAWE, the Hague, Netherlands, 61 pp.

Delin, G. N. and W. N. Herkelrath, 2014. Effects of dual-pump crude-oil recovery system, Bemidji, Minnesota, USA, *Groundwater Monitoring & Remediation*, Vol. 34, Issue 1, pp. 57-67.

Dillard, L. A., H. I. Essaid, and W. N. Herkelrath, 1997. Multiphase flow modeling of a crude-oil site with a bimodal permeability distribution, *Water Resources Research*, Vol. 33, No. 7, pp. 1617-1632.

Dougherty DE, DK Babu, 1984. "Flow to a partial penetrating well in a dual porosity reservoir", *Water Resources Research* 20(8)1116-1122.

Duffield GM, 2007. *User Guide for AQTESOLV Pro*, v. 4.5, HydroSOLVE, Inc., Herndon VA.

Durnford, D., J. Bookman, J. Billica, and J. Milligan. 1991. LNAPL Distribution in a Cohesionless Soil: a Field Investigation and Cryogenic Sampler. *Groundwater Monitoring and Remediation*, Vol. 11, No. 3, Summer, pp. 115-122.

Essaid, Hedeff I., B. A. Bekins, W. N. Herkelrath, and G. N. Delin, 2011. Crude oil at the Bemidji Site: 25 years of monitoring, modeling, and understanding, *Ground Water*, Vol. 40, No. 5, pp. 706-726.

Eganhouse, R. A., M. J. Baedecker, I. M. Cozzarelli, G. R. Aiken, and K. A. Thorn, 1993. Crude oil in a shallow sand and gravel aquifer – II. Organic geochemistry, *Applied Geochemistry*, Vol. 8, pp. 551-567.

Farr, A. M., R. J. Houghtalen, D. McWhorter (1990) “Volume Estimation of Light Non-aqueous Phase Liquids in Porous Media,” *Ground Water*, Vol. 28, No.1, pp. 48-56.

Ferris JG, 1951. “Cyclic fluctuations of water level as a basis for determining aquifer transmissibility”, *Internat. Union Geodesy & Geophysics, Asso. Sci. Hydrology Assembly. Brussels*, 2:148-155, Duplicate as U.S. Geological Survey Ground Water Note 1 (1952).

Ferris JG, DB Knowles, RH Brown, RW Stallman, 1962. *Ground-Water Hydraulics*, Water-Supply Paper 1536-E, U.S. Geological Survey, Denver CO.

Freeze, A. R. and J. A. Cherry, *Groundwater*, Prentice-Hall, Inc., Englewood Cliffs, New Jersey, 604 pp.

Head, Ian M., D. Martin Jones, and Steve R. Larter, 2003. Biological activity in the deep subsurface and the origin of heavy oil, *Nature*, vol. 426, pp. 344-352.

Hult, M. F., 1984. Ground-water contamination by crude oil at the Bemidji, Minnesota research site – and introduction, Ground-water contamination by crude oil at the Bemidji, Minnesota research site: U. S. Geological Survey toxic waste-ground-water contamination study, papers presented at the Toxic-Waste Technical Meeting, Tucson, AZ, Mar. 20-22, 1984.

Huntley, David, and G.D. Beckett, 2002. *Evaluating Hydrocarbon Removal from Source Zones and its Effect on Dissolve Plume Longevity and Magnitude*, American Petroleum Institute Publ. 4715, API Publishing Co., 1220 L Street, Washington, D.C. 20005.

Herkelrath, W.N., 1999, Impacts of remediation at the Bemidji oil-spill site, in Morganwalp, D.W. and H.T. Buxton, eds., USGS Toxics Substances Hydrology Program – Proceedings of Technical Meeting, Charleston, S.C., March 8-12, Vol. 3 of 3 – Subsurface Contamination from Point Sources: USGS Water Resources Investigation 99-4018C, pp. 195-200.

Herkelrath, W. N., 2014. Personal communication, oil saturation and porosity data based on laboratory analysis of 142 core samples collected from the North Pool during field seasons of 1990-1992, unpublished USGS data provided to our research team.

Hess, K. N., W. N. Herkelrath, H. I. Essaid, 1992. Determination of subsurface fluid contents at a crude-oil spill site, *Journal of Contaminant Hydrology*, v. 10, pp. 75-96.

Hvorslev MJ, 1951, *Time Lag and Soil Permeability in Ground-Water Observations*, Bulletin 36,

U.S. Army Corps of Engineers, Waterways Experiment Station, Vicksburg MS.

Hult, M. F., 1984. Ground-water contamination by crude oil at the Bemidji, Minnesota research site – and introduction, Ground-water contamination by crude oil at the Bemidji, Minnesota research site: U. S. Geological Survey toxic waste-ground-water contamination study, papers presented at the Toxic-Waste Technical Meeting, Tucson, AZ, Mar. 20-22, 1984.

ITRC, 2009. Evaluating Natural Source Zone Depletion at Sites with LNAPL, prepared by the Interstate Technology and Regulatory Council LNAPL team, 444 No. Capital St., Suite 445, Washington, D. C. 20001, 32 pp.

Jacob, C. E. and S. E. Lohman, 1952. Non-steady flow to a well of constant drawdown in an extensive aquifer, Amer. Geophys. Union Trans., vol.33, pp. 559-569.

Johnson, P. C., P. Lundegard, and Z. Liu, 2006. Source zone natural attenuation at petroleum hydrocarbon spill sites: 1. Site-specific assessment approach, Groundwater Monitoring & Remediation, v. 26, no. 4, pp.82-92.

Lenhard, R. J. and J. C. Parker, 1990. Estimation of free hydrocarbon volume from fluid levels in monitoring wells, Ground Water, Vol. 28, No. 1, pp. 57-67.

Lee, Steve, 2012. Personal communication dated 4/18/2012, copies of written correspondence between Lakeland Pipe Line Company and the Minnesota Pollution Control Agency for various dates from late September 1979 to January 1980, reporting updates on groundwater monitoring activities and laboratory results for the Pinewood, MN leak site, M.P. 926.5.

Lundegard, P. D. and P. C. Johnson, 2006. Source zone natural attenuation at petroleum hydrocarbon spill site – II: Application to a former oil field, Groundwater Monitoring & Remediation, v. 26, no. 4, pp.93-106.

Lundy, D.A., 2006. Field measurement of LNAPL mobility and soil properties through parametric analysis of product baildown tests, paper presented at the National Ground Water Association Conference and Exposition on Petroleum Hydrocarbons and Organic Chemicals in Ground Water: Prevention, Detection, and Remediation, Houston, TX, November 6-7, 2006.

Lundy, D.A., J.F. Dowd, B.L. Railsback, and T.C. Rasmussen, 2011. The relationship between lateral spreading and mass depletion for LNAPL in contact with groundwater, abstract and poster presented at the International Symposium on Bioremediation and Sustainable Environmental Technologies, Battelle Memorial Institute, Reno, NV, June 27-30, 2011.

Lundy, D.A. and J.F. Dowd, 2013a. A flowtube discharge and mass depletion model for testing LNAPL source zone stability, abstract and poster presented at the International Symposium on Bioremediation and Sustainable Environmental Technologies, Battelle Memorial Institute, Jacksonville, FL, June 10-13, 2013.

- Lundy, D.A. and J.F. Dowd, 2013b. A Flowtube Discharge and Mass Depletion Model for Testing LNAPL Source Zone Stability at a Crude Oil Pipeline Release Site, abstract and poster presented at the National Tanks Conference and Exposition, Denver, CO, Sept. 16-18, 2013.
- Lundy, D.A. and R. Leather, 2008. On the Development of LNAPL Conceptual Site Models for Risk-Based Decision-Making at Petroleum Hydrocarbon Sites, Paper presented at the National Groundwater Association Conference and Exposition on Petroleum Hydrocarbons and Organic Chemicals in Ground Water: Prevention, Detection, and Remediation, Houston, TX, November 3-4, 2008.
- Lundy, D. A., and L. M. Zimmerman, 1996. Assessing the recoverability of LNAPL plumes for recovery system conceptual design. Presentation and paper included in proceedings of the 10th annual National Outdoor Action Conference and Exposition, National Ground Water Association, Las Vegas, NV. May 13-15, 1996.
- Mace, R.E., R. S. Fisher, D. M. Welch, and S. P. Parra, 1997. Extent, mass, and duration of hydrocarbon plumes from leaking underground storage tank sites in Texas, Bur. Econ. Geol., University of Texas at Austin, Geologic Circular 97-1.
- Mahler, N, T. Sale, and M. Lyverse, 2012a. A mass-balance approach to resolving LNAPL stability, *Ground Water*, Vol. 50, No. 6, pp. 861-871.
- Mahler, N, T. Sale, T. Smith, and M. Lyverse, 2012b. Use of single-well tracer dilution tests to evaluate LNAPL flux at seven field sites, *Ground Water*, Vol. 50, No. 6, pp. 851-860.
- Molins, S., K. U. Mayer, R. T. Amos, and B. A. Bekins, 2009. Vadose zone attenuation of organic compounds at a crude oil spill site – Interactions between biochemical reactions and multicomponent gas transport. *Jour. Contaminant Hydrology*, 112, pp. 15-29.
- Mualem, Y., 1976. A new model for predicting the hydraulic conductivity of unsaturated porous media, *Water Resources Research*, Vol. 12, pp. 513-522.
- National Research Council, 1993. *Ground Water Vulnerability Assessment: Predicting Relative Contamination Potential Under Conditions of Uncertainty*. Washington, D.C.: National Academy Press.
- Neuman, S.P., 1972. Theory of flow in unconfined aquifers considering delayed response of the water table, *Water Resources Research* 8:1031-1045.
- Neuman, S.P., 1974. Effect of partial penetration on flow in unconfined aquifers considering delayed gravity response, *Water Resources Research* 10(2):303-312.
- Palaia, T., J.L. Gentry, R.A. Rewey, and J. Zimbron. 2013. Integration of Dye Tracing and Carbon Dioxide Trap Analyses for LNAPL Remediation Assessment, abstract and presentation at the International Symposium on Bioremediation and Sustainable Environmental Technologies, Battelle Memorial Institute, Jacksonville, FL, June 10-13, 2013.

Parker, J.C., R. J. Lenhard, T. Kuppusamy, 1987. "A Parametric Model for Constitutive Properties Governing Multiphase Flow in Porous Media." *Water Resources Research*, Vol. 23, No. 4, pp. 618-624.

Peters, K. E. and Moldowan, J. E., 1993. *The Biomarker Guide: Interpreting Molecular Fossils in Petroleum and Ancient Sediments*, Prentice Hall, Englewood Cliffs, N. J.

Pfannkuch, H. O., 1979. Interim report and recommendations on monitoring program for site M.P. 926.5, unpubl. consultant report for Lakehead Pipe Line Company, Inc.

Pickens J.F., G.E. Grisak, J.D. Avis, D.W. Belanger, 1987. Analysis and interpretation of borehole hydraulic tests in deep boreholes: Principles, model development, and applications, *Water Resources Research* 23(7):1341-1375.

Rasmussen T.C., L.A. Crawford, 1997. Identifying and removing barometric pressure effects in confined and unconfined aquifers, *Ground Water* 35(3):502-511.

Rasmussen T.C., K.G. Haborak, MH Young, 2003. Estimating aquifer hydraulic properties using sinusoidal pumping at the Savannah River site, South Carolina, USA, *Hydrogeology Journal* 11:466-482, DOI 10.1007/s10040-003-0255-7.

Rasmussen T.C., T.L. Mote, 2007. Monitoring surface and subsurface water storage using confined aquifer water levels at the Savannah River Site, USA, *Vadose Zone Journal* 6(2):327-335.

Rice, D. W., R. G. Grose, J. C. Michaelsen, B. P. Doohar, D. H. MacQueen, S. J. Cullen, W. E. Kastenber, L. G. Everette, and M. A. Marino, 1995. California Underground Leaking Fuel Tank (LUFT) Historical Case Analyses," Report submitted to the California State Water Resources Control Board and Senate Bill 1764 Advisory Committee, Nov. 16, 1995.

Sale, T. 2001. *Methods for Determining Inputs to Environmental Petroleum Hydrocarbon Mobility and Recovery Models*. American Petroleum Institute, Regulatory and Scientific Affairs, Washington, D. C., Publ. No. 4711, July 2001, 66 pp.

Schwille, F., 1967. Petroleum contamination of the subsoil – a hydrological problem, *The Joint Problems of the Oil and Water Industries*, ed. Peter Hepple, Elsevier, Amsterdam, pp. 23-53.

Schulze-Makuch D, DA Carlson, DS Cherkauer, P Malik, 1999. "Scale dependency of hydraulic conductivity in heterogeneous media", *Ground Water* 37(6):904-919.

Sihota, N.J., O. Singurindy, and K. Ulrich Mayer. 2011. CO₂-Efflux Measurements for Evaluating Source Zone Natural Attenuation Rates in a Petroleum Hydrocarbon Contaminated Aquifer, *Environ. Sci. Technol.*, v. 45, pp. 482-488.

Sihota, N.J. and K. Ulrich Mayer. 2012. Characterizing Vadose Zone Hydrocarbon Biodegradation Using Carbon Dioxide Effluxes, Isotopes, and Reactive Transport Modeling, *Vadose Zone Jour.*, doi.10-2136, vzt2011.0204, Soil Science Soc. Amer., Madison, WI, 14 pp.

Sihota, N. J. 2013. Personal communication. Provided copies of files with results of CO₂ efflux measurements over the North Pool and vicinity during the summer field seasons of 2010-2012.

Siegel, D. I. and D. A. Franzi, 1984. Inorganic geochemistry of groundwater and sediments in an aquifer contaminated by crude oil: preliminary results and project plan, Chapter G in *Ground-Water Contamination by Crude Oil at the Bemidji, Minnesota Research Site: U.S. Geol. Survey Toxic Waste—Ground-water Contamination Study, Water Resources Investigations Report 84-4188*, pp. 87-96.

Stumm, Werner and James J. Morgan, 1970. *Aquatic Chemistry, an Introduction Emphasizing Chemical Equilibria in Natural Waters*, Wiley-Interscience a Division of John Wiley & Sons, Inc., 583 pp.

Strobel, M. L., G. N. Delin, and C. J. Munson, 1998. Spatial variation of saturated hydraulic conductivity of sediments at the crude-oil spill site near Bemidji, Minnesota, Water Resources Investigations Report 98-4053, U. S. Geological Survey, Mounds View, MN, 13 pp.

Theis C.V., 1935. The relation between the lowering of the piezometric surface and the rate and duration of the discharge of a well using groundwater storage, *Trans. Amer. Geophys. Union* 16:519-524.

Thorn, K. A. and G. R. Aiken, 1998. Biodegradation of crude oil into nonvolatile organic acids in a contaminated aquifer near Bemidji, MN, *Organic Geochemistry*, vol. 29, no. 4, pp. 909-931.

Toll N.J., T.C. Rasmussen, 2007. Removal of barometric pressure effects and Earth tides from observed water levels, *Ground Water* 45(1):101-105.

van Genuchten, M.T., 1980. A closed-form equation for predicting the hydraulic conductivity of unsaturated soils," *Soil Sci. Soc. Amer. Jour.* Vol. 44, pp. 892-898.

Wright, H. E., Jr., 1972. Physiography of Minnesota in *Geology of Minnesota*, Sims, P. K. and Morey, G. B., eds., a centennial volume: Minnesota Geological Survey, p. 561-578.

Young M.H., T.C. Rasmussen, F.C. Lyons, K.D. Pennell, 2002. Optimized system to improve pumping rate stability during aquifer tests, *Ground Water* 40(6):629-637.

Zhu, Junlin, J. C. Parker, D. A. Lundy, and L. M. Zimmerman, 1993. Estimation of soil properties and free product volume from baildown tests, Proceedings of the 1993 NGWA/API Petroleum Hydrocarbons and Organic Chemicals in Ground Water: Prevention, Detection, and Remediation, Houston, TX. November 1993.

Appendix A - List of Gas Chromatograph (GC) Peak Compounds

No.	Peak ID	Compound ID	Formula	Molar Mass (gm/mole)	Mass Density (gm/mL)
1	nC4	Butane	C4H10	58.12	0.583
2	iC5	Isopentane (2-methylbutane)	C5H12	72.15	0.616
3	nC5	Pentane	C5H12	72.15	0.626
4	MTBE	Methyltertiarybutylether	C5H12O	88.15	0.7404
5	2 M Pent	2 Methylpentane	C6H14	86.18	0.653
6	nC6	C6 alkane (?)	C6H14	86.18	0.6548
7	C6 Olefin a	C6 Olefin a	C6H12	84.16	0.673
8	C6 Olefin b	C6 Olefin b	C6H13	84.16	0.673
9	C6 Olefin c	C6 Olefin c	C6H14	84.16	0.673
10	2,4 DMP	2,4 Dimethylpentane	C7H16	100.28	0.67
11	Bnz	Benzene	C6H6	78.11	0.8786
12	Isooctane	Isooctane = 2,2,4 Trimethylpentane	C8H18	114.18	0.692
13	nC7	Heptane	C7H16	100.2	0.6795
14	MCHX	Methylcyclohexane	C6H14	98.19	0.77
15	Tol	Toluene	C7H8	92.14	0.87
16	nC8	Octane	C8H18	114.23	0.706
17	EB	Ethylbenzene	C8H10	106.17	0.8665
18	m/p-xyl	m/p Xylene	C8H10	106.17	0.87
19	o-xyl	o Xylene	C8H10	106.17	0.86
20	nC9	Nonane	C9H20	128.26	0.718
21	1,2,4 TMB	1,2,4 Trimethylbenzene	C9H12	120.19	0.8761
22	nC10	Decane	C10H22	142.28	0.73
23	nC11	Undecane	C11H24	156.31	0.74
24	Naph	Naphthalene	C10H8	128.17	1.14
25	nC12	C13 Isoprenoid	C13H28	0.00	0.00
26	IP13	C14 Isoprenoid	C14H30	0.00	0.00
27	IP14	1 Methylnaphthalene	C11H10	142.2	1.001
28	nC13	Tridecane	C13H28	184.36	0.756
29	IP15	Acenaphthalene	C12H8	152.19	0.8987
30	nC14	Acenaphthene	C12H10	154.21	1.222
31	IP16	Pentadecane	C15H32	212.41	0.769
32	nC15	Fluorene	C13H10	166.223	1.202
33	nC16	Hexadecane	C16H34	226.44	0.77
34	IP18	Norpristane	C18H38	254.49	0.775
35	nC17	Heptadecane	C14H10	178.23	1.18
36	Pristane	2,6,10,14-tetramethylpentadecane	C19H40	268.52	0.783
37	nC18	Octadecane	C18H38	254.49	0.777
38	Phytane	Phytane	C20H42	282.55	0.791
39	nC19	Nonadecane	C19H40	268.49	0.789
40	nC20	Eicosane	C20H42	282.65	0.789
41	nC21	Heneicosane	CH3(CH2) ₁₉ CH 3	296.5742	0.795
42	nC22	Docosane	C22H46	310.60	0.798

No.	Peak ID	Compound ID	Formula	Molar Mass (gm/mole)	Mass Density (gm/mL)
43	nC23	Tricosane	C23H48	324.63	0.800
44	nC24	Tetracosane	C24H50	338.65	0.803
45	nC25	Pentacosane	C25H52	352.68	0.805
46	nC26	Hexacosane	C26H54	366.71	0.806
47	nC27	Heptacosane	C27H56	380.73	0.808
48	nC28	Octacosane	C28H58	394.76	0.810
49	nC29	Nonacosane	C29H60	408.79	0.811
50	nC30	triacontane	C30H62	422.81	0.813
51	nC31	Hentriacontane	C31H64	436.84	0.814
52	nC32	Dotriacontane	C32H66	450.87	0.815
53	nC33	Tritriacontane	C33H68	464.89	0.817
54	nC34	Tetracontane	C34H70	478.92	0.818
55	nC35	Pentatriacontane	C35H72	492.95	0.819
56	nC36	Hexatriacontane	C36H74	506.97	0.820
57	nC37	Heptatriacontane	C37H76	521.00	0.821
58	nC38	Octatriacontane	C38H78	535.03	0.822
59	nC39	Nonatriacontane	C39H80	549.05	0.823
60	nC40	Tetracontane	C40H82	563.08	0.823
Average MW and Density				248.89	0.812

Sources of data in table:

GC Peak Compound IDs from Torkelson Geochemistry, Tulsa, OK, which performed all GC analyses.

Physical properties for C4 to C17 compounds from various websites; properties for selected C13 and C14 compounds and all C18 to C25 alkanes calculated using expressions found in Riazi and Al-Sahhaf (1995).

Reference Cited

Riazi, M. R. and Al-Sahhaf, T. A., 1995. Physical properties of n-alkanes and n-alkylhydrocarbons: application to petroleum mixtures. Ind. Eng. Chem. Res., 34, 4145-4148.

Appendix B

List of Compounds that were Identified and Quantified with the GC/MS Analyses

No.	<u>PAH Compounds</u>	Formula	Molar Mass (gm/m)	Density (gm/ml)	Well 411 (ng/mg) Q	Well 423 (ng/mg) Q	Well 521 (ng/mg) Q	
1	cis/trans Decalin	C10H18	138.25	0.8965	838	688	838	
2	C1-Decalins	C10H19N	153.27	0.8699	1315	1108	1331	
3	C2-Decalins				1099	914	1101	
4	C3-Decalins				981	808	962	
5	C4-Decalins				820	724	835	
6	Naphthalene	C10H8	128.19	0.9625	511	437	357	
7	C1-Naphthalenes			1.14	1123	940	823	
8	C2-Naphthalenes				1955	1630	1622	
9	C3-Naphthalenes				1609	1329	1482	
10	C4-Naphthalenes				795	687	824	
11	Benzothiophene	C8H6S	134.2	1.14	42.1	34.3	39.6	
12	C1-Benzothiophenes				80.3	66.8	73.3	
13	C2-Benzothiophenes				124	102	102	
14	C3-Benzothiophenes				256	211	228	
15	C4-Benzothiophenes				173	141	162	
16	Biphenyl	C12H10	154.21	1.04	82.5	72.2	62.2	
17	Acenaphthylene	C12H8	152.19	0.8987	13.8	12	11.8	
18	Acenaphthene	C12H10	154.21	1.222	15.1	11.8	9.5	J
19	Dibenzofuran	C12H8O	168.19	1.0886	55.6	52	54.6	
20	Fluorene	C13H10	166.223	1.202	109	88.9	86.6	
21	C1-Fluorenes				227	194	209	
22	C2-Fluorenes				381	331	392	
23	C3-Fluorenes				466	389	455	
24	Carbazole	C12H9N	167.206	1.301	5.9	4.9	3.9	J
25	Anthracene	C14H10	178.23	0.969	21.1	31.1	37.8	
26	Phenanthrene	C14H10	178.23	1.18	197	136	138	
27	C1-Phenanthrenes/Anthracenes				532	400	457	
28	C2-Phenanthrenes/Anthracenes				687	532	643	
29	C3-Phenanthrenes/Anthracenes				605	488	593	
30	C4-Phenanthrenes/Anthracenes				332	282	330	
31	Dibenzothiophene	C12H8S	184.26	1.252	277	232	241	
32	C1-Dibenzothiophenes				538	428	478	
33	C2-Dibenzothiophenes				724	527	611	
34	C3-Dibenzothiophenes				557	428	527	
35	C4-Dibenzothiophenes				272	146	183	
36	Fluoranthene (Benzo(j))Floranthene	C20H12	252.3	1.286	7.7	6.3	7.9	J
37	Pyrene	C16H10	202.25	1.271	9.3	7.2	9.6	J
38	C1-Fluoranthenes/Pyrenes				68.9	57.9	74.1	
39	C2-Fluoranthenes/Pyrenes				91.1	76.1	96.4	
40	C3-Fluoranthenes/Pyrenes				128	85.8	104	
41	C4-Fluoranthenes/Pyrenes				116	89.7	117	

Appendix B conti.

No.	PAH Compounds	Formula	Molar Mass (gm/m)	Density (gm/ml)	Well 411 (ng/mg) Q	Well 423 (ng/mg) Q	Well 521 (ng/mg) Q
42	Naphthobenzothiophene	C16H10S	234.32		80.8	64	81
43	C1-Naphthobenzothiophenes				268	229	283
44	C2-Naphthobenzothiophenes				348	271	330
45	C3-Naphthobenzothiophenes				233	180	213
46	C4-Naphthobenzothiophenes				98.5	72.9	83.3
47	Benz(a)anthracene	C18H12	228.29	1.19	2.2 J	2.7 J	3.9 J
48	Chrysene/Triphenylene	C18H12	228.29		58.2	52.1	69
49	C1-Chrysenes				118	96.6	129
50	C2-Chrysenes				172	139	168
51	C3-Chrysenes				127	103	121
52	C4-Chrysenes				82.9	66.1	80.7
53	Benzo(b)fluoranthene	C20H12	252.309	1.286	4.1 J	2.7 J	3.9 J
54	Benzo(k,j)fluoranthene				0.8 J	0.5 J	0.4 J
55	Benzo(a)fluoranthene				<10 U	<10 U	<10 U
56	Benzo(e)pyrene	C20H12	252.31	1.286	10.3	8.1 J	11.1
57	Benzo(a)pyrene				2.1 J	2.5 J	3 J
58	Perylene	C20H12	252.31	1.286	<10 U	<10 U	<10 U
59	Indeno(1,2,3-c,d)pyrene	C22H12	276.33		<10 U	<10 U	<10 U
60	Dibenzo(a,h)anthracene	C22H14	278.35	1.232	<10 U	<10 U	<10 U
61	C1-Dibenzo(a,h)anthracenes				<10 U	<10 U	<10 U
62	C2-Dibenzo(a,h)anthracenes				<10 U	<10 U	<10 U
63	C3-Dibenzo(a,h)anthracenes				<10 U	<10 U	<10 U
64	Benzo(g,h,i)perylene	C22H12	276.33	1.378	2.2 J	1.7 J	2 J
Average	Total PAHs in ng/mg		199.59	1.15	19848	16220	18293
	Total PAHs in mg/liter at field temp				17959.6	14149.8	16187.2

Appendix B conti.

No.	<u>Biomarker Compounds</u>	Formula	Molar Mass (gm/m)	Density (gm/ml)	Well 411 (ng/mg) Q	Well 423 (ng/mg) Q	Well 521 (ng/mg) Q
	Individual Alkyl Isomers and Hopanes						
1	2-Methylnaphthalene	C11H10	142.2	1.01	1095	919	779
2	1-Methylnaphthalene	C11H10	142.2	1.001	869	726	664
3	2,6-Dimethylnaphthalene	C12H12	156.22	1.01	1027	863	879
4	1,6,7-Trimethylnaphthalene	C13H14	170.25	1.06	314	172	202
5	1-Methylfluorene	C14H12	182.25	1.095	201	161	168
6	4-Methyldibenzothiophene	C13H10S	198.28	1.1	378	289	318
7	2/3-Methyldibenzothiophene	C13H10S	198.28	1.1	295	252	282
8	1-Methyldibenzothiophene	C13H10S	198.28	1.1	101	76.4	88.9
9	3-Methylphenanthrene	C15H12	192.26	1.08	156	133	147
10	2/4-Methylphenanthrene	C15H13	192.26	1.08	255	179	194
11	2-Methylantracene	C15H14	192.26	1.08	3.3	2.9	4
12	9-Methylphenanthrene	C15H15	192.26	1.08	286	200	237
13	1-Methylphenanthrene	C15H16	192.26	1.08	160	132	158
14	3,6-Dimethylphenanthrene	C16H14	206.28	1.1	65.1	59.6	54
15	Retene	C18H18	234.33	1.105	74.4	67.2	78.5
16	2-Methylfluoranthene	C17H12	216.28	1.09	4.6	3.5	3.8
17	Benzo(b)fluorene	C17H12	216.28	1.09	14.2	11.4	14.1
18	C29-Hopane	C29H50	398.7	1.15	201	181	246
19	18a-Oleanane				<10	<10	<10
20	C30-Hopane	C30H52	412.73	1.15	293	264	336
21	C20-TAS	C26 to C29			11.4	7.3	10.8
22	C21-TAS				19.2	15.8	20.2
23	C26(20S)-TAS				4.3	3.8	5
24	C26(20R)/C27(20S)-TAS				18.8	16.5	20.8
25	C28(20S)-TAS				33.4	27.4	35
26	C27(20R)-TAS				12	9.4	12.1
27	C28(20R)-TAS				25.7	21	27.1
	Total Biomarkers, ng/mg				5918.8	4793.8	4981.9
	Total Biomarkers, mg/liter	Averages	212.31	1.08	5355.7	4182	4408.5

Appendix C -- GC Peak Moles Normalized to 1 Mole of Pristane in Oil Samples

Sequence:		1	2	3	4	5	6	7	8	9	10	11	12
		Reference	C1108A	C1108C									
Peak No.	Sample Id	Pipeline #3 4-10-84	Well 604A 6-28-89	(18.4) V 7-20-11	(20.4) V 7-20-11	604A 6-21-12	Well 315 7-24-10	Well 315 6-23-11	C-1009-A	Well 411 6-28-89	Well 411 7-28-10	Well 422	C-1056-A
1	nC4	3.216	0.639	0.000	0.001	0.006	0.006	0.005	0.001	0.261	0.003	0.004	0.000
2	iC5	2.783	1.483	0.005	0.100	0.080	0.135	0.140	0.032	0.772	0.059	0.063	0.014
3	nC5	3.657	2.081	0.002	0.140	0.001	0.037	0.010	0.001	1.112	0.007	0.037	0.033
4	MTBE	0.000	0.000	0.000	0.000	0.000	0.000	0.000	0.000	0.000	0.000	0.000	0.000
5	2M Pentane	1.857	1.473	0.006	0.447	0.008	0.185	0.052	0.010	1.013	0.038	0.122	0.142
6	nC6	2.981	2.341	0.003	0.267	0.000	0.019	0.001	0.004	1.692	0.001	0.088	0.298
7	olefin a	0.000	0.003	0.000	0.000	0.000	0.000	0.000	0.000	0.003	0.000	0.001	0.000
8	olefin b	0.000	0.003	0.000	0.000	0.000	0.000	0.000	0.001	0.002	0.000	0.000	0.001
9	olefin c	0.000	0.000	0.000	0.000	0.004	0.002	0.000	0.000	0.000	0.004	0.004	0.000
10	2,4 DMP	0.101	0.088	0.027	0.056	0.043	0.060	0.068	0.042	0.072	0.027	0.026	0.023
11	Bnz	0.582	0.376	0.010	0.044	0.022	0.108	0.093	0.016	0.275	0.029	0.028	0.037
12	Isooctane	0.012	0.005	0.000	0.001	0.005	0.008	0.004	0.001	0.000	0.000	0.006	0.000
13	nC7	2.752	2.393	0.003	0.522	0.000	0.001	0.002	0.008	2.085	0.003	0.227	0.748
14	MCHX	2.900	2.426	1.510	2.089	1.780	2.151	2.431	1.851	2.203	1.239	1.147	1.268
15	Tol	1.338	0.454	0.000	0.000	0.000	0.011	0.000	0.007	0.167	0.010	0.007	0.012
16	nC8	2.297	2.108	0.301	0.774	0.000	0.012	0.381	0.009	1.946	0.004	0.449	0.504
17	EB	0.352	0.405	0.331	0.469	0.130	0.365	0.436	0.308	0.772	0.472	0.385	0.302
18	m/p-xyl	1.213	0.875	0.782	1.080	0.628	0.955	1.108	0.843	0.900	0.643	0.437	0.643
19	o-xyl	0.667	0.514	0.066	0.287	0.046	0.044	0.167	0.047	0.511	0.046	0.056	0.038
20	nC9	2.614	2.323	0.242	0.903	0.286	0.292	0.271	0.296	2.210	0.293	0.697	0.485
21	1,2,4 TMB	1.311	1.094	1.164	1.221	0.999	1.140	1.315	1.188	1.061	1.053	0.783	1.049
22	nC10	2.044	1.976	0.089	0.371	0.043	0.092	0.100	0.106	1.920	0.126	0.492	0.157
23	nC11	2.012	2.038	0.222	0.204	0.411	0.167	0.059	0.154	2.004	0.151	0.466	0.166
24	Naph	0.207	0.363	0.240	0.296	0.325	0.364	0.274	0.373	0.366	0.355	0.324	0.337
25	nC12	1.866	1.892	0.277	0.268	0.211	0.181	0.253	0.174	1.839	0.182	0.326	0.204
26	IP13	0.706	0.656	0.633	0.618	0.619	0.678	0.659	0.705	0.657	0.690	0.658	0.692
27	IP14	0.510	0.580	0.602	0.579	0.513	0.607	0.624	0.622	0.505	0.617	0.587	0.589
28	nC13	1.712	1.758	0.125	0.119	0.052	0.152	0.123	0.106	1.591	0.109	0.104	0.090
29	IP15	0.561	0.689	0.660	0.638	0.678	0.714	0.673	0.746	0.701	0.726	0.698	0.715
30	nC14	1.788	1.866	0.335	0.328	0.324	0.383	0.341	0.386	1.801	0.378	0.199	0.333
31	IP16	0.769	0.896	0.732	0.709	0.642	0.788	0.738	0.712	0.921	0.723	0.782	0.690
32	nC15	1.611	1.833	0.160	0.136	0.152	0.181	0.142	0.180	1.798	0.186	0.177	0.171
33	nC16	1.314	1.476	0.078	0.007	0.044	0.049	0.021	0.108	1.368	0.047	0.051	0.041
34	IP18	0.818	0.863	0.761	0.760	0.717	0.728	0.784	0.727	0.858	0.731	0.765	0.721
35	nC17	1.296	1.397	0.022	0.087	0.038	0.034	0.064	0.039	1.306	0.034	0.052	0.045
36	Pristane	1.000	1.000	1.000	1.000	1.000	1.000	1.000	1.000	1.000	1.000	1.000	1.000
37	nC18	1.207	1.193	0.065	0.073	0.000	0.056	0.066	0.071	1.100	0.068	0.065	0.020
38	Phytane	0.762	0.837	0.814	0.824	0.746	0.783	0.854	0.856	0.831	0.838	0.818	0.766
39	nC19	1.047	1.098	0.045	0.064	0.059	0.073	0.048	0.070	0.998	0.052	0.069	0.054
40	nC20	0.842	0.993	0.073	0.082	0.152	0.113	0.073	0.094	0.823	0.115	0.102	0.119
41	nC21	0.845	0.894	0.020	0.038	0.112	0.017	0.022	0.008	0.713	0.014	0.049	0.070
42	nC22	0.743	0.769	0.036	0.044	0.087	0.022	0.016	0.050	0.583	0.010	0.056	0.014
43	nC23	0.643	0.638	0.032	0.018	0.030	0.021	0.028	0.014	0.486	0.023	0.029	0.011
44	nC24	0.610	0.621	0.038	0.034	0.069	0.038	0.032	0.081	0.425	0.072	0.000	0.047
45	nC25	0.664	0.595	0.145	0.131	0.135	0.109	0.145	0.118	0.384	0.121	0.130	0.117
46	nC26	0.498	0.502	0.073	0.088	0.072	0.019	0.017	0.087	0.377	0.007	0.078	0.093
47	nC27	0.453	0.417	0.030	0.029	0.000	0.047	0.012	0.005	0.294	0.045	0.034	0.050
48	nC28	0.380	0.323	0.046	0.035	0.013	0.009	0.053	0.012	0.240	0.008	0.021	0.008
49	nC29	0.333	0.232	0.035	0.037	0.016	0.016	0.000	0.013	0.172	0.016	0.024	0.019
50	nC30	0.265	0.160	0.016	0.015	0.040	0.001	0.014	0.030	0.081	0.039	0.048	0.039
51	nC31	0.198	0.055	0.000	0.000	0.018	0.001	0.157	0.000	0.043	0.001	0.000	0.000
52	nC32	0.176	0.042	0.008	0.008	0.009	0.010	0.010	0.004	0.038	0.004	0.003	0.008
53	nC33	0.162	0.045	0.033	0.031	0.021	0.009	0.035	0.009	0.049	0.005	0.007	0.007
54	nC34	0.151	0.014	0.003	0.007	0.061	0.000	0.012	0.003	0.056	0.000	0.060	0.056
55	nC35	0.087	0.011	0.011	0.004	0.005	0.005	0.018	0.001	0.009	0.013	0.013	0.001
56	nC36	0.063	0.005	0.011	0.001	0.001	0.011	0.004	0.012	0.007	0.002	0.013	0.007
57	nC37	0.045	0.010	0.001	0.001	0.007	0.002	0.005	0.009	0.003	0.009	0.002	0.002
58	nC38	0.053	0.001	0.002	0.003	0.003	0.002	0.001	0.002	0.003	0.003	0.009	0.002
59	nC39	0.039	0.003	0.002	0.002	0.001	0.002	0.002	0.001	0.003	0.001	0.001	0.002
60	nC40	0.030	0.002	0.002	0.002	0.001	0.002	0.001	0.004	0.003	0.001	0.002	0.002
Total No. of Moles		59.146	49.824	11.929	16.091	11.466	13.014	13.964	12.355	43.022	11.454	12.876	13.062
Bzn Mole Fraction		0.0098319	0.0075423	0.000798	0.002735	0.00191	0.008301	0.006627	0.001328	0.006383	0.0024991	0.002212	0.002824
GC-Bzn Concn (mg/L)		17.70	13.58	1.44	4.92	3.44	14.94	11.93	2.39	11.49	4.50	3.98	5.08
GC+6 % Bzn Concn (mg/L)		16.70	12.81			3.24	14.10	11.25		10.84	4.24	3.76	
Release Date: 8/20/1979		29087.00		1.35	4.64				2.25				4.80
Date Collected		4/10/84	6/28/89	7/20/11	7/20/11	6/21/12	7/28/10	6/23/11	6/21/11	6/28/89	7/28/10	7/27/10	6/21/11
Years Since Release		4.64	9.86	31.94	31.94	32.86	30.96	31.86	31.86	9.86	30.96	30.96	31.86

Appendix C conti.

13	14	15	16	17	18	19	20	21	22	23	24	25	26
Well 421B	Well 319 Well 306	Well 319 6-23-83	Well 319 6-28-89	Well 319 3-26-08	Well 319 7-28-10	C1112A (24.3) V	C1112A (26.0) V	Well 423 10-30-85	Well 423 6-28-89	Well 423 3-26-08	Well 423 7-28-10	Well 534A 7-28-10	Well 317 7-29-10
0.009	0.004	0.992	0.491	0.000	0.020	0.000	0.001	0.670	0.454	0.075	0.053	0.037	0.032
0.203	0.075	1.899	1.441	0.000	0.312	0.002	0.015	1.466	1.139	0.564	0.466	0.341	0.325
0.198	0.054	2.706	2.124	0.000	0.550	0.004	0.041	2.184	1.596	1.008	0.864	0.627	0.620
0.000	0.000	0.000	0.000	0.000	0.000	0.000	0.000	0.000	0.000	0.000	0.000	0.000	0.000
0.645	0.245	1.710	1.536	0.000	1.002	0.008	0.174	1.565	1.329	1.206	1.056	0.859	0.908
0.207	0.073	2.835	2.523	0.000	1.275	0.014	0.482	2.637	2.093	2.137	1.887	1.350	1.529
0.001	0.001	0.002	0.002	0.000	0.000	0.000	0.000	0.002	0.004	0.002	0.003	0.002	0.003
0.000	0.000	0.001	0.001	0.000	0.003	0.000	0.000	0.001	0.004	0.000	0.000	0.000	0.000
0.003	0.003	0.000	0.001	0.000	0.000	0.000	0.000	0.001	0.000	0.001	0.004	0.003	0.004
0.068	0.044	0.097	0.091	0.000	0.078	0.001	0.029	0.093	0.086	0.089	0.079	0.070	0.075
0.131	0.036	0.639	0.519	0.000	0.264	0.002	0.081	0.532	0.280	0.343	0.296	0.239	0.271
0.006	0.009	0.001	0.001	0.000	0.007	0.000	0.000	0.001	0.002	0.001	0.005	0.005	0.006
0.062	0.115	2.751	2.540	0.001	1.421	0.038	1.466	2.703	2.322	2.632	2.345	1.522	2.055
2.271	1.893	2.641	2.519	0.002	2.451	0.061	1.562	2.619	2.449	2.694	2.437	2.253	2.405
0.012	0.013	1.197	0.400	0.000	0.012	0.016	0.000	1.261	0.818	0.001	0.013	0.012	0.008
0.018	0.149	1.748	2.220	0.049	0.855	0.262	1.894	1.866	2.131	1.802	2.178	1.289	1.987
0.389	0.243	0.508	0.442	0.037	0.442	0.098	0.430	0.462	0.364	0.488	0.378	0.304	0.375
1.013	0.710	1.157	1.053	0.135	1.055	0.265	0.992	1.167	0.918	1.183	0.998	0.835	0.978
0.046	0.051	0.699	0.633	0.059	0.045	0.194	0.514	0.706	0.528	0.683	0.525	0.334	0.466
0.293	0.476	2.598	2.485	0.491	0.603	1.053	2.382	2.620	2.380	2.731	2.442	1.153	1.820
1.147	1.011	1.256	1.188	0.720	1.152	0.797	1.234	1.266	1.090	1.334	1.158	1.022	1.151
0.098	0.349	2.111	2.051	0.622	0.289	1.428	2.012	2.133	2.024	2.231	2.057	1.310	1.890
0.167	0.355	2.087	2.036	0.082	0.188	1.398	1.895	2.106	2.079	2.169	1.963	1.277	1.679
0.362	0.346	0.292	0.271	0.256	0.360	0.263	0.296	0.282	0.358	0.313	0.373	0.352	0.385
0.182	0.333	2.023	1.990	0.222	0.172	1.032	1.104	1.861	1.923	1.778	1.475	1.018	1.124
0.681	0.697	0.634	0.624	0.599	0.676	0.628	0.641	0.612	0.663	0.676	0.673	0.674	0.700
0.609	0.616	0.601	0.597	0.573	0.604	0.540	0.604	0.594	0.582	0.641	0.546	0.597	0.620
0.107	0.212	1.998	1.913	0.110	0.151	0.632	0.818	1.972	1.797	1.320	0.945	0.706	0.665
0.728	0.737	0.660	0.656	0.617	0.723	0.622	0.657	0.650	0.695	0.694	0.712	0.725	0.753
0.381	0.421	2.266	2.241	0.290	0.382	0.883	1.056	2.259	1.877	1.865	1.301	0.987	0.929
0.797	0.802	0.890	0.888	0.691	0.780	0.812	0.863	0.884	0.890	0.926	0.914	0.876	0.924
0.185	0.236	1.820	1.813	0.123	0.184	0.656	0.858	1.817	1.838	1.588	1.433	0.961	0.868
0.046	0.108	1.514	1.517	0.057	0.050	0.244	0.344	1.526	1.476	1.203	0.855	0.651	0.440
0.737	0.727	0.885	0.898	0.793	0.743	0.835	0.862	0.891	0.862	0.929	0.851	0.802	0.848
0.042	0.144	1.361	1.368	0.095	0.046	0.000	0.213	1.369	1.403	0.868	0.682	0.599	0.328
1.000	1.000	1.000	1.000	1.000	1.000	1.000	1.000	1.000	1.000	1.000	1.000	1.000	1.000
0.078	0.119	1.192	1.203	0.067	0.031	0.093	0.132	1.204	1.199	0.727	0.529	0.467	0.258
0.856	0.846	0.803	0.812	0.819	0.766	0.748	0.796	0.814	0.833	0.863	0.833	0.844	0.846
0.087	0.073	1.166	1.298	0.064	0.071	0.039	0.044	1.300	1.092	0.740	0.362	0.331	0.116
0.134	0.128	1.016	1.028	0.136	0.112	0.063	0.050	1.008	0.984	0.348	0.199	0.193	0.102
0.078	0.032	0.907	0.928	0.035	0.009	0.026	0.022	0.915	0.921	0.203	0.112	0.099	0.013
0.061	0.061	0.833	0.851	0.038	0.043	0.032	0.042	0.835	0.809	0.135	0.087	0.079	0.049
0.015	0.040	0.722	0.732	0.000	0.006	0.017	0.000	0.702	0.701	0.082	0.071	0.048	0.020
0.046	0.030	0.642	0.639	0.041	0.045	0.049	0.039	0.639	0.636	0.043	0.055	0.035	0.000
0.124	0.000	0.693	0.702	0.135	0.109	0.000	0.128	0.689	0.677	0.179	0.061	0.000	0.000
0.077	0.077	0.527	0.533	0.077	0.062	0.065	0.088	0.507	0.494	0.116	0.085	0.069	0.075
0.046	0.044	0.466	0.461	0.024	0.040	0.037	0.072	0.431	0.411	0.176	0.073	0.061	0.049
0.006	0.028	0.380	0.360	0.040	0.012	0.047	0.049	0.325	0.312	0.122	0.076	0.055	0.024
0.017	0.024	0.300	0.275	0.073	0.018	0.041	0.045	0.228	0.222	0.103	0.071	0.056	0.019
0.037	0.054	0.186	0.161	0.003	0.031	0.012	0.006	0.119	0.150	0.074	0.021	0.079	0.047
0.008	0.002	0.108	0.095	0.000	0.001	0.014	0.026	0.065	0.044	0.052	0.017	0.009	0.005
0.007	0.006	0.071	0.062	0.005	0.004	0.027	0.027	0.039	0.033	0.037	0.032	0.020	0.017
0.023	0.005	0.067	0.066	0.034	0.015	0.041	0.044	0.052	0.042	0.050	0.038	0.033	0.020
0.000	0.067	0.011	0.008	0.012	0.004	0.011	0.008	0.012	0.058	0.014	0.009	0.006	0.053
0.012	0.005	0.002	0.003	0.007	0.007	0.008	0.002	0.005	0.008	0.011	0.006	0.006	0.001
0.010	0.011	0.002	0.007	0.003	0.005	0.008	0.003	0.001	0.016	0.006	0.013	0.003	0.011
0.002	0.005	0.001	0.003	0.005	0.003	0.005	0.007	0.010	0.003	0.008	0.002	0.004	0.003
0.003	0.002	0.002	0.002	0.002	0.002	0.004	0.003	0.001	0.004	0.002	0.003	0.001	0.004
0.004	0.001	0.003	0.002	0.002	0.002	0.003	0.001	0.002	0.009	0.001	0.001	0.000	0.009
0.002	0.003	0.001	0.001	0.005	0.004	0.001	0.000	0.002	0.002	0.001	0.003	0.006	0.003
14.574	13.953	55.679	52.305	9.253	19.297	15.180	26.155	53.683	49.115	41.271	35.727	27.298	29.915
0.008978	0.002559	0.011477	0.009915	0	0.013677	0.000137	0.003099	0.0099139	0.005708	0.0083071	0.00829	0.0087717	0.009062
16.16	4.61	20.66	17.85	0.00	24.62	0.25	5.58	17.84	10.28	14.95	14.92	15.79	16.31
15.25	4.34	19.49	16.84	0.00	23.22			16.83	9.69	14.11	14.08	14.90	15.39
						0.23	5.26						
7/28/10	7/29/10	6/23/83	6/28/89		7/28/10	6/21/11	6/21/11	10/30/85	6/28/89	3/26/08	7/28/10	7/29/10	
30.96	30.96	3.84	9.86		30.96	31.86	31.86	6.20	9.86	28.62	30.96	30.96	-79.69

Appendix C conti.

27	28	29	30	31	32	33	34	35	36	37	38	39
Well 521	Well 521	Well 420D	Well 420D	Well 420D	6- Well	7- 533D	7- Well	C1103A	C1103A	C1109B	532A	6- Well 312
7-27-10	6-23-11	6-28-89	6-28-89	28-89	420D	29-10	29-10	(27.0) V	(27.5) V	(28.0) V	21-12	6-22-11
		Duplicate	Duplicate	TriPLICATE			C-1051-A					
0.020	0.026	0.055	0.053	0.055	0.028	0.005	0.005	0.001	0.001	0.001	0.002	0.006
0.177	0.228	0.178	0.172	0.178	0.243	0.085	0.049	0.007	0.022	0.000	0.004	0.115
0.288	0.394	0.210	0.204	0.213	0.409	0.167	0.085	0.016	0.053	0.000	0.000	0.243
0.000	0.000	0.000	0.000	0.000	0.000	0.000	0.000	0.000	0.000	0.000	0.000	0.000
0.409	0.545	0.365	0.354	0.369	0.651	0.432	0.147	0.101	0.215	0.001	0.000	0.577
0.443	0.719	0.459	0.447	0.469	0.941	0.717	0.283	0.201	0.399	0.000	0.000	1.094
0.002	0.001	0.002	0.002	0.001	0.002	0.002	0.001	0.001	0.001	0.000	0.000	0.001
0.000	0.000	0.000	0.000	0.000	0.000	0.000	0.002	0.000	0.000	0.000	0.000	0.000
0.004	0.002	0.002	0.002	0.001	0.003	0.003	0.000	0.001	0.001	0.000	0.000	0.002
0.041	0.050	0.042	0.042	0.043	0.060	0.049	0.017	0.021	0.033	0.001	0.000	0.060
0.093	0.133	0.115	0.113	0.120	0.136	0.149	0.043	0.025	0.047	0.002	0.027	0.125
0.001	0.001	0.002	0.003	0.002	0.006	0.004	0.004	0.002	0.004	0.001	0.000	0.007
0.694	0.934	1.170	1.145	1.193	1.379	1.291	0.665	0.743	0.991	0.013	0.001	1.670
1.603	1.801	1.784	1.748	1.793	2.073	1.882	0.798	1.248	1.552	0.149	0.013	2.215
0.006	0.013	0.294	0.289	0.319	0.007	0.011	0.015	0.007	0.001	0.406	0.000	0.015
0.982	1.074	1.750	1.718	1.065	1.494	1.267	1.059	1.257	1.371	0.195	0.015	1.220
0.455	0.239	0.386	0.372	0.154	0.227	0.256	0.382	0.198	0.213	0.251	0.024	0.396
0.548	0.586	0.569	0.561	0.614	0.676	0.714	0.529	0.542	0.580	0.175	0.006	1.037
0.290	0.386	0.496	0.499	0.593	0.363	0.139	0.296	0.435	0.462	0.000	0.024	0.225
1.557	1.660	2.327	2.294	2.419	1.904	1.334	1.705	2.004	2.007	0.732	0.430	1.197
0.871	0.881	0.905	0.911	0.993	0.955	0.994	0.950	0.912	0.905	0.281	0.232	1.239
1.534	1.533	1.933	2.036	2.082	1.722	1.039	1.697	1.858	1.800	0.908	0.826	0.749
1.685	1.633	2.125	2.102	2.084	1.713	0.669	1.821	1.823	1.675	0.948	1.207	0.132
0.342	0.242	0.340	0.338	0.253	0.344	0.342	0.336	0.244	0.237	0.154	0.263	0.288
1.448	1.401	1.951	1.951	2.021	1.306	0.378	1.558	1.361	0.941	0.685	0.860	0.239
0.682	0.632	0.673	0.681	0.634	0.693	0.678	0.666	0.661	0.606	0.624	0.667	0.628
0.597	0.605	0.584	0.602	0.603	0.614	0.591	0.595	0.630	0.586	0.541	0.535	0.594
1.034	1.110	1.797	1.822	1.930	0.928	0.148	1.205	1.023	0.679	0.427	0.477	0.125
0.700	0.638	0.712	0.736	0.659	0.748	0.694	0.700	0.686	0.640	0.609	0.683	0.648
1.148	1.418	1.880	1.924	1.960	1.245	0.330	1.379	1.518	0.947	0.471	0.545	0.331
0.879	0.825	0.803	0.950	0.886	0.932	0.766	0.830	0.909	0.850	0.731	0.778	0.727
1.098	1.144	1.836	1.875	1.805	1.420	0.160	1.461	1.271	0.896	0.239	0.416	0.166
0.685	0.833	1.481	1.478	1.499	0.951	0.062	0.976	0.908	0.490	0.135	0.203	0.088
0.855	0.891	0.864	0.861	0.880	0.852	0.803	0.846	0.915	0.866	0.826	0.847	0.785
0.563	0.609	1.402	1.388	1.352	0.833	0.081	0.823	0.616	0.291	0.128	0.186	0.122
1.000												
0.442	0.503	1.192	1.192	1.184	0.674	0.056	0.605	0.509	0.178	0.081	0.110	0.059
0.872	0.823	0.832	0.825	0.798	0.847	0.800	0.783	0.831	0.797	0.795	0.771	0.804
0.277	0.533	1.096	1.107	1.277	0.553	0.045	0.529	0.608	0.042	0.045	0.064	0.046
0.170	0.257	0.986	0.978	1.002	0.333	0.094	0.238	0.208	0.072	0.063	0.093	0.063
0.066	0.143	0.920	0.914	0.900	0.259	0.008	0.096	0.135	0.028	0.025	0.051	0.025
0.055	0.131	0.792	0.801	0.838	0.176	0.017	0.062	0.120	0.033	0.033	0.096	0.035
0.048	0.114	0.700	0.700	0.700	0.107	0.018	0.051	0.093	0.021	0.019	0.011	0.036
0.040	0.075	0.643	0.650	0.626	0.066	0.040	0.026	0.050	0.027	0.028	0.064	0.031
0.000	0.065	0.616	0.667	0.692	0.066	0.139	0.131	0.185	0.141	0.134	0.123	0.160
0.062	0.117	0.493	0.499	0.512	0.086	0.007	0.057	0.083	0.058	0.028	0.050	0.067
0.053	0.141	0.399	0.418	0.433	0.072	0.040	0.050	0.132	0.011	0.041	0.000	0.032
0.052	0.115	0.299	0.302	0.330	0.068	0.021	0.051	0.092	0.055	0.056	0.028	0.042
0.052	0.123	0.207	0.209	0.253	0.062	0.025	0.057	0.083	0.054	0.068	0.030	0.047
0.013	0.048	0.153	0.141	0.112	0.078	0.042	0.012	0.041	0.004	0.001	0.054	0.007
0.011	0.000	0.035	0.036	0.061	0.009	0.006	0.021	0.026	0.000	0.146	0.029	0.146
0.024	0.033	0.030	0.039	0.038	0.017	0.005	0.037	0.029	0.030	0.013	0.012	0.010
0.033	0.051	0.035	0.047	0.050	0.040	0.025	0.052	0.047	0.042	0.035	0.033	0.037
0.000	0.004	0.065	0.014	0.003	0.051	0.000	0.060	0.011	0.009	0.010	0.069	0.009
0.000	0.005	0.009	0.010	0.004	0.010	0.001	0.011	0.010	0.003	0.003	0.004	0.012
0.011	0.006	0.004	0.008	0.002	0.012	0.008	0.010	0.006	0.002	0.005	0.002	0.002
0.008	0.004	0.003	0.001	0.002	0.007	0.005	0.005	0.009	0.001	0.005	0.005	0.001
0.002	0.002	0.000	0.002	0.004	0.006	0.011	0.004	0.000	0.003	0.001	0.006	0.004
0.003	0.008	0.002	0.004	0.002	0.003	0.001	0.003	0.001	0.002	0.002	0.003	0.001
0.002	0.001	0.002	0.002	0.001	0.000	0.003	0.002	0.002	0.004	0.001	0.003	0.003
25.032	27.494	40.007	40.239	40.064	30.461	18.660	25.884	26.458	22.978	12.273	11.982	19.746
0.003701	0.004848	0.0028742	0.00281219	0.002999071	0.004478	0.00801	0.0016479	0.0009319	0.0020519	0.000155003	0.002238	0.006307
6.66	8.73	5.17	5.06	5.40	8.06	14.42	2.97	1.68	3.69	0.28	4.03	11.35
6.28	8.23	4.88	4.78	5.09	7.60	13.60					3.80	10.71
							2.80	1.58	3.48	0.26		
7/27/10	6/23/11	6/23/89	6/28/89	6/28/29	7/29/10	7/29/10	7/28/2010	6/20/11	6/20/11	6/21/11	6/21/12	
30.96	31.86	9.85	9.86	49.89	30.96	30.96	30.96	31.85	31.85	31.86	32.86	

Appendix D -- Part-1 of GC, PAH, Biomarker, UCM Mass in Grams, Percent, and Fractions Lost.

Table includes results of mass and density estimates of blends of identified compounds. Oil samples are in order of upgradient to downgradient along the regional water table.

Peak No.	Sample Id	GC Compound Fluid Molar Mass and Density		1		2		3		4		5	
		Compound MW, gm/mole	Compound Density, gm/ml	Reference Pipeline #3 4-10-84	Reference Pipeline 4-10-84	Well 604A 28-89	Well 604A 6-28-89	C1108A (18.4) V 7-20-11	C1108A (18.4) V 7-20-11	C1108C (20.4)V 7-20-11	C1108C (20.4)V 7-20-11	604A 6-21-12	604A 6-21-12
				Moles x MW, gm	Compound Mass / Density, ml	Compound Moles x MW, gm	Compound Mass / Density, ml	Compound Moles x MW, gm	Compound Mass / Density, ml	Compound Moles x MW, gm	Compound Mass / Density, ml	Compound Moles x MW, gm	Compound Mass / Density, ml
1	nC4	58.12	0.583	186.892	320.788	37.129	63.729	0.018	0.031	0.069	0.119	0.360	0.617
2	iC5	72.15	0.616	200.784	325.948	107.004	173.708	0.352	0.572	7.224	11.727	5.765	9.359
3	nC5	72.15	0.626	263.877	421.528	150.139	239.839	0.115	0.184	10.094	16.124	0.083	
4	MTBE	88.15	0.7404										
5	2M Pentane	86.18	0.653	160.026	245.062	126.958	194.422	0.511	0.783	38.556	59.045	0.684	1.047
6	nC6	86.18	0.6548	256.932	392.382	201.720	308.064	0.233	0.356	23.032	35.175	0.012	0.018
7	olefin a	84.1596	0.673	0.000	0.000	0.257	0.381	0.000	0.000	0.026	0.039	0.023	0.035
8	olefin b												
9	olefin c												
10	2,4 DMP	100.277	0.67	10.173	15.184	8.829	13.178	2.750	4.104	5.633	8.407	4.297	6.414
11	Bnz	78.11	0.8786	45.422	51.698	29.353	33.408	0.743	0.846	3.438	3.913	1.711	1.947
12	Isooctane	114.18	0.692	1.348	1.948	0.578	0.835	0.018	0.025	0.076	0.109	0.577	0.834
13	nC7	100.2	0.6795	275.792	405.875	239.765	352.856	0.309	0.455	52.312	76.987	0.034	0.050
14	MCHX	98.19	0.77	284.710	369.753	238.186	309.333	148.301	192.599	205.166	266.449	174.738	226.932
15	Tol	92.14	0.87	123.289	141.712	41.792	48.036	0.033	0.037	0.027	0.031	0.000	0.000
16	nC8	114.23	0.706	262.418	371.696	240.780	341.049	34.392	48.713	88.430	125.255	0.000	0.000
17	EB	106.17	0.8665	37.385	43.145	43.031	49.660	35.142	40.556	49.835	57.513	13.852	15.986
18	m/p-xyI	106.17	0.87	128.812	148.060	92.851	106.725	83.061	95.472	114.673	131.808	66.716	76.685
19	o-xyI	106.17	0.86	70.860	82.395	54.536	63.414	7.037	8.183	30.449	35.405	4.925	5.727
20	nC9	128.26	0.718	335.300	466.992	297.973	415.004	31.063	43.263	115.773	161.244	36.717	51.138
21	1,2,4 TMB	120.19	0.8761	157.612	179.902	131.489	150.085	139.933	159.723	146.697	167.443	120.013	136.986
22	nC10	142.28	0.73	290.868	398.450	281.139	385.121	12.667	17.352	52.801	72.330	6.065	8.309
23	nC11	156.31	0.74	314.469	424.958	318.525	430.439	34.682	46.867	31.809	42.985	64.204	86.762
24	Naph	128.17	1.14	26.551	23.291	46.549	40.833	30.724	26.951	37.955	33.294	41.667	36.550
25	nC12	184.36	0.76	344.085	452.150	348.860	458.425	51.101	67.151	49.434	64.960	38.839	51.037
26	IP13	198.39	0.77	140.155	182.664	130.175	169.658	125.592	163.684	122.616	159.806	122.828	160.082
27	IP14	142.2	1.001	72.507	72.434	82.510	82.428	85.576	85.491	82.336	82.254	72.903	72.831
28	nC13	184.36	0.756	315.572	417.423	324.034	428.617	23.097	30.552	21.999	29.099	9.667	12.788
29	IP15	152.19	0.8987	85.317	94.934	104.854	116.673	100.403	111.720	97.086	108.029	103.260	114.900
30	nC14	154.21	1.222	275.725	225.634	287.751	235.475	51.716	42.321	50.533	41.352	50.025	40.937
31	IP16	212.41	0.769	163.265	212.308	190.336	247.511	155.522	202.240	150.495	195.703	136.408	177.383
32	nC15	166.223	1.202	267.831	222.821	304.663	253.464	26.556	22.093	22.548	18.759	25.288	21.038
33	nC16	226.44	0.77	297.479	386.337	334.220	434.053	17.698	22.985	1.604	2.083	10.020	13.013
34	IP18	254.49	0.775	208.184	268.625	219.708	283.494	193.572	249.770	193.439	249.599	182.367	235.312
35	nC17	178.23	1.18	231.018	195.778	248.985	211.005	4.005	3.394	15.484	13.122	6.746	5.717
36	Pristane	268.52	0.783	268.520	342.937	268.520	342.937	268.520	342.937	268.520	342.937	268.520	342.937
37	nC18	254.49	0.777	307.061	395.188	303.635	390.779	16.560	21.313	18.569	23.898	0.000	0.000
38	Phytane	282.55	0.791	215.409	272.325	236.508	298.999	229.896	290.640	232.703	294.188	210.664	266.327
39	nC19	268.49	0.789	281.180	356.375	294.792	373.627	11.956	15.154	17.218	21.822	15.723	19.928
40	nC20	282.65	0.789	238.058	301.721	280.551	355.578	20.742	26.290	23.118	29.300	42.965	54.454
41	nC21	296.57	0.80	250.604	315.115	265.204	333.473	5.964	7.499	11.132	13.997	33.232	41.787
42	nC22	310.60	0.80	230.890	289.374	238.808	299.296	11.256	14.108	13.743	17.224	27.040	33.889
43	nC23	324.63	0.80	208.733	260.818	207.143	258.832	10.362	12.947	5.964	7.453	9.765	12.201
44	nC24	338.65	0.80	206.734	257.609	210.170	261.890	12.852	16.014	11.530	14.367	23.222	28.937
45	nC25	352.68	0.80	234.013	290.859	209.817	260.785	51.231	63.675	46.124	57.328	47.751	59.351
46	nC26	366.71	0.81	182.786	226.653	183.969	228.120	26.705	33.114	32.340	40.101	26.262	32.564
47	nC27	380.73	0.81	172.413	213.325	158.643	196.287	11.552	14.293	11.108	13.744	0.000	0.000
48	nC28	394.76	0.81	150.108	185.350	127.544	157.488	18.089	22.335	13.863	17.118	5.242	6.473
49	nC29	408.79	0.81	136.069	167.696	94.913	116.974	14.481	17.847	15.184	18.714	6.698	8.255
50	nC30	422.81	0.81	112.227	138.067	67.695	83.282	6.643	8.172	6.388	7.859	16.902	20.794
51	nC31	436.84	0.81	86.493	106.231	24.068	29.560	0.000	0.000	0.000	0.000	7.817	9.601
52	nC32	450.87	0.82	79.148	97.059	18.943	23.230	3.405	4.176	3.391	4.158	4.071	4.992
53	nC33	464.89	0.82	75.343	92.257	20.886	25.575	15.439	18.904	14.402	17.635	9.675	11.847
54	nC34	478.92	0.82	72.313	88.424	6.599	8.069	1.283	1.569	3.312	4.050	29.323	35.856
55	nC35	492.95	0.82	42.907	52.398	5.222	6.377	5.430	6.631	1.782	2.176	2.542	3.104
56	nC36	506.97	0.82	31.755	38.732	2.443	2.980	5.601	6.831	0.444	0.542	0.504	0.614
57	nC37	521.00	0.82	23.604	28.756	5.457	6.648	0.465	0.567	0.335	0.408	3.557	4.334
58	nC38	535.03	0.82	28.428	34.593	0.383	0.466	0.867	1.055	1.506	1.833	1.440	1.752
59	nC39	549.05	0.82	21.298	25.890	1.487	1.807	0.926	1.126	1.096	1.333	0.483	0.588
60	nC40	563.08	0.82	16.902	20.526	0.949	1.153	0.944	1.146	0.889	1.079	0.758	0.920

Appendix D – Part 1 conti.

6		7		8		9		10		11		12		13	
Well 315 7-27-10 Compound Moles x MW, gm	Well 315 7-27-11 Compound Mass / Density,	Well 315 6- 23-11 Compound Moles x MW, gm	Well 315 6-23-11 Compound Mass / Density,	C-1009-A Compound Moles x MW, gm	C-1009-A Compound Mass / Density, ml	Well 411 6-28-89 Compound Moles x MW, gm	Well 411 28-90 Compound Mass / Density, ml	Well 411 7-28-10 Compound Moles x MW, gm	Well 411 7-28-10 Compound Mass / Density, ml	Well 422 7- 27-2010 Compound Moles x MW, gm	Well 422 7- 27-2010 Compound Mass / Density, ml	C-1056-A Compound Moles x MW, gm	C-1056-A Compound Mass / Density,	Well 421B 7-26-10 Compound Moles x MW, gm	Well 421B 7-26-10 Compound Mass / Density,
0.320	0.549	0.281	0.483	0.044	0.075	15.177	26.050	0.193	0.331	0.217	0.372	0.029	0.049	0.526	0.903
9.720	15.779	10.070	16.348	2.316	3.760	55.684	90.396	4.250	6.899	4.522	7.340	0.983	1.596	14.660	23.798
2.658	4.245	0.716	1.144	0.095	0.151	80.228	128.159	0.513	0.819	2.638	4.215	2.353	3.759	14.292	22.830
15.955	24.433	4.440	6.800	0.828	1.268	87.261	133.631	3.303	5.058	10.557	16.166	12.263	18.780	55.595	85.138
1.606	2.453	0.090	0.137	0.317	0.484	145.839	222.723	0.054	0.083	7.554	11.536	25.724	39.285	17.832	27.233
0.000	0.000	0.000	0.000	0.027	0.039	0.281	0.418	0.036	0.054	0.092	0.137	0.000	0.000	0.085	0.126
6.008	8.967	6.850	10.224	4.166	6.217	7.254	10.827	2.676	3.993	2.615	3.903	2.281	3.404	6.784	10.125
8.438	9.604	7.228	8.227	1.281	1.458	21.451	24.415	2.236	2.545	2.225	2.532	2.881	3.279	10.220	11.632
0.885	1.280	0.474	0.685	0.124	0.179	0.000	0.000	0.000	0.000	0.673	0.973	0.055	0.079	0.697	1.008
0.138	0.203	0.205	0.301	0.800	1.177	208.963	307.525	0.342	0.504	22.707	33.417	74.937	110.283	6.188	9.107
211.178	274.258	238.689	309.986	181.785	236.085	216.315	280.929	121.652	157.989	112.634	146.278	124.543	161.744	222.973	289.576
1.036	1.191	0.012	0.014	0.673	0.773	15.373	17.671	0.910	1.046	0.605	0.695	1.077	1.237	1.064	1.223
1.383	1.959	43.499	61.614	1.024	1.450	222.342	314.932	0.401	0.569	51.331	72.707	57.592	81.575	2.046	2.898
38.714	44.678	46.330	53.468	32.711	37.750	40.687	46.263	50.101	57.820	40.851	47.145	32.025	36.960	41.321	47.687
101.381	116.530	117.619	135.194	89.478	102.849	95.603	109.888	68.263	78.464	46.436	53.375	68.253	78.451	107.532	123.600
4.697	5.462	17.753	20.643	4.957	5.764	54.217	63.043	4.909	5.708	5.903	6.864	3.983	4.631	4.875	5.669
37.493	52.219	34.701	48.330	37.949	52.854	283.441	394.764	37.547	52.293	89.355	124.449	62.173	86.592	37.627	52.405
136.979	156.350	158.043	180.394	142.755	162.944	127.542	145.579	126.590	144.492	94.121	107.432	126.047	143.872	137.888	157.388
13.093	17.935	14.174	19.416	15.019	20.574	273.236	374.297	17.875	24.487	69.977	95.859	22.356	30.624	13.906	19.049
26.045	35.196	9.199	12.432	24.148	32.632	313.311	423.393	23.640	31.946	72.904	98.519	25.907	35.009	26.152	35.340
46.598	40.875	35.082	30.773	47.835	41.961	46.888	41.129	45.515	39.925	41.571	36.466	43.150	37.851	46.364	40.670
33.345	43.818	46.566	61.190	32.057	42.125	338.991	445.457	33.504	44.026	60.117	78.997	37.638	49.458	33.636	44.200
134.449	175.229	130.812	170.488	139.828	182.239	130.420	169.976	136.912	178.438	130.526	170.115	137.244	178.870	135.015	175.965
86.266	86.180	88.691	88.603	88.479	88.391	71.845	71.774	87.761	87.673	83.440	83.356	83.824	83.740	86.632	86.545
28.103	37.173	22.666	29.981	19.580	25.900	293.233	387.874	20.111	26.602	19.153	25.335	16.580	21.932	19.791	26.179
108.639	120.885	102.419	113.964	113.584	126.387	106.610	118.627	110.528	122.986	106.274	118.253	108.769	121.030	110.818	123.309
59.043	48.317	52.544	42.998	59.532	48.717	277.774	227.311	58.344	47.745	30.762	25.174	51.395	42.058	58.770	48.093
167.403	217.689	156.800	203.901	151.195	196.613	195.527	254.262	153.520	199.636	166.012	215.881	146.628	190.674	169.224	220.058
30.136	25.072	23.666	19.689	29.855	24.837	298.925	248.690	30.929	25.731	29.382	24.444	28.497	23.708	30.698	25.539
11.053	14.354	4.764	6.187	24.442	31.742	309.771	402.300	10.594	13.759	11.486	14.916	9.369	12.167	10.315	13.396
185.298	239.094	199.583	257.526	184.988	238.694	218.330	281.716	185.962	239.951	194.574	251.063	183.367	236.602	187.607	242.074
6.091	5.162	11.465	9.716	7.011	5.941	232.760	197.255	6.068	5.142	9.202	7.799	7.977	6.760	7.410	6.279
268.520	342.937	268.520	342.937	268.520	342.937	268.520	342.937	268.520	342.937	268.520	342.937	268.520	342.937	268.520	342.937
14.311	18.419	16.721	21.520	17.945	23.095	280.031	360.400	17.418	22.417	16.419	21.131	5.080	6.538	19.805	25.489
221.151	279.585	241.367	305.142	241.754	305.631	234.893	296.957	236.794	299.361	231.024	292.066	216.488	273.689	241.799	305.688
19.560	24.790	12.832	16.263	18.716	23.721	268.057	339.743	13.953	17.685	18.395	23.314	14.597	18.500	23.423	29.687
31.903	40.435	20.737	26.283	26.570	33.676	232.733	294.972	32.442	41.118	28.942	36.681	33.612	42.601	37.871	47.998
4.949	6.223	6.552	8.239	2.461	3.094	211.419	265.842	4.280	5.381	14.401	18.108	20.866	26.237	23.042	28.973
6.717	8.419	5.003	6.270	15.409	19.312	180.991	226.836	3.220	4.035	17.365	21.764	4.434	5.557	18.961	23.764
6.974	8.714	9.243	11.550	4.387	5.482	157.653	196.993	7.502	9.374	9.328	11.656	3.567	4.457	5.007	6.257
12.815	15.968	10.726	13.366	27.401	34.143	144.015	179.455	24.468	30.490	0.000	0.000	16.002	19.940	15.465	19.270
38.344	47.659	50.971	63.352	41.464	51.536	135.429	168.327	42.606	52.956	45.837	56.971	41.255	51.276	43.777	54.411
6.914	8.574	6.240	7.737	31.725	39.338	138.375	171.585	2.722	3.375	28.756	35.657	34.185	42.389	28.392	35.206
17.873	22.114	4.450	5.506	2.086	2.581	111.942	138.504	17.313	21.421	12.757	15.785	18.881	23.362	17.370	21.492
3.390	4.186	20.949	25.867	4.568	5.640	94.711	116.946	3.247	4.010	8.199	10.124	3.031	3.742	2.181	2.693
6.569	8.096	0.000	0.000	5.231	6.447	70.274	86.608	6.405	7.893	9.643	11.885	7.910	9.748	6.793	8.372
0.425	0.523	6.083	7.484	12.805	15.753	34.068	41.912	16.320	20.078	20.491	25.209	16.540	20.349	15.650	19.254
0.646	0.794	68.663	84.332	0.000	0.000	18.969	23.298	0.232	0.284	0.000	0.000	0.000	0.000	3.289	4.039
4.720	5.788	4.437	5.442	1.878	2.304	17.047	20.904	1.638	2.008	1.181	1.448	3.570	4.378	3.100	3.801
4.099	5.019	16.111	19.728	4.289	5.252	22.974	28.132	2.127	2.604	3.188	3.903	3.279	4.015	10.631	13.018
0.000	0.000	5.762	7.046	1.425	1.743	27.029	33.050	0.000	0.000	28.619	34.995	26.698	32.646	0.000	0.000
2.279	2.784	8.891	10.858	0.647	0.790	4.194	5.122	6.601	8.061	6.272	7.660	0.639	0.780	5.881	7.182
5.671	6.917	2.088	2.546	6.319	7.707	3.777	4.607	1.254	1.530	6.715	8.190	3.686	4.495	5.134	6.262
1.025	1.249	2.857	3.481	4.806	5.855	1.354	1.650	4.777	5.820	0.989	1.205	0.956	1.165	1.073	1.307
1.298	1.580	0.692	0.842	0.965	1.174	1.715	2.087	1.387	1.687	4.684	5.700	0.924	1.125	1.467	1.785
1.057	1.284	0.996	1.211	0.481	0.584	1.808	2.197	0.604	0.734	0.396	0.482	1.205	1.465	2.449	2.977
1.124	1.365	0.693	0.841	2.159	2.621	1.854	2.251	0.807	0.980	1.114	1.353	0.919	1.116	1.032	1.253

Appendix D – Part 1 conti.

14		15		16		17		18		19		20		21	
Well 306 7-29-10 Compound	Well 306 7-29-10 Compound	Well 319 6-23-83 Compound	Well 319 6-23-83 Compound	Well 319 6-28-89 Compound	Well 319 6-28-89 Compound	Well 319 3-26-08 Compound	Well 319 3-26-08 Compound	Well 319 7-28-10 Compound	Well 319 28-10 Compound	C1112A (24.3) V Compound	C1112A (24.3) V Compound	C1112A (26.0) V Compound	C1112A (26.0) V Compound	Well 423 10-30-85 Compound	Well 423 10-30-85 Compound
Moles x MW, gm	Mass / Density,	Moles x MW, gm	Mass / Density,	Moles x MW, gm	Mass / Density,	Moles x MW, gm	Mass / Density, ml	Moles x MW, gm	Mass / Density, ml	Moles x MW, gm	Mass / Density,	Moles x MW, gm	Mass / Density, ml	Moles x MW, gm	Mass / Density,
0.244	0.420	57.680	99.004	28.510	48.935	0.027	0.046	1.164	1.997	0.020	0.035	0.060	0.103	38.958	66.868
5.423	8.803	137.022	222.438	103.961	168.768	0.000	0.000	22.523	36.563	0.125	0.202	1.088	1.766	105.791	171.739
3.873	6.187	195.220	311.854	153.276	244.850	0.012	0.019	39.709	63.433	0.300	0.479	2.925	4.673	157.563	251.699
21.130	32.358	147.382	225.700	132.373	202.715	0.000	0.000	86.386	132.291	0.725	1.110	14.978	22.938	134.874	206.545
6.318	9.649	244.316	373.116	217.461	332.104	0.027	0.041	109.875	167.800	1.246	1.903	41.545	63.447	227.233	347.027
0.063	0.093	0.163	0.242	0.162	0.241	0.000	0.000	0.000	0.000	0.000	0.000	0.025	0.037	0.180	0.268
4.416	6.591	9.710	14.492	9.174	13.692	0.000	0.000	7.847	11.712	0.081	0.121	2.881	4.300	9.360	13.971
2.788	3.174	49.913	56.809	40.508	46.105	0.000	0.000	20.614	23.463	0.162	0.184	6.332	7.206	41.570	47.314
0.997	1.440	0.096	0.138	0.137	0.198	0.019	0.027	0.802	1.159	0.000	0.000	0.045	0.065	0.083	0.120
11.488	16.907	275.672	405.698	254.546	374.607	0.093	0.137	142.410	209.580	3.762	5.536	146.853	216.119	270.797	398.523
185.826	241.333	259.281	336.728	247.325	321.201	0.164	0.214	240.663	312.550	5.955	7.734	153.363	199.172	257.115	333.915
1.177	1.353	110.254	126.729	36.850	42.356	0.000	0.000	1.111	1.277	1.428	1.642	0.042	0.048	116.188	133.549
17.031	24.123	199.692	282.849	253.602	359.209	5.546	7.856	97.622	138.275	29.930	42.394	216.353	306.450	213.200	301.984
25.814	29.791	53.909	62.215	46.906	54.132	3.918	4.521	46.956	54.191	10.362	11.958	45.705	52.747	49.062	56.621
75.335	86.592	122.813	141.164	111.817	128.525	14.297	16.433	112.009	128.746	28.143	32.349	105.332	121.071	123.912	142.428
5.437	6.322	74.220	86.302	67.256	78.205	6.244	7.261	4.805	5.588	20.617	23.973	54.542	63.421	74.904	87.098
61.104	85.103	333.215	464.088	318.786	443.992	62.970	87.702	77.278	107.629	135.080	188.134	305.560	425.571	336.101	468.107
121.537	138.724	150.998	172.352	142.794	162.989	86.573	98.816	138.500	158.086	95.835	109.389	148.367	169.349	152.167	173.687
49.657	68.023	300.285	411.350	291.746	399.652	88.445	121.158	41.073	56.264	203.206	278.364	286.203	392.059	303.495	415.746
55.463	74.950	326.208	404.822	318.255	430.074	12.840	17.352	29.374	39.695	218.573	295.369	296.148	400.200	329.198	444.863
44.407	38.954	37.386	32.795	34.748	30.481	32.756	28.734	46.127	40.462	33.690	29.553	37.944	33.284	36.158	31.718
61.331	80.593	372.955	490.087	366.926	482.165	40.986	53.858	31.672	41.619	190.245	249.994	203.465	267.366	343.053	450.794
138.349	180.311	125.786	163.938	123.755	161.291	118.906	154.971	134.122	174.801	124.553	162.330	127.246	165.840	121.452	158.288
87.633	87.546	85.402	85.316	84.935	84.851	81.460	81.379	85.885	85.799	76.718	76.641	85.818	85.732	84.510	84.426
39.125	51.752	368.387	487.284	352.624	466.434	20.340	26.904	27.895	36.898	116.536	154.148	150.857	199.547	363.562	480.902
112.225	124.875	100.454	111.777	99.841	111.094	93.870	104.451	110.098	122.508	94.665	105.335	100.052	111.330	98.916	110.066
64.996	53.188	349.494	286.002	345.636	282.845	44.763	36.631	58.984	48.269	136.218	111.472	162.867	133.279	348.365	285.077
170.414	221.605	189.089	245.890	188.632	245.296	146.816	190.918	165.698	215.473	172.484	224.927	183.290	238.348	187.707	244.093
39.252	32.656	302.454	251.626	301.299	250.665	20.413	16.982	30.634	25.486	109.047	90.721	142.597	118.633	302.030	251.272
24.445	31.747	342.936	445.372	343.489	446.090	12.863	16.705	11.267	14.633	55.307	71.827	77.867	101.126	345.540	448.753
184.989	238.695	225.256	290.653	228.446	294.769	201.858	260.462	188.966	243.827	212.620	274.348	219.283	282.946	226.649	292.450
25.578	21.676	242.615	205.606	243.749	206.567	16.987	14.396	8.150	6.907	0.000	0.000	37.892	32.112	244.020	206.796
268.520	342.937	268.520	342.937	268.520	342.937	268.520	342.937	268.520	342.937	268.520	342.937	268.520	342.937	268.520	342.937
30.245	38.925	303.284	390.327	306.088	393.936	17.064	21.961	7.919	10.192	23.605	30.380	33.513	43.311	306.380	394.312
238.973	302.115	226.963	286.931	229.539	290.188	231.344	292.471	216.442	273.631	211.280	267.105	224.980	284.424	230.135	290.942
19.704	24.973	313.078	396.803	348.517	441.720	17.187	21.783	19.039	24.130	10.571	13.398	11.734	14.872	349.110	442.471
36.167	45.840	287.198	364.003	290.496	368.182	38.462	48.747	31.754	40.245	17.800	22.560	14.052	17.810	284.827	360.998
9.603	12.075	269.069	338.333	275.258	346.115	10.491	13.192	2.560	3.219	7.739	9.731	6.568	8.259	271.283	341.117
19.008	23.822	258.621	324.129	264.405	331.377	11.927	14.948	13.306	16.676	9.908	12.418	12.917	16.189	259.272	324.945
13.126	16.402	234.515	293.033	237.597	296.885	0.000	0.000	2.096	2.619	5.488	6.857	0.000	0.000	227.750	284.581
10.069	12.547	216.432	270.809	216.432	269.693	13.946	17.378	15.220	18.966	16.477	20.532	13.347	16.632	216.484	269.758
0.000	0.000	244.390	303.757	247.509	307.633	47.691	59.276	38.296	47.599	0.000	0.000	45.153	56.121	243.070	302.116
28.375	35.185	193.178	239.539	195.301	242.171	28.262	35.045	22.609	28.035	23.922	29.663	32.344	40.107	185.740	230.316
16.621	20.565	177.246	219.304	175.689	217.377	9.037	11.182	15.178	18.780	13.923	17.227	27.293	33.769	164.180	203.137
11.076	13.677	150.105	185.346	142.065	175.418	15.884	19.613	4.925	6.081	18.694	23.083	19.538	24.126	128.344	158.476
9.610	11.844	122.569	151.058	112.449	138.586	29.706	36.611	7.348	9.055	16.791	20.694	18.298	22.551	93.074	114.708
22.789	28.036	78.487	96.559	68.179	83.877	1.216	1.496	12.973	15.960	5.095	6.268	2.628	3.233	50.397	62.001
0.838	1.029	47.349	58.155	41.602	51.095	0.000	0.000	0.577	0.708	6.297	7.734	11.273	13.845	28.542	35.056
2.884	3.536	31.909	39.129	27.764	34.047	2.356	2.889	1.773	2.174	12.397	15.202	12.264	15.039	17.722	21.733
2.521	3.087	31.063	38.036	30.546	37.403	15.919	19.492	6.798	8.324	18.934	23.185	20.448	25.038	24.004	29.393
31.885	38.988	5.305	6.487	3.771	4.611	5.723	6.998	1.952	2.387	5.155	6.304	3.843	4.699	5.586	6.831
2.659	3.247	0.871	1.064	1.392	1.700	3.474	4.243	3.254	3.974	4.015	4.904	1.231	1.504	2.318	2.831
5.607	6.839	1.069	1.304	3.721	4.538	1.670	2.037	2.604	3.176	4.000	4.879	1.453	1.772	0.428	0.522
2.676	3.260	0.416	0.507	1.749	2.131	2.701	3.291	1.323	1.611	2.723	3.317	3.514	4.281	5.346	6.513
1.118	1.360	1.247	1.517	1.121	1.364	1.113	1.354	1.234	1.502	2.238	2.723	1.832	2.229	0.723	0.880
0.526	0.640	1.733	2.106	0.879	1.068	1.297	1.577	1.155	1.404	1.610	1.957	0.726	0.883	1.105	1.344
1.611	1.957	0.391	0.475	0.594	0.721	2.615	3.176	2.083	2.530	0.470	0.570	0.165	0.201	1.309	1.590

Appendix D – Part 1 conti.

22		23		24		25		26		27		28		29	
Well 423 6-28-89	Well 423 6-28-89	Well 423 3-26-08	Well 423 3-26-08	Well 423 7-28-10	Well 423 7-28-10	Well 534A 7-28-10	Well 534A 7-28-10	Well 317 7-29-10	Well 317 7-29-10	Well 521 7-27-10	Well 521 7-27-10	Well 521 6-23-11	Well 521 6-23-11	Well 420D 6-28-89	Well 420D 6-28-89
Compound Moles x MW, gm	Compound Mass / Density,	Compound Moles x MW, gm	Compound Mass / Density,	Compound Moles x MW, gm	Compound Mass / Density,	Compound Moles x MW, gm	Compound Mass / Density, ml	Compound Moles x MW, gm	Compound Mass / Density, ml	Compound Moles x MW, gm	Compound Mass / Density, ml	Compound Moles x MW, gm	Compound Mass / Density,	Compound Moles x MW, gm	Compound Mass / Density,
26.380	45.280	4.343	7.454	3.079	5.285	2.142	3.676	1.865	3.200	1.181	2.028	1.525	2.618	3.210	5.509
82.144	133.350	40.679	66.037	33.623	54.583	24.596	39.928	23.438	38.049	12.745	20.691	16.432	26.675	12.818	20.809
115.149	183.943	72.731	116.184	62.345	99.592	45.247	72.280	44.737	71.465	20.809	33.242	28.457	45.458	15.182	24.253
114.566	175.446	103.974	159.225	90.984	139.332	74.053	113.405	78.285	119.885	35.275	54.019	47.002	71.979	31.432	48.134
180.416	275.528	184.177	281.272	162.637	248.376	116.330	177.657	131.742	201.194	38.149	58.261	62.004	94.691	39.564	60.422
0.338	0.503	0.182	0.271	0.293	0.435	0.205	0.305	0.257	0.382	0.145	0.215	0.087	0.129	0.165	0.245
8.638	12.892	8.943	13.348	7.963	11.886	7.003	10.452	7.486	11.173	4.101	6.121	5.015	7.486	4.249	6.342
21.900	24.926	26.779	30.479	23.135	26.332	18.703	21.288	21.175	24.101	7.237	8.237	10.411	11.850	8.982	10.223
0.215	0.310	0.080	0.116	0.564	0.815	0.602	0.870	0.653	0.944	0.113	0.163	0.127	0.183	0.212	0.307
232.645	342.376	263.722	388.111	235.014	345.864	152.542	224.492	205.927	303.056	69.555	102.362	93.628	137.789	117.282	172.601
240.460	312.285	264.528	343.542	239.243	310.705	221.270	287.363	236.190	306.740	157.412	204.431	176.861	229.690	175.211	227.546
75.328	86.584	0.063	0.073	1.155	1.328	1.066	1.225	0.764	0.878	0.586	0.674	1.225	1.408	27.125	31.178
243.468	344.855	205.898	291.640	248.802	352.410	147.253	208.573	226.936	321.439	112.181	158.897	122.703	173.800	199.870	283.101
38.641	44.595	51.862	59.852	40.184	46.375	32.316	37.294	39.794	45.925	48.357	55.808	25.410	29.324	40.956	47.266
97.510	112.081	125.578	144.343	105.920	121.747	88.651	101.898	103.886	119.409	58.200	66.897	62.197	71.491	60.399	69.424
56.072	65.200	72.538	84.347	55.756	64.832	35.509	41.289	49.481	57.536	30.804	35.818	40.932	47.595	52.711	61.292
305.198	425.067	350.243	487.804	313.244	436.274	147.938	206.042	233.482	325.184	199.653	278.069	212.951	296.589	298.455	415.675
131.012	149.540	160.297	182.966	139.130	158.806	122.864	140.239	138.280	157.836	104.634	119.432	105.888	120.863	108.767	124.149
287.969	394.478	317.395	434.788	292.684	400.937	186.412	255.358	268.898	368.353	218.200	298.904	218.089	298.752	275.041	376.768
324.967	439.145	339.031	458.151	306.869	414.688	199.551	269.663	262.451	354.663	263.458	356.025	255.318	345.024	332.210	448.933
45.839	40.209	40.089	35.166	47.856	41.979	45.135	39.592	49.355	43.294	43.892	38.501	31.056	27.242	43.559	38.210
354.605	465.975	327.707	430.629	271.981	357.401	187.754	246.722	207.156	272.217	266.880	350.699	258.317	339.446	359.677	472.639
131.625	171.548	134.150	174.838	133.495	173.985	133.787	174.366	138.885	181.010	135.363	176.419	125.454	163.505	133.611	174.136
82.772	82.889	91.130	91.039	77.685	77.607	84.858	84.773	88.114	88.026	84.898	84.813	86.042	85.956	82.988	82.905
331.285	438.207	243.422	321.986	174.230	230.463	130.203	172.226	122.613	162.187	190.674	252.214	204.720	270.794	331.339	438.279
105.818	117.746	105.662	117.572	108.396	120.615	110.380	122.822	114.617	127.537	106.564	118.575	97.102	108.048	108.299	120.507
289.413	236.836	287.641	235.386	200.565	164.128	152.268	124.606	143.212	117.194	176.987	144.834	218.626	178.908	289.893	237.228
189.068	245.862	196.749	255.850	194.106	252.414	186.091	241.992	196.293	255.257	186.716	242.804	175.216	227.850	170.625	221.879
305.465	254.131	264.025	219.655	238.250	198.211	159.667	132.834	144.357	120.097	182.484	151.817	190.195	158.232	305.168	253.884
334.309	434.167	272.352	353.704	193.660	251.506	147.323	191.329	99.721	129.508	155.185	201.539	188.531	244.846	335.293	435.445
219.464	283.180	236.468	305.120	216.582	279.461	204.066	263.311	215.933	278.623	217.559	280.722	226.806	292.653	219.908	283.752
250.088	211.939	154.712	131.112	121.502	102.968	106.716	90.437	58.547	49.616	100.388	85.074	108.585	92.021	249.907	211.785
268.520	342.937	268.520	342.937	268.520	342.937	268.520	342.937	268.520	342.937	268.520	342.937	268.520	342.937	268.520	342.937
305.111	392.679	184.900	237.966	134.658	173.305	118.901	153.026	65.680	84.531	112.431	144.699	128.115	164.884	303.369	390.437
235.497	297.721	243.871	308.307	235.225	297.377	238.439	301.439	239.032	302.190	246.304	311.384	232.480	293.907	235.209	297.356
293.142	371.536	198.612	251.726	97.074	123.034	88.762	112.499	31.016	39.311	74.278	94.141	143.207	181.505	294.209	372.888
278.073	352.438	98.474	124.808	56.299	71.354	54.616	69.222	28.867	36.587	48.020	60.862	72.706	92.150	278.771	353.322
273.133	343.443	60.180	75.671	33.240	41.797	29.385	36.950	3.865	4.860	19.613	24.662	42.502	53.443	272.926	343.183
251.156	314.773	41.901	52.515	26.884	33.693	24.606	30.838	15.211	19.064	17.223	21.586	40.612	50.899	245.970	308.273
227.721	284.545	26.535	33.156	23.070	28.826	15.498	19.366	6.369	7.959	15.548	19.427	37.014	46.251	227.171	283.858
215.282	268.259	14.472	18.033	18.552	23.117	11.828	14.738	0.000	0.000	13.617	16.968	25.299	31.524	217.639	271.196
238.743	296.737	63.254	78.619	21.599	26.846	0.000	0.000	0.000	0.000	0.000	0.000	23.076	28.681	217.192	269.951
181.214	224.704	42.557	52.771	31.260	38.762	25.157	31.194	27.370	33.939	22.790	28.259	42.830	53.109	180.613	223.959
156.322	193.416	67.175	83.115	27.789	34.382	23.361	28.904	18.752	23.202	20.293	25.108	53.613	66.335	151.809	187.832
123.260	152.198	48.341	59.691	30.199	37.289	21.837	26.964	9.422	11.634	20.505	25.319	45.513	56.199	118.042	145.755
90.726	111.814	42.220	52.033	28.881	35.594	22.718	27.998	7.830	9.651	21.221	26.153	50.180	61.843	84.637	104.310
63.572	78.209	31.275	38.477	8.860	10.900	33.603	41.340	19.724	24.265	5.454	6.709	20.135	24.771	64.864	79.799
19.124	23.488	22.897	28.123	7.316	8.986	3.803	4.671	2.078	2.553	5.008	6.150	0.000	0.000	15.433	18.954
14.694	18.019	16.475	20.203	14.437	17.704	8.950	10.975	7.456	9.143	10.811	13.258	14.656	17.973	13.491	16.544
19.533	23.918	23.263	28.485	17.890	21.906	15.551	19.042	9.085	11.125	15.573	19.068	23.665	28.978	16.291	19.949
27.861	34.068	6.788	8.300	4.371	5.345	2.864	3.501	25.562	31.257	0.000	0.000	1.961	2.397	31.217	38.172
3.761	4.593	5.568	6.800	2.923	3.570	2.791	3.409	0.581	0.709	0.000	0.000	2.303	2.812	4.446	5.430
8.016	9.777	2.987	3.643	6.567	8.010	1.405	1.714	5.547	6.766	5.795	7.069	3.137	3.826	2.045	2.494
1.808	2.202	4.269	5.201	1.010	1.230	1.993	2.428	1.793	2.184	4.220	5.141	2.048	2.496	1.561	1.901
2.327	2.832	1.305	1.588	1.391	1.693	0.379	0.461	1.915	2.331	0.964	1.173	1.330	1.619	0.000	0.000
4.900	5.957	0.398	0.484	0.773	0.940	0.000	0.000	5.114	6.217	1.436	1.745	4.318	5.248	0.864	1.050
1.225	1.487	0.634	0.770	1.474	1.790	3.240	3.934	1.920	2.331	1.212	1.472	0.827	1.004	1.329	1.614

Appendix D – Part 1 conti.

30		31		32		33		34		35		36	
Well 420D 6-28-89 Duplicate Compound	Well 420D 6-28-89 Duplicate Compound	Well 420D 6-28-89 Triplicate Compound	Well 420D 6-28-89 Triplicate Compound	Well 420D 7-29-10 Compound	Well 420D 7-29-10 Compound	Well 533D 7-29-10 Compound	Well 533D 7-29-10 Compound	C-1051-A Compound	C-1051-A Compound	C1103A (27.0) V Compound	C1103A (27.0) V Compound	C1103A (27.5) V Compound	C1103A (27.5) V Compound
Moles x MW, gm	Mass / Density, ml	Moles x MW, gm	Mass / Density, ml	Moles x MW, gm	Mass / Density, ml	Moles x MW, gm	Mass / Density, ml	Moles x MW, gm	Mass / Density, ml	Moles x MW, gm	Mass / Density, ml	Moles x MW, gm	Mass / Density, ml
3.104	5.327	3.206	5.503	1.602	2.750	0.286	0.490	0.319	0.547	0.035	0.060	0.055	0.095
12.424	20.168	12.841	20.846	17.535	28.465	6.106	9.913	3.527	5.725	0.484	0.786	1.601	2.600
14.739	23.544	15.381	24.571	29.541	47.190	12.026	19.212	6.153	9.829	1.185	1.894	3.790	6.055
30.536	46.763	31.790	48.683	56.119	85.941	37.257	57.055	12.660	19.387	8.693	13.313	18.505	28.338
38.510	58.813	40.434	61.751	81.127	123.895	61.757	94.314	24.389	37.247	17.341	26.483	34.416	52.560
0.177	0.264	0.107	0.160	0.199	0.295	0.161	0.239	0.117	0.174	0.045	0.066	0.062	0.092
4.203	6.273	4.287	6.398	6.013	8.975	4.944	7.379	1.714	2.558	2.127	3.175	3.319	4.954
8.839	10.060	9.385	10.682	10.655	12.127	11.674	13.287	3.332	3.792	1.926	2.192	3.683	4.192
0.299	0.432	0.194	0.280	0.652	0.943	0.452	0.654	0.455	0.658	0.218	0.314	0.449	0.648
114.739	168.857	119.563	175.957	138.205	203.392	129.403	190.439	66.610	98.028	74.442	109.554	99.262	146.081
171.651	222.923	176.010	228.584	203.596	264.411	184.838	240.050	78.399	101.817	122.577	159.191	152.440	197.974
26.665	30.650	29.370	33.758	0.683	0.785	0.986	1.133	1.350	1.552	0.607	0.698	0.052	0.060
196.259	277.987	121.706	172.388	170.675	241.749	144.737	205.010	120.961	171.333	143.585	203.378	156.643	221.874
39.535	45.626	16.340	18.857	24.081	27.791	27.226	31.421	40.585	46.838	21.012	24.250	22.619	26.104
59.553	68.452	65.182	74.922	71.792	82.519	75.840	87.173	56.147	64.537	57.556	66.157	61.628	70.836
53.024	61.656	62.919	73.162	38.514	44.784	14.745	17.145	31.446	36.565	46.194	53.714	49.043	57.027
294.211	409.764	310.244	432.095	244.196	340.105	171.067	238.255	218.624	304.490	257.096	358.073	257.372	358.456
109.436	124.913	119.329	136.205	114.749	130.977	119.428	136.318	114.177	130.324	109.660	125.168	108.802	124.189
289.622	396.742	296.276	405.857	245.077	335.722	147.825	202.500	241.394	330.677	264.338	362.107	256.114	350.841
328.630	444.095	325.792	440.259	267.771	361.853	104.517	141.239	284.611	384.610	284.984	385.114	261.876	353.887
43.315	37.995	32.465	28.478	44.052	38.642	43.774	38.398	43.126	37.830	31.284	27.442	30.312	26.590
359.767	472.757	372.541	489.544	240.744	316.353	69.704	91.595	287.173	377.365	250.864	329.652	173.485	227.970
135.014	175.964	125.785	163.936	137.385	179.055	134.425	175.197	132.056	172.109	131.204	170.999	120.164	156.611
85.564	85.479	85.762	85.676	87.377	87.290	83.986	83.902	84.611	84.526	89.641	89.551	83.360	83.277
335.821	444.208	355.789	470.621	170.996	226.185	27.265	36.065	222.186	293.896	188.682	249.580	125.194	165.600
111.942	124.559	100.247	111.547	113.804	126.632	105.690	117.603	106.590	118.605	104.398	116.165	97.441	108.425
296.755	242.844	302.233	247.326	192.007	157.125	50.819	41.587	212.675	174.039	234.101	191.572	146.055	119.521
201.895	262.543	188.204	244.739	198.002	257.480	162.674	211.539	176.297	229.254	193.200	251.002	180.468	234.679
311.680	259.301	300.027	249.606	236.105	196.427	26.602	22.132	242.855	202.043	211.263	175.760	148.962	123.928
334.747	434.736	339.413	440.797	215.339	279.661	14.058	18.257	221.013	287.029	205.595	267.007	110.956	144.098
219.131	282.750	223.946	288.962	216.939	279.921	204.478	263.843	215.185	277.658	232.881	300.491	220.289	284.244
247.314	209.589	240.942	204.188	148.550	125.890	14.352	12.163	146.707	124.328	109.751	93.009	51.904	43.986
268.520	342.937	268.520	342.937	268.520	342.937	268.520	342.937	268.520	342.937	268.520	342.937	268.520	342.937
303.280	390.322	301.276	387.743	171.632	220.890	14.343	18.459	154.012	198.213	129.652	166.862	45.347	58.362
233.209	294.828	225.410	284.968	239.303	302.533	226.004	285.720	221.164	279.601	234.873	296.932	225.113	284.593
297.095	376.547	342.911	434.615	148.439	188.136	12.197	15.459	141.995	179.968	163.340	207.021	11.292	14.311
276.294	350.183	283.160	358.885	94.108	119.276	26.709	33.852	67.400	85.425	58.500	74.589	20.218	25.625
271.066	340.844	266.943	335.659	76.688	96.429	2.367	2.977	28.403	35.715	40.107	50.431	8.348	10.497
248.645	311.626	260.142	326.034	54.734	68.597	5.328	6.677	19.339	24.237	37.250	46.685	10.184	12.764
227.259	283.968	227.258	283.967	34.729	43.395	5.916	7.392	16.702	20.869	30.186	37.719	6.889	8.607
220.193	274.379	211.882	264.024	22.220	27.688	13.541	16.873	8.859	11.039	16.995	21.178	9.234	11.506
235.107	292.218	243.892	303.138	23.397	29.081	48.986	60.885	46.298	57.545	65.078	80.887	49.767	61.856
183.022	226.945	187.681	232.723	31.509	39.071	2.561	3.176	21.069	26.125	30.467	37.779	21.396	26.531
159.248	197.035	164.669	203.742	27.316	33.798	15.374	19.022	19.010	23.520	50.388	62.345	4.121	5.099
119.021	146.964	130.410	161.027	26.866	33.173	8.185	10.106	20.251	25.005	36.344	44.877	21.775	26.887
85.612	105.511	103.627	127.714	25.168	31.017	10.089	12.434	23.303	28.719	33.963	41.857	22.259	27.433
59.581	73.299	47.185	58.049	32.963	40.553	17.805	21.905	5.014	6.169	17.153	21.103	1.504	1.851
15.734	19.325	26.786	32.898	3.881	4.767	2.436	2.992	9.371	11.509	11.367	13.960	0.000	0.000
17.494	21.453	17.054	20.913	7.574	9.288	2.415	2.961	16.861	20.677	13.034	15.984	13.415	16.451
21.719	26.595	23.459	28.726	18.539	22.701	11.767	14.409	24.046	29.444	21.970	26.902	19.730	24.159
6.938	8.484	1.654	2.023	24.315	29.733	0.000	0.000	28.613	34.988	5.300	6.481	4.305	5.264
4.853	5.926	1.934	2.362	4.867	5.943	0.557	0.680	5.195	6.344	4.908	5.993	1.307	1.596
4.206	5.130	1.196	1.459	6.236	7.606	3.980	4.854	5.318	6.486	3.250	3.964	0.843	1.028
0.780	0.951	0.984	1.199	3.440	4.191	2.355	2.868	2.843	3.463	4.477	5.454	0.400	0.487
0.863	1.050	1.893	2.304	2.961	3.604	6.147	7.480	2.373	2.887	0.000	0.000	1.711	2.082
2.052	2.494	0.846	1.028	1.688	2.052	0.709	0.862	1.847	2.245	0.776	0.943	0.855	1.040
1.047	1.272	0.468	0.568	0.100	0.122	1.776	2.157	1.038	1.261	1.101	1.337	2.337	2.838

Appendix D – Part 1 conti.

37		38		39	
C1109B (28.0) V Compound	C1109B (28.0) V Compound	Well 532A 6-21-12 Compound	Well 532A 6-21-12 Compound	Well 312 6- 22-11 Compound	Well 312 6- 22-11 Compound
Moles x MW, gm	Mass / Density, ml	Moles x MW, gm	Mass / Density,	Moles x MW, gm	Mass / Density, ml
0.047	0.081	0.087	0.150	0.332	0.570
0.015	0.024	0.287	0.465	8.270	13.425
0.016	0.026	0.000	0.000	17.507	27.966
0.097	0.149	0.030	0.046	49.747	76.182
0.020	0.031	0.019	0.029	94.267	143.962
0.012	0.018	0.000	0.000	0.082	0.122
0.067	0.100	0.034	0.050	6.064	9.051
0.149	0.169	2.094	2.383	9.728	11.072
0.085	0.122	0.000	0.000	0.850	1.228
1.280	1.884	0.104	0.154	167.300	246.210
14.657	19.035	1.254	1.629	217.472	282.431
37.386	42.972	0.000	0.000	1.419	1.632
22.314	31.606	1.735	2.458	139.355	197.387
26.684	30.796	2.548	2.940	42.062	48.542
18.561	21.334	0.684	0.786	110.047	126.490
0.000	0.000	2.528	2.940	23.865	27.750
93.933	130.825	55.168	76.836	153.569	213.885
33.757	38.531	27.830	31.765	148.961	170.028
129.147	176.914	117.579	161.067	106.620	146.054
148.174	200.235	188.592	254.854	20.699	27.972
19.796	17.365	33.672	29.537	36.889	32.359
126.254	165.906	158.634	208.455	44.147	58.012
123.856	161.422	132.388	172.542	124.614	162.409
76.939	76.863	76.063	75.987	84.520	84.435
78.639	104.020	87.999	116.401	22.974	30.388
92.643	103.085	103.965	115.684	98.547	109.655
72.598	59.409	84.088	68.812	51.042	41.769
155.372	202.045	165.253	214.893	154.321	200.678
39.679	33.011	69.122	57.505	27.573	22.940
30.468	39.569	45.936	59.657	20.000	25.974
210.226	271.259	215.646	278.253	199.892	257.925
22.889	19.397	33.118	28.067	21.817	18.489
268.520	342.937	268.520	342.937	268.520	342.937
20.710	26.654	27.890	35.894	15.003	19.310
224.759	284.145	217.827	275.382	227.047	287.038
12.002	15.211	17.271	21.890	12.276	15.559
17.681	22.409	26.384	33.440	17.883	22.665
7.531	9.470	14.983	18.840	7.418	9.328
10.318	12.931	29.708	37.233	11.017	13.808
6.327	7.905	3.559	4.447	11.745	14.676
9.439	11.762	21.732	27.080	10.475	13.052
47.114	58.558	43.224	53.724	56.329	70.012
10.123	12.553	18.485	22.921	24.673	30.594
15.662	19.379	0.000	0.000	12.030	14.885
22.118	27.311	11.050	13.645	16.635	20.541
27.989	34.494	12.131	14.951	19.293	23.778
0.258	0.318	22.954	28.239	3.034	3.733
63.884	78.463	12.801	15.722	63.765	78.316
5.756	7.058	5.574	6.836	4.715	5.782
16.151	19.777	15.332	18.774	17.015	20.835
4.593	5.616	33.183	40.576	4.400	5.380
1.468	1.793	1.793	2.190	5.770	7.046
2.714	3.311	0.880	1.073	1.118	1.364
2.825	3.442	2.558	3.116	0.678	0.826
0.640	0.779	2.964	3.607	1.899	2.311
0.832	1.011	1.440	1.750	0.821	0.998
0.809	0.983	1.614	1.960	1.533	1.861

Appendix D – Part 2 of GC, PAH, Biomarker, UCM Mass in Grams, Percent, and Fractions Lost.

Tabulation of sums of incremental masses/volumes with additional UCM mass to obtain a mass balance of composition-calculated and laboratory-measured density values.

	1		2		3		4		5	
	Reference Pipeline 4-10- 84	Reference Pipeline 4- 10-84	Well 604A 6- 28-89	Well 604A 6- 28-89	C1108A (18.4) V 7-20-11	C1108A (18.4) V 7-20-11	C1108C (20.4) 7- 20-11	C1108C (20.4) 7- 20-11	604A 21-12	6-604A 21-12
	Compound Moles x MW, gm	Compound Mass / Density, ml	Compound Moles x MW, gm	Compound Mass / Density, ml						
Totals of Incremental Mass & Volumes										
Sums of incremental mass and volume values:	9507.7	12160.2	8499.0	10705.1	2148.1	2636.8	2576.3	3223.4	2094.9	2571.9
GC compound blend density, gm/ml	0.7819	%s	0.7939	%s	0.8147		0.7992		0.8145	%s
Average PAH blend density, gm/ml	0.0141	1.65	0.0141	1.65					0.0141	1.61
Average Biomarker blend, gm/ml	0.0042	0.49	0.0042	0.49					0.0042	0.48
Est. Unidentified Compounds, gm/ml	0.0553	6.46	0.0433	5.06					0.0433	4.94
Estimated Lab Oil Density, gm/ml	0.8555	8.61	0.8555	7.20					0.8762	7.03
Total mass of estimated density blend, gm =	<u>10403.0</u>		<u>9158.7</u>						<u>2253.4</u>	
Total GC compound mass lost, gm	0.0000		1244.33						8149.6	
Percentage GC mass lost relative to ref. oil	0.0000		11.96	%					78.34	
Fraction GC mass lost relative to ref. oil	0.0000		0.1196						0.7834	
Total Mass (GC, PAH, etc) Adjust Percent Lost	0.0010		11.100						72.829	
Total Mass (GC, PAH, etc) Adjust Fraction Lost	0.0010		0.1110						0.7283	
Remains=1 Minus Fraction of Total Mass Lost	1.0000		0.8890						0.2717	
Lab-Determined Fluid Properties at 8.5 deg C										
Oil Density, gm/ml	0.8555		0.8555						0.8940	
Oil Viscosity, cp	13.0		13.0						36.1	
Air-Water Tension, dynes/cm									67.8	
Air-Oil Tension, dynes/cm									28.3	
Oil-Water Tension, dynes/cm									11.9	

Appendix D – Part 2 conti.

6		7		8		9		10		11		12		13	
Well 315 7-27-10	Well 315 7-27-11	Well 315 6-23-11	Well 315 6-23-11	C-1009-A	C-1009-A	Well 411 6-28-89	Well 411 28-89	Well 411 7-28-10	Well 411 7-28-10	Well 422 7-27-2010	Well 422 7-27-2010	C-1056-A	C-1056-A	Well 421B 7-26-10	Well 421B 7-26-10
Compound		Compound		Compound		Compound		Compound		Compound		Compound		Compound	
Moles x MW, gm	Mass / Density, ml	Moles x MW, gm	Mass / Density, ml	Moles x MW, gm	Mass / Density, ml	Moles x MW, gm	Mass / Density, ml	Moles x MW, gm	Mass / Density, ml	Moles x MW, gm	Mass / Density, ml	Moles x MW, gm	Mass / Density, ml	Moles x MW, gm	Mass / Density, ml
2196.5	2690.6	2377.0	2918.7	2182.9	2662.4	7448.5	9312.6	2061.9	2513.0	2303.6	2873.9	2246.7	2788.6	2420.7	2992.2
0.8164	%s	0.8144	%s	0.8199		0.7998	%s	0.8205	%s	0.8016	%s	0.8057		0.8090	%s
0.0180	2.02	0.0180	2.02			0.0162	1.88	0.0162	1.83	0.0162	1.87			0.0162	1.86
0.0054	0.60	0.0054	0.60			0.0044	0.51	0.0044	0.50	0.0044	0.51			0.0044	0.51
0.0488	5.49	0.0531	5.96			0.0425	4.93	0.0425	4.81	0.0425	4.92			0.0425	4.87
0.8885	8.12	0.8908	8.58			0.8629	7.31	0.8836	7.14	0.8647	7.30			0.8721	7.23
2390.6		2600.0				8036.1		2220.4		2485.0				2609.4	
8012.4		7803.0				2366.9		8182.6		7918.0				7793.6	
77.02		75.01				22.75		78.66		76.11				74.92	
0.7702		0.7501				0.2275		0.7866		0.7611				0.7492	
70.768		68.575				21.089		73.039		70.559				69.496	
0.7077		0.6858				0.2109		0.7304		0.7056				0.6950	
0.2923		0.3142				0.7891		0.2696		0.2944				0.3050	
0.8885		0.8908				0.8629		0.8976		0.8914				0.8857	
30.9		31.8				13.9		44.7		38.0				25.0	
66.9		66.3						65.1		63.8				66.7	
28.5		28.5						27.3		27.1				26.5	
20.2		19.2						18.7		19.4				19.2	

Appendix D – Part 2 conti.

14		15		16		17		18		19		20		21	
Well 306 7-29-10	Well 306 7-29-10	Well 319 6-23-83	Well 319 6-23-83	Well 319 6-28-89	Well 319 6-28-89	Well 319 3-26-08	Well 319 3-26-08	Well 319 7-28-10	Well 319 7-28-10	C1112A (24.3) V	C1112A (24.3) V	C1112A (26.0) V	C1112A (26.0) V	Well 423 10-30-85	Well 423 10-30-85
Compound		Compound		Compound		Compound		Compound		Compound		Compound		Compound	
Moles x MW, gm	Mass / Density, ml	Moles x MW, gm	Mass / Density, ml	Moles x MW, gm	Mass / Density, ml	Moles x MW, gm	Mass / Density, ml	Moles x MW, gm	Mass / Density, ml	Moles x MW, gm	Mass / Density, ml	Moles x MW, gm	Mass / Density, ml	Moles x MW, gm	Mass / Density, ml
2434.1	2998.4	9256.2	11682.1	8980.7	11299.9	1890.8	2329.7	2821.2	3592.9	2785.3	3445.2	4145.2	5213.9	9009.4	11336.2
0.8118	%'s	0.7923	%'s	0.7948	%'s	0.8116	%'s	0.7852	%'s	0.8085		0.7950		0.7947	%'s
0.0162	1.85	0.0162	1.89	0.0162	1.89	0.0162	1.85	0.0162	1.91					0.0162	1.89
0.0044	0.50	0.0044	0.52	0.0044	0.51	0.0044	0.50	0.0044	0.52					0.0044	0.51
0.0425	4.86	0.0425	4.97	0.0425	4.95	0.0425	4.86	0.0425	5.01					0.0425	4.95
0.8749	7.21	0.8554	7.38	0.8579	7.35	0.8747	7.21	0.8483	7.44					0.8578	7.36
2623.3		9993.2		9693.7		2037.8		3047.8						9724.6	
7779.8		409.8		709.4		8365.2		7355.2						678.4	
74.78		3.94		6.82		80.41		70.70						6.52	
0.7478		0.0394		0.0682		0.8041		0.7070						0.0652	
69.390		3.648		6.317		74.611		65.444						6.042	
0.6939		0.0365		0.0632		0.7461		0.6544						0.0604	
0.3061		0.9635		0.9368		0.2539		0.3456						0.9396	
0.8890		0.8532		0.8566		0.9091		0.8773						0.8546	
31.4		9.7		11.3		99.9		18.1						10.2	
67.7								68.0							
27.9								26.4							
18.0								19.4							

Appendix D – Part 2 conti.

22		23		24		25		26		27		28		29	
Well 423 6-28-89	Well 423 6-28-89	Well 423 3-26-08	Well 423 3-26-08	Well 423 7-28-10	Well 423 7-28-10	Well 534A 7-28-10	Well 534A 7-28-10	Well 317 7-29-10	Well 317 7-29-10	Well 521 7-27-10	Well 521 7-27-10	Well 521 6-23-11	Well 521 6-23-11	Well 420D 6-28-89	Well 420D 6-28-89
Compound Moles x MW, gm	Compound Mass / Density, ml	Compound Moles x MW, gm	Compound Mass / Density, ml	Compound Moles x MW, gm	Compound Mass / Density, ml	Compound Moles x MW, gm	Compound Mass / Density, ml	Compound Moles x MW, gm	Compound Mass / Density, ml	Compound Moles x MW, gm	Compound Mass / Density, ml	Compound Moles x MW, gm	Compound Mass / Density, ml	Compound Moles x MW, gm	Compound Mass / Density, ml
8527.5	10702.6	6464.0	8135.5	5441.2	6881.7	4290.7	5385.9	4457.2	5670.7	4181.2	5191.6	4677.0	5817.7	7681.7	9486.0
0.7968	%s	0.7945	%s	0.7907	%s	0.7967	%s	0.7860	%s	0.8054	%s	0.8039	%s	0.8098	%s
0.0162	1.88	0.0162	1.89	0.0162	1.90	0.0162	1.88	0.0162	1.91	0.0162	1.86	0.0162	1.87	0.0162	1.85
0.0044	0.51	0.0044	0.51	0.0044	0.52	0.0044	0.51	0.0044	0.52	0.0044	0.51	0.0044	0.51	0.0044	0.51
0.0425	4.94	0.0425	4.96	0.0425	4.98	0.0425	4.94	0.0425	5.01	0.0425	4.89	0.0425	4.90	0.0425	4.87
0.8599	7.34	0.8576	7.36	0.8538	7.39	0.8598	7.34	0.8491	7.43	0.8685	7.26	0.8670	7.28	0.8729	7.23
9202.8		6977.3		5875.4		4630.5		4815.0		4508.8		5044.0		8280.2	
1200.3		3425.7		4527.6		5772.5		5588.0		5894.2		5359.0		2122.8	
11.54		32.93		43.52		55.49		53.72		56.66		51.51		20.41	
0.1154		0.3293		0.4352		0.5549		0.5372		0.5666		0.5151		0.2041	
10.691		30.507		40.306		51.417		49.724		52.543		47.765		18.931	
0.1069		0.3051		0.4031		0.5142		0.4972		0.5254		0.4777		0.1893	
0.8931		0.6949		0.5969		0.4858		0.5028		0.4746		0.5223		0.8107	
0.8583		0.8635		0.8644		0.8709		0.8687		0.8783		0.8732		0.8697	
12.1		12.9		13.2		16.5		15.0		23.9		22.5		18.5	
				68.9		69.8		70.1		65.1		66.4			
				25.6		26.6		27.1		27.4		26.5			
				20.7		20.2		20.8		20.7		18.9			

Appendix D – Part 2 conti.

30		31		32		33		34		35		36	
Well 420D 6-28-89 Duplicate		Well 420D 6-28-89 TriPLICATE		Well 420D 7-29-10		Well 533D 7-29-10		C-1051-A		C1103A (27.0) V		C1103A (27.5) V	
Compound Moles x MW, gm	Compound Mass / Density, ml	Compound Moles x MW, gm	Compound Mass / Density, ml	Compound Moles x MW, gm	Compound Mass / Density, ml	Compound Moles x MW, gm	Compound Mass / Density, ml	Compound Moles x MW, gm	Compound Mass / Density, ml	Compound Moles x MW, gm	Compound Mass / Density, ml	Compound Moles x MW, gm	Compound Mass / Density, ml
7741.9	9556.3	7768.9	9595.0	5075.3	6321.9	2903.2	3702.6	4556.3	5593.8	4676.1	5772.1	3751.2	4699.6
0.8101	%s	0.8097	%s	0.8028	%s	0.7841	%s	0.8145		0.8101		0.7982	
0.0162	1.85	0.0162	1.85	0.0162	1.87	0.0162	1.91						
0.0044	0.50	0.0044	0.51	0.0044	0.51	0.0044	0.52						
0.0425	4.87	0.0425	4.87	0.0425	4.91	0.0425	5.02						
<u>0.8732</u>	7.23	<u>0.8728</u>	7.23	<u>0.8659</u>	7.29	<u>0.8472</u>	7.45						
<u>8344.9</u>		<u>8374.3</u>		<u>5474.2</u>		<u>3136.8</u>							
2058.1		2028.7		4928.9		7266.2							
19.78		19.50		47.38		69.85							
0.1978		0.1950		0.4738		0.6985							
18.354		18.091		43.927		64.645							
0.1835		0.1809		0.4393		0.6465							
0.8165		0.8191		0.5607		0.3535							
0.8697		0.8697		0.8717		0.8803							
18.5		18.5		18.0		22.7							
				68.4		69.9							
				26.6		27.6							
				20.0		19.7							

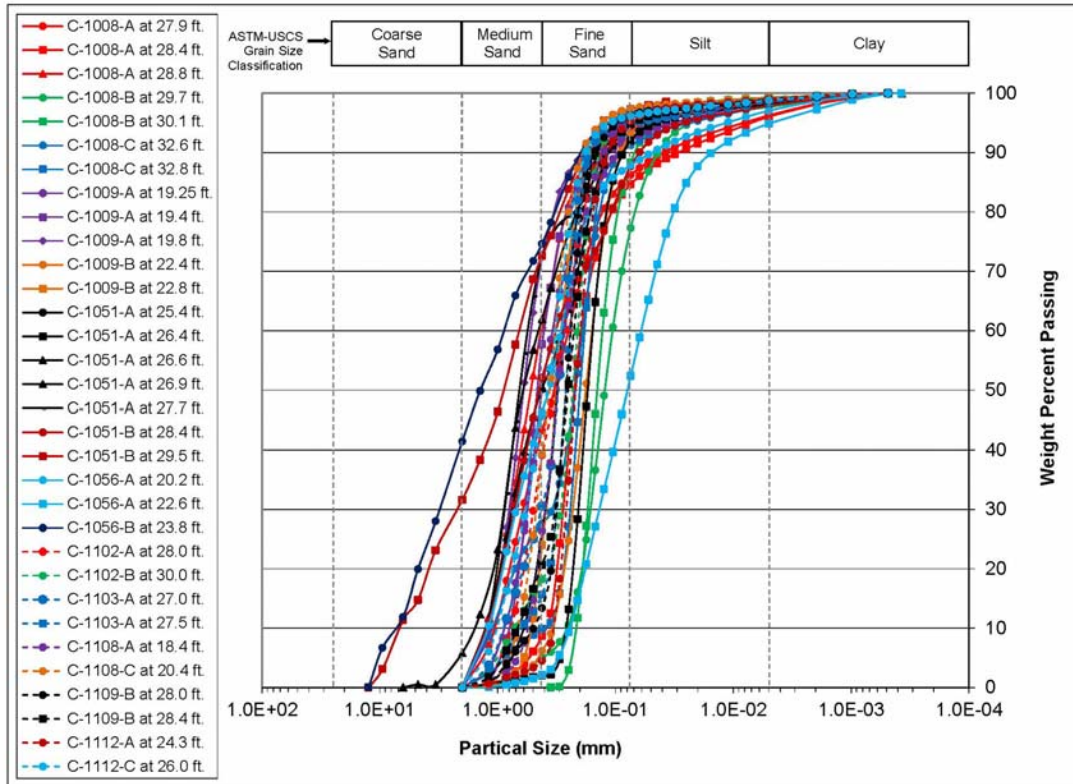
Appendix D – Part 2 conti.

37		38		39	
C1109B (28.0) V	C1109B (28.0) V	532A 6- 21-12	532A 6- 21-12	Well 312 6- 22-11	Well 312 6- 22-11
Compound Moles x MW, gm	Compound Mass / Density, ml	Compound Moles x MW, gm	Compound Mass / Density, ml	Compound Moles x MW, gm	Compound Mass / Density, ml
2376.0	2956.5	2420.3	2990.6	3019.6	3843.6
0.8037		0.8093	%'s	0.7856	%'s
		0.0162	1.86	0.0162	1.91
		0.0044	0.51	0.0044	0.52
		0.0425	4.87	0.0425	5.01
		<u>0.8724</u>	7.23	<u>0.8487</u>	7.43
		<u>2609.0</u>		<u>3262.2</u>	
		7794.0		7140.9	
		74.92		68.64	
		0.7492		0.6864	
		69.502		63.539	
		0.6950		0.6354	
		0.3050		0.3646	
		0.9001		0.8769	
		78.5		19.9	

Appendix E – Grain size and Water Retention Plots, and van Genuchten

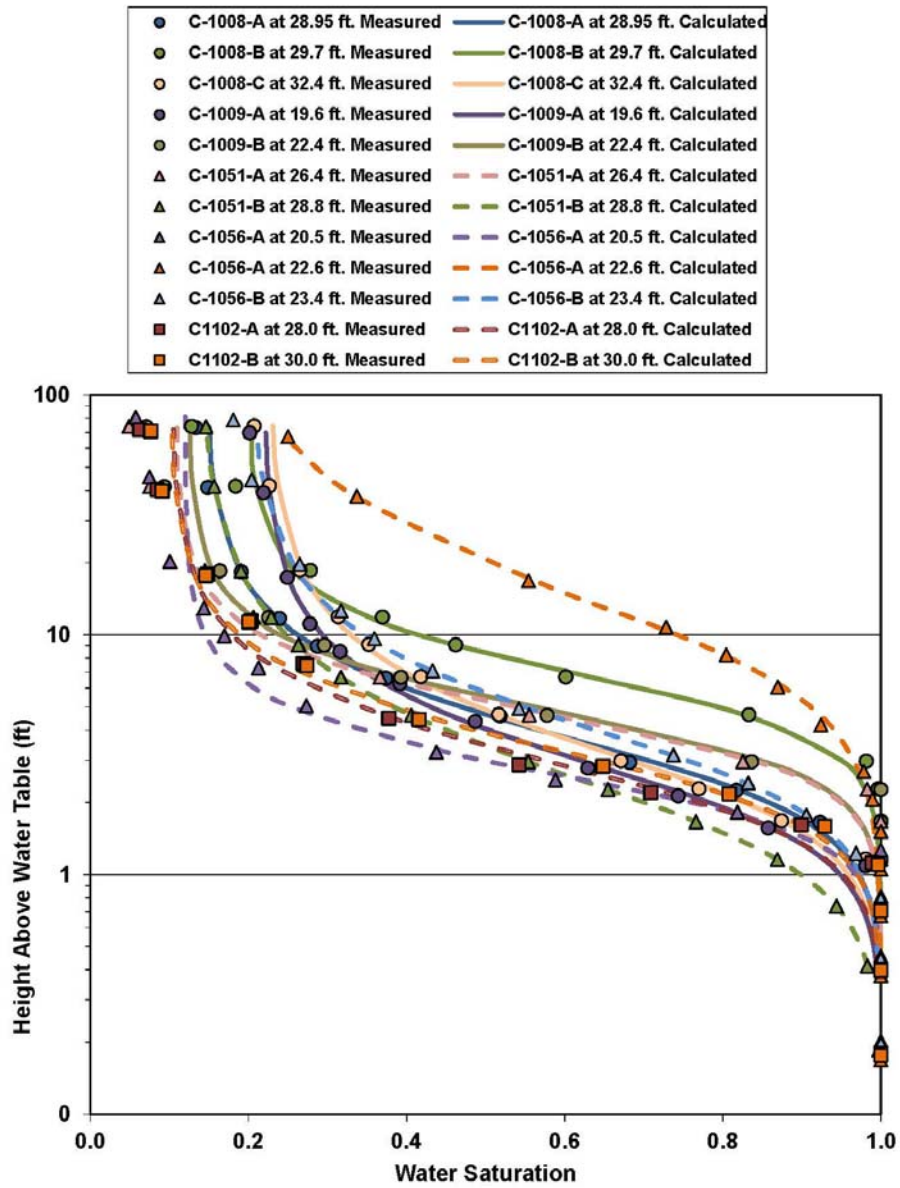
Parameter Plots of 2006 API Database and Bemidji Core Data

Grain Size Distributions



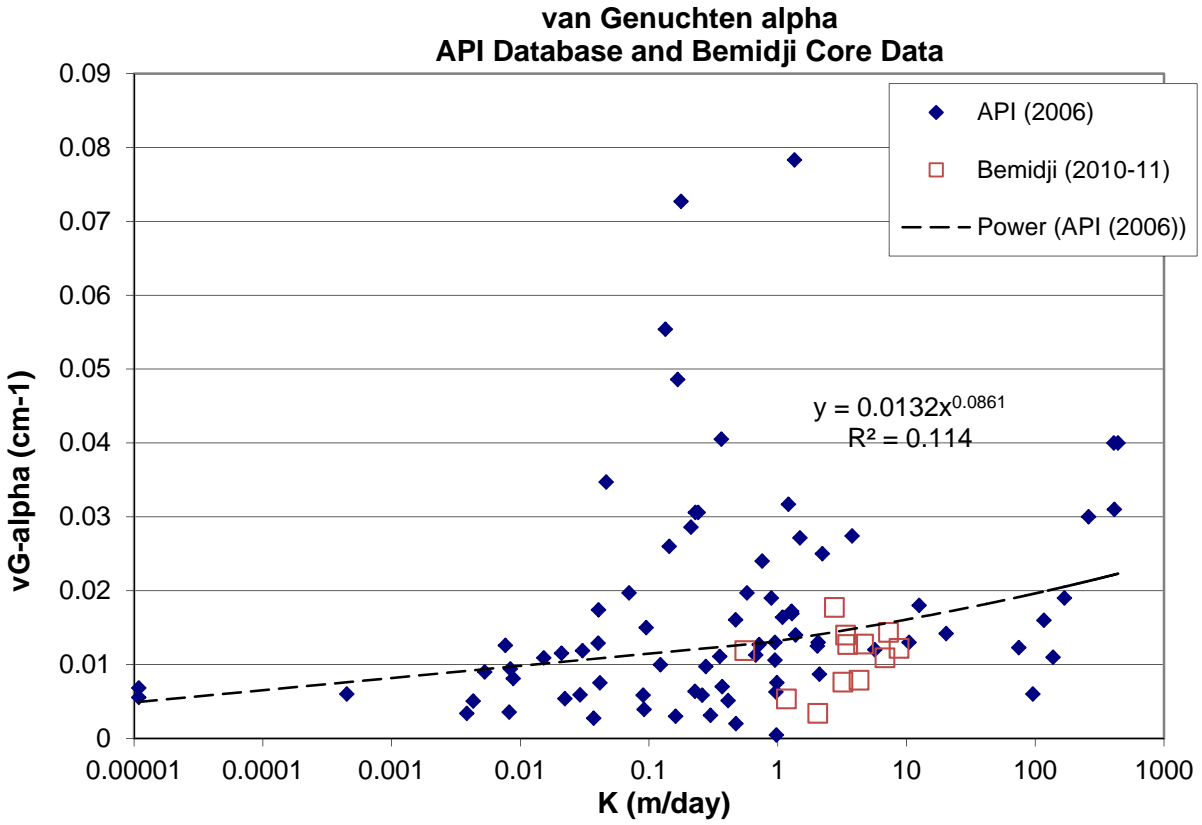
Appendix E conti.

Water Retention Curves



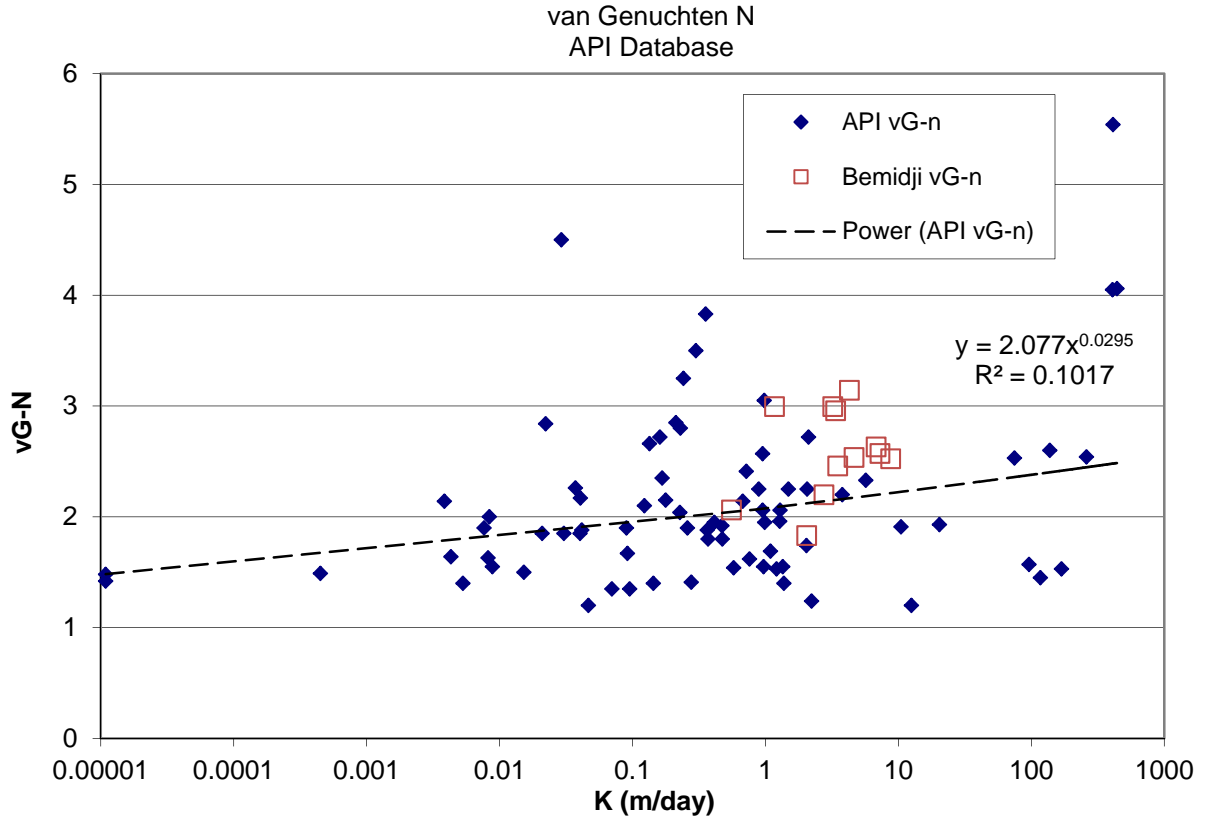
Appendix E conti.

Plot of vG-alpha as a Function of Hydraulic Conductivity, K.



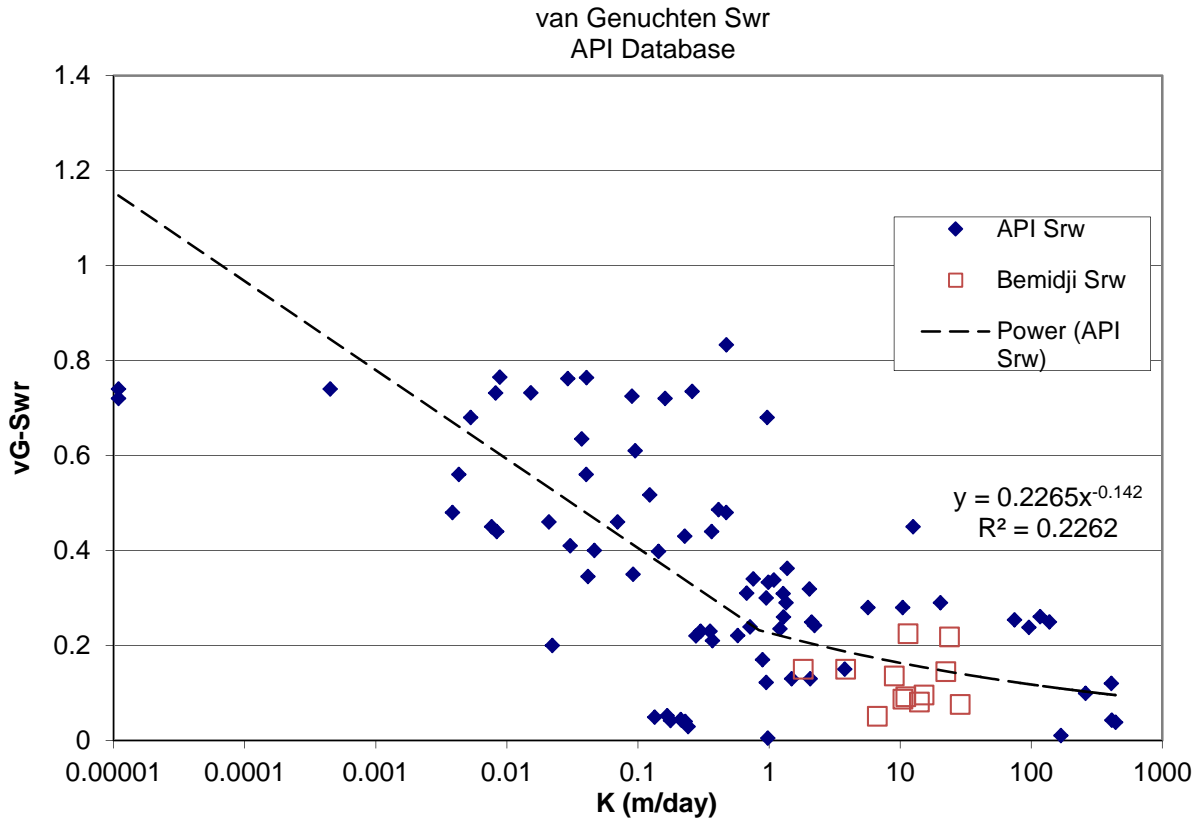
Appendix E conti.

Plot of vG -n as a Function of Hydraulic Conductivity, K.



Appendix E conti.

Plot of Residual Water Saturation as a Function of Hydraulic Conductivity, K.



Appendix F – Baildown Test Analysis for Well 315

Selected worksheets from the API LNAPL Transmissivity workbook.

API LNAPL Transmissivity Workbook
Calculation of LNAPL Transmissivity from Baildown Test Data

STEP 1: RESET OUTPUT SUMMARY	STEP 4: LNAPL TRANSMISSIVITY SUMMARY
	Mean LNAPL Transmissivity (ft ² /d) 0.59
STEP 2: ENTER DATA & VIEW FIGURES	Standard Deviation (ft ² /d) 0.08
STEP 3: CHOOSE WELL CONDITIONS	Coefficient of Variation 0.13

Appendix F conti.

Well Designation: 315 USGS Research Site near Bemjidi, MN
 Date: 24-Jul-10

Ground Surface Elev (ft msl)	0.0	Enter These Data	r_{e1}	<table border="1" style="margin: auto;"> <tr> <td style="text-align: center;">Drawdown Adjustment (ft)</td> </tr> <tr> <td style="text-align: center;">0.025</td> </tr> </table>	Drawdown Adjustment (ft)	0.025
Drawdown Adjustment (ft)						
0.025						
Top of Casing Elev (ft msl)	0.0					
Well Casing Radius, r_c (ft):	0.083					
Well Radius, r_w (ft):	0.083					
LNAPL Specific Yield, S_y :	0.057					
LNAPL Density Ratio, ρ_r :	0.889					
Top of Screen (ft bgs):	0.0					
Bottom of Screen (ft bgs):	0.0					
LNAPL Baildown Vol. (gal.):	0.1					
Effective Radius, r_{e3} (ft):	0.083	Calculated Parameters				
Effective Radius, r_{e2} (ft):	0.083					
Initial Casing LNAPL Vol. (gal.):	0.24					
Initial Filter LNAPL Vol. (gal.):	0.00					

	Enter Data Here					Water Table Depth (ft)	LNAPL Drawdown s_1 (ft)
	Time (min)	DTP (ft btoc)	DTW (ft btoc)	DTP (ft bgs)	DTW (ft bgs)		
Initial Fluid Levels:	0	22.30	23.8	22.30	23.8	22.47	
Enter Test Data:	0.001	22.735	23.4500	22.73	23.45	22.81	0.41
	5.000	22.580	23.7000	22.58	23.70	22.70	0.25
	9.000	22.490	23.4800	22.49	23.48	22.60	0.16
	11.000	22.470	23.4300	22.47	23.43	22.58	0.14
	15.000	22.440	23.4500	22.44	23.45	22.55	0.12
	20.000	22.400	23.4900	22.40	23.49	22.52	0.07
	27.000	22.380	23.3400	22.38	23.34	22.49	0.05
	31.000	22.380	23.3700	22.38	23.37	22.49	0.05
				#N/A	#N/A	#N/A	#N/A
				#N/A	#N/A	#N/A	#N/A
				#N/A	#N/A	#N/A	#N/A
				#N/A	#N/A	#N/A	#N/A
				#N/A	#N/A	#N/A	#N/A
				#N/A	#N/A	#N/A	#N/A
				#N/A	#N/A	#N/A	#N/A
				#N/A	#N/A	#N/A	#N/A
				#N/A	#N/A	#N/A	#N/A
				#N/A	#N/A	#N/A	#N/A

Appendix F conti.

Generalized Bouwer and Rice (1976)

Well Designation:	315
Date:	24-Jul-10

$$T_n = \frac{r_e^2 \ln(R/r_e) \ln(s_n(t_1)/s_n(t))}{2(-J)(t-t_1)}$$

Enter early time cut-off for least-squares model fit

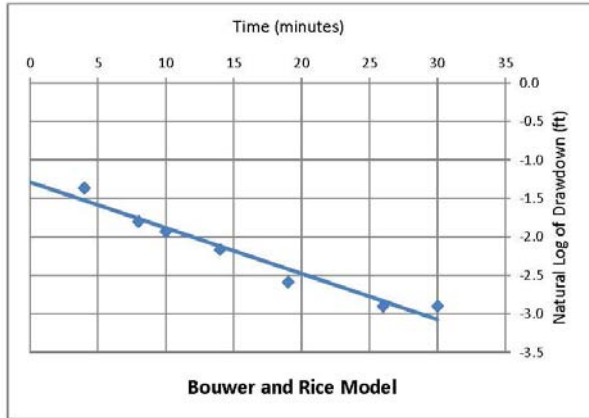
Time_{cut} <- Enter or change value here
 Initial Drawdown = 0.25924

Model Results: T_n (ft²/d) = +/- ft²/d

L_e/r_e	18.1
C	1.51
R/r_e	8.64

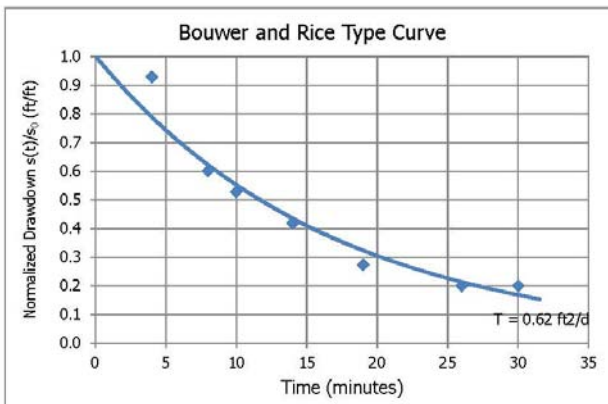
J-Ratio	-1.026
---------	--------

Coef. Of Variation	0.10
--------------------	------



0.620

C coefficient calculated from Eq. 6.5(c) of Butler, The Design, Performance, and Analysis of Slug Tests, CRC Press, 2000.



Appendix F conti.

Cooper and Jacob (1946)

Well Designation:	315
Date:	24-Jul-10

$$V_n(t_i) = \sum_j^i \frac{4\pi T_n s_j}{\ln\left(\frac{2.25 T_n t_j}{r_e^2 S_n}\right)} \Delta t_j$$

Enter early time cut-off for least-squares model fit

Time _{cut} (min):	1	<- Enter or change values here
Time Adjustment (min):	0.6	

Trial S_n: 0.035 <- Enter d for default or enter S_n value

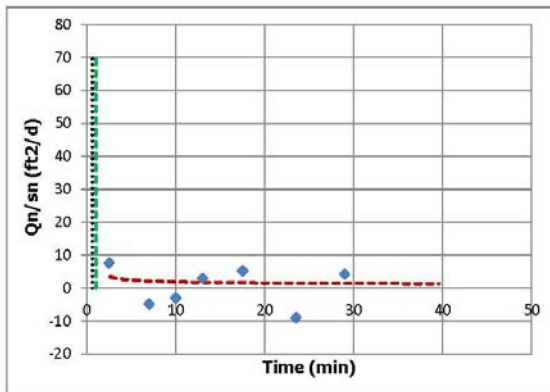
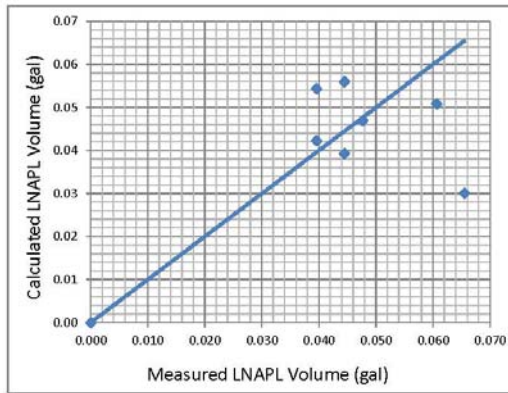
Root-Mean-Square Error: 0.042 <- Minimize this using "Solver"

0.035 <- Working S_n

Trial T_n (ft²/d): 0.509 <- By changing T_n through "Solver"

Add constraint T_n > 0.00001

Model Result: T_n (ft²/d) = 0.51



Appendix F conti.

Cooper, Bredehoeft and Papadopoulos (1967)

Well Designation:	315
Date:	24-Jul-10

Enter early time cut-off for least-squares model fit

Time _{cut} (min):	1	<-- Enter or change values here
Initial Drawdown s _n (ft):	0.25924	

Trial S_n: 0.020 <-- Enter d for default

Root-Mean-Square Error: 0.292 <-- Minimize this using "Solver"

Trial T_n (ft²/d): 0.652 <-- By changing T_n through "Solver"

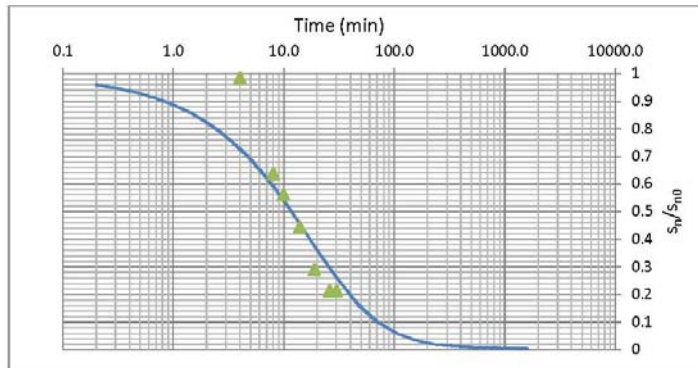
0.014 <-- Working S_n

Add constraint T_n > 0.00001

Model Result:

T_n (ft²/d) = 0.652

T _{min}	0.2
T _{max}	10



J-Ratio
-1.026

Appendix G.

Parametric Analysis of Mean Oil Transmissivity for Three Baildown Tests

APPENDIX G - Example Oil Transmissivity Parametric Analysis Basic Input Data for Slug Withdrawal or Baildown Test Analysis

Location and Timing of Baildown Test				Comments About Data
Well Name:	Aver of 315, 411, 421B			
Site Name:	USGS-National Crude Oil Research Site, near Bemidji, MN			
Database:	Carsel & Parish (1988)			
Start Date:	7/26/2010			Date of bailing the well.
Clock time of start of bailing:	18:00			
Clock time of end of bailing:	18:04			Four small bailer withdrawals
Time spend Bailing well:	0:04:00	(hr:min:sec)		Calculated value based on transducer.
Time of last fluid measurement:	15:00			Clock time of last measurement.
End Date:	7/27/2010	(m/d/yr)		Date of last fluid level measurement.
Test Well Characteristics				
Borehole Diam.:	2.38	(inches)	0.060 (meters)	Data from well log.
Casing ID:	2.00	(inches)	0.051 (meters)	Data from well log.
Casing OD:	2.38	(inches)	0.060 (meters)	Data from well log.
Screen ID:	2.00	(inches)	0.051 (meters)	Data from well log.
Screen OD:	2.38	(inches)	0.060 (meters)	Data from well log.
Measuring Point satckup above ground	1.00	(feet)	0.305 (meters)	Data from well log.
Oil-wet screen length:	1.47	(feet)	0.447 (meters)	Data from pretest fluid levels.
Wtr-wet screen length:	1.55	(feet)	0.473 (meters)	Data from pretest fluid levels.
Aquifer thickness:	60.00	(feet)	18.293 (meters)	Data from logs and site hydrogeology.
Specific oil yield of filter pack sand:	0.054	(dimensionless)		The well has no sand pack
Specific water yield of filter pack sand:	0.0400	0.03	(dimensionless)	The well has no sand pack
Oil and Water Volumes Bailed				
Volume of free LNAPL bailed:	0.28	(gallons)	1.04 (liters)	Measured in field after bailing.
Volume of groundwater bailed:	0.96	(gallons)	3.62 (liters)	Measured in field after bailing.
Fluid Properties				
Specific gravity of oil:	0.891	(dimensionless)		Laboratory measurement.
Dynamic viscosity of oil:	33.50	(centipoise)		Laboratory measurement.
Air-water surface tension:	66.3	(dynes/cm)		Laboratory measurement.
Air-oil surface tension:	19.9	(dynes/cm)		Laboratory measurement.
Oil-water interfacial tension:	27.4	(dynes/cm)		Laboratory measurement.
Groundwater Temperature	47.3	degrees F	8.5 deg C	Average of transducer temperatures
Soil Properties--Filter Pack Sand				
Hydraulic conductivity:	800	(ft/day)	Not relevant here.	Value based on laboratory measurement.
Effective Porosity:	0.3	(dimensionless)		Estimate or laboratory measurement.
Irreducible water saturation:	0.1	(dimensionless)		Estimate or laboratory measurement.
van Genuchten alpha:	4.2	(1/feet)		Initial estimate based on soil texture.
van Genuchten n:	2.1	(dimensionless)		Initial estimate based on soil texture.
van Genuchten m:	0.52	(dimensionless)		Initial estimate based on soil texture.
Soil Properties--Formation				
Hydraulic conductivity:	1	(ft/day)	Preliminary Estimates	Use if different from that calculated.
Effective Porosity:	0.25	(dimensionless)		Estimate or laboratory measurement.
Irreducible water saturation:	0.25	(dimensionless)		Estimate or laboratory measurement.
van Genuchten alpha:	2.5	(1/feet)		Initial estimate based on soil texture.
van Genuchten n:	1.50	(dimensionless)		Initial estimate based on soil texture.
van Genuchten m:	0.33	(dimensionless)		Initial estimate based on soil texture.

* NB : The surface and interfacial tensions are estimated from other data.

Sample	TGI Job	Density of NAPL (gm/ml)	Viscosity of NAPL (centipoise)	Surface Tension Air/Water (dynes/cm)	Interfacial Tension NAPL/Water (dynes/cm)	Surface Tension Air/NAPL (dynes/cm)	Temperature of Measurements	Approx. API Gravity (8.5 deg C)
Well 411 7-26-10	10110	0.8976	44.7	65.1	18.7	27.3	8.5C	26.1

Appendix G conti.

Well ID : Aver of 315, 411, 421B

Parametric Equation Approach to Estimating Hydraulic Properties, Fluid Saturations, and Conductivities in the Formation
 Based on the papers by Parker, Lenhard, and Koppasamy (1987) and Lenhard and Parker (1990)
 Assumes the API (2006) database of matrix properties correlate with hydraulic conductivity using expressions in Luny (2006).
 Assumes static equilibrium between the free oil inside and outside a well screen.

Fluid Properties
 Specific gravity of oil: 0.8006 (dimensionless)
 Dynamic viscosity of free oil: 33.50 centipoise
 Air-water surface tension: 18.30 dynes/cm
 Oil-water surface tension: 19.90 dynes/cm
 Oil-water interfacial tension: 27.40 dynes/cm
 BET-N₂ surface area: 3.32 m²/g
 BET-CO₂ surface area: 2.42 m²/g
Free Oil Thickness in Well: 1.47 feet
 Elevation at Oil-WR Interface: 0 feet
 Elevation increment for calculations: 0.07335 feet

Soil Properties of Formation
 Hydraulic conductivity: 3.03E-01 ft/day
 Effective Porosity: 0.25 (dimensionless)
 Irreducible water saturation: 1.98E-01 (dimensionless)
 van Genuchten alpha: 5.26E-1 /feet
 van Genuchten n: 2.79 (dimensionless)
 van Genuchten m: 0.64 (dimensionless)

Calculated Results
 Geometric mean Oil Conductivity (above-below oil table): 8.10E-05 ft/day
Oil Transmissivity of oil layer (above-below oil table): 3.76E-01 ft²/day
 Geometric mean oil saturation within free oil layer: 1.81E-02
 Specific Volume of Oil (above-below oil table): 1.24E-01 ft³/ft³
 Specific Volume of Water (above & below oil table): 3.01E-01 ft³/ft³
 Estimate of oil storativity: 2.28E-03
Mean LNAPL Transmissivity Determined with C&P data: 3.760E-01 ft²/day

Matches: Mean LNAPL Transmissivity Determined with C&P data: 3.760E-01 ft²/day

Table of Calculations:

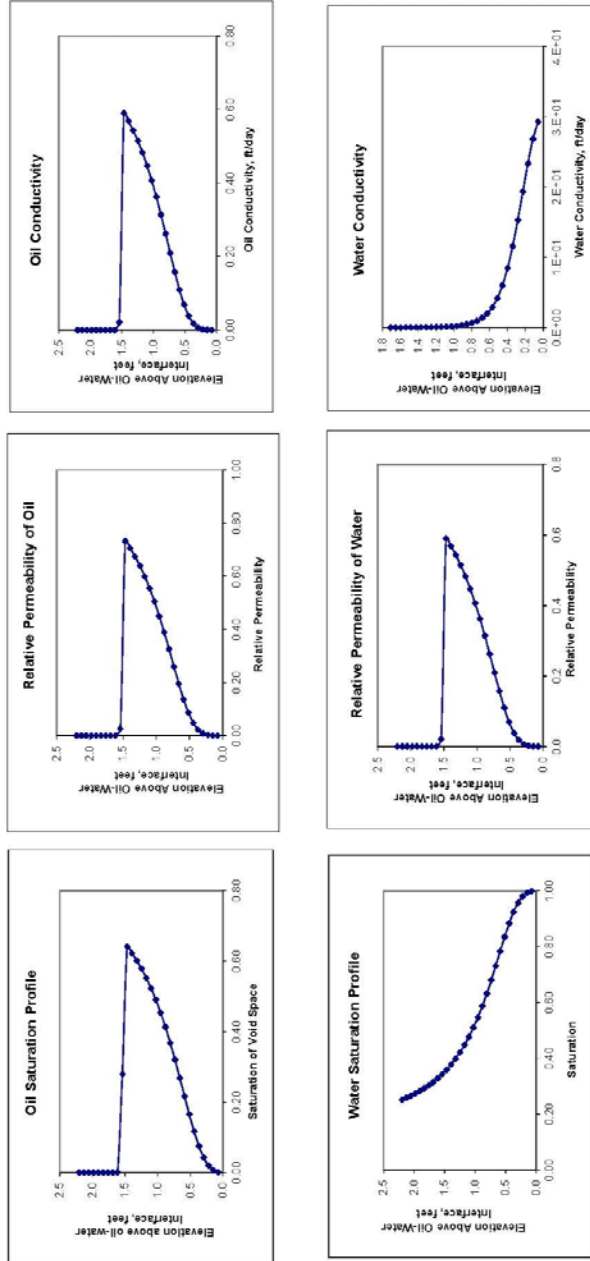
Bottom-up Order of Rev	Elevation Above of Oil-WR Interface (feet)	Oil-Water Capillary Head (feet)	Total Oil-Water Sat'n	Water Sat'n	Oil Sat'n	Water Relative Perm.	Oil Relative Perm.	Water K (mD)	Oil K (mD)	Increment Oil Trans. (ft ² /day)	Increment Water Specific Volume (ft ³ /ft ³)	Increment Oil Specific Volume (ft ³ /ft ³)	k-Water 1st Term	k-Water 2nd Term	k-Oil 1st Term
30	2.20	0.653	0.241	0.150	1.00E-04	2.67E-04	1.53E-11	8.08E-03	1.23E-11	9.15E-13	4.61E-03	1.83E-06	3.61E-01	7.37E-04	1.08E-02
29	2.13	0.588	0.233	0.152	1.00E-04	3.25E-04	1.66E-11	5.98E-03	1.34E-11	9.79E-13	4.73E-03	1.83E-06	3.72E-01	8.59E-04	1.08E-02
28	2.05	0.523	0.215	0.155	1.00E-04	4.10E-04	1.78E-11	1.79E-03	1.45E-11	1.05E-12	4.87E-03	1.83E-06	3.83E-01	1.07E-03	1.08E-02
27	1.98	0.457	0.217	0.160	1.00E-04	5.13E-04	1.91E-11	1.54E-02	1.54E-11	1.13E-12	5.02E-03	1.83E-06	3.95E-01	1.32E-03	1.08E-02
26	1.91	0.392	0.209	0.166	1.00E-04	6.47E-04	2.06E-11	1.29E-02	1.69E-11	1.22E-12	5.18E-03	1.83E-06	4.08E-01	1.55E-03	1.08E-02
25	1.83	0.327	0.201	0.177	1.00E-04	8.23E-04	2.23E-11	1.06E-02	1.87E-11	1.32E-12	5.36E-03	1.83E-06	4.22E-01	1.75E-03	1.08E-02
24	1.76	0.261	0.193	0.195	1.00E-04	1.04E-03	2.42E-11	8.20E-02	1.94E-11	1.43E-12	5.56E-03	1.83E-06	4.36E-01	1.92E-03	1.08E-02
23	1.69	0.196	0.185	0.231	1.00E-04	1.26E-03	2.63E-11	4.14E-02	2.10E-11	1.56E-12	5.78E-03	1.83E-06	4.52E-01	2.07E-03	1.08E-02
22	1.61	0.131	0.177	0.322	1.00E-04	1.78E-03	2.89E-11	5.49E-02	2.30E-11	1.70E-12	6.02E-03	1.83E-06	4.69E-01	2.20E-03	1.08E-02
21	1.54	0.065	0.169	0.622	2.76E-01	2.32E-03	2.64E-02	7.11E-02	2.12E-02	1.96E-03	6.29E-03	5.12E-03	4.87E-01	2.31E-03	1.08E-02
20	1.47	0.000	0.160	1.0	0.939	3.12E-03	7.32E-01	5.47E-02	5.93E-02	4.33E-02	6.59E-03	1.17E-02	5.07E-01	2.40E-03	5.69E-01
19	1.39	0.0	0.152	1.0	0.978	4.20E-03	7.03E-01	1.27E-01	5.68E-02	4.17E-02	6.95E-03	1.14E-02	5.27E-01	2.50E-03	6.30E-01
18	1.32	0.0	0.144	1.0	0.998	5.71E-03	6.74E-01	1.73E-01	5.43E-02	3.89E-02	7.31E-03	1.10E-02	5.46E-01	1.04E-02	6.90E-01
17	1.25	0.0	0.136	1.0	0.422	7.85E-03	6.39E-01	2.38E-01	5.13E-02	3.78E-02	7.73E-03	1.05E-02	5.73E-01	1.37E-02	8.20E-01
16	1.17	0.0	0.128	1.0	0.448	1.05E-02	5.99E-01	3.31E-01	4.83E-02	3.54E-02	8.21E-03	1.01E-02	5.95E-01	1.82E-02	8.01E-01
15	1.10	0.0	0.120	1.0	0.477	1.43E-02	5.53E-01	4.68E-01	4.47E-02	3.28E-02	8.79E-03	9.59E-03	6.26E-01	2.43E-02	7.79E-01
14	1.03	0.0	0.112	1.0	0.510	2.18E-02	5.03E-01	6.61E-01	4.07E-02	2.89E-02	9.35E-03	8.99E-03	6.59E-01	3.32E-02	7.53E-01
13	0.95	0.0	0.104	1.0	0.546	3.13E-02	4.49E-01	5.48E-01	3.62E-02	2.66E-02	1.00E-02	8.32E-03	6.88E-01	4.54E-02	7.29E-01
12	0.88	0.0	0.096	1.0	0.587	4.43E-02	3.89E-01	1.37E+00	3.14E-02	2.30E-02	1.08E-02	7.57E-03	7.21E-01	6.92E-02	6.93E-01
11	0.81	0.0	0.088	1.0	0.632	6.06E-02	3.29E-01	1.93E+00	2.62E-02	1.92E-02	1.16E-02	6.75E-03	7.57E-01	8.67E-02	6.54E-01
10	0.73	0.0	0.080	1.0	0.680	9.54E-02	2.60E-01	2.89E+00	2.09E-02	1.54E-02	1.25E-02	5.85E-03	7.93E-01	1.07E-01	6.09E-01
9	0.66	0.0	0.072	1.0	0.731	1.38E-01	1.96E-01	4.19E+00	1.50E-02	1.10E-02	1.34E-02	4.99E-03	8.25E-01	1.67E-01	5.59E-01
8	0.59	0.0	0.064	1.0	0.784	2.19E-01	1.36E-01	6.03E+00	1.03E-02	8.06E-03	1.44E-02	3.97E-03	8.55E-01	2.75E-01	5.01E-01
7	0.51	0.0	0.056	1.0	0.835	3.18E-01	8.60E-02	8.45E+00	6.93E-02	5.08E-03	1.53E-02	3.02E-03	8.85E-01	3.10E-01	4.37E-01
6	0.44	0.0	0.048	1.0	0.883	4.38E-01	6.20E-02	1.15E+01	5.10E-02	3.83E-03	1.62E-02	2.14E-03	9.31E-01	3.68E-01	3.68E-01
5	0.37	0.0	0.040	1.0	0.925	5.04E-01	4.79E-02	1.53E+01	3.79E-02	2.81E-03	1.70E-02	1.45E-03	9.55E-01	5.93E-01	2.99E-01
4	0.29	0.0	0.032	1.0	0.957	6.38E-01	3.12E-03	1.93E+01	2.79E-02	1.40E-03	1.79E-02	7.83E-04	9.75E-01	6.54E-01	2.22E-01
3	0.22	0.0	0.024	1.0	0.980	7.70E-01	2.08E-03	2.33E+01	1.69E-03	1.20E-02	1.89E-02	3.62E-04	9.88E-01	7.75E-01	1.51E-01
2	0.15	0.0	0.016	1.0	0.994	8.85E-01	2.89E-04	2.65E+01	1.23E-04	1.70E-05	1.82E-02	1.19E-04	9.88E-01	8.88E-01	8.68E-01
1	0.07	0.0	0.008	1.0	0.999	9.66E-01	9.27E-05	2.93E+01	7.47E-05	5.49E-07	1.83E-02	1.73E-05	9.95E-01	9.67E-01	3.31E-01

Appendix G conti.

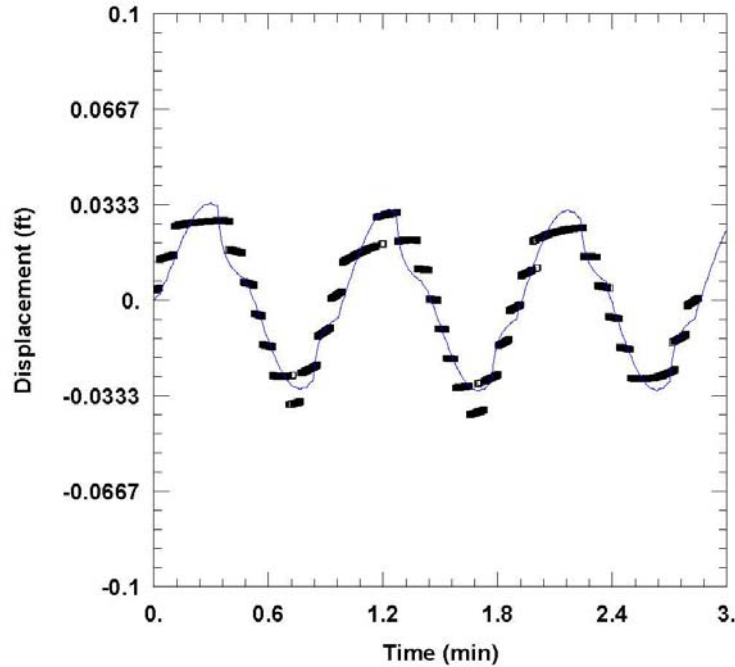
k-Oil 2nd Term	k-Oil 3rd Term	Log of Water Salt	Log of DI K	Log of Oil Barn.
9.73E-00	5.73E-01	-0.599	-0.0524	-4.000
9.73E-00	5.73E-01	-0.588	-0.0874	-4.000
9.67E-00	5.67E-01	-0.576	-0.0844	-4.000
9.61E-00	5.61E-01	-0.563	-0.0812	-4.000
9.55E-00	5.55E-01	-0.549	-0.0780	-4.000
9.50E-00	5.50E-01	-0.534	-0.0746	-4.000
9.44E-00	5.44E-01	-0.519	-0.0710	-4.000
9.38E-00	5.38E-01	-0.502	-0.0673	-4.000
9.32E-00	5.32E-01	-0.485	-0.0635	-4.000
9.26E-00	5.26E-01	-0.465	-0.0597	-3.954
9.20E-00	5.20E-01	-0.444	-0.0559	-3.908
9.14E-00	5.14E-01	-0.423	-0.0526	-3.862
9.08E-00	5.08E-01	-0.400	-0.296	-0.221
8.98E-00	5.08E-01	-0.375	-0.288	-0.238
8.88E-00	5.08E-01	-0.349	-0.316	-0.258
8.78E-00	5.08E-01	-0.322	-0.350	-0.281
8.68E-00	5.08E-01	-0.293	-0.391	-0.320
8.58E-00	5.08E-01	-0.263	-0.441	-0.348
8.48E-00	5.08E-01	-0.231	-0.503	-0.394
8.38E-00	5.08E-01	-0.197	-0.584	-0.458
8.28E-00	5.08E-01	-0.162	-0.689	-0.545
8.18E-00	5.08E-01	-0.126	-0.803	-0.651
8.08E-00	5.08E-01	-0.089	-0.959	-0.783
7.98E-00	5.08E-01	-0.078	-1.159	-0.933
7.88E-00	5.08E-01	-0.054	-1.416	-1.123
7.78E-00	5.08E-01	-0.034	-1.748	-1.371
7.68E-00	5.08E-01	-0.019	-2.134	-1.705
7.58E-00	5.08E-01	-0.009	-2.775	-2.189
7.48E-00	5.08E-01	-0.003	-3.655	-2.825
7.38E-00	5.08E-01	0.000	-5.127	-3.625

Appendix G conti.

Fluid Saturation and LNAPL Mobility Parameter Plots
 Well ID: Aver of 315, 411, 421B

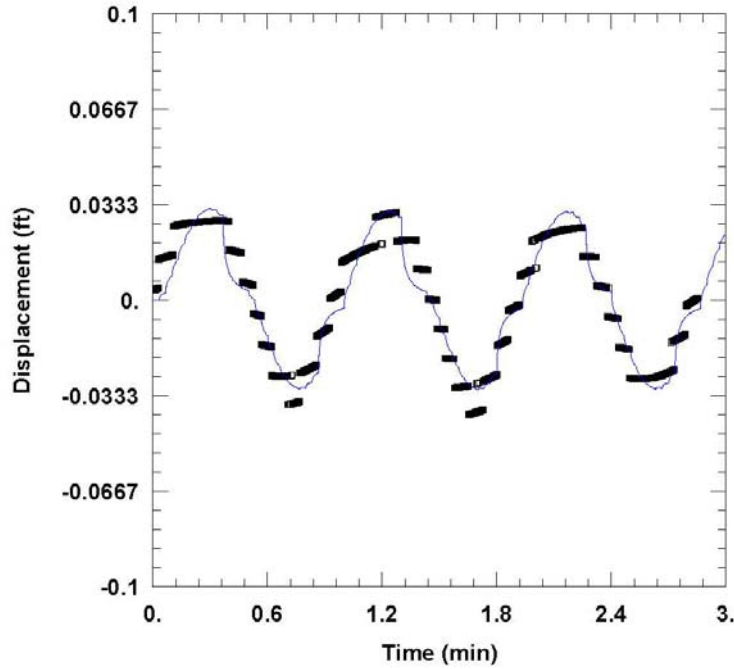


Appendix H – AQTESOLV Printouts for Periodic Slug Tests



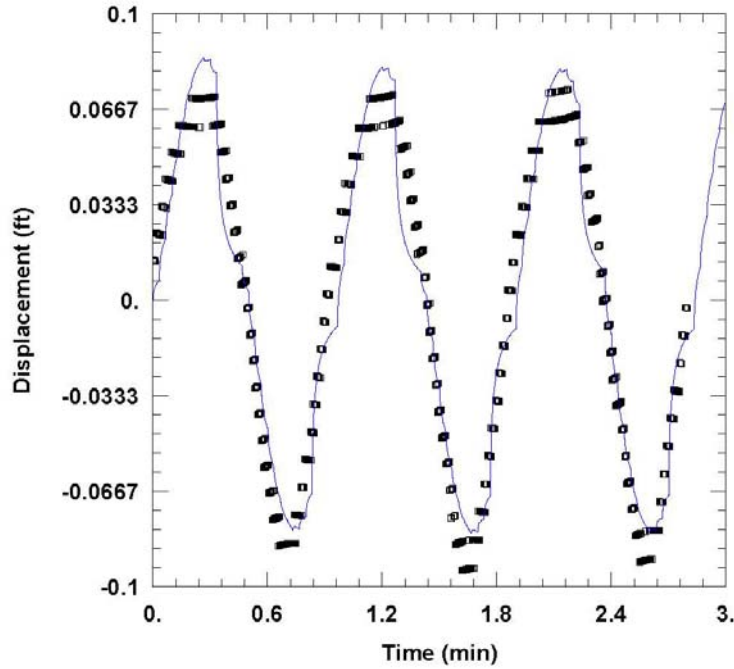
RESPONSE AT OBS. WELL 9205A					
Data Set: C:\...\20140208.OscillatingSlug_Bemidji_531A_9205A_Theis.aqt					
Date: <u>02/08/14</u>			Time: <u>21:20:13</u>		
PROJECT INFORMATION					
Location: <u>Bemidji, MN</u>					
Test Well: <u>531A</u>					
Test Date: <u>June 2010</u>					
WELL DATA					
Pumping Wells			Observation Wells		
Well Name	X (ft)	Y (ft)	Well Name	X (ft)	Y (ft)
531A	1124544.17289091	06	9205A	1124552.17289095	24
SOLUTION					
Aquifer Model: <u>Confined</u>			Solution Method: <u>Theis</u>		
T = <u>1.897E+4 ft²/day</u>			S = <u>0.002045</u>		
Kz/Kr = <u>0.001015</u>			b = <u>48. ft</u>		

Appendix H Conti.



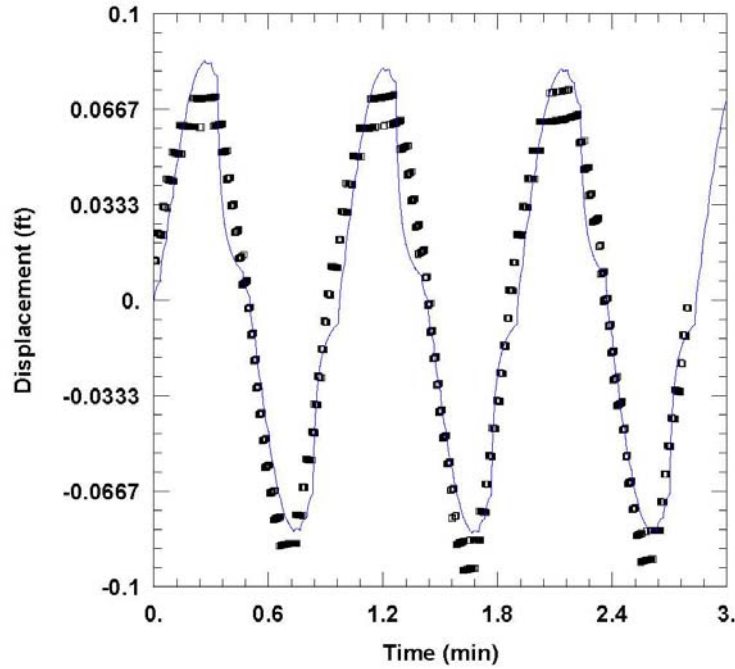
RESPONSE AT OBS. WELL 9205A					
Data Set: C:\...\20140209.OscillatingSlug_Bemidji_531A_9205A_DoughertyBabu.aqt					
Date: <u>12/01/14</u>			Time: <u>13:50:55</u>		
PROJECT INFORMATION					
Location: <u>Bemidji, MN</u>					
Test Well: <u>531A</u>					
Test Date: <u>June 2010</u>					
AQUIFER DATA					
Saturated Thickness: <u>48. ft</u>			Anisotropy Ratio (Kz/Kr): <u>0.07359</u>		
WELL DATA					
Pumping Wells			Observation Wells		
Well Name	X (ft)	Y (ft)	Well Name	X (ft)	Y (ft)
531A	1124544.17	289091.06	9205A	1124552.17	289095.24
SOLUTION					
Aquifer Model: <u>Confined</u>			Solution Method: <u>Dougherty-Babu</u>		
T = <u>1.043E+4 ft²/day</u>			S = <u>0.0006733</u>		
Kz/Kr = <u>0.07359</u>			Sw = <u>-4.868</u>		
r(w) = <u>0.1 ft</u>			r(c) = <u>0.083 ft</u>		

Appendix H Conti.



RESPONSE AT OBS. WELL 9205B					
Data Set: C:\...\20140119_Sinusoidal_Bemidji_531A_9205B_Theis.aqt					
Date: 01/23/14			Time: 11:29:32		
PROJECT INFORMATION					
Test Well: 531A					
Test Date: 07/23/2010					
WELL DATA					
Pumping Wells			Observation Wells		
Well Name	X (ft)	Y (ft)	Well Name	X (ft)	Y (ft)
531A	0	0	□ 9205B	4.056	0
SOLUTION					
Aquifer Model: <u>Confined</u>			Solution Method: <u>Theis</u>		
T = 1.065E+4 ft ² /day			S = 0.001066		
Kz/Kr = 0.002024			b = 48. ft		

Appendix H Conti.



RESPONSE AT OBS. WELL 9205B					
Data Set: C:\...\20140122_Sinusoidal_Bemidji_531A_9205B_DoBabu.aqt					
Date: <u>01/25/14</u>			Time: <u>00:38:07</u>		
PROJECT INFORMATION					
Test Well: <u>531A</u>					
Test Date: <u>07/23/2010</u>					
AQUIFER DATA					
Saturated Thickness: <u>48. ft</u>			Anisotropy Ratio (Kz/Kr): <u>0.009949</u>		
WELL DATA					
Pumping Wells			Observation Wells		
Well Name	X (ft)	Y (ft)	Well Name	X (ft)	Y (ft)
<u>531A</u>	<u>0</u>	<u>0</u>	<u>9205B</u>	<u>4.056</u>	<u>0</u>
SOLUTION					
Aquifer Model: <u>Confined</u>			Solution Method: <u>Dougherty-Babu</u>		
T = <u>5927.1 ft²/day</u>			S = <u>0.0001116</u>		
Kz/Kr = <u>0.009949</u>			Sw = <u>-5.</u>		
r(w) = <u>0.1 ft</u>			r(c) = <u>0.083 ft</u>		